Imperial College London

Doctoral Thesis

# Permeability of fracture networks generated through geomechanical fracture-growth simulations

*Author:*
Robin Nicholas Thomas

*Supervisors:*
Prof. Robert W. Zimmerman
Dr. Adriana Paluszny

*A thesis submitted in fulfilment of the requirements for the degree of Doctor of Philosophy*

*in the*

Petroleum Engineering & Rock Mechanics Group
Department of Earth Science and Engineering

October 2019

IMPERIAL COLLEGE LONDON

# *Abstract*

Faculty of Engineering
Department of Earth Science and Engineering

Doctor of Philosophy

**Permeability of fracture networks generated through geomechanical fracture-growth simulations**

by Robin Nicholas Thomas

Fracture networks in subsurface rocks significantly impact the mechanical and hydraulic properties of the Earth. Realistic models of fracture networks underpin a variety of important geoscience fields. The physics of how fractures propagate and interact control how networks develop, but such processes are not routinely incorporated into discrete fracture network (DFN) models.

This thesis presents a novel approach to model deformation of isotropic, homogeneous, and linear elastic brittle rocks, leading to the development of dense three-dimensional fracture networks. These networks provide realistic representations of subsurface networks that honour the physical process of concurrent fracture growth and interaction. This thesis proposes a number of novel developments that advance the field of discrete fracture modelling, with the aim of growing dense networks in a realistic manner. It presents a number of new validations for fracture growth and interaction, providing benchmarks for the accuracy required to generate realistic networks.

Towards the goal of generating realistic fracture networks, several topics are studied numerically. A method for examining fracture interaction in three-dimensions is introduced, which quantifies the change in stress a fracture undergoes due to a neighborhood of nearby fractures. Fracture interaction is examined spatially in novel fracture interaction maps. Realistic fracture growth is demonstrated in both tension and compression. The effect of fracture interaction on mutual fracture growth is demonstrated on fracture arrays. The hydraulic properties of a spent $UO_2$ fuel pellet are quantified using an effective permeability computation method.

The thesis concludes by presenting six geomechanical discrete fracture networks (GDFNs). The primary influences on the geometric and hydraulic properties of these GDFNs are the stresses causing growth and fracture interaction, rather than the random process of initial fracture insertion. GDFNs provide a new way of understanding subsurface processes, and improve our capacity to model hydro-mechanical processes in fractured rock masses.

# Declaration of Authorship

I, Robin Nicholas Thomas, declare that this thesis titled, 'Permeability of fracture networks generated through geomechanical fracture-growth simulations' and the work presented in it are my own. I confirm that:

- This work was done wholly or mainly while in candidature for a research degree at this University.
- Where any part of this thesis has previously been submitted for a degree or any other qualification at this University or any other institution, this has been clearly stated.
- Where I have consulted the published work of others, this is always clearly attributed.
- Where I have quoted from the work of others, the source is always given. With the exception of such quotations, this thesis is entirely my own work.
- I have acknowledged all main sources of help.
- Where the thesis is based on work done by myself jointly with others, I have made clear exactly what was done by others and what I have contributed myself.

The copyright of this thesis rests with the author. Unless otherwise indicated, its contents are licensed under a Creative Commons Attribution-Non Commercial 4.0 International Licence (CC BY-NC).

Under this licence, you may copy and redistribute the material in any medium or format. You may also create and distribute modified versions of the work. This is on the condition that: you credit the author and do not use it, or any derivative works, for a commercial purpose.

When reusing or sharing this work, ensure you make the licence terms clear to others by naming the licence and linking to the licence text. Where a work has been adapted, you should indicate that the work has been changed and describe those changes.

Please seek permission from the copyright holder for uses of this work that are not included in this licence or permitted under UK Copyright Law.

*The popular stereotype of the researcher is that of a skeptic and a pessimist. Nothing could be further from the truth! Scientists must be optimists at heart, in order to block out the incessant chorus of those who say "It cannot be done."*

Academician Prokhor Zakharov, University Commencement
*Sid Meier's Alpha Centauri, 1999*

# *Acknowledgements*

This PhD project was funded by the Natural Environment Research Council, Radioactive Waste Management Limited, and Environment Agency as part of the HydroFrame project (NE/L000660/1), through the Radioactivity and the Environment (RATE) programme. I have also received funds from the European Commission through the TRUST Collaborative Project (309067) and the CONTAIN CCS Grand Challenge in Geological Storage (contract number GA/12F/101).

---

The document before you is the product of seven consecutive years of learning and working in the Department of Earth Science & Engineering at Imperial College London, including my undergraduate degree and PhD project. I have immensely enjoyed this time, and I will carry the lessons I have learned here for life - not as a scar, but as a debt[1]. There are too many people to pay respects to in this short section, as so many have taught and supported me through this time, but I might as well try anyway.

The first in line to thank must certainly be my supervisors. Adriana Paluszny has served as a constant source of inspiration and wisdom since I began my MSci project with her all the way back in 2014. At the time, I could not have guessed at how hard working and supportive she could be. Adriana has put an inordinate amount of time and patience towards cultivating my technical and professional skills. She has instilled into me a fascination for problem solving, basic research, and, of course, C++. I could not have asked for a better supervisor and friend than Adriana. Robert Zimmerman has been a dedicated and generous mentor, guiding our research towards greater heights. His unsurpassed knowledge, experience, and attention to detail has been a great asset to our work. He is also responsible for handling all sorts of onerous administrative tasks, including coordinating the HydroFrame project, and securing further funding for me towards the end of the project, without which this work would be much weaker. I am immensely fortunate to have been supervised by Robert and Adriana. Their continued commitment to teaching and supervision is an ongoing blessing that the Department will benefit from for decades to come.

The Rock Mechanics group at Imperial College has been home to many other great scientists during my time, who laid the foundations on which my own work has been built. Morteza Nejati's name can be found throughout this thesis for good reason. During his PhD, he designed and implemented methods for stress intensity factor calculation and fracture surface contact resolution. Without these advancements, the achievements of this thesis simply would not have been possible. Philipp Lang contributed the flow and effective permeability calculation method, another part of the ICGT which enabled this work to come together.

Other researchers have also made brilliant contributions to the Imperial College Geomechanics Toolkit, including Saeed Salimzadeh and Vasia Tsaparli. I thank Ivar Stefansson for visiting in 2018 to work with us on the ICGT, sharing many brilliant insights in the process. Adriana's name must be mentioned again - ICGT simply could not exist without her long term

[1] At least, until I pay all of those student loans off.

commitment to careful development and maintenance. I must also thank the various students I have co-supervised with Adriana during various summers, in particular, Sofia Roucan, whose RhinoPython script for imaging cut-planes through fractures has seen use in several places in this thesis. Completing a PhD within the RATE programme has been incredibly rewarding, providing me with a network of other researchers, support staff, and friends. Particular thanks must be given to the organizers of the two summer schools I was able to attend (Chernobyl in 2015, and the Grimsel Test Site in 2016).

I have been fortunate to find so many great friends within the Department of Earth Science & Engineering. A particular highlight has been lunchtimes and crosswords with the 'extended' Minerals Processing Group[2], where we would put down our scientific tools to gawp at the arcane English language. The two student societies I have been most involved with are the Science Fiction & Fantasy and Tabletop Gaming societies. I've seen too many people pass through these groups to mention specific names, but rest assured, if we ever shared a table, rulebook, screen, sofa, beanbag, or committee, you contributed to some of the best times I had as a student[3]. In short, Imperial College London is great place to be if you are a nerd.

In spite of this fine city's attempts to chew me up and spit me out, the help my of many friends and housemates has ensured I have remained un-spewed and un-salivated. To my undergraduate housemates (Frey, Gabby, James H, Jemma, and Luke) I owe a great debt[4] for your emotional support and patience through times both weird and wonderful. I am particularly thankful for my housemates during my postgraduate years. James W, we shared a great year together, and it was always a tremendous pleasure to come back home and hear about all the masters course drama. As long as we both keep our professional feet on geological ground, I'm sure we will cross paths again and again. Jonny, by now, you are more like a sibling than a housemate. Your infectious enthusiasm carried me through the latter years of my project.

Finally, I must thank those closest to my heart, my family. The patience, advice, and love of my parents and brothers made all the steps that led to this completed thesis possible. And, of course, Zoe. Your companionship has made me a better person. I could never have known how important your unconditional support would be to both my work and my life. Our journey began many years ago, right at the start of our first degrees, and long may it continue - towards the ultimate goal of owning several cats and/or dogs.

[2]Better known as the 'Cool People', including but not limited to: Angus, Becky, Cata, Christian, Dennis, Diego, Izzy, Jen, Jorge, Juliana, Lucho, Pablo, Pancho, Paulina, and Ruben.

[3]Particular thanks to my long term RPG group, including the bright minds of Aviv, Chris, Diba, Jonah, Peter, and Sanchit.

[4]Figuratively, not monetarily.

# Contents

**Abstract** i

**Declaration of Authorship** iii

**Acknowledgements** v

**Contents** vii

**List of Figures** xii

**List of Tables** xv

**Symbols** xvi

**Abbreviations** xxi

**1 Introduction** 1
- 1.1 Background of the HydroFrame project . . . 1
- 1.2 Motivation . . . 2
  - 1.2.1 Radioactive waste disposal . . . 2
  - 1.2.2 Quantification of fractured rock effective permeability . . . 3
  - 1.2.3 Incorporating geomechanics into discrete fracture networks . . . 5
- 1.3 Thesis overview . . . 6
  - 1.3.1 Related publications . . . 8

**2 A finite element based methodology for simulating discrete fractures in geological media** 10
- 2.1 Introduction . . . 10
- 2.2 Linear elastic fracture mechanics . . . 11
  - 2.2.1 Mathematical description of linear elasticity . . . 13
    - 2.2.1.1 Implications of assuming linear elasticity . . . 13
  - 2.2.2 Fracture initiation . . . 15
  - 2.2.3 Fracture tip stress intensity factors . . . 16

2.2.4 Fracture extension . . . 17
2.3 The Imperial College Geomechanics Toolkit . . . 18
2.3.1 Validations of ICGT . . . 20
2.3.2 Finite element based growth algorithm . . . 21
2.3.3 Domain geometry and discretisation . . . 21
2.3.4 Computation of stress and displacement . . . 25
2.3.5 Fracture surface contact algorithm . . . 26
2.3.5.1 Contact problem description . . . 26
2.3.5.2 Traction-based Augmented Lagrangian approach . . . 28
2.3.5.3 Gap-based Augmented Lagrangian approach . . . 28
2.3.6 Stress intensity factor computation . . . 29
2.3.6.1 Disk-shaped domain integral . . . 30
2.3.6.2 Displacement correlation . . . 33
2.3.6.3 Sampling domain radius . . . 34
2.3.7 Fracture growth . . . 35
2.3.7.1 Mixed mode propagation criterion . . . 35
2.3.7.2 Propagation angle criterion . . . 36
2.3.7.3 Propagation length criterion . . . 37
2.3.7.4 Fracture extension . . . 37
2.3.7.5 Fracture intersection handling . . . 38
2.3.7.6 Implications for SIF computation following intersection . . . 40
2.3.7.7 Simulation end condition . . . 41
2.4 Contemporary methods for modelling fractured media . . . 41
2.4.1 Continuum based methods . . . 41
2.4.1.1 Smeared fracture models . . . 42
2.4.1.2 Continuum models with discrete fractures . . . 43
2.4.2 Discrete element methods . . . 44
2.4.3 Combined finite-discrete element methods . . . 45
2.4.4 Perturbation methods . . . 45
2.5 Validation of stress intensity factors around static fractures . . . 46
2.5.1 Analytical solutions for stress intensity factors . . . 47
2.5.1.1 Uniaxial tension . . . 47
2.5.1.2 Uniaxial compression . . . 47
2.5.2 Error calculation . . . 49
2.5.3 Error for different domain radii . . . 50
2.6 Quantification of boundary effects on stress intensity factors . . . 52
2.7 Discussion . . . 54

**3 Understanding fracture interaction through study of stress intensity factor perturbations 58**
3.1 Introduction . . . 58
3.2 Stress intensity factor perturbations due to interaction . . . 61
3.2.1 Identification of interaction effects . . . 61
3.2.2 Numerical variation of stress intensity factors . . . 62
3.2.3 Comparison to other methods . . . 63
3.3 SIF perturbations for common geometries . . . 64
3.4 Quantification of interaction . . . 66

3.4.1 Definition of circumferential SIF perturbation, $C$ . . . 67
3.4.2 Definition of maximum SIF perturbation, $M_i$ . . . 68
3.4.3 Definition of the amplification to shielding ratio, $\epsilon_i$ . . . 68
3.4.4 Comments on interaction measures . . . 70
3.4.5 Variation of $C$ and $M$ with separation . . . 70
3.5 Interaction maps . . . 72
3.5.1 Interaction variation maps of $C_i$ in tension . . . 75
3.5.2 Interaction variation maps of $M_i$ in tension . . . 76
3.5.3 Interaction variation maps of $\epsilon_i$ in tension . . . 77
3.5.4 Interaction during compression . . . 78
3.6 Discussion . . . 81
3.6.1 Geological context . . . 81
3.6.2 Computational considerations . . . 82
3.6.3 Recommended use of interaction measures . . . 83
3.6.4 Contrasting $C$ and $M_i$ . . . 84
3.7 Conclusions . . . 84

**4 Growth of multiple fractures under tension and compression 86**
4.1 Introduction . . . 86
4.1.1 Fracture interaction in geological media . . . 86
4.1.2 Modelling of three-dimensional fracture propagation . . . 87
4.2 Modified two-step Paris-type extension criterion . . . 90
4.3 Growth of isolated fractures . . . 92
4.3.1 Tension . . . 92
4.3.2 Compression . . . 93
4.3.3 Comparison with experimental results . . . 94
4.4 Effect of fracture propagation exponent on growth . . . 97
4.4.1 Low growth rate exponents . . . 97
4.4.2 High growth rate exponents . . . 98
4.4.3 Effects due to maximum extension lengths . . . 99
4.5 Growth of multiple fractures . . . 101
4.5.1 Fracture growth exponent effects on arrays . . . 102
4.5.2 Outcrop visualisation of arrays . . . 104
4.5.3 Non-uniform arrays . . . 106
4.6 Discussion . . . 106
4.7 Conclusion . . . 109

**5 Permeability analysis of fractured media 111**
5.1 Introduction . . . 111
5.1.1 Representative element volumes for fractured systems . . . 112
5.1.2 Analytical methods for calculating effective permeability . . . 113
5.1.3 Numerical methods for calculating porous flow and permeability . . . 115
5.1.3.1 Dual-porosity methods . . . 115
5.1.3.2 Discrete fracture network approaches to porous flow and permeability . . . 116
5.1.4 Chapter summary . . . 117
5.2 Flow methodology . . . 117

5.2.1 Element-wise permeability . . . 118
5.2.2 Governing equations for flow . . . 119
5.2.3 Finite element domain configuration . . . 120
5.2.4 Validation . . . 122
5.3 Flow in a static fracture network: spent $UO_2$ fuel study . . . 122
5.3.1 Spent $UO_2$ fuel background . . . 122
5.3.2 Fuel assembly and structure . . . 124
5.3.2.1 Fracturing of fuel pins . . . 125
5.3.3 AGR fuel fracture analysis . . . 126
5.3.3.1 Imaging . . . 126
5.3.3.2 Fracture analysis . . . 127
5.3.3.3 Fracture network reconstruction . . . 130
5.3.3.4 $UO_2$ porosity and permeability . . . 132
5.3.3.5 Fracture permeability . . . 133
5.3.3.6 Flow and equivalent permeability . . . 134
5.3.4 Results and discussion . . . 135
5.3.5 Conclusion . . . 138

**6 Growth and flow in geomechanical fracture networks 140**
6.1 Introduction . . . 140
6.1.1 Review of discrete fracture network permeability studies . . . 143
6.1.1.1 Discrete fracture networks with uniform apertures . . . 143
6.1.1.2 Discrete fracture networks with mechanical apertures . . . 145
6.1.1.3 Geomechanical discrete fracture networks . . . 146
6.1.2 Characterisation of fracture networks . . . 149
6.1.2.1 Real networks . . . 151
6.1.3 Synthetic networks . . . 153
6.2 Challenges in growing dense fracture networks . . . 154
6.2.1 Stress intensity factor smoothing . . . 155
6.2.2 Discretisation in late-stage GDFNs . . . 155
6.2.3 Fracture intersection example . . . 157
6.2.4 Flow channeling through fracture intersections . . . 159
6.3 Generated geomechanical discrete fracture networks . . . 159
6.3.1 Changes in geometry during growth GDFNs . . . 163
6.3.1.1 Changes in geometry of GDFN B in detail . . . 166
6.3.2 Statistical analysis of fracture geometry during GDFN growth . . . 169
6.3.3 Outcrop visualisation of GDFNs . . . 171
6.3.4 Fracture surface area frequency analysis . . . 173
6.4 Hydraulic properties of geomechanical discrete fracture networks with uniform fracture apertures . . . 174
6.4.1 Visualisation of GDFN effective permeability using ellipsoids . . . 175
6.4.2 Flow comparison with stochastic discrete fracture networks . . . 178
6.4.2.1 Stochastic network generation . . . 179
6.4.2.2 Directional permeabilities of geomechanical and stochastic discrete fracture networks . . . 180
6.4.2.3 Percolation in GDFNs and SDFNs . . . 181
6.4.2.4 Permeability magnitudes in GDFNs and SDFNs . . . 186

6.4.3 Intersections in geomechanical discrete fracture networks . . . . . 186
6.4.4 Influence of mesh refinement on effective permeability . . . . . 188
6.5 Effective permeability of geomechanical discrete fracture networks with variable fracture apertures . . . . . 190
6.5.1 Mechanical fracture aperture calculation . . . . . 190
6.5.2 Permeability of geomechanical discrete fracture networks under different stress magnitudes . . . . . 191
6.5.3 Aperture distribution and total fracture void space . . . . . 192
6.5.4 Directional permeability for different tensile stress magnitudes . . 194
6.6 Discussion . . . . . 199
6.6.1 Parameters influencing geomechanical discrete fracture network generation . . . . . 199
6.6.2 Percolation in geomechanical discrete fracture networks . . . . . 201
6.6.3 Further methods for improving geomechanical network realism . . 202
6.6.4 Comparing geomechanical networks to subsurface networks . . . . 204
6.7 Conclusions . . . . . 206

**7 Conclusions** **208**
7.1 Future work . . . . . 211

**Bibliography** **214**

# List of Figures


1.1 Artist's impression of a geological disposal facility . . . . . 4

2.1 Fracture tip deformation modes . . . . . 16
2.2 Typical fatigue fracture growth behaviour described by a Paris-type law. . 18
2.3 Fracture surface discretisation . . . . . 23
2.4 Non-quarter point and quarter point quadratic finite elements . . . . . 24
2.5 Cut plane through four meshes . . . . . 24
2.6 Schematic of vectors $\mathbf{g}_T$ and $\mathbf{g}_N$ for one node . . . . . 27
2.7 Schematic diagrams of the volumetric domain and disk-shaped domain integral methods . . . . . 31
2.8 Local coordinate system used for the Displacement Correlation (DC) method . . . . . 34
2.9 Growth of fracture using fracture tip growth vectors . . . . . 37
2.10 Analytical and numerical stress intensity factors around an isolated fracture 48
2.11 Stress intensity factor and propagation angle error for an inclined fracture under three stress states, with the domain radius $R_d$ set to $0.5|B_d|$ . . . . 51
2.12 Stress intensity factor and propagation angle error for an inclined fracture under three stress states, with the domain radius $R_d$ set to $a/10$ . . . . . 55
2.13 SIFs on fractures in different size domains for different numbers of fracture tip nodes. . . . . 56
2.14 Change in SIFs relative to the analytical solution for an inclined penny shaped fracture under tension depending on the size of the domain. . . . . 57

3.1 Perturbation of stress intensity factors on an inclined fracture under tension due to interaction . . . . . 62
3.2 Comparison of stress intensity factor perturbations with other models . . 64
3.3 Example mesh around two fractures with separation $\Delta/2r = 0.05$ . . . . . 65
3.4 Change in mode I stress intensity factor resulting from close fracture interaction . . . . . 66
3.5 Methods used to quantify fracture interaction by calculation of $C$, $M_i$, and $\epsilon$ . . . . . 69
3.6 Variation of $C$ and $M_I$ with fracture separation for three common geometries as a function of increasing fracture separation . . . . . 71
3.7 Sensitivity of interaction measures to mesh refinement . . . . . 72
3.8 Schematic demonstrating creation of stress intensity factor variation maps 73
3.9 Stress intensity factor variation maps of $C_I$, $C_{II}$ and $C_{III}$ . . . . . 74
3.10 Stress intensity factor variation maps of $M_I$, $M_{II}$, and $M_{III}$ . . . . . 76
3.11 Stress intensity factor variation maps of $\epsilon_I$, $\epsilon_{II}$, and $\epsilon_{III}$ . . . . . 78

3.12 Geometry of two interacting fractures and the resulting effect on the stress intensity factors for both tension and compression . . . 79
3.13 Stress intensity factor variation maps for coplanar fractures under compression. . . . 81

4.1 Fracture arrays observed in outcrops. . . . 87
4.2 Examples of fractures interacting across scales . . . 88
4.3 Growth of an isolated fracture growth under tension . . . 93
4.4 Growth of an isolated fracture growth under compression . . . 95
4.5 Effect of attenuating $K_{II}$ on the fracture geometry in growth under compression . . . 96
4.6 Comparison between experimental wing cracks and simulated inclined flaws under tension and compression . . . 96
4.7 Fracture tips of isolated fractures grown in tension with growth rate exponent $\beta_n = 2$ . . . 98
4.8 Fracture tips of isolated fractures grown in tension with growth rate exponent $\beta_n = 20$ . . . 99
4.9 Fracture tips for two inclined fractures grown in tension in separate models with different values of $\beta_n$ . . . 100
4.10 A fracture array after 34 growth steps under tension . . . 102
4.11 Three fracture arrays grown from the same initial flaws in tension with different values of $\beta_f$ and $\beta_n$ . . . 103
4.12 Cut-plane visualisations of a three-dimensional fracture array . . . 105
4.13 Four fracture arrays, grown in tension from the same initial flaw set, arranged in a spiral, each with different values of $\beta_f$ and $\beta_n$ . . . 107
4.14 Cut-plane visualisations of a three-dimensional fracture array, initially grown from a spiral array . . . 108

5.1 Schematic comparing meshes generated for mechanical deformation and flow simulation . . . 121
5.2 Periodic fracture model used to validate the $\mathbf{k}_{ef}$ computation method . . . 123
5.3 Schematic of the $UO_2$ fuel pellet and cladding in the context of AGR reactors . . . 124
5.4 Cross section and axial section of element 1 fuel pins . . . 126
5.5 Optical microscope images of cross section scans of spent AGR fuel after successive grinding and polishing stages . . . 128
5.6 Examples of tracing fractures on pellet images from different grinding stages 129
5.7 Three-dimensional discrete fracture network reconstructed from five images of spent fuel . . . 131
5.8 Subsections of high resolution $UO_2$ optical microscopy images for porosity analysis . . . 132
5.9 Distributions of fluid pressure in the pellet for the three flow simulations . 135
5.10 Fluid flow in the pellet for the three flow simulations . . . 136

6.1 Three-dimensional DFN from cut-planes through a granite block, from Gonzalez-Garcia et al. [2000] . . . 152
6.2 Effect of smoothing on SIFs . . . 156
6.3 Geometry of two fractures growing and intersecting . . . 157
6.4 Geometry of two intersected fractures . . . 158

6.5 Effect of fracture intersections on flow in a connected dataset containing nine fractures grown under tension . . . 160
6.6 Initial and final geometries of GDFNs A and B, each containing thirty initial fractures . . . 164
6.7 Initial and final geometries of GDFNs C and D, each containing sixty initial fractures . . . 165
6.8 Initial and final geometries of GDFNs E and F, each containing ninety initial fractures . . . 165
6.9 Growth steps from 0 to 5 for GDFN B . . . 167
6.10 Selected growth steps from 10 to 55 for GDFN B . . . 168
6.11 Fracture surface area statistics from GDFN B . . . 169
6.12 Fracture surface area statistics from GDFN C . . . 170
6.13 Ten cut-planes through GDFN C at growth step 33 . . . 172
6.14 Histograms of fracture sizes at three steps in GDFN C . . . 173
6.15 Geometry and ellipsoid visualisation of the effective permeability tensor from GDFN E at steps 0, 1, 5, and 19 . . . 178
6.16 Geometries of six stochastic discrete fracture networks in perspective and cut-plane view . . . 181
6.17 Permeability along the directional axes in the six GDFNs compared to SDFN set one . . . 182
6.18 Permeability along the directional axes in the six GDFNs compared to SDFN set two . . . 183
6.19 Permeability along the directional axes in the six GDFNs compared to SDFN set three . . . 184
6.20 Intersection patterns in GDFNs and SDFNs . . . 187
6.21 Total length of fracture intersections plotted against $P_{32}$ in GDFNs and SDFNs . . . 188
6.22 Permeability in the $x$, $y$, and $z$ axes for the same GDFN growth sequence with different levels of mesh refinement . . . 189
6.23 Example of the mechanical fracture apertures on a growing, isolated, penny shaped fracture . . . 191
6.24 Four views of apertures of fractures in GDFN E under a tensile stress . . . 193
6.25 Total volume of void space due to fracture porosity in GDFN E resulting from different aperture distributions . . . 194
6.26 Fluid velocity from flow along the $x$-axis in GDFN E, step 18 . . . 196
6.27 Directional permeability compared to fracture intensity of GDFN E across its growth steps . . . 197
6.28 Directional permeability in compared to total fracture void space of GDFN E across its growth steps . . . 198

# List of Tables


3.1 $C_i$, $M_i$, and $\epsilon_i$ values from interacting fractures under tension and compression . . . . . 79

5.1 Equivalent permeability tensors of seven flow simulations . . . . . 137

6.1 $P_{xy}$ system used for definition of fracture frequency, intensity, and density 149
6.2 Parameters used during generation of GDFNs . . . . . 161
6.3 Summary of generated geomechanical fracture networks . . . . . 162
6.4 Effective permeability of GDFN E from growth step 0 to step 9 . . . . . 176
6.5 Effective permeability of GDFN E from growth step 10 to step 19 . . . . . 177
6.6 Description of stochastic discrete fracture networks generated for comparison with geomechanical DFNs . . . . . 179

# Symbols

| | |
|---|---|
| $x$, $y$, and $z$ | Cartesian coordinate axes |
| $K$ | Stress intensity factor (combined) |
| $K_I$ | Mode I stress intensity factor |
| $K_{II}$ | Mode II stress intensity factor |
| $K_{III}$ | Mode III stress intensity factor |
| $K_C$ | Critical stress intensity factor (combined) |
| $K_{IC}$ | Mode I critical stress intensity factor |
| $K_{IIC}$ | Mode II critical stress intensity factor |
| $K_{IIIC}$ | Mode III critical stress intensity factor |
| $J$ | $J$ integral |
| $\sigma$ | Cauchy stress tensor |
| $\varepsilon$ | Infinitesimal strain tensor |
| $\sigma_0$ | Initial stress tensor |
| $\varepsilon_0$ | Initial infinitesimal strain tensor |
| $\mathbf{D}$ | Linear elastic stiffness matrix |
| $\underline{\partial}$ | Differential matrix operator |
| $F$ | Force |
| $\mathbf{u}$ | Displacement vector |
| $\mathcal{G}$ | Energy release rate |
| $E$ | Young's modulus |
| $\mu$ | Shear modulus |
| $\nu$ | Poisson's ratio |
| $\beta$ | Paris (or growth rate) exponent |
| $n$ | Tip node |
| $R_d$ | Domain radius |
| $K_V$ | Comparative stress intensity factor |
| $\Delta a_n$ | Tip extension length |
| $\varphi$ | Fracture growth angle (normal) |
| $\psi$ | Fracture growth angle (twisting) |

| | |
|---|---|
| $\mathbf{p}_\varphi$ | Fracture growth vector in local tip space |
| $\mathbf{g}_N$ | Fracture normal gap |
| $\mathbf{x}^m$ | Position vector for master surface ($x$ direction along fracture surface) |
| $\mathbf{x}^s$ | Position vector for master surface ($y$ direction along fracture surface) |
| $\mathbf{u}^m$ | Displacement vector for master surface ($x$ direction along fracture surface) |
| $\mathbf{u}^s$ | Displacement vector for master surface $y$ direction along fracture surface) |
| $\mathbf{g}_T$ | Fracture tangential gap |
| $\mathbf{n}$ | Fracture normal vector |
| $\Omega$ | Simulation domain |
| $\delta\Pi$ | Total virtual work |
| $\delta\Pi_\Omega$ | Virtual work from internal stresses and body forces |
| $\delta\Pi_\sigma$ | Virtual work from pre-defined tractions |
| $\delta\Pi_c$ | Virtual work from contact forces |
| $\lambda_N$ | Normal Lagrange multiplier |
| $\lambda_T$ | Tangential Lagrange multiplier |
| $e$ | Penalty parameter |
| $I$ | Interaction integral |
| $\mathbf{u}^{\text{aux}}$ | Auxiliary displacement field |
| $\mathbf{e}^{\text{aux}}$ | Auxiliary strain field |
| $\sigma^{\text{aux}}$ | Auxiliary stress field |
| $J^{\text{act}}$ | Actual energy release rate |
| $J^{\text{aux}}$ | Auxiliary energy release rate |
| $s$ | Point in the domain near a fracture tip |
| $K_I^{\text{aux}}$ | Auxiliary mode I stress intensity factor |
| $K_{II}^{\text{aux}}$ | Auxiliary mode II stress intensity factor |
| $K_{III}^{\text{aux}}$ | Auxiliary mode III stress intensity factor |
| $A$ | Integration domain for the disk-shaped domain integral |
| $\Gamma$, $\Gamma_0$, $\Gamma_+$, $\Gamma_-$ | Boundaries enclosing integration domain $A$ |
| $x_1$, $x_2$, $x_3$ | Local tip coordinate axes (Frenet frame) |
| $\sigma_{ij}$ | Cartesian components of the stress tensor, local to a fracture tip |
| $e_{ij}$ | Cartesian components of the strain tensor, local to a fracture tip |

| | |
|---|---|
| $u_i$ | Cartesian components of the displacement, local to a fracture tip |
| $\sigma_{ij}^{\text{aux}}$ | Auxiliary components of the stress tensor, local to a fracture tip |
| $e_{ij}^{\text{aux}}$ | Auxiliary components of the strain tensor, local to a fracture tip |
| $u_j^{\text{aux}}$ | Auxiliary components of the displacement, local to a fracture tip |
| $W_I$ | Strain energy density |
| $\delta_{ij}$ | Kronecker delta |
| $q$ | Smooth function in region enclosed by $\Gamma_c$ (see Section 2.3.6) |
| $m$ | Normal vector to integration domain $A$ |
| $u$ | Displacement magnitude in $x$ direction |
| $v$ | Displacement magnitude in $y$ direction |
| $w$ | Displacement magnitude in $z$ direction |
| $\Delta u$, $\Delta v$ and $\Delta w$ | Displacement of a point on a fracture surface (see Figure 2.8) |
| $\theta$, $r$ | Polar coordinate system perpendicular to fracture front |
| $\kappa$ | Kolosov parameter |
| $m_+$, $m_-$ | Paired points behind fracture tip on different sides of a fracture (see Figure 2.8) |
| $L_n$ | Average fracture tip length |
| $L_f$ | Fracture circumference |
| $N_f$ | Number of fracture tip nodes |
| $B_d$ | Local fracture tip segment length |
| $a$ | Fracture radius |
| $R_1$ | Ratio of mode I fracture toughness to mode II |
| $R_2$ | Ratio of mode I fracture toughness to mode III |
| $\Delta a_v$ | Maximum fracture tip extension length per step |
| $\mathbf{Q}$ | Rotation matrix between tip local coordinate space and global space |
| $\mathbf{p}_v$ | Fracture growth vector in global space |
| $\theta$ | Angle around a circular fracture |
| $b$ | Fracture inclination |
| $p_0$ | Initial fracture fluid pressure |
| $\tau_c$ | Cohesive stress |

| | |
|---|---|
| $e_K$ | Stress intensity factor error |
| $K_i^N$ | Stress intensity factor computed numerically |
| $K_i^A$ | Stress intensity factor calculated analytically |
| $e_a$ | Propagation angle error |
| $\varphi^N$ | Propagation angle computed numerically |
| $\psi^N$ | Twisting angle computed numerically |
| $\varphi^A$ | Propagation angle calculated analytically |
| $\psi^A$ | Twisting angle calculated analytically |
| $K_i^{int}$ | Stress intensity factor on a fracture in the presence of an interacting fracture |
| $K_i^{iso}$ | Stress intensity factor on an isolated fracture |
| $\Delta/2r$ | Separation between two interacting fractures |
| $C$ | Circumferential stress intensity factor perturbation |
| $C_i$ | Circumferential stress intensity factor perturbation for mode $i$ |
| $M_i$ | Maximum stress intensity factor perturbation for mode $i$ |
| $\epsilon_i$ | Amplification to shielding ratio for mode $i$ |
| $\kappa_i^a$ | Stress intensity factors around a tip, including only amplified tips and zero otherwise, for mode $i$ |
| $\kappa_i^s$ | Stress intensity factors around a tip, including only shielded tips and zero otherwise, for mode $i$ |
| $C_i^a$ | Area of stress intensity factor curve for only amplified tips |
| $C_i^s$ | Area of stress intensity factor curve for only shielded tips |
| $\mathrm{d}a/\mathrm{d}N$ | Advance of a fracture tip per load cycle |
| $c$ | Material constant in the Paris law (Equation 4.1) |
| $\mathcal{G}_n$ | Energy release rate at tip node $n$ |
| $\mathcal{G}_{max}$ | Maximum energy release rate amongst all tip nodes in a domain |
| $\beta_f$ | Fracture growth rate exponent |
| $\beta_n$ | Tip growth rate exponent |
| $\Delta a_f$ | Maximum extension of fracture $f$ |
| $\mathbf{k}_{eq}$ | Equivalent permeability |

| | |
|---|---|
| $\mathbf{k}_{ef}$ | Effective permeability |
| $k_{xx}$, $k_{yy}$, and $k_{zz}$ | Permeability along the cartesian axes ($x$, $y$, and $z$ respectively) |
| $h$ | Fracture aperture |
| $Q$ | Horizontal volumetric flux |
| $w$ | Fracture width |
| $\eta$ | Fluid viscosity |
| $k_f$ | Fracture permeability |
| $T$ | Fracture transmissivity |
| $k_m$ | Matrix permeability |
| $\nabla p$ | Pressure gradient |
| $e$ | Finite element |
| $k^e$ | Element permeability of element $e$ |
| $V_e$ | Volume of element $e$ |
| $V_\Omega$ | Volume of the domain omega |
| $\left\langle \frac{\partial p_f}{\partial x_i} \right\rangle$ | Volume weighted average of pressure gradient in direction $i = x, y, z$ |
| $\langle u_i \rangle$ | Volume weighted average of flux in direction $i = x, y, z$ |
| $\mathbf{U}$ | Flow velocity vector |
| $\mathbf{k}$ | Permeability tensor (see Equation 5.8) |
| $k_\mathrm{w}$ | Permeability parallel to fractures in an anisotropic sugar cube model |
| $k_\mathrm{h}$ | Permeability perpendicular to fractures in an anisotropic sugar cube model |
| $n_f$ | Number of fractures in an anisotropic sugar cube model (see Equation 5.9) |
| $h_\mathrm{cube}$ | Height of cubic domain |
| $a_f$ | Fracture aperture in an anisotropic sugar cube model (see Equation 5.9) |
| $P$ | Porosity |
| $d$ | Average pore size |
| $k_{UO_2}$ | Uranium dioxide matrix permeability |
| $\nabla p_r$ | Radial pressure gradient |
| $\mathbf{U}_r$ | Radial flow velocity |
| $k_r$ | Radial permeability |
| $k_1$, $k_2$, and $k_3$ | Eigenvectors of the permeability tensor |

# Abbreviations

| | |
|---|---|
| AL | Augmented Lagrangian |
| BEM | Boundary element method |
| CAD | Computer aided design |
| CSMP++ | Complex systems modelling platform |
| DFN | Discrete fracture network |
| DEM | Discrete/distinct element method |
| DC | Displacement correlation |
| DDM | Displacement discontinuity method |
| XFEM | Extended finite element method |
| FDM | Finite difference method |
| FEM | Finite element method |
| FDEM | Finite-discrete element methods |
| GDF | Geological disposal facility |
| GDFN | Geomechanical discrete fracture network |
| ICGT | Imperial College Geomechanics Toolkit |
| LEFM | Linear elastic fracture mechanics |
| NURBS | Non-uniform rational B-splines |
| SDFN | Stochastic discrete fracture network |
| SIF | Stress intensity factor |

# Chapter 1

# Introduction

## 1.1 Background of the HydroFrame project

This PhD project is part of the HydroFrame research project, whose goal was to improve the UK's capability to model hydro-mechanical and biogeochemical processes occurring in fractured rock masses around a geological disposal facility (GDF) for radioactive waste. HydroFrame was one of three projects in the Radioactivity and the Environment (RATE) research program established by the UK Natural Environment Research Council (NERC) to enhance protection of the environment and human health from releases of radioactivity from nuclear power plants, legacy sites, and future waste repositories [British Geological Survey, 2017].

Radioactive waste poses a unique risk to health and the environment, as it contains active radionuclides with extremely long half-lives. No conventional waste disposal method is suitable for high-level waste, as it will remain radioactive for hundreds of thousands of years. This problem creates the requirement for temporary storage of waste in less secure facilities [Holt, 2015]. The consensus for providing a safe, sustainable, and long-term solution to radioactive waste is to dispose of it in geological disposal facilities (GDFs). This will create multiple barriers between the waste and the environment. Despite this consensus, many scientific and engineering challenges posed by locating and constructing such a facility are unsolved, and no facilities for high-level civilian nuclear waste have yet been completed.

The HydroFrame project is divided into six work packages and involves three institutions, concerned with different subjects that are important for understanding processes in fractured rock. This PhD is part of work package 1, and has developed methods for estimating the repository-scale hydraulic conductivity of fractured rock, based on

geologically realistic fracture network geometries. The remaining packages cover seismic monitoring and characterisation of fractures (work packages 2 and 3, University of Leeds), thermo-hydro-mechanical modelling of fractured rock masses (work package 4, Imperial College London), colloid and tracer transport experiments (work package 5, University of Birmingham) and biogeochemical processes affecting actinide mobility (work package 6, Imperial College London).

Work package 1 began in 2015 with two objectives:

- To develop a methodology for quantitatively estimating the macroscopic-scale hydraulic transmissivity of a fracture network from a simple set of geometrical attributes
- To investigate and develop a methodology for generating networks that have geometrically realistic fracture properties emerging from geomechanical processes

The first of these objectives focused on a stochastic discrete fracture network study, demonstrating that effective medium theory and heuristic methods provides good estimates for effective permeabilities [Ebigbo et al., 2016]. The second of these objectives is the primary focus of this thesis. In this introduction, the context and importance of this objective is explained, and the structure of this thesis and a summary of the resulting scientific contributions are given.

## 1.2 Motivation

### 1.2.1 Radioactive waste disposal

A wide number of options for radioactive waste disposal have been considered. The vast majority of countries investigating the issue have concluded that the only responsible method of disposal that sufficiently isolates the waste from the environment is deep geologic disposal [Radioactive Waste Management, 2016a]. Therefore, research has been carried out worldwide, with many countries evaluating potential sites and developing disposal technologies [Witherspoon and Bodvarsson, 2006]. This is not limited to nations which have nuclear power programs, as waste is produced from a variety of sources, including medicine and industry [Radioactive Waste Management, 2016b].

The most significant challenge for disposal programs has been identifying a suitable site for a facility. Important properties of rock for siting a GDF include low permeability, favourable groundwater flow directions, thermal stability, distance from seismotectonically active areas, and sufficient depth of burial to avoid glacial effects [Chapman

et al., 1986]. Not only must the site be thoroughly characterised and understood by the scientific community, but local authorities, land owners, and communities must be in agreement. Advanced programmes include Finland, where the Onkalo spent nuclear fuel facility is under construction, and is expected to begin operating in the 2020s [Posiva Oy, 2018]. Sweden has also formally selected the Forsmark site and are currently in planning stages, expecting to begin construction in the 2020s [SKB, 2018]. The UK have recently begun a process to site a facility, with the aim to have a site chosen within the next twenty years [UK Government, 2018]. An unsuccessful siting process initiated in 2008 and ending in 2013 highlighted the need for developing a better understanding of the processes taking place in fractured rock surrounding a potential GDF. The USA similarly spent many years planning the Yucca Mountain nuclear waste repository which was later rejected [USDOE Blue Ribbon Committee, 2012].

Disposal of waste will begin by processing it into a solid form and sealing it inside durable metal containers. These will be placed between 500 and 1000 m below ground in the target formation. The void between the canister and rock is filled with impermeable bentonite clay. The facility will house high, medium and low level radioactive waste, with relatively few facilities on the surface and an extensive network of tunnels (see Figure 1.1) [Radioactive Waste Management, 2015]. Four types of rock formation where a facility could be constructed, and provide a long term barrier, are recognised: crystalline rock, unsaturated tuff, clay-rich rock, and evaporites [Tsang et al., 2015]. These geologies are favoured because of their very low rock matrix permeabilities and mechanical properties. In each case, the concept of disposal is broadly the same, but different hydrogeological issues are associated with each formation type.

In all formation types, particularly crystalline rock, evaluating fluid flow in fractured rock is vital to ensuring the geological barrier is sufficient to isolate waste from the environment. In rocks with extremely low permeability, the vast majority of transport occurs in natural fracture networks, and is therefore difficult to characterise due to complex network connectivity, fracture morphology, and anisotropy [Nelson, 2001, Rutqvist and Stephansson, 2003].

### 1.2.2 Quantification of fractured rock effective permeability

For an unfractured porous rock, permeability is a material property controlled by pore morphology and interconnectivity, and can be determined through laboratory testing using Darcy's law. A fracture network can have several orders of magnitude higher permeability than the rock matrix [Leckenby et al., 2005]. The "effective permeability" of a rock mass is a quantity used to summarise its hydraulic properties as a combination

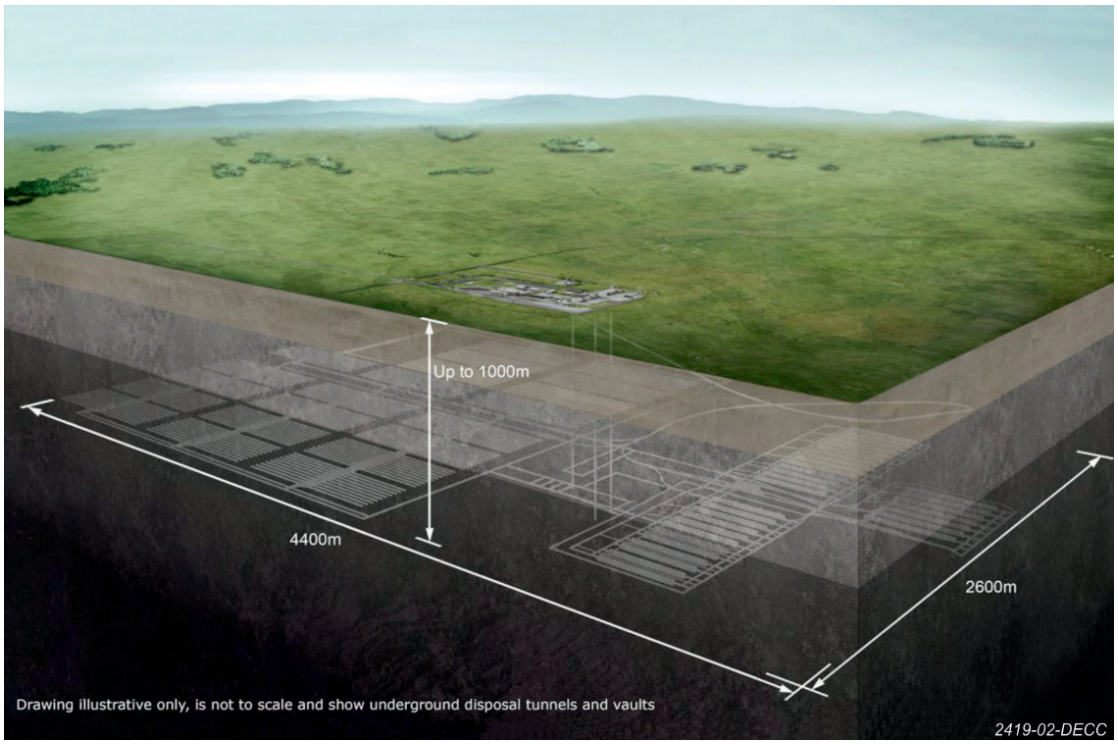



FIGURE 1.1: Artist's impression of what a GDF may look like in the UK, including surface facility, access tunnels and repositories. From Radioactive Waste Management [2015].

of both the permeability of the matrix and the additional permeability from the fracture network. This property will be one of the key parameters used to evaluate the suitability of a rock mass for siting a GDF. Methods for calculating the effective permeability of a rock mass are highly sought after for applications in hydrogeology. Such methods are based on parameters measured from core or outcrop samples, such as fracture density and length. Issues of property dependence with scale [Bonnet et al., 2001] and sampling uncertainty [Berkowitz, 2002] of fracture networks further complicate efforts to quantify a rock's effective permeability.

Analytical methods for calculating effective permeability, derived by Snow [1969], Oda [1985] and others, are accurate for idealised fractures. They cannot be readily extended to describe flow in complex fracture networks, due to the geometric complexity of the problem. Because the mathematics describing fluid flow are well understood, numerical modelling has become a useful method for simulating flow in complex fractured media [Jing and Hudson, 2002, Lei et al., 2017a, Neuman, 2005]. Many authors [*e.g.*, de Dreuzy, 2002, Koudina et al., 1998, Leung, 2012, Mourzenko et al., 2011, Thovert et al., 2017] have approached this problem by simulating fluid flow through stochastically generated discrete fracture networks. Generally these studies follow a similar workflow. A numerical methodology is first established for solving flow in a volume containing a rock matrix and fractures. Fractured networks are generated by placing fractures in random

locations and orientations. Many volumes are simulated and their resulting permeabilities are compared to network statistics, particularly fracture density and connectivity [de Dreuzy, 2002, Ebigbo et al., 2016, Mourzenko et al., 2011]. These analyses have produced a number of mathematical relationships which predict permeability based on network characteristics.

### 1.2.3 Incorporating geomechanics into discrete fracture networks

Whilst progress has been made towards characterising fractured rock, much of this work has assumed that the geometry of fractures is fairly simplistic. Stochastic discrete fracture network studies do not reproduce key characteristics of fracture networks found in rocks. These include non-planar fracture surfaces, abutting and cross cutting at intersections, variable fracture apertures resulting from rock deformation, and fracture interaction [Nelson, 2001]. Thus, to complement conclusions made through analysis of stochastic networks, the influence of geomechanics on fracture network permeability must be understood.

Recent studies of discrete fracture networks have begun to incoporate geomechanics in several ways. The effect of fracture geometry has been explored by generating networks with non-disk shaped fractures [Cvetkovic et al., 2004, Thovert et al., 2017]. Using power law distributions of fracture lengths better reproduces observed networks across several scales [Bonneau et al., 2016, Thovert et al., 2017]. Psuedo-mechanical rules have been incorporated into network generation processes, creating 'kinetic' discrete fracture networks which have some features of mechanically grown networks. Three-dimensional examples include Bonneau et al. [2016], who insert additional fractures preferentially in regions where stress is concentrated by other fractures, and Davy et al. [2013] and Maillot et al. [2016a], whose model grows and arrests fractures to create realistic intersections.

A direct approach to incorporate geomechanics into discrete fracture networks is to simulate the full physics of fracture growth (*i.e.*, linear elastic fracture mechanics). By doing so, realistic features found in fracture networks will emerge as a result of the boundary conditions, initial geometry, and fracture interactions. In two-dimensions, properties such as fracture spacing [Olson, 2004, Renshaw and Pollard, 1994] and mechanical apertures [Paluszny and Matthäi, 2010, Philip et al., 2005] emerge as a result of directly simulating propagation of multiple fractures. However, until now, dense three-dimensional fracture networks have not been generated due to the various challenges posed by growth of non-planar fractures in complex domains. These challenges can now be overcome, and realistic growth can be simulated, following recent advancements

including the use of automatic meshing [Paluszny et al., 2007, Paluszny and Zimmerman, 2013], accurate and fast fracture tip calculations [Nejati et al., 2015a], and realistic three-dimensional fracture interaction [Thomas et al., 2017b].

This thesis presents for the first time a fully three-dimensional fracture growth model that has been used to generate dense geomechanical fracture networks and examine their permeabilities. The Imperial College Geomechanics Toolkit (ICGT) is the finite element based simulator that implements this novel method [Paluszny et al., 2013, Paluszny and Zimmerman, 2011]. New methods within ICGT, and validations of the physical processes taking place in the model, are provided throughout the present work. Novel results are presented which advance several scientific fields, including fracture interaction (Chapter 3), numerical fracture growth (Chapter 4), and characterisation of nuclear materials (Chapter 5). Furthermore, the primary goal of generating dense networks with geomechanical features has been achieved, with six examples of these networks detailed in Chapter 6. The hydraulic properties of these networks have been analysed by comparison to a suite of stochastic networks with uniform fracture apertures. The impact of mechanical fracture apertures on flow in geomechanical networks is also quantified. The generated networks reach fracture intensities of a similar order of magnitude as deep crystalline fracture networks.

## 1.3 Thesis overview

This thesis is split into five main chapters, ordered to follow the modelling framework to grow fractures and simulate flow. Each chapter includes its own review of relevant literature, methodology, results and discussion.

- Chapter 2 introduces the fundamental physical process of fracturing as described by linear elastic fracture mechanics. The ICGT is then introduced and the process of growing fractures using this methodology is described. This includes descriptions of how domain geometry is defined, and how a discretising mesh is generated to conform to this geometry in each growth step. The methods for solving for mechanical fields, resolving fracture surface contact, computing stress intensity factors, and propagating fractures are also introduced. The chapter also includes an overview of other approaches to simulating fractured media, and critically analyses them for the purpose of investigating natural fracture growth. The chapter concludes by validating the computation of fracture tip stress intensity factors in the context of fracture growth, demonstrating that the material and fractures respond realistically to both tension and compression.

- Chapter 3 studies the mechanical interactions between static fractures in various geometries. The change in the stress intensity factors between an isolated and interacting fracture is exploited to quantify the magnitude and type of interaction a fracture experiences. These changes are plotted spatially using novel 'fracture interaction maps' for various fracture orientations under tension and compression. This provides a new technique for understanding how fractures modify stress at one another's tips, in three dimensions.

- Chapter 4 examines the growth of isolated fractures and fractures in arrays, towards the goal of validating growth and understanding the effect of fracture interaction on growth. Growth is demonstrated for tension and compression on isolated fractures, and compared to experiments on wing cracks. The effect of the Paris-type growth law governing variable extension is considered in detail for both individual and multiple fracture cases. The effect of interaction and competition during growth is demonstrated on *en échelon* fracture arrays.

- Chapter 5 reviews methods for modelling the flow and permeability in fractured rocks. The finite element-based method for solving flow on domains with fractures is described, and validated for a sugar cube geometry. A case study on spent nuclear fuel is detailed, demonstrating the method's effectiveness for characterising effective permeability. Six cut-planes through a fractured uranium dioxide fuel pellet, imaged by the National Nuclear Laboratory, are used to create a scale model containing a network of discrete fractures. The effective permeability of the pellet is quantified for a range of porosities, fracture apertures and flow conditions. The effective permeability results match experimental studies on spent fuel pellets, and the study demonstrates that numerical approaches are powerful tools for characterising hazardous materials.

- Chapter 6 details features found in real fracture networks which do not arise in stochastic networks. A review of discrete fracture network studies details how other methods are beginning to include these features without direct simulation of fracture growth processes. Chapter 6 details the specific challenges which arise in geometrically complex domains containing many mutually growing fractures. Six geomechanical fracture networks (GDFNs) are generated and critically examined. The flow properties and permeability of these networks are examined, and compared to a suite of stochastic discrete fracture networks (SDFNs), quantifying the impact of geomechnical effects on fracture networks.

The thesis is summarised in Chapter 7, highlighting the specific parts of the results which are novel, and proposes many avenues for future research.

### 1.3.1 Related publications

This thesis includes work from several publications produced during this PhD. These publications are listed chronologically as follows:

- Thomas, R. N., Paluszny, A., & Zimmerman, R. W. 2017. Quantification of fracture interaction using stress intensity factor variation maps. *Journal of Geophysical Research: Solid Earth*, 122(10), 7698–7717. http://doi.org/10.1002/2017JB014234
  - Forms the basis of Chapter 3, which includes some additional figures not found in the paper, including interaction maps with different geometries and maps for compression.
- Thomas, R. N., Paluszny, A., Hambley, D., Hawthorne, F. M., & Zimmerman, R. W. 2018. Permeability of observed three dimensional fracture networks in spent fuel pins. *Journal of Nuclear Materials*, 510, 613–622. http://doi.org/10.1016/j.jnucmat.2018.08.034
  - Included in Chapter 5 as a case study to demonstrate the effective permeability computation method.

Further publications are in preparation for journal submission:

- Thomas, R. N., Paluszny, A., & Zimmerman, R. W. Growth of three-dimensional fractures, arrays, and networks in brittle rocks under tension and compression. *Computers and Geotechnics*, *Under review.*
  - Explains the three-dimensional growth methodology and results from Chapters 2 (stress intensity factor validation), 4 (growth of isolated fractures and fracture arrays under different fracture growth exponents), and 6 (growth of a fracture network, and visualisation of the network using cut-planes).
- Thomas, R. N., Paluszny, A., & Zimmerman, R. W. Permeability of 3D geomechanically fractured rock masses with realistic aperture distributions.
  - Presents the geomechanical fracture networks from Chapter 6 and details their mechanical and hydraulic properties.

During the PhD, research results were presented at several international conferences. In chronological order, these were:

- Thomas, R. N., Ebigbo A., Paluszny, A., & Zimmerman, R. W. 2018. Permeability of three-dimensional rock masses containing geomechanically-grown anisotropic fracture networks. *American Geophysical Union fall meeting, San Francisco.* Poster presentation.

- Thomas, R. N., Paluszny, A., & Zimmerman, R. W. 2017. Change in three-dimensional rock mass permeability during the growth of geomechanical fractures. *Interpore $10^{th}$ annual meeting, Rotterdam.* Oral presentation.

- Paluszny, A., Thomas, R. N., & Zimmerman, R. W. 2018. Finite element-based simulation of the growth of dense three-dimensional fracture networks. *$52^{nd}$ American Rock Mechanics Association conference, Seattle.* Paper and oral presentation.

- Thomas, R. N., Paluszny, A., & Zimmerman, R. W. 2018. Effect of Fracture Growth Velocity Exponent on Fluid Flow through Geomechanically-grown 3D Fracture Networks. *$2^{nd}$ Discrete Fracture Network Engineering conference, Seattle.* Paper and oral presentation.

- Thomas, R. N., Paluszny, A., & Zimmerman, R. W. 2019. Permeability change during the growth of dense 3D geomechanical fracture networks. *Interpore - $11^{th}$ annual meeting, Valencia.* Oral presentation.

# Chapter 2

# A finite element based methodology for simulating discrete fractures in geological media

## 2.1 Introduction

Fractures are present in rock masses over a wide range of length scales and have a fundamental effect on the mechanical, hydraulic, and seismic properties of rock [Jaeger et al., 2009]. Permeability may be increased or decreased depending on fracture orientation and fill [Bratton et al., 2006], or may be almost entirely responsible for the hydraulic properties of rock when there is effectively no flow taking place within the rock matrix. This is particularly true for fractured crystalline rocks with very low matrix permeabilities [Crider, 2015]. Understanding the origin of fractures in rocks, and the detail of how they propagate and interact, is key to simulating realistic fracture patterns. Purely analytical approaches to understanding fractures often find difficulties in resolving the detailed emerging geometry of one or more fractures during growth. Additionally, the quantification of other fracture growth effects for discrete multi-fracture systems, such as non-planar fracture surface accretion and interaction between fractures, becomes complex. Experimental approaches provide a basis for the current understanding of brittle failure, including characterising three-dimensional internal fracture geometries for a variety of natural and engineered materials [Tatone and Grasselli, 2014]. However, physical experiments in geomechanics can only test a few variables at a time, with significant limitations for sample size, and for observations of fast processes such as fracturing.

Numerical methods seek to overcome experimental limitations through detailed modelling of the physical processes that control deformation. The geometry of fractures can be explicitly modelled to follow the change of shape during growth, capturing the effects of propagation in response to mechanical boundary conditions. Models which discretely represent and discretise both the rock matrix and fracture surfaces are vital when solving flow and transport equations in highly fractured rocks. A variety of approaches are currently being studied for numerical modelling of three-dimensional discrete fractures, including the finite element method (FEM) [Hadjab-Souag et al., 2007, Paluszny and Zimmerman, 2013, Zhang et al., 2016], extended finite element method (XFEM) [Belytschko et al., 2009, Gupta and Duarte, 2014, Prévost and Sukumar, 2016], boundary element method (BEM) [Meng et al., 2013], displacement discontinuity method (DDM) [Kumar and Ghassemi, 2016, Tang et al., 2016], phase-field method [Borden et al., 2014], discrete element method (DEM) [Lisjak and Grasselli, 2014] and perturbation method [Lazarus, 2011].

This chapter presents the fundamental physics governing the propagation of fractures in linear elastic media, and introduces a numerical method which seeks to model this phenomena. Section 2.2 introduces linear elastic fracture mechanics (LEFM) in the context of geological materials, and the implications of modelling rock fracture growth using LEFM. Section 2.3 introduces the Imperial College Geomechanics Toolkit (ICGT), and details the full algorithm used to grow fractures. This includes the methods for automatically generating the discretising mesh, solving for deformation, stress and fracture surface contact, computing stress intensity factors, and growing fractures. Section 2.4 provides an overview of other contemporary methods for simulating fractured media. Section 2.5 concludes this chapter by validating the fracture tip Stress Intensity Factors (SIFs) computed on static fractures, demonstrating that fractures and fractured domains in ICGT respond to mechanical stress in a realistic manner. This validation is the primary way that ICGT is validated in the thesis, as it demonstrates that the medium responds to deformation in a linear elastic way, and shows that the propagation direction predicted by the SIFs is accurate, even at low levels of mesh refinement. Further validations of ICGT are presented in Chapters 3, 4, and 5 for interacting fractures, growing fractures, and flow in fractures respectively.

## 2.2 Linear elastic fracture mechanics

Fracture mechanics is a mature field of science which seeks to fully describe the physical processes taking place during of fracture extension, including the formation of fractures, and changes which may occur in the material surrounding the fracture [Anderson and

Anderson, 2005, Antolovich et al., 2018, Borstad et al., 2017]. Because fracturing is relevant to a wide range of scientific fields, researchers who investigate fractures often apply the principles of fracture mechanics within their own field. This is particularly true for geological applications, where geologists are often focused on understanding bulk-rock failure, rather than the stress state or failure of individual fractures. This section provides an overview of linear elastic fracture mechanics and its relevance to geological applications.

The key early analytical contributions to Linear Elastic Fracture Mechanics (LEFM) theory were from Inglis [1913], Griffith [1921], Irwin [1961], and Paris et al. [1961]. These early efforts were driven by the need to understand the failure of engineered structures and develop quantitative criteria for the onset of fracturing. Inglis [1913] was the first to calculate the stress distribution around an elliptical notch in a body under remote load. This provided the first stress-based criteria to predict failure of a material. Griffith [1921]'s work followed on from Inglis, incorporating thermodynamics to describe the energy balance during fracturing. Griffith developed a fracture criterion based on this energetic argument, and introduced the fracture toughness of the material. Griffith also theorised that microflaws were prevalent in materials, providing the required energy concentrations to initiate fracturing. Both Inglis [1913] and Griffith [1921] used the assumption of a linear-elastic material, and an idealized elliptical crack to describe the flaw shape [Antolovich et al., 2018]. These remain common assumptions, for example, in many analytical solutions for fracture[1] tip SIFs.

Much later, Irwin [1961] examined the plasticity arising in the fracture tip region. This widely observed behaviour presented a conundrum for analytical approaches to fracturing, as non-linear plastic deformation violates the assumption of linear-elasticity. In the process of seeking a framework which was independent of the geometry of a specific problem, Irwin introduced the Stress Intensity Factor (SIF), $K$, as a key parameter in LEFM, which quantifies the energy of the advancing crack [Irwin, 1956b]. The equations containing $K$ provide the analytical basis for the field of LEFM [Antolovich et al., 2018]. Furthermore, this provided a criterion for propagation, when $K$ was equal to the critical stress intensity factor ($K_C$) of the material. Paris et al. [1961] went on to show that the newly formalised LEFM theory could predict fatigue fracture propagation due to cyclic loading. In particular, Paris showed that the SIF had excellent correlation with the fracture growth rate. A popular method for calculating $K$ was later developed by Rice [1968], known as the $J$ integral, which idealises the fracture tip plastic deformation as non-linear elastic.

[1]Nomenclature for fractures differs between fracture mechanics and geological literature. The term 'crack' is common in fracture mechanics, whereas geological literature uses 'fracture' as a generic term for a discontinuity in rock. The terms are used interchangeably in this thesis.

The contributions of Inglis, Griffith, Irwin, Paris and many other authors provided the analytical basis for the field [Antolovich et al., 2018]. However, these approaches are highly limited to specific geometries of idealised fractures. Numerical approaches can enable any arbitrary fracture geometries to be simulated, and, by incorporating the fundamental principles of LEFM, can be used to predict realistic growth.

### 2.2.1 Mathematical description of linear elasticity

The LEFM approach to material deformation treatshe rock as a linear elastic, homogeneous, and isotropic material. Stress and strain are governed by

$$\sigma = \mathbf{D}(\varepsilon - \varepsilon_0) + \sigma_0 \tag{2.1}$$

where $\sigma$ is the Cauchy stress tensor, $\varepsilon$ is the infinitesimal strain tensor, $\sigma_0$ and $\varepsilon_0$ are the initial stress and strain, and $\mathbf{D}$ is a linear elastic stiffness matrix [Cook et al., 2007]. For a static system,

$$\underline{\partial}\sigma + F = 0 \tag{2.2}$$

where $\underline{\partial}$ is the differential matrix operator, and $F$ represents body forces exerted on the object. The displacement vector $\mathbf{u}$ of a point in the linear elastic medium can be related to the strain by the following relationship:

$$\varepsilon = \partial\mathbf{u}. \tag{2.3}$$

Equations 2.1, 2.2, and 2.3 govern the deformation of the solid elastic domain. LEFM assumes that the domain is embedded with fractures, with shapes that are best described as high aspect ratio (height divided by length) ellipsoidal voids. The presence of a fracture perturbs the stress field around it. This perturbation depends on many factors, including the type and direction of the loading stress, the shape of the fracture, the orientation of the fracture, and other stress concentrators (*e.g.*, other fractures, boundaries, and heterogeneities). The particular value of the stress near a fracture's tip determines whether the fracture will propagate, and the extent and angle of propagation [Anderson and Anderson, 2005].

#### 2.2.1.1 Implications of assuming linear elasticity

Linear elastic properties are routinely assumed in solid mechanics for a variety of materials, including rocks [Jaeger et al., 2009]. In practice, no rock behaves exactly in this manner, however, this assumption enables formulation of the fundamental equations

which describe rock deformation without significant additional complexity. Numerical approaches can incorporate material non-linearities and inelastic properties, with drawbacks that include an increase in the complexity of the numerical solution. This would have significant implications for the computational cost of simulations and complicate the implementation of such a method. Through the validation of the method in Sections 2.5, this thesis demonstrates that simulated fracture behaviour, and the behaviour of the material surrounding the fracture, is realistic (*i.e.*, matches LEFM analytical solutions) when linear elasticity is assumed for the rock matrix.

For a wide range of incremental changes in stress, real rocks behave linearly. The presence of fractures in a rock fundamentally changes its behaviour, causing the linear relationship between stress and strain to become non-linear. In particular, in the region very close to a fracture's tip and surface behaves inelastically, known as the inelastic or crack-tip-yielding zone [Anderson and Anderson, 2005]. The greater the size of this region, the more significantly the stress distribution departs from the assumption of infinite stress at the fracture tip. Modelling a non-linear solid requires an iterative solver with a discrete time step [*e.g.*, Henao et al., 2016, Mediavilla et al., 2006], which requires much more computational time relative to a linear approach, particularly in three-dimensions.

The extent to which a rock responds inelastically depends on its temperature. Simulations of fracture growth in this work can therefore be assumed to be only applicable to relatively cool, near surface rocks. For example, granite at high pressure (640 bars) is shown to respond elastically at 430° C, and becomes progressively more inelastic as temperatures increase [Goetze, 1971]. Most of the crust is within these constraints, with crustal elastic thickness estimates of 10 to 40 km in regions with shallow continental crust, and up to 200 km in regions with deep continental crust [McKenzie et al., 2005, Tesauro et al., 2012]. This includes depths relevant to radioactive waste disposal (less than 1 km from the Earth's surface) [Radioactive Waste Management, 2016a], making the simulations in this work readily applicable to crustal rocks.

Isotropic properties are also assumed for the elastic medium studied in this thesis. Specifically, in order to use the equations described in Section 2.2.1, it must be assumed that the principle axes of strain coincide with the principal axes of stress, *i.e*, symmetrical stresses result in a symmetrical strain. Rocks are rarely isotropic on scales relevant to fracturing, and are instead anisotropic due to variable porosity, fabrics, layers, mineral heterogeneity, and interbedding. Many of these features are known to influence the formation of fracture patterns [Olson, 1993]. This thesis focuses on fracture growth in a homogeneous rock matrix, meaning fracturing is dictated only by the stress boundary conditions, and how the stress distribution is modified by the geometry of domain. Stress

conditions are well documented as being the primary factor influencing the activation and growth of fractures in heterogeneous rocks [Anders et al., 2014]. Inhomogeneity can be modelled in future work without modifying the methodology, for example, by locally varying the Young's modulus, Poisson's ratio, or critical stress intensity factor in different regions of the domain.

### 2.2.2 Fracture initiation

Fracture initiation is widely agreed to follow the theory proposed by Griffith [1921]. The stress needed to break bonds between atoms in materials is much higher than the measured fracturing stress. This is reconciled by assuming that microflaws, or Griffith flaws, are present throughout a material and concentrate stress to the point of failure [Lawn, 1993]. Microflaw theory was developed from observations of centimetre-scale cracks in glass; however, its description of failure is also applicable to fractures in geological materials [Hoek and Martin, 2014].

Rocks are highly heterogeneous and therefore have many potential fracture nucleation zones at different scales, such as sections of grain boundaries, joints, faults, and bedding-plane partings [Walsh and Brace, 1964]. Many of these flaws have anisotropic distributions, leading to the observation that many fracture populations to have preferred orientations. Fracture orientations are also influenced by the stress field causing failure, usually caused by tectonic forces (uplift, burial, extension, and compression) [Nelson, 2001].

Nucleation of fractures is not described by the original theory proposed by Griffith [1921]. In this thesis, fractures are assumed to grow from initial flaws, and additional fractures are not nucleated. Rather, the extension of fractures is assumed to 'upscale' processes taking place at the crack tip, where fractures extend by concentrating stress on other existing flaws and connecting them. Therefore, the nucleation of new fractures, whilst not explicitly implemented in the present method, is represented as part of the growth process occurring. Other numerical techniques (smeared fracture models, damage models and phase-field methods) avoid this limitation by making fracture nucleation the same process as growth of new fractures [Francfort and Marigo, 1998, Zhou et al., 2017]. Smeared fracture models also facilitate seeding of new flaws in locations dictated by the stress distribution [Lee et al., 2016, Tanné et al., 2018].

### 2.2.3 Fracture tip stress intensity factors

Stress intensity factors (SIFs) quantify the energy at the tip of a fracture in three deformation modes: opening (mode I), in-plane shear (mode II) and out-of-plane shear (mode III) [Irwin, 1956b]. Figure 2.1 shows schematically the type of deformation associated with each mode. They are one of several methods that can be used to quantify the energy released at a fracture tip during crack growth [Anderson and Anderson, 2005, Irwin, 1956b]. They can be used to evaluate failure criteria for modelling fracture propagation [Brace, 1960, Lawn, 1993, Paris and Erdogan, 1963]. They have become a key part of fitness-for-purpose analyses when considering the impact of interacting cracks on a material's lifetime [Wiesner et al., 2000]. If the value of the SIF for each of these modes is known ($K_I$, $K_{II}$, and $K_{III}$), growth criteria can be evaluated to decide whether the fracture grows, and at what length and angle it grows.

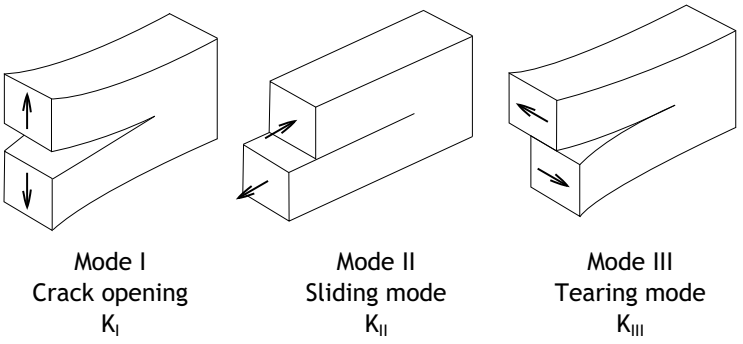



FIGURE 2.1: Fracture tip deformation modes at the fracture tip and their respective stress intensity factors.

Stress intensity factors were introduced by Irwin [1956a] along the energy release rate, $\mathcal{G}$. This is the rate of change in potential energy with fracture area for a linear elastic material. When $\mathcal{G}$ reaches a critical value, the fracture has sufficient energy at that point of the tip to extend. The energy release rate is related to the SIFs by the following expression:

$$\mathcal{G} = J = \frac{K_I^2 + K_{II}^2}{E'} + \frac{K_{III}^2}{2\mu} \tag{2.4}$$

where $E'$ is the Young's modulus and $\mu$ is the shear modulus of the material. The form of $E'$ depends on whether conditions are plane stress ($E' = E$) or plane strain ($E' = E/(1-\nu^2)$, where $\nu$ is Poisson's ratio). A plane strain condition must be assumed to relate $\mathcal{G}$ to $K_{I-III}$, which occurs on the fracture front [Nakamura and Parks, 1988]. SIFs depend on the geometry of the fracture and the type of loading, meaning analytical solutions for the SIFs on fractures with non-standard shapes are not readily available. For such arbitrary fracture geometries, the $J$ integral developed by Rice [1968] can be used to find $\mathcal{G}$ and the three SIFs. Rice [1968]'s method has formed the basis of various

methods which are used to find the SIFs in computational modelling approaches to LEFM [*e.g.*, Banks-Sills, 1991, Nejati et al., 2015a, Paluszny and Zimmerman, 2011]. Displacement-based numerical approaches can also sample the relative deformation of the two surfaces of a fracture to determine their relative displacement, and therefore the SIFs. These methods are discussed in detail in Section 2.3.6.

### 2.2.4 Fracture extension

Macroscopic failure of rock is the result of individual small fractures forming and coalescing at a small scale to form macroscopic fractures. Griffith [1921] was the first to postulate that microfractures and other small heterogeneities must be prevalent throughout materials in order for macroscopic fractures to grow. Subsequently, microfractures have been identified throughout rocks at a wide range of length scales [Anders et al., 2014]. They predominantly form as opening mode fractures, and in isotropic rocks, align their fracture planes perpendicular to the direction of least compressive principal stress. In anisotropic rocks, they are often associated with grain interfaces and other small scale heterogeneities. When a rock is critically stressed under any stress regime, microfractures are widely activated, particularly in regions ahead of larger fracture tips where stress is concentrated. Microfracture activation before macroscopic failure can be quantified by observing acoustic emission [*e.g.*, Nasseri et al., 2006, Wei et al., 2016].

Fracture mechanics predicts a spectrum of different fracture growth rates, all of which are relevant to rock failure. Griffith [1921]'s original analysis predicted rapid extension once the energy released in propagation is sufficient to supply the surface energy to create the new fracture [Anders et al., 2014]. Such growth would be unstable, as the driving stress required to grow the fracture would reduce as the fracture becomes larger [Antolovich et al., 2018]. However, it is also widely accepted that fractures in geological materials which are not critically stressed can grow in a stable manner. Segall [1984] recognised that sets of joints in outcrops must have grown quasi-statically, assisted by crack tip chemical reactions. Martin and Chandler [1994] show axial and lateral strain curves for a granite under uniaxial compression, marking the transition between stable and unstable crack growth.

Low velocity fracture growth is of particular interest to subsurface fracturing, where fracture networks are known to grow gradually over millions of years. Two key theories which formally describe low-velocity fracture growth behaviour are sub-critical and fatigue crack growth. The first theory is widely used to study growth of fractures through the relationship between the velocity of tip advance and the magnitude of $K_I$ [Atkinson, 1984]. The relative growth velocity criterion was first proposed by Charles [1958] and

was extended to a relative growth extension criterion by Renshaw and Pollard [1994]. The theory incorporates the effects of non-mechanical effects, including the rate of stress corrosion reactions at the fracture tips [Ko and Kemeny, 2013].

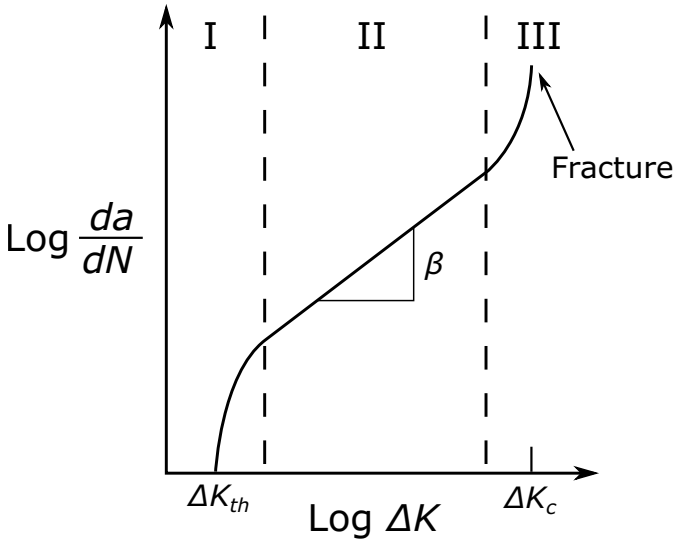



FIGURE 2.2: Typical fatigue fracture growth behaviour described by a Paris-type law. After Anderson and Anderson [2005].

The second theory, fatigue crack growth, is governed by a power law-type relationship known as the Paris law for fatigue crack growth. Fatigue refers to when a material is loaded in repeated load cycles, and the Paris criterion quantifies the advance of a fracture tip for each individual load cycle [Paris and Erdogan, 1963]. This criterion proposes that the extension of a crack front point is proportional to the local energy release rate ($\mathcal{G}$), such that the point with the maximum energy grows fastest, while other points grow proportionally slower [Pugno et al., 2006]. Figure 2.2 provides a schematic plot of typical fracture growth behaviour below the critical SIF. This plot splits the curve of log $K$ against load cycles into three regions, where region II is governed by Paris' law. Stable, slow propagation velocities of cracks growing in region II are known to correlate with the magnitude of the SIF. For example, in double torsion tests on granite, a linear increase in the SIF results in a logarithmic increase in fracture growth velocity [Nara and Kaneko, 2006]. The slope of the curve in region II is $\beta$, also known as the fracture growth rate exponent, or Paris exponent.

## 2.3 The Imperial College Geomechanics Toolkit

This section describes the ICGT, a finite element-based simulator to numerically model three-dimensional discrete fracture growth under mixed mode conditions, as described

in Section 2.2. The growth method is driven primarily by fracture tip stress intensity factors, which determine the growth of multiple interacting fractures [Nejati et al., 2015a, 2016, Thomas et al., 2017b]. Fractures are represented discretely, and geometry is tracked independently of the underlying discretising mesh [Paluszny and Zimmerman, 2013]. Thus, fractures do not follow any pre-defined path, and are not constrained by the mesh. Fractures grow in response to elastic deformation, and guide the evolving discretisation requirements of the domain.

The method uses LEFM principles to govern growth, using the three SIFs to control whether fracture tips fail and the direction and extent of growth. The computation of SIFs has been validated in several publications [Nejati et al., 2015a, 2016, Thomas et al., 2017b] and in Section 2.5 in the context of growth, demonstrating that fracture growth will be highly accurate across a wide range of mesh densities. Furthermore, the interaction between fractures is also validated [Thomas et al., 2017b] and leads to realistic mutual growth in high fracture density simulations (see Chapters 3 and 4). These aspects of the ICGT enable the generation of realistic geomechanical fracture networks, explored in Chapter 6.

The ICGT is implemented in C++, and was developed from the application programming interface called the Complex Systems Modelling Platform (CSMP++) [Matthai et al., 2007]. CSMP++ was originally developed to solve specific challenges encountered in modelling geological media. These challenges included (1) representing and discretising structures accurately across several length scales, (2) handling extreme material property ranges and discontinuities, and (3) handling transient and episodic events adaptively. ICGT has significantly expanded on CSMP++'s capabilities for solving the first two challenges in order to solve fracture problems. The third challenge is relevant to thermal and hydraulic coupling, which has provided means to simulate hydraulic fracture propagation in ICGT [Salimzadeh et al., 2017a,b].

Paluszny et al. [2007] first detailed the discretisation of discrete fractures in CSMP++. Subsequently, growth of fractures [Paluszny and Matthäi, 2009] and flow were incorporated [Paluszny and Matthäi, 2010]. Later, fracture growth was extended to three dimensions [Paluszny and Zimmerman, 2011]. The push towards three dimensional fractures led to the development of new numerical techniques: SIF computation [Nejati et al., 2015a,b], fracture surface contact [Nejati et al., 2016], fragmentation [Paluszny et al., 2013], fluid flow [Ebigbo et al., 2016, Lang et al., 2014, 2015] and the use of Non-Uniform Rational B-Splines (NURBS) surfaces in fracture modelling [Paluszny and Zimmerman, 2013]. These advancements make the ICGT uniquely suited to studying

geomechanics the fracture networks, because relationships between key fracture properties (*e.g.*, geometry, apertures, fluid flow, interaction) emerge as a result of simulating the physical processes occurring in fractured rocks.

The ICGT makes use of two further pieces of software during the fracture growth workflow. ICEM CFD is a commercial octree mesher, produced by ANSYS, and handles the automatic generation of meshes in this work [Ansys, Inc., 2012]. The ICGT generates a script before meshing, which is passed to ICEM CFD along with the model's geometry. ICEM CFD executes this script and returns with a mesh composed of triangles and tetrahedra, which is parsed into the finite element handling classes in ICGT. This process provides significant control on the mesh that is generated, and benefits from the fast meshing algorithms that a commercial meshing platform provides. Furthermore, the mesh can be further modified post-generation. The second external piece of software is SAMG (Algebraic Multigrid Processes for Systems), produced by Fraunhofer, which handles the solution of large matrices as required by the FEM [Stüben et al., 2017].

### 2.3.1 Validations of ICGT

ICGT has been widely validated during its development, ensuring it realistically models a range of physical processes. This validation has been performed against LEFM-based analytical solutions of fracture properties. Several processes key to the generation of fracture networks are validated in this thesis. A full chronological list of published validations of ICGT is as follows:

- Stress intensity factor computation: Nejati et al. [2015b] for quarter points and displacement correlation, Nejati et al. [2015a] for the disk-shaped domain integral method, and Section 2.5 for all combinations of implemented computation methods and quarter points, on meshes optimised for fracture growth. Thomas et al. [2017b] also includes a validation of stress intensity factors which is now superseded by the more thorough study in Section 2.5.
- Fracture growth: Paluszny and Matthäi [2009] in two dimensions on interacting fractures in PMMA, and Chapter 4 in three dimensions for isolated fractures under tension and compression in rock. The growth and aperture evolution of hydraulic fractures is also validated by Salimzadeh et al. [2017a].
- Flow and permeability: Paluszny and Matthäi [2010] in two dimensions, and Lang et al. [2014] and Section 5.2.4 in three dimensions, comparing equivalent permeabilities with analytical solutions for sugar cube models and parallel fractures.

- Friction and contact: Nejati et al. [2016] in three dimensions and Section 2.5 through the validation of stress intensity factors, against analytical solutions for penny shaped fractures.
- Fracture interaction: Thomas et al. [2017b] and Chapter 3, for coplanar fractures, and Chapter 4 for fracture arrays.

### 2.3.2 Finite element based growth algorithm

Algorithm 1 details the steps taken to grow fractures in ICGT.

Initialise volume and fractures
**while** current growth step number $<$ maximum growth steps **do**
  Define matrix and initial fracture geometry
  Discretise volume and surfaces (Section 2.3.3)
  Assign material properties and apply boundary condition
  Compute deformation ($\sigma$ and $\varepsilon$, Equation 2.1)
  Resolve fracture surface contact (Augmented-Lagrangian gap based algorithm, Section 2.3.5)
  **for** each fracture **do**
    **for** each tip node $n$ **do**
      Compute domain radius $R_d$ (Equation 2.15 and 2.16)
      Determine stress intensity factors $K_I$, $K_{II}$, $K_{III}$ (Section 2.3.6) and $K_V$ (Equation 2.17)
      **if** $K_V \geq K_{IC}$ **then**
        Compute tip extension length $\Delta a_n$ (Equations 4.2 and 4.3)
        Compute growth angle $\varphi$ (Equation 2.18)
        Form growth vector $\mathbf{p}_\varphi$ and compute new tip location (Section 2.3.7.4)
      **end**
    **end**
    Handle collisions against boundaries and other fractures (Section 2.3.7.5)
    Update fracture geometry (Section 2.3.7.4)
  **end**
**end**

**Algorithm 1:** Finite element based quasi-static fracture growth algorithm.

### 2.3.3 Domain geometry and discretisation

The ICGT handles geometric objects, such as fractures, separately from the mesh, as described by Paluszny and Zimmerman [2011]. This removes conventional restrictions of FEM-based fracture growth, allowing fractures to grow in any direction. The meshing strategy employed for simulations in this thesis is executed by generating a script file in the ICGT before each growth step, which is used as input into ICEM CFD along with the present growth step's geometry. ICEM CFD runs the script to generate the mesh,

and the output mesh file is read into the ICGT, after which the simulation resumes. Therefore, the interaction between ICGT and ICEM CFD is governed by the details in the script, which provides constraints for the types and sizes of elements which are placed in different regions and surfaces in the domain. To ensure meshes are generated fully automatically in complex domains, the script specifies relatively few constraints and uses the distance between fracture tip nodes as the key length scale to control local mesh refinement. This section describes how the resulting mesh is organised and the constraints which the script specifies for the octree meshing algorithm used by ICEM CFD.

The geometry is made up of points, curves and surfaces collected into entities. Entities are sorted into families for convenient use of element operations and material property assignment. Fractures are stored as surfaces and curves, and the matrix is initially represented by a set of surfaces, which are the boundaries of the domain. The meshing process changes each surface into a set of triangles, and each tip curve into a set of segments [Paluszny and Zimmerman, 2011]. The octree mesher ensures that the resulting mesh is watertight, *i.e.*, the volumetric domain is completely filled with volumetric elements, and no voids remain within the boundaries. The created fracture becomes a polyhedron which grows by adding surfaces to its tip curve. Families of entities are maintained between the geometry and mesh. Families in the mesh are classified as fracture or matrix, and tip curves are a set of segments with sets for the fractures and the matrix. This formulation allows tips to be present in the matrix rather than the fracture, for cases where fractures intersect with the volume boundaries.

In the domain geometry, a fracture is represented by a surface, which may be non-planar following growth. Once meshed, two layers of coincident, isoparametric quadratic triangles reproduce the shape of the fracture. The layers are connected at the fracture tip. This configuration of fractures ensures that, when the deformation is computed using the FEM, the fracture acts as a void in the domain, behaving as a real fracture would, as a discontinuity in a material. Example fracture meshes are shown in Figure 2.3. Images (A) and (B) show two possible meshes on a fracture, where the size of the triangular elements is either a fixed size ('static') or variable ('dynamic'), with smaller elements at the fracture tip reducing in size towards the centre. Static and dynamic fracture surface refinements are found to produce very similar results, and since the latter provides a fracture surface mesh with fewer elements, dynamic refinement is used throughout this work.

Figure 2.3C shows the detail of the mesh at the tips of the fracture, including quarter point elements at the fracture tip. The separation between the two initially coincident sides of the fracture is exaggerated to demonstrate how the two sides of the fracture

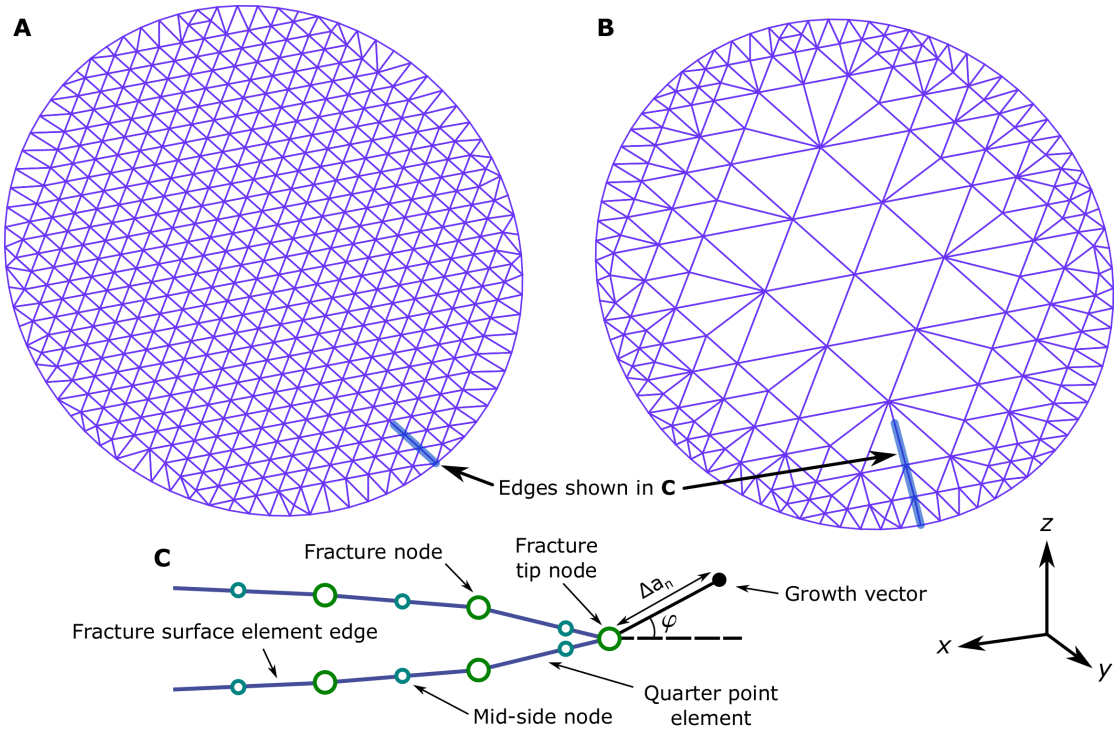



FIGURE 2.3: Discretisation of fracture surfaces. A: Penny-shaped fracture discretised using isoparametric quadratic triangles with fixed size elements on the surface. The fracture is oriented such that its surfaces have a normal vector of (1, 0, 1) and has a radius of 1 m. B: Penny-shaped fracture discretised with dynamically sized elements. C: Schematic representation of the highlighted element edges in A, demonstrating how elements are split on the fracture surface.

connect along the tip. Quarter point elements are widely used in finite element-based fracture mechanics to improve the accuracy of mechanical fields (stress, displacement, and strain) at the fracture tip [Banks-Sills and Sherman, 1986, Fu et al., 2013, Khoei et al., 2013]. The mid-side node of a quarter point element is moved to a position one quarter of the way from the fracture tip node to the far end of the element. This improves the sampling of the fracture tip singularity and leads to improved SIF accuracies. Figure 2.4 shows standard quadratic elements (A and B) and quarter point versions of these elements (C and D). Section 2.5 demonstrates the improvement in the SIFs provided by using quarter point elements.

The present CSMP++ based implementation of the FEM enables element sizes to vary considerably in the domain, providing significant reductions in computation time, whilst ensuring that variables are calculated accurately. Meshes are finer (*i.e.*, have more, smaller elements) in the region close to the fracture tip, as this area is resampled to calculate the SIFs for growth. The number of tip nodes along the edge of a fracture controls this dynamic refinement. A "fracture tip" is defined as the edge of a triangular element along the edge of the fracture, and "fracture tip nodes" are the nodes connecting these edges. The length of a tip is calculated as the number of nodes divided by the

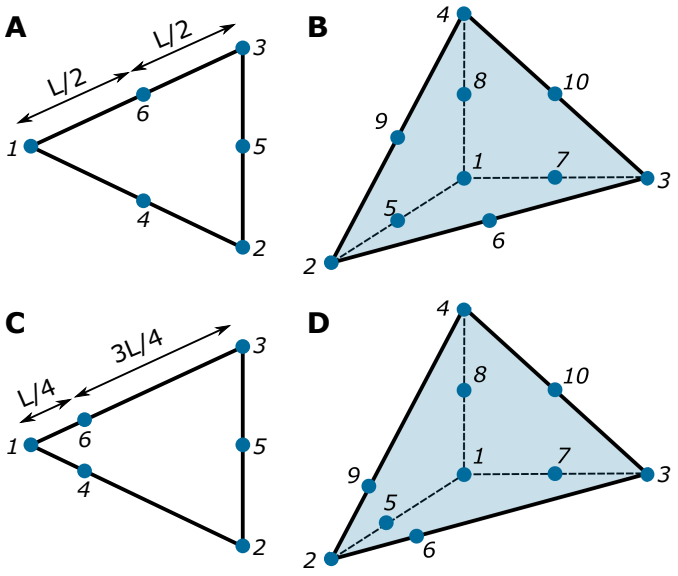



FIGURE 2.4: Detail of non-quarter point and quarter point quadratic finite elements. A and B show standard two and three-dimensional elements. Nodes numbered according to internal definitions of CSMP++ [Matthai et al., 2007].

fracture's circumference, *i.e.* all tips on fractures have the same length. The length of the fracture tip defines the minimum local element size that the mesher is required to insert. Finite elements gradually become larger as their distance to the fractures increases. Figure 2.5 shows the changes in the mesh around a fracture which has different numbers of tip nodes.

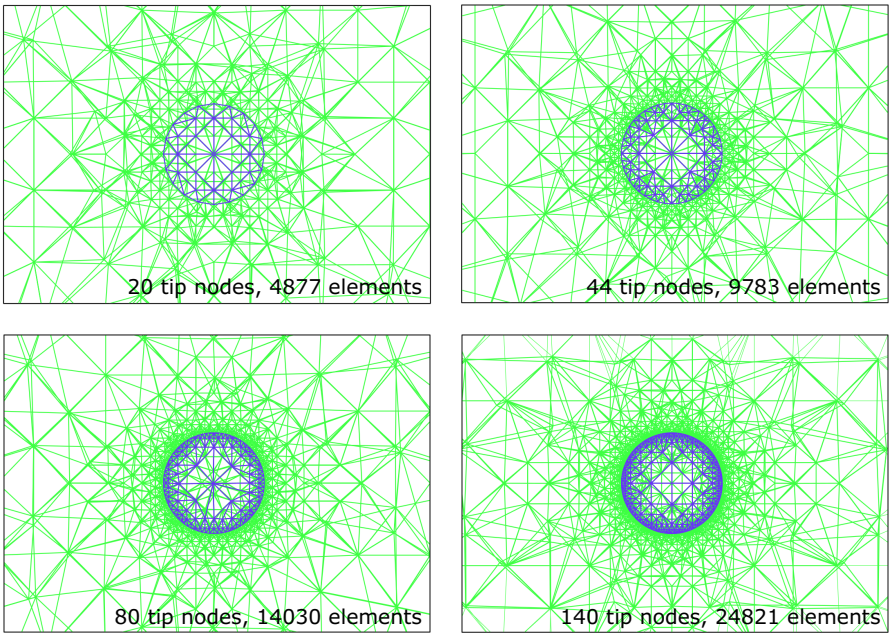



FIGURE 2.5: Cut-plane through four different meshes around a fracture with different numbers of tip nodes. The total number of elements in each volume is given in the corner of each cut-plane, and includes both volumetric and surface elements.

The length of the fracture tip provides the only length scale which controls finite element sizes. This approach yields several benefits. It ensures that smaller elements are placed only in regions which will be resampled, where higher accuracy is required to quantify fracture tip stresses. Much larger elements can be used in the rest of the domain, which dramatically speeds up simulation time. With only one parameter controlling the mesh density, analysis on how simulation performance and accuracy depends on mesh refinement is simplified. When a fracture's tip advances during growth simulations, the fracture tip length is modified locally as a result. Subsequently, the next mesh will automatically size elements along the new tip in a similar manner to the previous step, providing continuity to the general arrangement of elements in the mesh, without any form of intervention or additional requirements for fracture advance.

Re-meshing strategies for three-dimensional fracture growth are often dismissed by other researchers, due to an assumption that re-meshing would be prohibitively expensive, or perhaps not practical to achieve without manual intervention. Gupta and Duarte [2014] suggest user intervention is required to create meshes as a simulation progresses, and that appropriate fracture tip meshes are difficult to construct where fractures have complex geometries. However, modern meshing software is very capable of efficiently creating meshes automatically during simulations. Following advancements in methods for calculating stress intensity factors Nejati et al. [2015a,b], there are no longer strict requirements on the structure of meshes very close to the fracture tip [Zimmerman and Paluszny, 2012]. These advancements in meshing can be utilised whilst ensuring that the automatically created mesh conforms to the fracture surfaces.

### 2.3.4 Computation of stress and displacement

Before the stress state at fracture tips can be considered, the stress and displacement throughout the medium must be calculated using the FEM. The first of these is referred to here as the 'standard' deformation algorithm, and is best suited to deforming the medium in tension. This involves solving the equations described in Section 2.2.1, which are given in a form suited to implementation in the FEM. For simulations where fracture surfaces are not expected to be in contact, a single FEM inversion is required to calculate the stress and deformation. Because the mesh is split along fracture elements during mechanical deformation, the fracture is treated as a void in the material. The gap between element pairs on the each face of the fracture can be found from the discontinuity in the displacement between those elements.

In principle, this formulation can also be used to compress or shear the medium. However, in order to accurately resolve friction and contact between the fracture surfaces,

a second method is available. This second method resolves the contact between fracture surfaces and is suited to shear or compressive boundary conditions, described in Section 2.3.5. The result of both of these methods are fully resolved stress and displacement fields throughout the domain. The contact algorithm also produces aperture distributions during the method, whereas for the standard deformation algorithm, these must be separately calculated during an additional post-processing stage, described in Section 6.5.

### 2.3.5 Fracture surface contact algorithm

Friction between the two surfaces of a fracture can have a significant effect on the stress state at its tips [Barton et al., 1985]. Contact between fracture surfaces can occur under most stress conditions, and is particularly important to consider during compression or shear. A variety of approaches have been used to resolve fracture surface contact in FEM models, including the large time increment approach in XFEM [Dolbow et al., 2001, Trollé et al., 2012], and the Augmented Lagrangian (AL) approach [Fischer and Wriggers, 2005, Puso and Laursen, 2004, Wriggers and Zavarise, 1993]. First introduced by Alart and Curnier [1991], Nejati et al. [2016] extended AL to the gap-based Augmented-Lagrangian contact resolution method. Liu and Borja [2008] found that the AL method produced more accurate results and converged much faster than the large time increment approach of Dolbow et al. [2001]. The gap-based AL method extends the AL method to three dimensions. The method accurately resolves the frictional forces between the two surfaces of fractures, using an iterative approach. The result is a fully resolved traction and aperture distribution across the surface of each fracture.

#### 2.3.5.1 Contact problem description

Nejati [2015] introduced the main governing equations of the contact problem in strong and weak forms. The strong form builds the partial differential equations which satisfy the equilibrium conditions throughout the solid, based on equations of balance, kinematic relations, and constitutive equations. When fracture surfaces are in contact, the frictional contact constitutive law, based on the Coulomb frictional law, governs the boundary conditions over the fracture surfaces. Whilst the domain is subject to quasi-static loads where time-based effects are not considered, for the contact problem, time must be discretised because of non-linearity and path dependency of frictional forces.

The two surfaces of each fracture are organised into a master surface and a slave surface, intersecting at the fracture tip. These surfaces are separated by a normal gap function

$\mathbf{g}_N$ given by

$$\mathbf{g}_N = (\mathbf{x}^s - \mathbf{x}^m) \cdot \mathbf{n} = (\mathbf{u}^s - \mathbf{u}^m) \cdot \mathbf{n} - \hat{\mathbf{g}}_N \tag{2.5}$$

where $\mathbf{x}^m$, $\mathbf{x}^s$, $\mathbf{u}^m$ and $\mathbf{u}^s$ are the position and displacement vectors of master and slave surfaces. When the master and slave surface come into contact, an initial tangential gap vector ($\mathbf{g}_T$) is given by

$$\mathbf{g}_T = (\mathbb{I} - \mathbf{n} \otimes \mathbf{n})(\mathbf{x}^s - \mathbf{x}^m) - \hat{\mathbf{g}}_T = (\mathbb{I} - \mathbf{n} \otimes \mathbf{n})(\mathbf{u}^s - \mathbf{u}^m) - \hat{\mathbf{g}}_T \tag{2.6}$$

where $\mathbf{n}$ is the normal of the fracture surface element, $\mathbf{n} \otimes \mathbf{n}$ is the tensor product of $\mathbf{n}$. Equations 2.5 and 2.6 are used to detect whether fracture surfaces are in contact, and enforce displacements normal to the surfaces. Figure 2.6 shows schematically the calculation of $\mathbf{g}_N$ from the resulting separation between two initially coincident nodes.

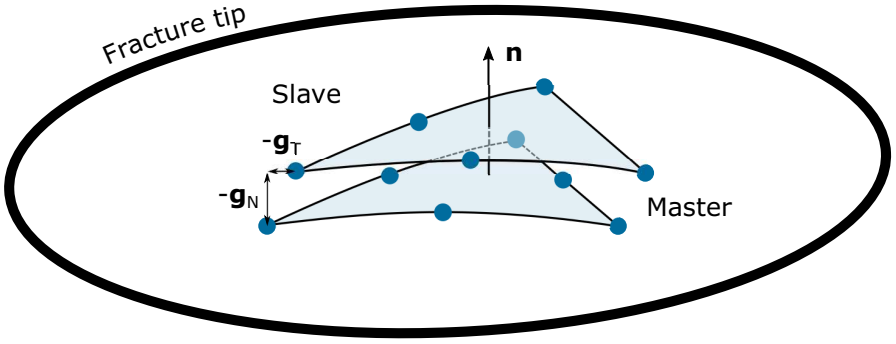



FIGURE 2.6: Schematic of vectors $\mathbf{g}_T$ and $\mathbf{g}_N$ for one node. Parent elements are labelled with 'master' and 'slave' definitions.

The contact problem is solved using a weak form of the contact equilibrium equation, because the strong form requires strong continuity in the displacement field, which is not guaranteed in a numerical approximation. In contrast, the weak form is an integral equation which itself holds the pre-defined boundary conditions of the boundary value problem, making it better suited to being the basis of numerical approximations [Nejati, 2015]. By applying the principle of virtual work to the material points in the domain ($\Omega$), the weak form of the equilibrium equation is given by an integral equation:

$$\delta\Pi = \delta\Pi_\Omega - \delta\Pi_\sigma + \delta\Pi_c = 0 \tag{2.7}$$

where $\delta\Pi$ is the total virtual work, $\delta\Pi_\Omega$ is the contribution of internal stresses and body forces to the total virtual work, $\delta\Pi_\sigma$ is the virtual work of pre-defined tractions and $\delta\Pi_c$ is the virtual work of the contact forces. These terms are given in full by Nejati [2015]. The contact contribution $\delta\Pi_c$ is the term of interest, as this is where constraints are introduced to guide the optimisation process.

#### 2.3.5.2 Traction-based Augmented Lagrangian approach

The method combines two numerical methods in optimisation theory: the Lagrange multiplier and penalty method. Lagrange multipliers add active constraints to the weak formulation by introducing normal ($\lambda_N$) and tangential ($\lambda_T$) Lagrange multipliers as unknown contact tractions [Fischer and Wriggers, 2005]. In this way, exact kinematic contact constraints are enforced, but additional effort is required to compute additional unknowns. The penalty method avoids the exact solution and additional unknowns by introducing an approximation of the constraint conditions, removing the constraints from the formulation. Violations of the conditions are then penalised by using a large positive penalty parameter ($e$) [Fischer and Wriggers, 2005]. The downside of the penalty method is that the value of the penalty parameter must be selected carefully, as a smaller parameter would violate constraints, but a large value may ill-condition the system of equations. Therefore, in the context of an automated numerical technique, selecting $e$ becomes non-trivial.

AL combines the Lagrange multiplier and penalty method, taking the benefits of both approaches. Also referred to as a nested AL [Simo and Laursen, 1992] or an Uzawa-type algorithm [Nejati et al., 2016, Ning et al., 2018], application of the AL method results in a double loop algorithm. In the inner loop, constant Lagrange multipliers are used with penalty terms to enforce the contact constraints. In the outer loop, the Lagrange multipliers are updated based on the computed tractions from the inner loop. More iterations are required, but contact constraints can be enforced accurately by using small penalty parameters. Because the contact problem is quasi-static, the outer loop applies the load to the domain in an incremental manner, splitting the total load evenly between each outer loop.

#### 2.3.5.3 Gap-based Augmented Lagrangian approach

The gap-based AL approach is a further modification of the standard traction-based AL method [Nejati, 2015]. When dealing with fracture surfaces, there is no traction on the fracture tips, because these points are excluded from the contact domain. Lagrange multipliers are defined individually at the finite element nodes, and interpolated over elements using standard FEM shape functions. Therefore, traction values are required at the fracture tip in order to have a complete distribution of traction over the surfaces; otherwise, the elements adjacent to the fracture tips cannot be interpolated.

The gap-based AL solves the handling of the fracture tip regions by assuming that tips remain sharp. Therefore, the gaps are zero on the tip nodes, and increase in a square root

variation with the normal distance from the tip. This approximation is valid because, near the fracture front in a three-dimensional configuration, plane strain conditions are known to arise [Nakamura and Parks, 1988]. These fields predict that displacements adjacent to the tip over a plane perpendicular to the fracture front are given as square root functions of distance from the tip. Therefore, the penalty parameter is regularised with a singular square root variation over the fracture surface. A further change in the gap-based AL is that the standard Lagrange multipliers are replaced with augmented normal and tangential gaps. These augmented gaps are constant during the inner loop, and updated in the outer loop. The full algorithm is summarised in Algorithm 3 in Nejati [2015]. Through the computation of fracture tip stress intensity factors, the accuracy of the algorithm is quantified for a range of mesh refinements in Section 2.5.

### 2.3.6 Stress intensity factor computation

The model applies the disk-shaped domain integral method ('disk method') to calculate the SIFs, outlined in full by Nejati et al. [2015a], which evaluates the interaction ($I$) integral around the tip of the fracture. Instead of integrating over a structured concentric mesh, the I-integral is solved numerically over a 2D virtual disk domain, embedded in the three-dimensional matrix domain. Thus, the I-integral is resolved on an arbitrarily tetrahedral mesh. The $I$-integral computes the value of the strain energy release rate, $\mathcal{G}$, from which separate values of $K_I$, $K_{II}$ and $K_{III}$ are calculated [Nakamura and Parks, 1988].

An alternative SIF calculation method is the Displacement Correlation (DC) method. It samples only two points behind the fracture tip, and determines the SIFs based on their relative displacement. The DC method has been validated for tetrahedral domains by Nejati et al. [2015b]. DC has several benefits over the disk-shaped domain integral method, including its fast computation time and smaller sampling region. In general, it has been shown to be less accurate than the disk-shaped domain integral [Thomas et al., 2017b], contour integral, or cutoff function methods [Gupta et al., 2017] for a variety of meshes. The present work uses DC to provide a comparison to the disk-shaped domain integral in Section 2.5, and in simulations which have a large computational cost (*i.e.*, the generation of geomechanical fracture networks in Chapter 6).

When fractures grow closer to each other, the region between them becomes smaller and therefore more costly to discretise. Thus, the accuracy of any SIF calculation method that relies on values taken from the surrounding domain is less accurate. The behaviour of the disk-shaped domain integral was examined in detail by Thomas et al. [2017b],

demonstrating that when multiple tips of different fractures are close, the computed amplification of stress matches that of other semi-analytical and numerical methods.

#### 2.3.6.1 Disk-shaped domain integral

The disk-shaped domain integral is an energy approach to finding the SIFs [Nejati et al., 2015a]. Such approaches calculate $\mathcal{G}$, then subsequently find the SIFs, using an integral based on the $J$ integral [Rice, 1968]. The SIFs cannot be directly found from $J$ or $\mathcal{G}$ using the relation in Equation 2.4. Instead, a different form of $J$ has been used, utilising the interaction ($I$) integral [Chen and Shield, 1977, Nakamura and Parks, 1988]. This has been shown to be one of the most accurate methods for calculating SIFs in mixed-mode problems [Banks-Sills, 1991, Bremberg and Faleskog, 2015]. Equation 2.4 is still important for relating the SIFs to $\mathcal{G}$, as these quantities are later used to govern propagation (see Section 2.3.7).

Use of the $I$ integral introduces the concept of two states of equilibrium for a cracked body. The FEM solution constitutes the actual state, with displacement ($\mathbf{u}$), strain ($\mathbf{e}$) and stress ($\sigma$) values throughout the domain. This actual state will be accurate in the domain and close to the fracture, but very close to the tip, will not reproduce the near tip conditions (*i.e.*, the stress singularity) due to the limits of the discretisation. A second state is defined as the auxiliary state, given by known asymptotic fields, which are functions of the SIFs. This state has its own forms of the displacement, strain and stress fields ($\mathbf{u}^{\text{aux}}$, $\mathbf{e}^{\text{aux}}$, and $\sigma^{\text{aux}}$). The values of the auxiliary field are found from plane strain fields[2], which are known to prevail close to the tip and are relatively independent of the far-field conditions [Nakamura and Parks, 1988, Nejati et al., 2015a]. Each field will have its own energy release rate, and therefore $J$ value, known as the actual ($J^{\text{act}}$) and auxiliary ($J^{\text{aux}}$) fields. The superimposed $J$ integral is the combination of $J^{\text{act}}$, $J^{\text{aux}}$ and $I$,

$$J^{\text{sup}}(s) = J^{\text{act}}(s) + J^{\text{aux}}(s) + I(s) \tag{2.8}$$

where $s$ is a point near the fracture tip, and $I$ is the interaction integral, which relates the two states of equilibrium. Equation 2.4 is modified to include the influence of the auxiliary field,

$$J^{\text{sup}}(s) = \frac{(K_I(s) + K_I^{\text{aux}}(s))^2 + (K_{II}(s) + K_{II}^{\text{aux}}(s))^2}{E'} + \frac{(K_{III}(s) + K_{III}^{\text{aux}}(s))^2}{2\mu} \tag{2.9}$$

where $K_i$ is the SIF for mode i $= I, II, III$ and $K_i^{\text{aux}}$ is the SIF for mode $i$ due to the auxiliary state.

[2]The analytical solutions for plane strain fields are available in Anderson and Anderson [2005], or more conveniently in Nejati et al. [2015a], appendix A.

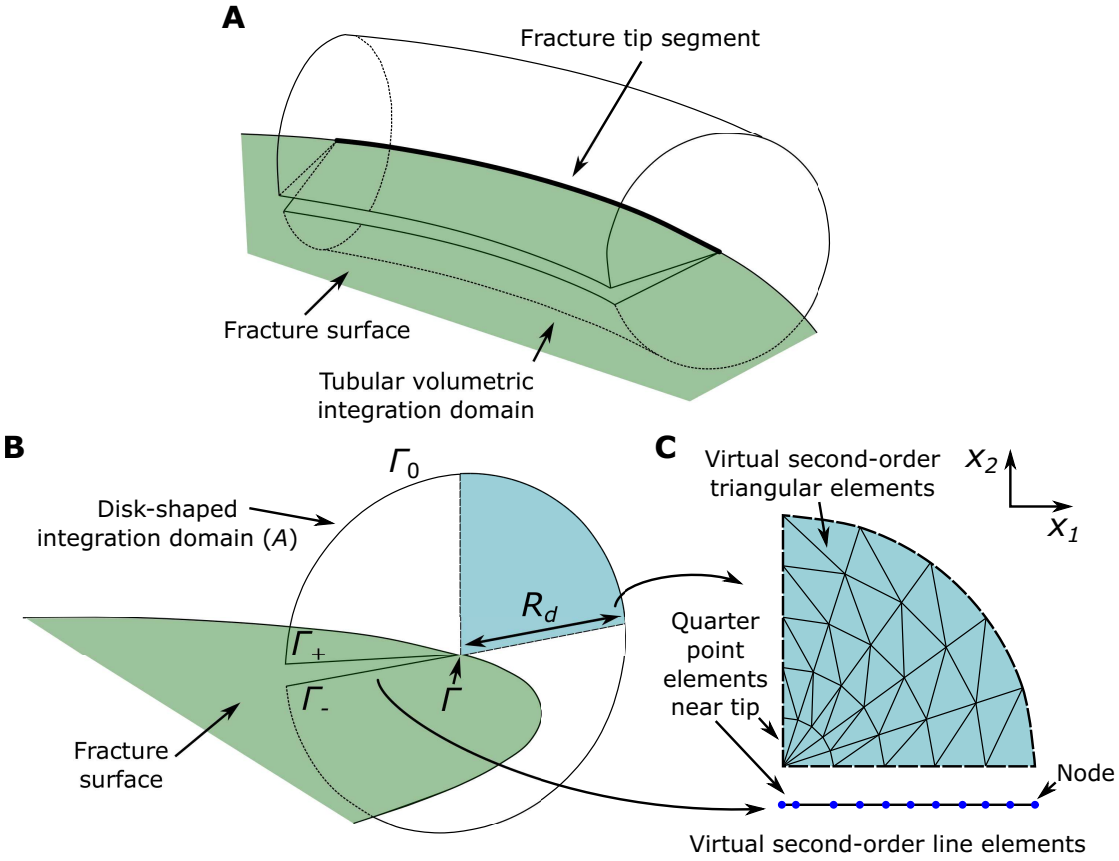



FIGURE 2.7: Schematic diagrams of the volumetric domain and disk-shaped domain integral methods for SIF calculation. A: Domain used in the volumetric domain integral method along the tip of a fracture. B: Domain used in the disk-shaped domain integral method. C: Detail of one quadrant of the virtual mesh, with virtual triangle and line quadratic finite elements shown. Nodes and mid-side nodes are shown on the line elements, but omitted on the triangular elements for clarity. Triangle elements in the lower left corner have quarter points, where the mid-side node is placed closer to the fracture tip.

In the standard volumetric domain integral approach, $I$ is calculated over a volume around the fracture tip, and the SIFs can be given purely as a form of $I$. Figure 2.7A shows a diagram of a volumetric domain along a fracture tip. These methods typically require a structured mesh at the fracture tip [*e.g.*, Nahta and Moran, 1993]. Implementing the standard approach for an unstructured mesh is cumbersome, and the method has further requirements on the conditions at the tip, requiring expensive calculations and analytical descriptions of the geometry [Nejati et al., 2015a]. These drawbacks are significant for approaches where meshes are unstructured and fracture geometries are arbitrary, hence, the disk-shaped domain integral method is used in this work to solve $I$ integral and subsequently find the SIFs.

Nejati et al. [2015a] introduced the disk-shaped domain integral method, for which the key equation is introduced here. The method reduces the region of interest from a volume (usually a tube around the fracture front) to a disk. To make the method fully flexible

for any unstructured mesh, the two-dimensional surface of this disk, perpendicular to the fracture front (Figure 2.7B), is resampled with a virtual mesh (Figure 2.7C). Figure 2.7B and C show the formal definition of the disk domain, where $A$ is the integration domain and $R_d$ is the domain radius of the integration. The terms $\Gamma$, $\Gamma_0$, $\Gamma_+$, and $\Gamma_-$ are the boundaries enclosing $A$, with $\Gamma$ being the point at the centre $A$, $\Gamma_0$ being the outer boundary of $A$, and $\Gamma_+$ and $\Gamma_-$ as the top and bottom edge where $A$ meets the fracture surfaces, respectively. The local tip coordinate system is shown in Figure 2.7C with axes $x_1$ (along the fracture plane) and $x_2$ (normal to the fracture plane). Line elements are positioned where $A$ touches the fracture plane (on $\Gamma_+$ and $\Gamma_-$). This mesh is virtual as it is not active during the FEM, and constructed only during computation of the SIFs and subsequently discarded.

The following form of the $I$ integral is evaluated over domain $A$,

$$I(s) = \int_A \left( \sigma_{ij} \frac{\partial u_j^{\text{aux}}}{\partial x_1} + \sigma_{ij}^{\text{aux}} \frac{\partial u_j}{\partial x_1} - W_I \delta_{1i} \right) \frac{\partial q}{\partial x_i} \mathrm{d}A - \int_{\Gamma_+ - \Gamma_+} \sigma_{2j} \frac{\partial u_j^{\text{aux}}}{\partial x_1} m_2 q \mathrm{d}\Gamma \quad (2.10)$$

where $\sigma_{ij}$, $e_{ij}$, and $u_i$ are the Cartesian components of the stress tensor, strain tensor and displacement vector in the $x_1, x_2$ coordinate system, $\sigma_{ij}^{\text{aux}}$, $e_{ij}^{\text{aux}}$, and $u_j^{\text{aux}}$ are the components of the stress tensor, and strain tensor, and displacement vector which are given by the auxiliary field, $W_I$ is the mutual strain energy density ($W_I = 1/2(e_{ij}^{\text{aux}}\sigma_{ij} + e_{ij}\sigma_{ij}^{\text{aux}})$), $\delta_{ij}$ is the Kronecker delta, $q$ is a smooth scalar function in the region enclosed by $\Gamma_c = \Gamma_0 + \Gamma_+ + \Gamma_- - \Gamma$, equaling unity on $\Gamma$ and vanishing on $\Gamma_0$, and $m$ is a vector normal to the plane of $A$. The smooth scalar function $q$ is introduced to avoid to avoid the particular form of the contour integrals in the original $J$ integral, such that the last term in Equation 2.10 is instead transformed into an area integral over $A$, together with contour integrals over the fracture surface. For a numerical implementation, this is both more convenient and more accurate [Nikishkov and Atluri, 1987].

The full numerical implementation is given in Algorithm 1 in Nejati et al. [2015a]. The two terms in Equation 2.10 are solved over the virtual triangular elements and virtual line elements respectively, then combined. Three auxiliary states are used, one for each deformation mode (pure mode I, II and III), producing three forms of Equation 2.10 ($I_I(s)$, $I_{II}(s)$ and $I_{III}(s)$). The SIFs can then be can be related to $I$ by combining Equations 2.8 and 2.9,

$$I(s) = \frac{2}{E'}(K_I K_I^{\text{aux}} + K_{II} K_{II}^{\text{aux}}) + \frac{1}{\mu} K_{III} K_{III}^{\text{aux}}. \quad (2.11)$$

In each pure mode auxiliary state, the other SIF terms vanish, therefore one expression can be formed per SIF:

$$K_I(s) = \frac{E'}{2} I_I(s), K_{II}(s) = \frac{E'}{2} I_{II}(s), K_{III}(s) = \mu I_{III}(s). \tag{2.12}$$

The disk-shape domain integral method has been validated within ICGT, first by Nejati et al. [2015a], and then by Thomas et al. [2017b] in the context of fracture interaction. A further validation is presented in Section 2.5 focused on evaluating its accuracy on meshes which are configured for fracture growth.

#### 2.3.6.2 Displacement correlation

Displacement correlation (DC) is a direct approach for computing the SIFs, in that it is fully based on the FEM solution adjacent to the tip. Because the three deformation modes are explicitly related to a type of displacement around the tip (see Figure 2.1), the displacement of the finite elements just behind the fracture tip is directly related to these modes and their respective SIFs. The method and its ICGT implementation are detailed by Nejati [2015] and its key details are reproduced here in brief.

A plane strain condition is known to prevail locally around a fracture, such that three-dimensional deformation fields approach two-dimensional plane strain fields [Nakamura and Parks, 1988]. This property is exploited for both disk and DC methods. Williams [1957] expressed the linear elastic stress fields for a two-dimensional cracked plate subjected to an arbitrary load, now known as the Williams series expansions [Anderson and Anderson, 2005]. Near the tip, the first terms of the Williams series are dominant, providing an expression for the singular stress field near the tip. A fracture tip coordinate system for the method is shown in Figure 2.8, with displacements $u$, $v$ and $w$ relating to modes II, I and III respectively. In terms of the SIFs near the fracture tip, the local displacements are

$$\begin{Bmatrix} u \\ v \end{Bmatrix} = \frac{K_I}{2\mu}\sqrt{\frac{r}{2\pi}} \begin{Bmatrix} \cos\frac{\theta}{2}\left(\kappa - 1 + 2\sin^2\frac{\theta}{2}\right) \\ \sin\frac{\theta}{2}\left(\kappa + 1 - 2\cos^2\frac{\theta}{2}\right) \end{Bmatrix} + \frac{K_{II}}{2\mu}\sqrt{\frac{r}{2\pi}} \begin{Bmatrix} \sin\frac{\theta}{2}\left(1 + \kappa + 2\cos^2\frac{\theta}{2}\right) \\ \cos\frac{\theta}{2}\left(1 - \kappa + 2\sin^2\frac{\theta}{2}\right) \end{Bmatrix} \tag{2.13}$$

where $u$, $v$, and $w$ are the displacements in the global coordinate system ($x$, $y$, $z$), $\theta$ and $r$ are the polar coordinates for a local system perpendicular to the fracture front, $\mu = E/2(1+\nu)$ is the shear modulus, $\nu$ is the Poisson's ratio, and $\kappa$ is the Kolosov parameter ($\kappa = 3-4\nu$). The displacements are then related to the SIFs by the following

expressions:

$$\Delta u = K_{II}\left(\frac{\kappa+1}{\mu}\right)\sqrt{\frac{r}{2\pi}}, \Delta v = K_{I}\left(\frac{\kappa+1}{\mu}\right)\sqrt{\frac{r}{2\pi}}, \Delta w = K_{III}\left(\frac{4}{\mu}\right)\sqrt{\frac{r}{2\pi}} \tag{2.14}$$

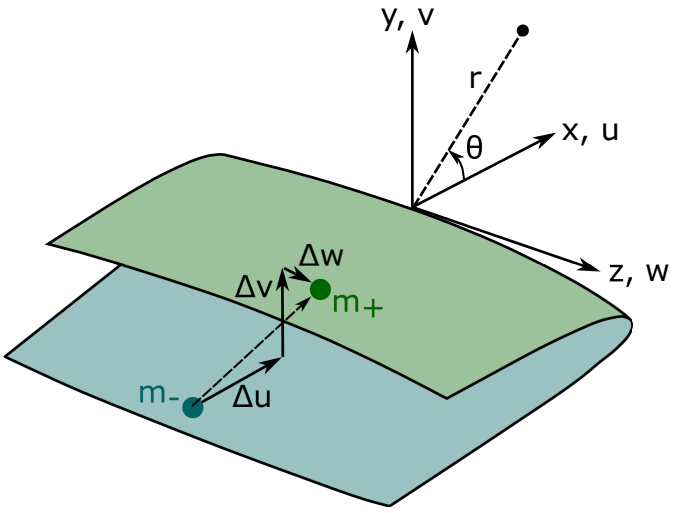



FIGURE 2.8: Local coordinate system used for the Displacement Correlation (DC) method.

Conventional methods for calculating $\Delta u$, $\Delta v$ and $\Delta w$ from a FEM solution rely on the displacements along structured meshes [*e.g.*, Ingraffea and Manu, 1957]. To use DC on an unstructured, three-dimensional finite element mesh, Nejati et al. [2015b] introduced a method which samples two points, rather than a line along the fracture surface. These points ($m_+$ and $m_-$) are shown in Figure 2.8. These two points are at a distance $R_d$ from the fracture tip, and are initially coincident. A search algorithm is used to find the elements which contain $m_+$ and $m_-$, and then $\Delta u$, $\Delta v$ and $\Delta w$ can be extracted from the shape functions of that element. Nejati et al. [2015b] explores the potentially significant changes in the accuracy of this DC method as local mesh conditions change. This analysis is repeated in Section 2.5 to validate DC and demonstrate its accuracy relative to the disk method.

#### 2.3.6.3 Sampling domain radius

For both the $I$-integral and the DC method, a domain radius ($R_d$) can be defined as the size of the region sampled around the fracture tip. For the $I$-integral, the domain is the radius of integration around the fracture tip. For DC, the domain radius is the distance at which the displacement field is sampled. The choice $R_d$ has a complex relationship with the accuracy of the SIFs. Large values of $R_d$ violate the assumption of plane strain conditions by sampling too far away from the tip, whilst small domains may sample the crack tip fields in regions where the numerical error is highest. Nejati et al. [2015a]

quantified $R_d$ using the average fracture tip length $L_n = L_f/N_f$, where $L_f$ is the fracture circumference, and found that the most accurate results were obtained when $R_d$ is in the range of 0.5 - 1.5 $L_n$. When fractures are grown using the present method, $L_n$ increases as tips become further apart.

This thesis considers two values of $R_d$ for the purpose of computing accurate SIFs on progressively growing fractures. The first of these methods is based on the size of the local fracture tip,

$$R_d = 0.5\,|B_d| \tag{2.15}$$

where $B_d$ is the local tip segment length. This formulation highlights the variability of tip segment sizes and proposes to use the local tip length $|B_d|$ as opposed to an average tip length $L_n$. A factor of 0.5 is chosen, as it places the sampling domain close to the tip centre, but aims to sample the tip ahead of the quarter point node. The second $R_d$ formulation tested is a factor of the radius of the fracture,

$$R_d = \frac{a}{10} \tag{2.16}$$

where $a$ is the fracture radius. The radius of a fracture with an arbitrary shape grown over multiple steps is not clearly defined. Instead, the radius of a non-uniform fracture at a particular tip can be considered as the the distance computed along the fracture surface between the centre and the tip node, rather than the Euclidean distance from tip to centre. Testing this alternative formulation of $R_d$ allows demonstration of the importance of varying $R_d$ with mesh refinement. The results of testing these two definitions of $R_d$ are detailed in Section 2.5.

### 2.3.7 Fracture growth

Three growth criteria govern fracture growth in the ICGT, together determining whether failure occurs (Section 2.3.7.1), the angle of growth (Section 2.3.7.2), and the length of growth (Section 2.3.7.3 and 4.2). Subsequently, a vector is created at each growing tip which extends the tip, as described in Section 2.3.7.4.

#### 2.3.7.1 Mixed mode propagation criterion

Fracture propagation is a combined response to all three deformation modes. Thus, a mixed mode failure criterion is introduced which depends on tension and shear simultaneously for loading, including tension, compression, and shear [Richard et al., 2014]. Three-dimensional mixed mode criteria determine if a fracture will propagate based on a

comparative stress intensity factor ($K_v$), derived from the values of $K_I$, $K_{II}$, and $K_{III}$, exceeding the local fracture toughness of the material [Richard et al., 2004]. Richard et al. [2014] reviewed a range of criteria and compared their predictions to experimental data, demonstrating that the most accurate condition for fracture failure is

$$K_v = \frac{K_I}{2} + \frac{1}{2}\sqrt{K_I^2 + 4(R_1 K_{II})^2 + 4(R_2 K_{III})^2} = K_{IC} \tag{2.17}$$

where $R_1$ and $R_2$ are the ratios of the mode I fracture toughness to the mode II and III fracture toughness ($R_1 = K_{IC}/K_{IIC}$, $R_2 = K_{IC}/K_{IIIC}$, where subscript $C$ refers to the critical stress intensity factor). For rocks, values of $K_{IIC}$ tend to be higher than $K_{IC}$, and $K_{IIIC}$ tend to be lower. The values used in this work are $K_{IC} = 1.8 \times 10^6$, $K_{IC}/K_{IIC} = 1/1.3268$ and $K_{IC}/K_{IIIC} = 1/0.6297$, as found through studies investigating the point of failure for pure modes II and III in rocks [Aliha et al., 2015, Chang et al., 2002, Wei et al., 2016].

When $K_I$ is negative due to a closing fracture tip (*e.g.*, in the case of an initial fluid pressure opening the fracture), $K_I$ is set to zero and failure is based purely on the shear modes.

#### 2.3.7.2 Propagation angle criterion

The mixed mode criterion of Richard et al. [2004] calculates the angle of the fracture propagation vector as a function of modal SIFs. It calculates two angles that are perpendicular and tangent to the crack front, and has been experimentally validated [Richard and Eberlein, 2013]. The perpendicular angle ($\varphi$, or fracture deflection angle along its plane, see Figure 2.3C) is calculated from the three SIFs as follows:

$$\varphi = \mp \left[ A \frac{|K_{II}|}{K_I + |K_{II}| + |K_{III}|} + B \left( \frac{|K_{II}|}{K_I + |K_{II}| + |K_{III}|} \right)^2 \right] \tag{2.18}$$

where $A$ = 140° and $B$ = -70°. Angle $\varphi$ is negative when $K_{II} > 0$ and positive for $K_{II} < 0$ and $K_I \geq 0$. As with the failure criterion, if $K_I$ is negative, it is set to zero to avoid introducing errors into the propagation angle. This can arise if a fracture closes from an initially open state. The tangent angle $\psi$ is not incorporated into fracture growth this work, to avoid additional complexities which arise when fracture tips fragment, but has been explored in other experimental and numerical methods [Cambonie et al., 2019, Cambonie and Lazarus, 2014, Leblond et al., 2015]. Instead, it is used as part of the quantification of the accuracy of the fracture growth angle in Section 2.5, and is

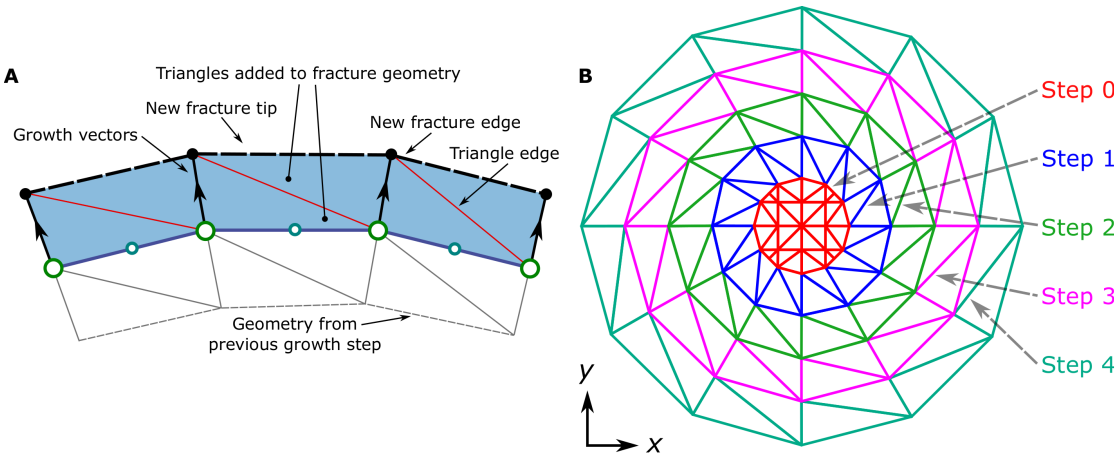



FIGURE 2.9: Growth of fracture using fracture tip growth vectors and the addition of triangles. A: Schematic representation of the process of extending the fracture during growth. Growth vectors provide new fracture tips at their ends and a new edge by connecting new tips. The area between the old and new tips is filled with two triangular surfaces.B: Annotated schematic of a fracture after 4 steps of growth, demonstrating the sequential addition of new triangles in each growth step. Triangle edges are coloured by the growth step they were added in.

calculated in a similar way to $\varphi$, using $K_{III}$ in place of $K_{II}$ with different constants:

$$\phi = \mp \left[ C \frac{|K_{III}|}{K_I + |K_{II}| + |K_{III}|} + D \left( \frac{|K_{III}|}{K_I + |K_{II}| + |K_{III}|} \right)^2 \right] \tag{2.19}$$

where $C = 78^{\circ}$ and $D = -33^{\circ}$. Figure 2.3 shows the fracture geometry (A) and tip (B), including a vector with angle $\varphi$ in the context of a discretised fracture tip.

#### 2.3.7.3 Propagation length criterion

A novel two-step Paris-type extension is used in this thesis to extend fracture tips. The method uses the value of $\mathcal{G}_n$ at each fracture tip $n$ to calculate an extension length $\Delta a_n$ which varies from tip to tip. The result is an extension length for each tip which is between 0 and $\Delta a_v$, the maximum fracture extension length per step for the volume. The criterion is introduced in full in Section 4.2, and the results and implications the novel two-step extension criterion are discussed in Chapter 4 in detail.

#### 2.3.7.4 Fracture extension

A growth vector ($\mathbf{p}_\varphi$) can be defined with length derived from the modified Paris law, and direction by the angle criterion. Vector $\mathbf{p}_\varphi$ is formulated in the local tip-orthogonal coordinate system, with axes $x_{1-3}$ that match a Frenet frame [Paluszny and Zimmerman, 2011]. Vector $x_1$ points forward along the direction of growth in the previous step, or if

the fracture has not yet grown, along a vector passing through the fracture's centre and the tip node. Vector $x_2$ is in the direction normal to the fracture plane adjacent to the node. Vector $x_3$ is directed along the fracture's tip, perpendicular to both $x_1$ and $x_2$. The angle $\varphi$ is then between the local axes $x_1$ and $x_2$, where $\varphi = 0^{\text{o}}$ means $\mathbf{p}_\varphi$ follows the same direction as $x_1$, and $\varphi = 90^{\text{o}}$ degrees means $\mathbf{p}_\varphi$ follows the same direction as $x_2$. Formally, the growth vector for one tip is formulated as follows:

$$\mathbf{p}_\varphi = \Delta a_n \left[\cos\varphi \;\; \sin\varphi \;\; 0\right]^T . \tag{2.20}$$

In global space, this vectors are defined as

$$\mathbf{p}_v = \mathbf{p}_\varphi \mathbf{Q} \tag{2.21}$$

where rotation matrix $\mathbf{Q}$ transforms the growth vector from local to global space. The extended fracture geometry is updated by creating a new fracture tip loop (constructed from connected tip nodes) along the points at the end of each vector. This can be defined as a strip of triangles or as a deformation of the spline representing the fracture surface [Paluszny and Zimmerman, 2013]. The geometry is updated by placing two triangles between each pair of tips.

Figure 2.9A shows a schematic of a fracture tip advancing due to growth vectors, including the arrangement of new triangles which are added to the fracture geometry. Figure 2.9B shows the geometry of a fracture with twelve tip nodes, grown over four growth steps. The fracture is initially a flat circle, and grows at a uniform extension length in each step with $\varphi = 0$, and is visualised from a perpendicular viewpoint for demonstration purposes. Each step is coloured to show how new surfaces are added to the fracture. The triangles in the initial step (0) are generated from the mesh. Handling of fractures intersecting boundaries and other fractures is discussed and demonstrated in Section 2.3.7.5. The new fracture geometry is brought forward to the next step, and subsequently the domain is remeshed. The new mesh is constrained in the same way as the original, *i.e.*, finite element sizes are fixed at the fracture tip, and increase in size towards the boundaries.

#### 2.3.7.5 Fracture intersection handling

Fracture intersections are handled during the addition of new surfaces at fracture tips. Intersections are relevant to Chapter 6, where geomechanical networks are generated with many intersecting fractures. The manner in which fracture intersections are handled in DFNs is key to their realism. In nature, intersecting fractures can form either 'T' or 'X' intersections, depending on whether fractures terminate against one another or

cross, respectively [Sanderson and Nixon, 2015]. A further complexity is that the type of intersection may vary in space, *i.e.*, a fracture may cross at one point but terminate in another, being partially a 'T' and partially an 'X' intersection.

The geometry of fracture intersections in the ICGT are handled after the growth vectors have been generated (see Section 2.3.7.4). At this point, each fracture tip node has a vector created using the distribution of SIFs. For each fracture, each tip node vector is passed through a series of checks, testing if the vector intersects or is close to the boundary, or passes through another fracture's surface. When a fracture's growth vector intersects either a boundary or a fracture's surface, that growth vector is truncated such that it ends on the intersecting surface. If a tip is close to the boundary, in order to avoid performing calculations at volume boundaries where values become unknown, tips are 'snapped' onto the boundary along the shortest path.

In the present implementation, tips which intersect boundaries and fractures are deactivated so that they do not propagate further. Future implementations can handle this differently, for example, allowing cross cutting in some or all cases, without any additional changes to the rest of the method. To handle the special case where two vectors intersect different boundaries, a special method creates a single triangular surface that fills the corner. Therefore, when new surfaces are added to the fracture, modifications to the growth vectors ensure fractures do not go out of bounds, and that 'T' intersections are created when fractures first intersect.

Due to the deactivation of fracture tips upon intersection, growth generally will not result in 'X' intersections, because growth is not evaluated on deactivated tips. Some empirical criteria attempt to model fracture behaviour at the intersections, for example, Renshaw and Pollard [1995] for general frictional surfaces in linear elastic materials, and Cheng et al. [2014] for hydraulic fractures. These criteria require additional sampling of local stress fields at each intersected crossing fracture at every step, adding significant computational cost to each growth step. Conversely, deactivation of tips is favourable in terms of computational cost, because SIFs are not evaluated at terminated tips. The complexity of fracture surfaces adds another challenge to computing cross cutting, as combined 'T' and 'X' intersections are not considered, and these empirical criteria use the angle of intersection between the fractures as an input parameter, thereby assuming fractures are planar. This work follows a simpler approach and assumes that only 'T' intersections occur when fractures grow and intersect.

'X' intersections can arise in the present implementation of ICGT in two ways. First, randomly inserted flaws can cross cut one another. This 'X' intersection will then remain in the simulation from the start. Furthermore, if both growth vectors on one fracture tip do not intersect a fracture, but the line between the ends of the growth vectors do,

the new surfaces are created using these vectors, and the new tip is deactivated. This case will result in a small part of the fracture crossing. Examples of fracture intersection in ICGT are explored in Section 6.2.3 with example geometries.

#### 2.3.7.6 Implications for SIF computation following intersection

Once a fracture tip intersects a free surface (*i.e.*, either another fracture or a boundary), the assumptions which enable calculation of SIFs at the corner point (see Section 2.3.6) are no longer valid. The implication of a fracture tip intersecting a free surface is that, at the point where the corner forms between the fracture tip and the free surface, a stress singularity occurs independently from the fracture tip singularity [Bažant and Estenssoro, 1979, Benthem, 1977]. At this exact corner point, SIFs lose their meaning as the inverse square root singular field is no longer present, as it is altered by the corner singularity [Nakamura and Parks, 1988]. Furthermore, additional deformation in modes II and III occur because they become coupled at the corner point [Pook et al., 2014]. A corner of this type will occur wherever a part of a tip is on a boundary and the adjacent part is not.

This change in fracture tip behaviour has implications for growth of fracture tips which are close to intersected nodes. Nejati [2015] examines the performance of the disk-shaped domain integral method on computing SIFs close to free surfaces (Figure 4.12 in Nejati [2015]). This method is demonstrated as being able to resolve the SIFs with good accuracy until the exact corner point is very close. The effect of the free surface on mode II and III coupling is also resolved as well. Nejati [2015] recommends that very fine meshes are used to compute SIFs in regions which are very close to free surface intersections.

In growing networks, corner SIF effects may change propagation of partially intersected fractures, with several features of this model working to reduce this effect. SIFs are computed at the centre of each fracture tip, rather than at the nodes, so the SIFs are always sampled at some distance from the intersection point, rather than at or close to it. Using the Displacement Correlation method also avoids sampling the region ahead of the intersection, where relatively few elements will be placed between the tip and the free surface. Dynamically refining intersecting tips would significantly increase mesh refinement in late growth step networks where many intersections occur, with significant implications for the computational cost of late stage GDFNs.

#### 2.3.7.7 Simulation end condition

In Chapter 4, growth simulations continue to run until they are grown to a specific number of growth steps. For the geomechanical networks in Chapter 6, a criterion to stop the simulation once the network is fully developed is implemented. Network growth is terminated when no further fracture tips grow in the domain. This can be the result of fractures terminating against the domain boundaries or other fractures, deactivating their tips for growth. Additionally, it is possible that the stress conditions in the domain no longer lead to growth, if the mixed mode failure criterion is not satisfied. For example, non-terminated tips may be shadowed by other fractures which have grown to their full extent. In future work, further growth in these cases may be possible by increasing the stress boundary condition when no further growth occurs in the domain.

## 2.4 Contemporary methods for modelling fractured media

A diverse range of methods for simulating fracturing are present in the literature. These can be grouped into continuum-based, discontinuum-based, or hybrid methods. Each of these methods takes a different approach to representing a fractured domain, meaning that each is suited to studying different physical properties of fractured rock. Most of these methods are not LEFM based, and instead use joint dislocation, element removal, or local damage to model fractures, thereby avoiding modelling the full physics of fracture growth. Reviews of previous work to model fracture growth in geological materials include Jing and Hudson [2002], who provide a general overview of the different numerical methods. Lisjak and Grasselli [2014] provide a more recent review focused on discrete element models. Rabczuk [2013] reviews continuum methods, including popular failure criteria and fracture representation schemes. Lei et al. [2017a] review the use of Discrete Fracture Networks (DFNs) for modelling geometrical, geomechanical and hydromechanical properties of fracture networks in geological media, highlighting the integration of DFNs with continuum, discontinuum, and hybrid methods. Lecampion et al. [2018] focuses on hydraulic fracture growth, where poroelastic effects are incorporated, highlighting many propagation models in the process.

### 2.4.1 Continuum based methods

Continuum based methods treat the domain as a single continuous body that contains fractures growing in response to deformation. Discontinuities can be described geometrically or non-geometrically, depending on whether they are represented by a geometric feature or a material property. In continuum methods, equations are solved using either

the finite difference method (FDM), the finite element method (FEM) or the boundary element method (BEM). Of these methods, FDM is now less favoured as it requires a structured mesh [Liu et al., 2018]. BEMs are not well suited for studying fracture mechanics and flow as they assume a homogeneous domain, but still see some use [Meng et al., 2013].

#### 2.4.1.1 Smeared fracture models

A smeared fracture, homogenisation, or damage zone approach is one in which rock mass deformation and strength moduli are reduced in fractured regions [Hadjab-Souag et al., 2007, Saksala et al., 2015, Wong et al., 2002, Zhou et al., 2017]. These methods intend to describe many fractures in a rock, or fractures across many scales, and avoid the computational expense of discretely representing each fracture. Representing a fracture by locally reducing the material's strength mimics experiments which observe a reduction in the Young's modulus as damage becomes more intense [*e.g.*, Martin and Chandler, 1994]. In smeared fracture modes, nucleation of fractures is an inherent part of the fracturing process and does not need to be handled separately [Francfort and Marigo, 1998]. However, slip, rotation, and separation effects cannot be explicitly captured. The lack of discrete fractures severely limits their applicability to studying hydraulic transmissivity, as fracture connectivity and anisotropy cannot be considered.

Examples of damage zone models include Saksala et al. [2015], who introduce discontinuities to their model after a zone is sufficiently damaged, using different damage models to handle the phases of fracturing. Zhou et al. [2017] examine the fracturing of three-dimensional heterogeneous concrete, composed of large particles representing aggregates, with mortar infill between them. Their results demonstrate that strain localisation occurs when loads are increased, such that at peak load, elements form in bands representing fractures in the domain. Hadjab-Souag et al. [2007] use the open source FEM package OOFEM to model two-dimensional fracturing of concrete, where the zone of the fracture is a smeared zone of macrocrack intensity.

Phase-field methods use the variational theory of quasi-static fracture growth [Francfort and Marigo, 1998]. This theory predicts propagation in the same manner as Griffith's theory, whilst also predicting the nucleation of new fractures. Phase-field models are a type of damage or smeared fracture model [Lee et al., 2016, Tanné et al., 2018]. Commercial modelling codes that use smeared damage zones include RS$^3$, ANACAP, and FLAC3D [Rutqvist et al., 2017].

#### 2.4.1.2 Continuum models with discrete fractures

Continuum methods which include discrete fractures are also referred to as combined continuum-interface methods, because elements or nodes in the domain are given special properties if they are part of a discontinuity [Riahi et al., 2010]. By modelling the fractures discretely, linear elastic fracture mechanics can be used in its full form to calculate stress concentrations at fracture tips [Hoek and Bieniawski, 1984]. The maximum number of fractures a method can represent within one model varies considerably. It is widely accepted that, when discretely representing fractures, there will be limits to the number and scale of fractures which can be simulated together, primarily due to the computational cost [Rabczuk, 2013].

Meng et al. [2013] use the Boundary Element Method (BEM) to model the growth of individual, three-dimensional rock fractures. BEM is appealing for fracture growth applications due to the vastly reduced requirements for meshing, as only the fracture and the boundary need to be discretised. Meng et al. [2013] also incorporate fracture tip twisting to growth at the tip, creating a segmented tip under some stress states.

The Displacement Discontinuity Method (DDM) is a numerical technique that has been developed specifically for fracture problems. It has been shown to be equivalent to the BEM [Liu and Li, 2014]. The DDM technique provides three components of displacement between the fracture surfaces (normal and orthogonal shear). Recent examples of the use of the DDM for three-dimensional fractures include Tang et al. [2016], who use the finite volume method to solve for fluid flow inside hydraulic fractures, and the DDM to handle the volume deformation. Their method enables the propagation of fractures, but is limited to predefined growth pathways in a single plane. Other applications of DDM allow multiple fractures to grow along arbitrary paths, to investigate interaction effects or fracture curving during hydraulic propagation [Kumar and Ghassemi, 2016, Sheibani, 2013]. In some models, there is a discrepancy between the numerical fracture tip stress intensity factors calculated through the DDM and analytical solutions, and so an empirically-derived correction constant is introduced to the stress intensity factor equations [Sheibani, 2013, Tang et al., 2016].

Standard FEM approaches that attempt to create meshes conforming exactly to fracture geometries require that the elements themselves define fracture boundaries. This restricts the possible fracture geometries, and means that geometry is significantly controlled by mesh refinement [Rabczuk, 2013]. Approaches which separate the handling of the model geometry (where the geometry includes the fractures, boundaries, and other features of the domain) and the discretising mesh have been developed to overcome this challenge [Paluszny and Zimmerman, 2013]. The mesh is created automatically in each

step to conform to the model's geometry. Changes to the shape of fractures or other objects in the domain are applied to the geometry, rather than the mesh, which avoids the challenge of splitting the complex finite element domain.

Belytschko and Black [1999] designed an influential 2D continuum model with discrete fractures that avoids remeshing by representing fractures separately from the mesh. Nodes near the fracture tip are enriched to improve stress intensity factor computation, and are tracked to deal with deviations from a straight crack. Criteria are also introduced to determine the crack propagation angle based on stress intensity factors (in this case, a maximum circumferential stress criterion). This numerical method became known as the extended finite element method (XFEM) [Belytschko et al., 2009]. The advantage of such an approach is that the mesh can be completely independent from the geometry of fractures, so that remeshing of the domain is not required. Additionally, XFEM methods can use both structured and unstructured meshes [Prévost and Sukumar, 2016]. Gupta and Duarte [2014] show a particularly advanced model, which uses XFEM principles to grow three-dimensional hydraulic fractures. O'Hara et al. [2016] demonstrate a generalised version of XFEM (GFEM) which is capable of growing and coalescing multiple interacting fractures in three dimensions. Despite the appeal of a continuum method for fracture growth which avoids re-meshing, in practice, XFEM approaches often require re-meshing in order to resolve stresses and fracture propagation in initially coarsely discretised regions of the model [Salimzadeh et al., 2017b, Yang et al., 2018].

### 2.4.2 Discrete element methods

Discrete methods use the discrete (or distinct) element method (DEM). DEMs use particles as elements in the domain which simulate the micromechanical behaviour of rocks [Lisjak and Grasselli, 2014]. Each particle is rigid and circular, representing a small part of the overall rock. At particle contacts, shear and normal stiffnesses and friction are defined, and the momentum equation is solved [Riahi et al., 2010]. When a bond between particles breaks, the load on surrounding bonds increases due to stress concentration. In this way, fracture propagation arises when breakages coalesce. The DEM is widely applied to many problems, and its contributions to understanding rock mechanics include simulation of relay ramp formation [Imber et al., 2004]. Lei et al. [2014a] replicated two-dimensional fracture networks from outcrop data, and investigated the hydraulic behaviour of these systems. They combined this analysis with fracture growth via the DEM, demonstrating significant changes in flow regimes following changes in mechanical conditions.

Particle-based methods such as the DEM have several shortcomings, which recent models have worked to overcome. Fracture surfaces are inherently rough as they are separations between discrete particles. Real fractures have variable separations with roughness not defined by a typical particle size. Smooth-joint contact models have been developed to overcome this [Mas Ivars et al., 2011]. The debonding of particles in DEM methods is an abstraction of the real processes arising in rock. Rules which are implemented to dictate when failure occurs are arbitrary and not based on fracture mechanics principles. Verification of DEM models may therefore also be indirect. Commercial DEM tools include 3DEC and UDEC produced by ITASCA [Karampinos et al., 2015].

### 2.4.3 Combined finite-discrete element methods

The finite-element and discrete-element methods can also be used in tandem, commonly known as FDEM (and interchangeably, FEMDEM) models [Lei et al., 2014b]. In these models, the domain is made up of jointed and broken finite elements over which physical properties such as stress are calculated. The discrete element method subsequently handles the deformation of the medium. The joint constitutive model, originating from Bandis et al. [1983], handles apertures and closure of broken elements. This method has been applied to radioactive waste disposal applications by Lisjak et al. [2016], investigating damage zone formation and sealing, and Marschall et al. [2017], investigating spalling around excavated tunnels. Three-dimensional simulations of fracture growth using FDEM methods are not yet widespread due to the computational cost [Lisjak et al., 2018]. Some examples of three-dimensional fracture simulations often have a severely reduced extent of the third axis [*e.g.*, Lei et al., 2017b, Yan and Zheng, 2017]. Efforts to improve the speed of FDEM simulations by utilising Graphical Processing Units and parallel programming have recently been successful [Lisjak et al., 2018]. It is likely that the speed of computation for a wide range of different models can be achieved in the same way. Examples of commercial FDEM methods include Irazu-FEMDEM [Lisjak et al., 2018].

### 2.4.4 Perturbation methods

Rice [1985] introduced the perturbation method for modelling the deformation of a crack front. Lazarus [2011] reviews the use of the perturbation method from a mechanical perspective. Further important advancements in the use of the method since this review included in this section. The method is based on a traditional linear elastic fracture mechanics approach following the analytical approaches of Griffith [1921] and Irwin [1961] (*i.e.*, fracture growth is controlled by the local crack tip fields, with propagation

controlled by stress intensity factors or the strain energy release rate). The perturbation method predicts that small deviations from a uniform fracture tip are corrected by the variation in the SIFs, which will encourage more or less local growth to make the front uniform [Rice, 1985]. This is achieved by numerical iteration of Bueckner-Rice weight functions, providing the first-order variation of the SIFs arising from a small perturbation of the front, without resolving the full mechanical fields.

The perturbation method has been expanded to work in three dimensions and for mixed mode deformation [Rice et al., 1994]. The method is particularly effective at resolving the advancing position of the crack front at high detail during growth [Favier et al., 2006, Lazarus, 2003], and has been used to reproduce experiments of peeling fractures [Budzik and Myhre Jensen, 2014, Vasoya et al., 2016]. Advancements of the method which are relevant to geological fractures include twisting and fragmentation induced by mixed mode conditions (mode I and III) [Cambonie and Lazarus, 2014, Leblond et al., 2011], handling multiple propagating and coalescing fractures in the same plane [Legrand and Lazarus, 2015], and incorporation of heterogeneity ahead of the fracture tip [Gao and Rice, 1989]. Since the method meshes and solves only the conditions at the tip of a fracture, the displacement over its surface is not resolved, limiting its suitability for applications requiring accurate apertures, such frictional contact and fluid flow.

## 2.5 Validation of stress intensity factors around static fractures

This section describes the validation of SIFs and propagation angles for a range of mesh refinements and boundary conditions. Previously, the accuracy of SIFs have been assessed by Nejati et al. [2015b] for DC, Nejati et al. [2015a] for the disk-shaped domain integral, Nejati et al. [2016] for contact, and Thomas et al. [2017b] for interaction. Validation of the SIF is significant for the growth method for several reasons. First, if fracture tip SIFs are accurate compared to analytical solutions, this demonstrates that the finite element solution of the stress and displacement fields is accurate, and that the material around the fracture tip responds as if it is adjacent to a real fracture in the material. Second, because the growth of a fracture can be determined by the three SIFs, growth of the present inclined fracture will be accurate. Growth in subsequent steps does not have an associated analytical solution due to the complex fracture surface which emerges, therefore, further validation of multi-step growth must be performed by comparing the resulting geometry to fractures in both experiments and outcrops (as explored in Section 4.3).

In this section, the errors in the SIFs and the angles of fracture propagation are investigated, in order to quantify the effect that discretisation and computation errors have on growth. Two formulations of $R_d$ are evaluated for use in growth modelling.

### 2.5.1 Analytical solutions for stress intensity factors

#### 2.5.1.1 Uniaxial tension

The analytical solutions for the SIFs along the tip of an inclined penny shaped fracture under uniform tension are provided by Kassir and Sih [1975]:

$$K_I = 2\sigma\sqrt{a/\pi}\sin^2 b \tag{2.22}$$

$$K_{II} = \frac{2\sigma\sqrt{a\pi}}{2-\nu}\sin 2b\cos\theta \tag{2.23}$$

$$K_{III} = \frac{2\left(1-\nu\right)\sigma\sqrt{a/\pi}}{2-\nu}\sin 2b\cos\theta \tag{2.24}$$

where $K$ is the stress intensity factor (SIF) with units Pa $\mathrm{m}^{1/2}$, $I$, $II$ and $III$ are the crack tip deformation modes (see Figure 2.1), $\sigma$ is the applied normal far-field stress, $a$ is the fracture radius, $\theta$ is the angle around the fracture, $b$ is the inclination of the fracture plane relative to the load, and $\nu$ is the Poisson's ratio of the medium. $K_I$ is constant around penny shaped fractures of any inclination, and equal to 0 when the fracture is parallel to the direction of stress. $K_{II}$ and $K_{III}$ change sign on either side of the fracture (top and bottom for $K_{II}$ and sides for $K_{III}$). Figure 2.10 compares these analytical solutions to the results for a 1 m fracture at the centre of a cubic 20 $\times$ 20 $\times$ 20 m domain, inclined at 45° to the extension ($z$) direction. The results match the analytical solution very well. Small scatter is found on all the modes as a result of the mesh discretisation. In this figure, the material property values and far-field loads used are $\nu = 0.25$, Young's modulus $E = 1$ Pa, and normal stress $\sigma = 1$ Pa applied at the top boundary of the domain as a Neumann condition. These values of $\sigma$ and $E$ are chosen in this section and in Chapter 3 such that the results could be normalised conveniently, because these are the two variables which alter the magnitude of the SIFs in the present analytical solutions.

#### 2.5.1.2 Uniaxial compression

Analytical solutions for SIFs on an elliptical fracture under uniaxial compression are provided by Nejati [2015]. These solutions consider compressive stresses and pressures

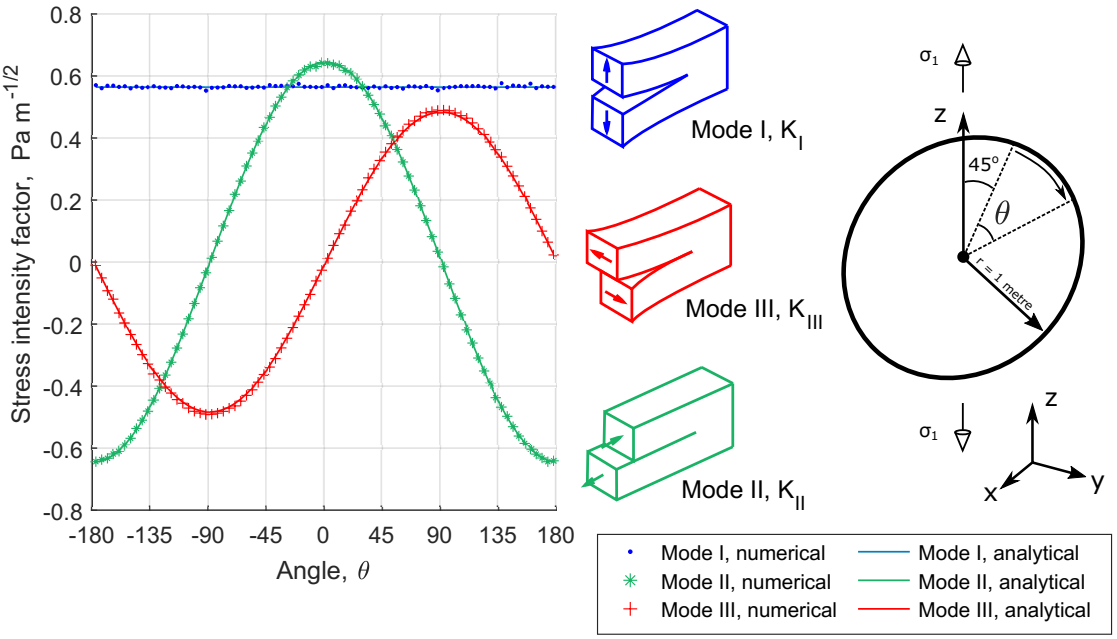



FIGURE 2.10: Analytical and numerical stress intensity factors around an isolated fracture. The fracture is in tension, inclined 45° to the stress field. The analytical solution is calculated using Equations 2.22, 2.23 and 2.24. The 1 m fracture has 80 tip nodes and is at the centre of a cubic 20 × 20 × 20 m domain. The crack tip deformation modes are shown in schematic form to the right of their respective curves.

to be positive. Similar to the conditions for uniaxial tension, the circular fracture is inclined relative to the compressive load direction with angle $b$. These analytical solutions also provide a fluid pressure term ($p_0$) which would be initially applied on the fracture surfaces. To incorporate this into the numerical solution, before the domain is compressed, the standard deformation algorithm solves for the volume deformation when fractures are opened by an initial fluid pressure. This is set as a Neumann boundary condition, and results in a non-uniform final aperture. Subsequently, the fluid pressure is removed, and the induced aperture is retained. The compressive stress is then applied to the top of the cubic domain.

Two conditions are possible based on what happens during and after fracture closure. When the surfaces stick together, no deformation occurs after closure, and only the applied shear and normal stress before closure contribute to deformation. This 'stick' condition therefore refers only to the deformation which occurs when the fracture closes, with no further deformation occurs after this point. In contrast, when the surfaces slip, there is additional deformation due to effective shear stress over the surfaces during slip. SIFs for the stick condition are as follows:

$$K_I = \sigma\alpha_1\sqrt{a/\pi} \tag{2.25}$$

$$K_{II} = \sigma\alpha_1\frac{2\sqrt{a/\pi}}{2-\nu}\cos\theta \tag{2.26}$$

$$K_{III} = \sigma\alpha_1 \frac{2(1-\nu)\sqrt{a/\pi}}{2-\nu} \sin\theta \tag{2.27}$$

where $\alpha_1$ is defined as

$$\alpha_1 = \frac{-2p_0}{\sigma}. \tag{2.28}$$

To form the slip version of the equations, Equation 2.25 is the same, and Equations 2.26 and 2.27 are modified by changing $\alpha_1$ for $\alpha_2$, where $\alpha_2$ is defined as

$$\alpha_2 = 2\left[\mu\left(\sin^2 b - \frac{p_0}{\sigma}\right) + \frac{\tau_c}{\sigma}\right] - \sin 2b - \frac{2p_0\,(1-\cot b)}{\sigma} \tag{2.29}$$

where $\mu$ is the coefficient of friction, and $\tau_c$ is the cohesive stress. The first two terms of $\alpha_2$ are associated with deformation during sliding, and the last term is associated with deformation during closure. The analytical solutions for slip conditions are therefore defined as follows:

$$K_I = \sigma\alpha_1\sqrt{a/\pi} \tag{2.30}$$

$$K_{II} = \sigma\alpha_2 \frac{2\sqrt{a/\pi}}{2-\nu} \cos\theta \tag{2.31}$$

$$K_{III} = \sigma\alpha_2 \frac{2(1-\nu)\sqrt{a/\pi}}{2-\nu} \sin\theta \tag{2.32}$$

### 2.5.2 Error calculation

The SIF error $e_K$ is calculated as a single value for each fracture, combining all three modes:

$$e_K = \frac{\sum_{i=I}^{III} \int_{L_f} \left|K_i^A - K_i^N\right| dl}{\sum_{i=I}^{III} \int_{L_f} \left|K_i^N\right| dl} \tag{2.33}$$

where $i$ is one of the three deformation modes ($I$, $II$ or $III$), $L_f$ is the fracture circumference, $K_i^A$ is the relevant analytical solution for the mode $i$ SIF, $K_i^N$ is the numerical solution for the mode $i$ SIF, and $dl$ is the distance between fracture tip nodes.

To relate $e_K$ directly to fracture growth, the numerical propagation angles $\varphi^N$ and $\psi^N$ are compared to the analytical propagation angles $\varphi^A$ and $\psi^A$ obtained from the analytical SIFs and Equations 2.18 and 2.19. Whilst the twisting angle $\psi$ is not used for growth, it is incorporated in the following error calculation in order to incorporate all aspects of the criterion of Richard et al. [2004]. The propagation angle error, $e_a$ is defined as

$$e_a = \frac{\int_{L_f} \left|\varphi^A - \varphi^N\right| dl + \int_{L_f} \left|\psi^A - \psi^N\right| dl}{\int_{L_f} \left|\varphi^A\right| dl + \int_{L_f} \left|\psi^A\right| dl}. \tag{2.34}$$

Hence, this method provides the cumulative error along the entire fracture tip.

### 2.5.3 Error for different domain radii

Figures 2.11 and 2.12 compare the number of fracture tip nodes to $e_K$ and $e_a$ for tension, compression in stick, and compression in slip. The fracture has a 1 m radius, inclined at 45° to the $z$ axis. The domain is 20 × 20 × 20 m in size, chosen to ensure no boundary effects change the SIFs along the fracture tip. In tension, the top boundary is assigned a Neumann stress boundary condition in the $z$ direction of $\sigma = \pm 1 \times 10^7$ Pa. The bottom boundary is fixed, and the remaining boundaries have no conditions (*i.e.* are free to deform with the volume). In compression, the direction of the Neumann stress condition is reversed. To produce slip and stick conditions, the friction coefficient ($\mu$) is set to 0 and 100 respectively in the compressive cases. Other material properties are Young's Modulus $E = 10 \times 10^9$ Pa, $\nu = 0.3$ and $\tau_c = 0$. In order to have non-zero SIFs in stick conditions, an initial fluid pressure of $5 \times 10^6$ Pa is applied uniformly across the fracture surface. The points sampled for DC are at a distance of $R_d$ behind the fracture tip. The number of tip nodes around the fracture has a linear relationship with the number of elements in the domain. Two values of the $R_d$ are shown in order to demonstrate the differences in accuracy between the cases, $R_d = 0.5\,|B_d|$ (Figure 2.11) and $R_d = a/10$ (Figure 2.12).

The increase in SIF and propagation angle accuracy with mesh refinement is consistent for all boundary conditions. The disk-shaped domain integral with quarter point elements is the most accurate method for most tip numbers. Some exceptions include compression in slip with $R_d = a/10$ (Figure 2.12B) where the disk-shaped domain integral without quarter point elements is marginally more accurate. The error in the angle is particularly small for fractures with more than 40 tips, especially given that this is the total error along the entire tip. Thus, fractures grown with coarse meshes will still produce accurate geometries. $R_d = 0.5\,|B_d|$ is the more accurate of the two domain radii, particularly when quarter points are used. Without quarter points, $R_d = 0.5\,|B_d|$ becomes less accurate for finer meshes, suggesting that quarter points are key to producing good SIFs with very small $R_d$.

Setting $R_d = 0.5\,|B_d|$ has additional benefits for growth simulations. If $R_d$ changes dynamically based on the tip size, and hence adapts to local mesh refinement, $R_d$ will remain suitable to the local tip conditions. For example, if parts of the fracture have propagated more than others, tips will be further apart, implying that the mesh in the vicinity of the larger tips will be coarser. In these cases, a larger integration radius will allow more elements to be sampled. In contrast, $R_d$ values based on the fracture radius are less suitable when fracture surfaces become irregular, as one value of the radius will not be generally representative of the entire fracture.

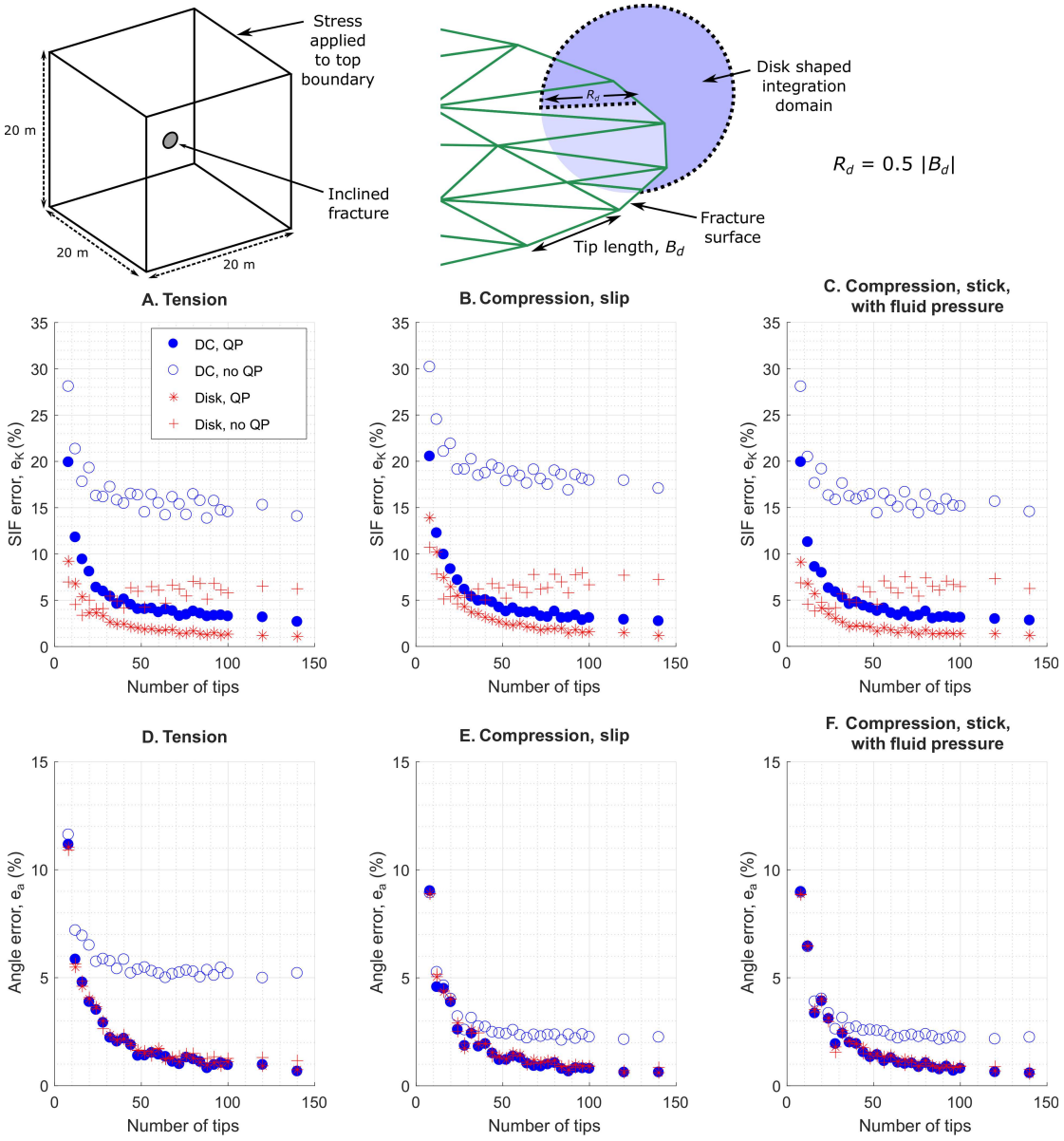



FIGURE 2.11: Stress intensity factor and propagation angle error for an inclined fracture under three stress states, with the domain radius $R_d$ set to $0.5|B_d|$. The number of tips correlates with the mesh density at the fracture tip, and linearly with the total number of elements in the domain. Results are shown for four calculations: using Displacement Correlation (DC) and the disk-shaped domain integral (Disk), and with and without quarter points (QP) at the fracture tip. For 8 tip nodes, there are 1264 elements in the domain, and for 140 tip nodes, there are 22784 elements.

## 2.6 Quantification of boundary effects on stress intensity factors

At the surface of an elastic solid, stress is concentrated, known as surface or interface stress [He and Li, 2006]. These boundary effects are also known as finite size effects [Anderson and Anderson, 2005]. For a spheroidal inclusion near the edge of a linear-elastic half plate, the stress interaction between these features is observable when the inclusion is within several of its diameters of the free surface [Al-Ostaz et al., 1998]. Pollard and Holzhausen [1979] demonstrate that stress and displacement increase on fluid filled fractures near the Earth's surface. In particular, they note that $K_I$ increases asymmetrically along the fracture, with the largest increase occurring at the tip closest to the surface.

In this thesis, the majority of fractures are examined at the centre of a large domain. Typically, fractures begin simulations as 1 m fractures near the centre of a 20 $\times$ 20 $\times$ 20 m domain, meaning they are as far from the boundaries as possible. However, fracture networks grown in Chapter 6 contain fractures which begin closer to the boundary of the domain, and grow towards and intersect boundaries. Identifying how boundary effects change the stress on fractures is important, because the additional boundary stress concentration will modify growth. Pollard and Holzhausen [1979] examine fractures in similar domains to those examined in this thesis, however, do not provide an analytical solution against which the surface stress concentration can be quantified. Instead, the deviation from the analytical solution for an isolated fracture (*i.e.*, far from the domain boundaries) is used in this section to quantify how much SIFs are modified by the presence of the free surface boundary.

Figure 2.13 shows how SIFs are changed by boundary effects in the ICGT. Three cubic domain sizes are shown, with sides of length 20, 5, and 2.5 m. The SIFs are shown on a fracture at the centre of the domain, which, in all three cases, has the same radius (1 m), centre (0, 0, 0), and normal vector to its plane (0, 1, 1). The boundary conditions and material properties used are the same in Section 2.5.3 to examine SIF accuracy with changing mesh refinement (Young's modulus of 1 Pa, Poisson's ratio of 0.3, and a tensile Neumann stress condition applied on the $+Z$ boundary with magnitude 1 Pa, with the $-Z$ boundary fixed at zero displacement). Two numbers of tip nodes are shown, 20 (subfigures A, C, and E) and 80 (subfigures B, D, and F). Each graph also shows the analytical solution for an inclined penny shaped fracture under tension (Equations 2.22, 2.23, and 2.24).

For a relatively large 20 $\times$ 20 $\times$ 20 m domain, Figure 2.13A and B show that fracture SIFs closely match the analytical solution at both 20 and 80 tip nodes, as discussed in

Section 2.5. When the domain is smaller, the accuracy relative to this analytical solution reduces. Figure 2.13C and D in a $5 \times 5 \times 5$ m domain show that all three SIFs are slightly modified. This change is asymmetric along the fracture's tip, with nodes at the top of the fracture (at $0^o$, closest to the $+Z$ boundary) being most perturbed. The change for a domain with 5 m sides is very small, but is much more significant for the 2.5 m domain (Figure 2.13E and F), where all tip nodes are changed relative to the analytical solution. The stress perturbation effect is non-uniform, particularly significant on the upper half of the fracture (from $-90^o$ to $+90^o$), as observed by [Pollard and Holzhausen, 1979]. Despite the refinement being significantly lower in the 20 tip case, both mesh refinements demonstrate a similar change in SIFs, suggesting that boundary concentration effects are invariant of local mesh refinement. The impact of mesh refinement on boundary effects is considered further in the next figure.

Figure 2.14 tests ten different domain sizes, using the same geometry, material properties, and boundary conditions as used in Figure 2.13, to quantify how mesh refinement alters SIFs relative to the analytical solution. For each domain size, a fracture is tested with three different numbers of tip nodes (20, 80, and 160), thereby testing a progressively more refined domain. Equation 2.33 is used to quantify the difference between the SIFs and the analytical solution, providing one value per simulation. A dashed, red line shows the diameter of the fracture which is the smallest possible domain that could contain the same size fracture without boundary intersections.

As the simulated domains approach the minimum possible size, the change in the SIFs becomes larger. For the 20 m domain, the deviation from the analytical solution is similar to those observed in Figure 2.11A for all three numbers of tips, and is purely the result of numerical error with no influence from the boundary. Smaller domains lead to larger deviations from the analytical solution, with a larger rate of change for domains smaller than 6 m (or three times the fracture diameter). A significant observation is that the SIF change between three numbers of tip nodes is the same, *i.e.*, the same gap between the 20 tip node domain and 80 tip node domain persists, regardless of domain size. This suggests that the stress concentration due to boundary proximity is the same regardless of the mesh refinement.

Stresses are applied at the top ($+Z$) boundary throughout this thesis, leading to higher stress concentrations at the top of the domain. This means that fractures near the top boundary will be relatively more stressed than those which are lower in the domain. This will lead to a preference for fracture growth on fractures near the top boundary. Furthermore, fracture tips close to the $+Z$ boundary will experience a relatively higher stress than other tips, which will change the SIF distribution, and therefore lead to changes in the angle and extent of growth.

## 2.7 Discussion

This chapter has introduced the ICGT in the context of other fracture simulators available at the present time. Section 2.5 compares the numerically calculated SIFs around an isolated fracture to analytic al solutions for fractures in tension and compression, providing the most up to date validation of SIFs in ICGT. This validation is vital as the SIFs underpin many aspects of ICGT on which this thesis relies. Chapter 3 investigates the interaction between static fractures, where SIFs are the key way interaction is quantified. The effect of local mesh configuration is considered further, as this can have an impact on interaction effects. Chapter 4 introduces the growth of fractures, and the growth criteria ICGT uses to control this growth. These are completely based on either $\mathcal{G}$ or the SIFs. The accuracy of the SIFs shown here, in particular, the error in the propagation angle, provide confidence that the growth we observe is accurate.

The SIF results in Section 2.5 are for an idealised fracture (penny shaped, circular disk) in order to match the analytical solutions. After growth, fractures become non-planar and can no longer be validated in this way. Instead, the geometries must be compared to experimentally observed growth. Chapter 4 covers the methodology and validation for fracture growth under tension and compression.

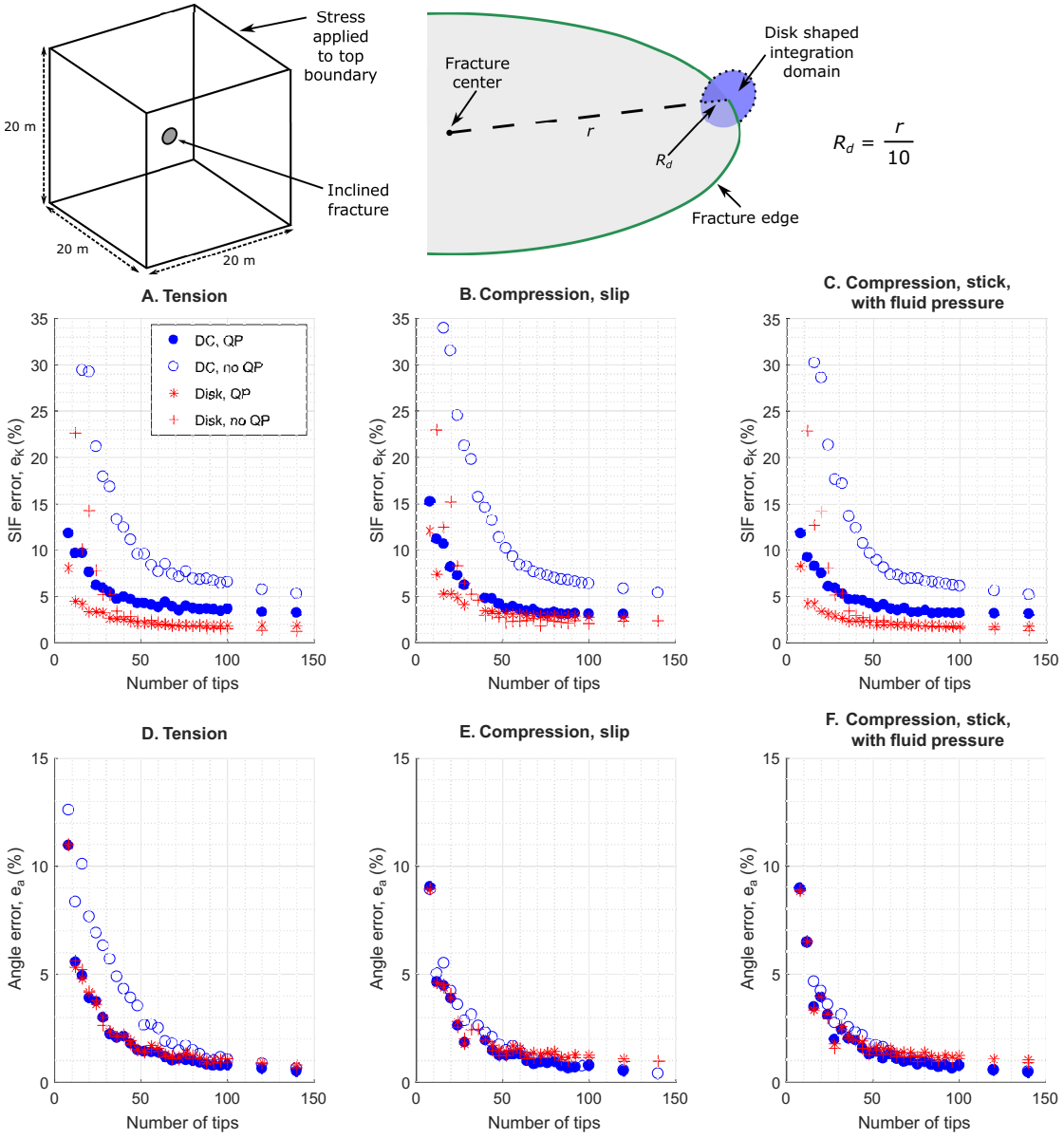



FIGURE 2.12: Stress intensity factor and propagation angle error for an inclined fracture under three stress states, with the domain radius $R_d$ set to $a/10$. Meshes and computation methods used are the same as in Figure 2.11.

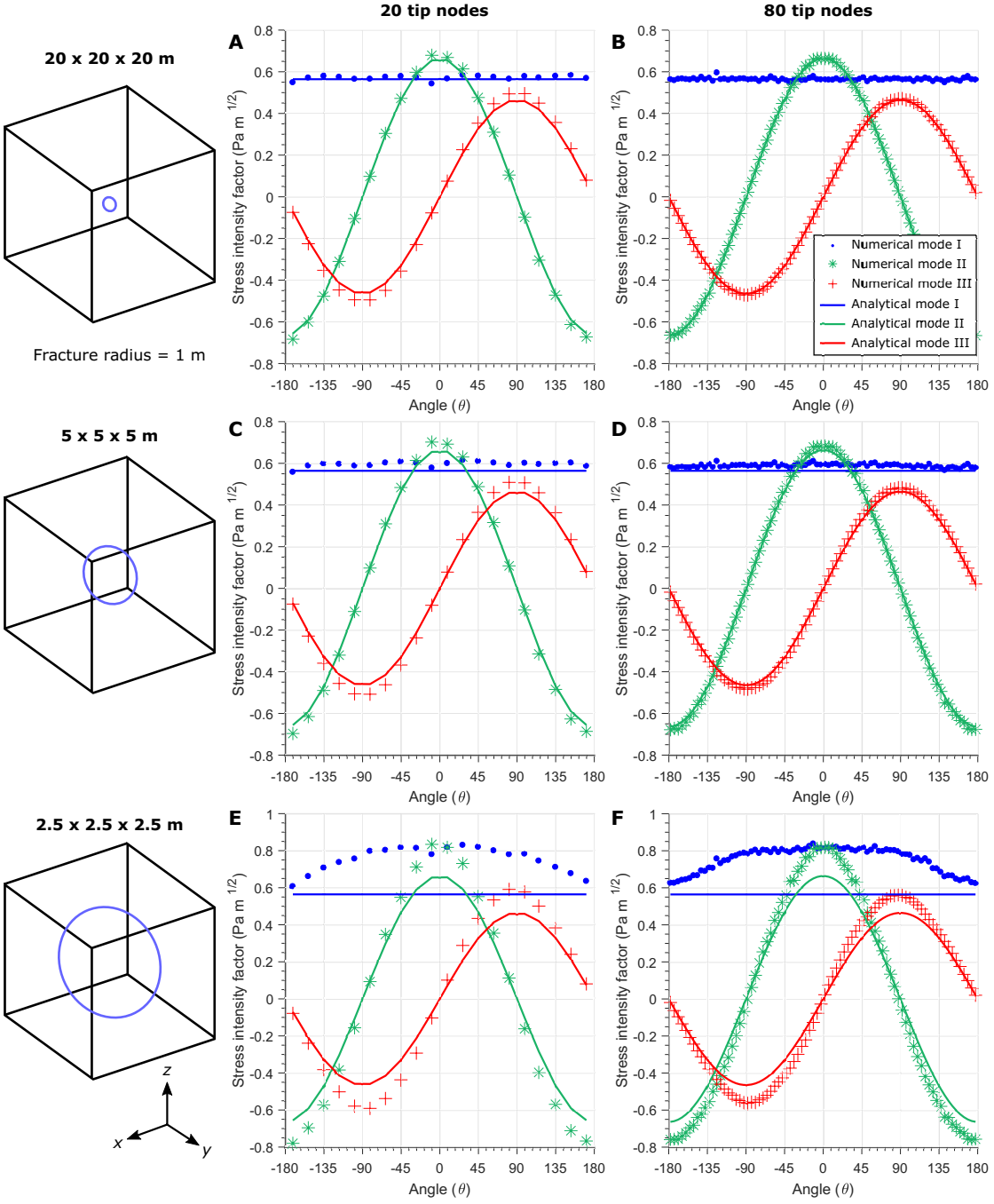



FIGURE 2.13: Change in SIFs on fractures due to domain size effects. Three cubic domains are examined with a fixed size fracture. The left column shows a schematic of the domain, and the graphs on the right of each domain show the SIF result for two meshes with different numbers of tip nodes (20 and 80). On all graphs, 0° is at the top of the fracture, closest to the upper boundary.

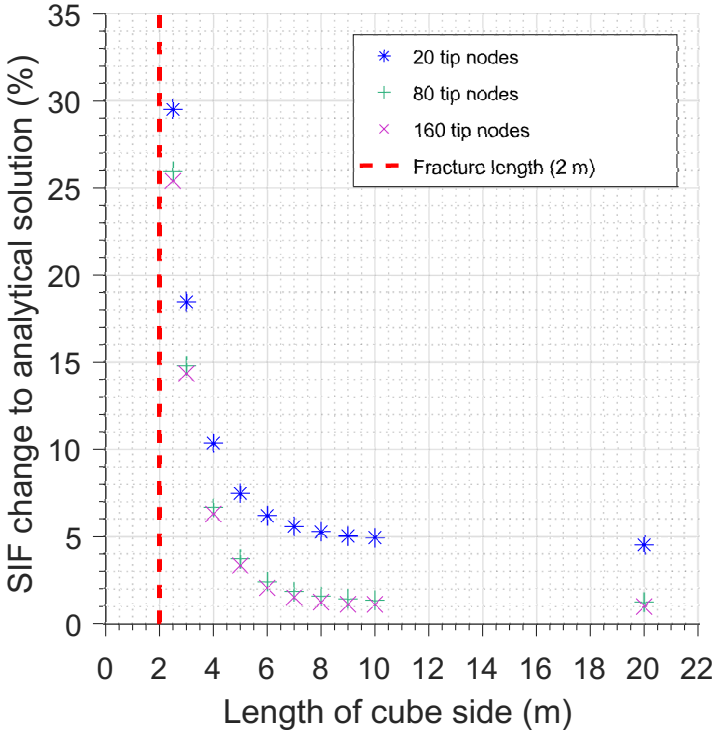



FIGURE 2.14: Change in SIFs relative to the analytical solution for an inclined penny shaped fracture under tension depending on the size of the domain. The analytical solutions for each deformation mode are given by Equations 2.22, 2.23, and 2.24, and the SIF change relative to this solution is found using Equation 2.33. The red dashed line indicates the diameter of the fracture, *i.e.*, no domain can be smaller than this and contain a 1 m radius fracture. Three different numbers of fracture tip nodes are examined to demonstrate how the perturbation caused by the boundary varies due to mesh refinement.

# Chapter 3

# Understanding fracture interaction through study of stress intensity factor perturbations

## 3.1 Introduction

Fracture interaction in brittle rocks is of great interest at a variety of scales. Fractures alter the surrounding stress state of the medium, enhancing or reducing stress depending on the mode of deformation, location, and fracture orientation [Olson and Pollard, 1991]. Predicting the behaviour of a fracture system requires a thorough understanding of the stress state within the material, and the current fracture geometries. This is not straightforward to characterise in many settings, particularly for geological materials due to their heterogeneity, anisotropy, and the uncertainty of subsurface characteristics relative to exposed outcrops. At smaller scales, linkage of micro and meso-scale fractures has a large control on the hydraulic properties of rocks and reservoirs, with implications for hydrocarbon production [Nelson, 2001] and radioactive waste disposal [Tsang et al., 2015]. Analysis of fractures in outcrops indicates the paleostress environment at the time of their formation [Fox et al., 2007]. At larger scales, interaction effects are a key control over the formation of geological structures [Delaney and Pollard, 1981], rift evolution [Gawthorpe and Leeder, 2000] and fault slip during earthquakes [Green et al., 2015, Zachariasen and Sieh, 1995]. Determining when faults transition from soft to hard-linkage requires accurate observations and a detailed history of displacement [Duffy et al., 2015].

When a fracture is present in a tensile stress field, it alters the stress in its local area in two ways [Kachanov, 1993, Price and Cosgrove, 1990, Rives et al., 1992]. First, a fracture generates a shielding zone around its surface, also known as a stress shadow, in which local stress is reduced. Second, at the tip of a fracture, an amplification zone is generated, also known as the concentration zone, in which local stress is increased. When another fracture enters these zones, this change in stress results in significant changes to their behaviour. When the fractures are similar in size, they induce a reciprocal effect upon one another. In full three-dimensional space, this interaction is complex, and the change in stress varies significantly over each fracture, particularly when fractures overlap or under more complicated external stresses than tension. Interaction is important because it may both enhance and preclude growth, and is a controlling mechanism for the self-organisation of fracture patterns. In turn, self-organisation may influence the ensuing mechanical and flow properties of the fracture pattern [Olson, 2004, Olson and Pollard, 1991]. Field-based approaches to understanding close fracture interaction involve quantifying how fractures grow based on initial separation and overlap (*e.g.* Figure 3 in Schultz [2000] and Figure 9 in Lamarche et al. [2017]).

Numerical simulations are instrumental in understanding fracture interactions. A variety of techniques have been utilised to numerically model fractured geological media [Jing and Hudson, 2002], many of which include discrete fractures. Stress intensity factor (SIF) based fracture modelling has received great attention in material design to predict failure [Busfield et al., 2005, Kamaya, 2008b, Moussa, 2002, Stonesifer et al., 1993]. SIFs provide an effective method for analysing fracture propagation and interaction [Lam and Phua, 1991, Paris and Erdogan, 1963]. SIFs have also been used in geological models to predict fracture behaviour [Olson, 2004, Paluszny and Zimmerman, 2013, Philip et al., 2005, Renshaw and Pollard, 1994] but have not yet been routinely adopted for investigating geological fracture interaction.

Kachanov [1987] presented an approximate method for calculating how the SIFs of one fracture are affected by another fracture. The system is simplified by using a transmission factor which depends on the fracture geometry and orientation of the stress field, but not the magnitude of the stresses. The three-dimensional formulation of this method incorporates the idea that fracture interaction may amplify (increase) or shield (decrease) stress locally depending on the geometry. Other early analytical approaches include that of Fabrikant [1987], who used an iterative procedure to evaluate each fracture's effect on another. More recently, work has expanded on these methods to improve accuracy or investigate more complex systems of fractures. Laures and Kachanov [1991] extended this analysis to three-dimensional microcrack arrays using the same method as Kachanov [1987], focusing on cases where one fracture interacts with a group of smaller fractures. They showed that three-dimensional interaction effects are generally weaker than 2D

interaction effects. Gross [1982] first introduced the method of polynomial expansions of tractions on fractures, providing approximate SIFs for multiple straight cracks. Benveniste et al. [1989] used a superposition scheme for which Kachanov's method is a special case. Zhan and Wang [2006] used a first-order average traction method to study the same set of geometries as Kachanov [1987].

Numerical methods for calculating SIFs provide a convenient means to study SIF alteration, because any arbitrary fracture geometry can be investigated. In 2D, Pengcheng et al. [2012] demonstrated amplification and shielding using the displacement correlation method to find SIFs. Yan [2010] investigated the interaction of circular arc cracks in tension. Fan et al. [2016] investigated the case of two fractures in compression using the FEM and compared their numerical results to photoelastic and uniaxial compressive experiments. Legrand and Lazarus [2015] used a finite perturbation method to study fracture interaction in 2D, closely matching Kachanov's method predicting the increase in SIFs under tension. Along with SIF perturbations, they studied fracture growth and coalescence, evaluating growth using a fatigue law to govern fracture propagation. Kamaya [2008a] used the FEM to study SIF variation along the tips of surface cracks, using the SIF perturbation to accurately predict growth [Kamaya, 2008b]. Most of these studies investigate interaction of static geometries and yield interaction relationships that depend either on distance or on relative spatial and geometric arrangements, but only explore specific geometries such as coplanar or stacked configurations. To aid in interpretation of fracture interaction and growth, there is a need for methods which can simulate interaction in full three-dimensional space, without constraining the size, orientation or number of fractures. A flexible numerical approach can be readily applied to any fracture geometry, subjected to arbitrary boundary conditions, while analytical and semi-analytical approaches may be constrained to specific geometries and conditions.

In this chapter, ICGT is employed is used to investigate and quantify three-dimensional fracture interaction [Paluszny and Zimmerman, 2011, 2013]. Fracture interaction is analysed by investigating changes in the SIFs for all modes of fracture tip deformation. Characterisation of interaction is captured by three novel measures for quantifying the spatial distribution of fracture growth energy. Interaction is quantified based on the perturbation of the SIFs by comparing interacting fractures to undisturbed single fractures in the same stress field. The spatial variation of these interaction measures are proposed as 'interaction maps', or 'stress intensity factor variation maps', used interchangeably in this chapter. These maps provide a new way to assess the extent and magnitude of fracture interaction. This chapter presents work first published in Thomas et al. [2017b], with additional figures and analysis, including interaction maps for compression. The numerical values in the interaction maps and data on the graphs is available on the UK National Geoscience Data Centre (see Thomas et al. [2017a]).

## 3.2 Stress intensity factor perturbations due to interaction

The fracture modelling workflow introduced in Chapter 2 is used here to simulate one or two static fractures in a domain. Interaction is examined between static fractures, *i.e.* propagation is not considered until the following chapters. Static fractures can be set in identical positions between different simulations, therefore, comparisons between the SIFs at exactly the same points on one fracture in different interacting cases is possible. Fractures which have grown will have fracture tips in different locations between simulations depending on the extent of interaction. Therefore, comparing the SIFs on grown fractures would not provide an identical comparison due to the change in geometry.

The material property values and far-field loads used throughout this chapter are Poisson's ratio $\nu = 0.25$, Young's modulus $E = 1$ Pa, and normal stress $\sigma = 1$ Pa. Fractures are placed at the center of a 20 $\times$ 20 $\times$ 20 m cube.

### 3.2.1 Identification of interaction effects

The interaction between a pair of fractures is investigated by quantifying changes in the SIFs. These changes depend on fracture proximity, size, relative position and the type of stress applied, and have been widely observed [Fan et al., 2016, Kachanov, 1987, Kamaya, 2008a, Legrand and Lazarus, 2015, Olson and Pollard, 1991, Yan, 2010]. The present method of examining interaction, explored by other authors [Kamaya, 2008a, Legrand and Lazarus, 2015, Yu et al., 2009], is to first calculate the SIFs around a fracture that is interacting with others ($K_i^{int}$). Then, all but one of the fractures from the domain are removed, and SIFs are calculated for that isolated fracture ($K_i^{iso}$). In this way, the same geometry for one fracture is tested twice (once in isolation and once in interaction), and the changes in the SIFs can be examined through the ratio between $K_i^{int}$ and $K_i^{iso}$. The fracture spacing convention introduced by Kachanov and Laures [1989] is used in this work, where the spacing is scaled by the fracture radius and reported in the form $\Delta/2r$.

An example of the difference between interacting and isolated SIFs is shown in Figure 3.1. The graph shows the SIFs for an inclined fracture, centred at (0, 0, 0) with a radius of 1 m, at the centre of a 20 $\times$ 20 $\times$ 20 m cube. The analytical solutions of the SIFs for an isolated fracture of the same inclination are plotted as lines (Equations 2.22, 2.23 and 2.24). A second fracture is placed in the same plane, centred at (0, -1.6, 1.6). Compared to an isolated fracture where the analytical solution is a close match (*e.g.* Figure 2.10), the numerical SIFs are are now altered due to the proximity of another fracture. Modes I and II are increased around $\theta = 0^{\circ}$, and mode III is unaffected. The distribution of this change has a complex relationship with the location of the

interacting fracture. A reciprocal effect is also induced on the interacting fracture. This work provides a methodology for quantifying and summarising these changes, aiming to provide practical information for predicting fracturing behaviour.

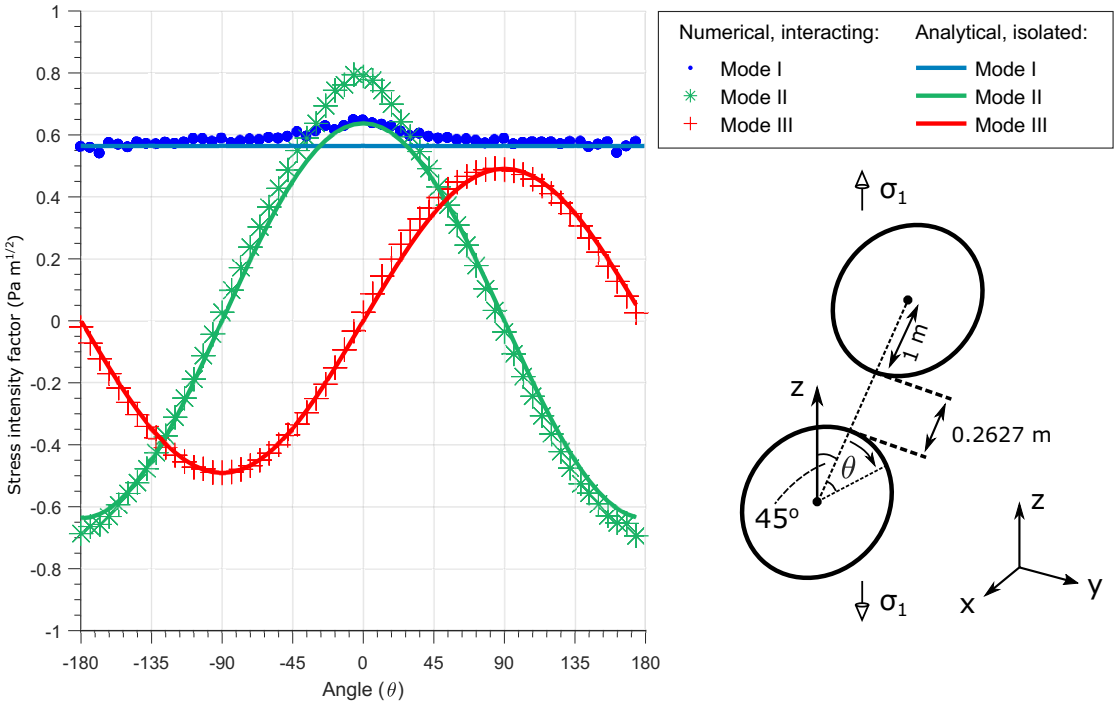



FIGURE 3.1: Perturbation of stress intensity factors on an inclined fracture under tension ($\sigma = 1$ Pa) due to interaction. The same geometry as Figure 2.10(a) is simulated, but an additional fracture that is coplanar to the initial fracture has been added, separated by 0.2627 m, as shown in the schematic diagram. The analytical solution for the isolated case (Equations 2.22, 2.23 and 2.24) is used as a comparison to highlight the SIF perturbation. The fracture has 80 tip nodes, and the elastic medium's properties are $\nu = 0.25$, Young's modulus $E = 1$ Pa.

### 3.2.2 Numerical variation of stress intensity factors

In this work, it is assumed that any difference between $K_i^{int}$ and $K_i^{iso}$ is due to interaction effects. However, both $K_i^{int}$ and $K_i^{iso}$ will be subject to discretisation errors, creating additional small differences. The magnitude of these errors depends on the level of refinement (*i.e.*, the number of tip nodes around each fracture, which controls local element sizes and the total number of elements in the domain) used in a simulation, and are quantified in Section 2.5. The two different fracture domains will have different meshes, but their tip nodes are in the same locations for both calculations, and the mesh around each fracture has a similar structure. By using a numerical result with the same local mesh around the fracture, similar magnitude discretisation errors are present at each tip in both $K_i^{int}$ and $K_i^{iso}$. Therefore, the ratio $K_i^{int}$ and $K_i^{iso}$ calculated at each pair of tips factors out these errors. Whilst replacing $K_i^{iso}$ with an analytical solution ($K_i^A$) reduces the number of terms which contain numerical error, this would compound

discretisation errors along with SIF perturbations. Additionally, analytical solutions for isolated SIFs are only available for specific geometries and boundary conditions, whereas stress fields around fractures can be simulated numerically for any orientation.

### 3.2.3 Comparison to other methods

No exact analytical solution is available for the change in SIFs due to interaction. Instead, results can be compared to the perturbations found through other semi-analytical or numerical methods [Legrand and Lazarus, 2015]. The first method for comparison is Kachanov and Laures [1989], whose results provide an approximate solution that closely matches semi-analytical methods for calculating SIFs for interacting fractures, derived from LEFM principles [Fabrikant, 1987, Gross, 1982]. The second method utilises the results of Legrand and Lazarus [2015], obtained using the finite perturbation method.

Figure 3.2 shows the SIF perturbation quantified through the ratio $K_i^{int}/K_i^A$, obtained using these two methods, and the present method, for a fracture under tension when a second coplanar fracture is nearby. The fractures are oriented perpendicular to the stress field, and are shown for two separations, $\Delta/2r = 0.05$, and $\Delta/2r = 0.00025$. Both fractures have 160 tip nodes, providing a high level of refinement in order to minimise discretisation errors. At $\theta = 0^o$, where the two fractures are closest together, $K_i^{int}$ is higher than $K_i^A$ as a result of interaction. At the $\Delta/2r = 0.05$ separation, $K_i^{int}/K_i^A = 1.3$, and decreases as the angle increases around the fracture. At separation $\Delta/2r = 0.00025$, $K_i^{int}$ is significantly higher, and $K_i^{int}/K_i^A = 3.2$. $K_i^{int}$ decreases at a much faster rate with angle at the close separation. At $\theta = 60^o$, both separations converge to similar values of $K_i^{int}/K_i^A$. At $160^o$, the far side of the fracture is almost unchanged by interaction, yielding values very close to the isolated solution.

All three methods yield a very similar trend. The present simulation results match those of Kachanov and Laures [1989] particularly well, except for the case where the fractures are very close ($\theta < 20^o$). In this region, the present simulation results have higher $K_i^{int}/K_i^A$ and match Legrand and Lazarus [2015]'s results closely. $\Delta/2r = 0.00025$ is a particularly challenging case to discretise, because the region between the fractures becomes very small relative to the fracture size. To place sufficient elements in this region requires an unreasonably high mesh density, leading to simulations requiring more computer memory than were available during testing. Discretised methods that rely on sampling of this region produce scattered SIF values where the fractures are close, which can be seen in Figure 3.2 for the $\Delta/2r = 0.00025$ case. Similar scatter was reported by Legrand and Lazarus [2015] for $\Delta/2r < 10^{-4}$.

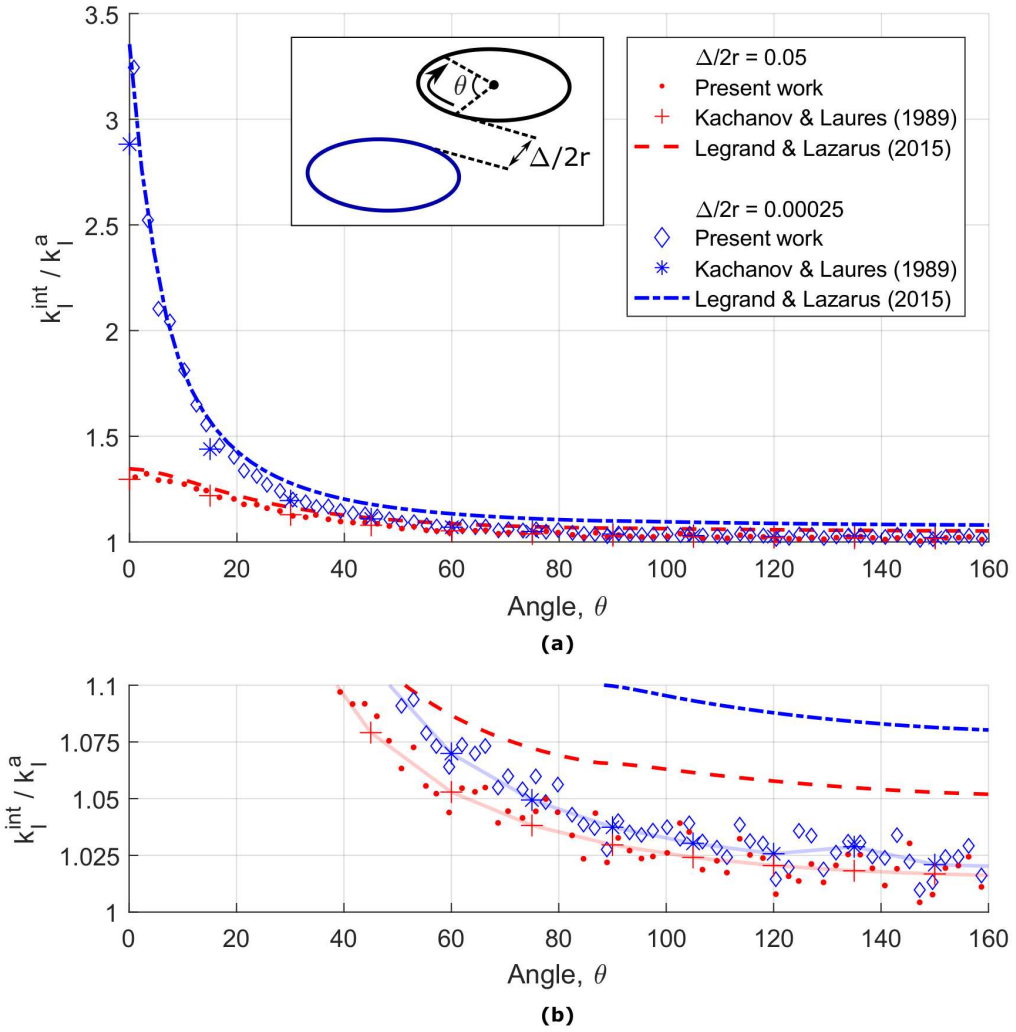



FIGURE 3.2: Comparison of stress intensity factor perturbations with other models. (a) SIF ratio between the interacting and isolated fractures ($K_i^{int}/K_i^A$). The fractures are perpendicular to the stress field and are plotted for two separations ($\Delta/2r = 0.05$, and $\Delta/2r = 0.00025$). Both fractures have 160 tip nodes. Results by Kachanov and Laures [1989] and Legrand and Lazarus [2015] are provided for the same geometry. (b) The same data from (a), but with the y-axis limits changed to (1.0-1.1). Lines have been placed to connect Kachanov and Laures [1989]'s points for ease of visualisation.

Figure 3.3 shows an example mesh used in Figure 3.2 with 30 tips and $\Delta/2r = 0.05$, with two fractures in the model to demonstrate the way refinement is focused on the fracture tip.

## 3.3 SIF perturbations for common geometries

Figure 3.4 shows $K_I^{int}/K_I^{iso}$ for six fracture pairs in two geometries to demonstrate how the magnitude and 'sign' of the interaction changes as the fracture orientation changes. The top row (a-c) shows coplanar interaction where mode I is amplified along the closest

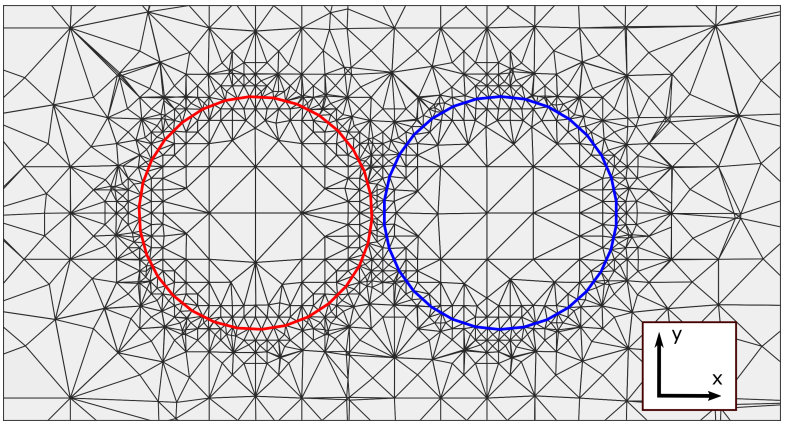



FIGURE 3.3: Example mesh around two fractures with separation $\Delta/2r = 0.05$. Each fracture has 30 tip nodes. Volumetric elements are cut by the visualisation plane, so some appear to be thin and elongated, whereas they actually pertain to a well formed tetrahedral element.

part of the fracture. As the separation between fractures increases, $K_i^{int}/K_i^{iso}$ is much lower, becoming effectively equal to unity at $\Delta/2r = 1.50$. The bottom row (d-f) show a stacked configuration where mode I is uniformly shielded as a result of interaction. This effect is diminished with increasing separation, but could be said to have a larger range than the coplanar geometry, because, at $\Delta/2r = 1.50$, mode I is still reduced, as observed by other analyses of stacked cases [Kachanov, 1993]. In the stacked configuration, mode II varies in a similar but opposite manner to mode I, where it is amplified rather than shielded. Mode II is perturbed uniformly all the way around the fracture, because the fracture tips are all the same distance from the interacting fracture.

Coplanar and stacked geometries are the 'end member' cases for fracture interaction, where pure amplification and pure shielding take place, respectively. The transition between these cases is the overlapped case, where part of the fracture is shielded and part is amplified. As the fractures move from coplanar to stacked, the mode I SIF change becomes negative at the point where the fractures are overlapped, and positive where they do not overlap (demonstrated in Figures 3.5 and 3.11). Mode II and III SIFs also change their perturbation behaviour across this transition, giving rise to the changes in growth angle which are well known to occur as fracture offset changes [Thomas and Pollard, 1993]. This behaviour, whilst intuitive for many applications of fracture mechanics, can be quantified and better understood through further analysis of SIF perturbations. Moreover, the relative orientation of the fractures will further affect the manner in which interaction takes place (see Section 3.5).

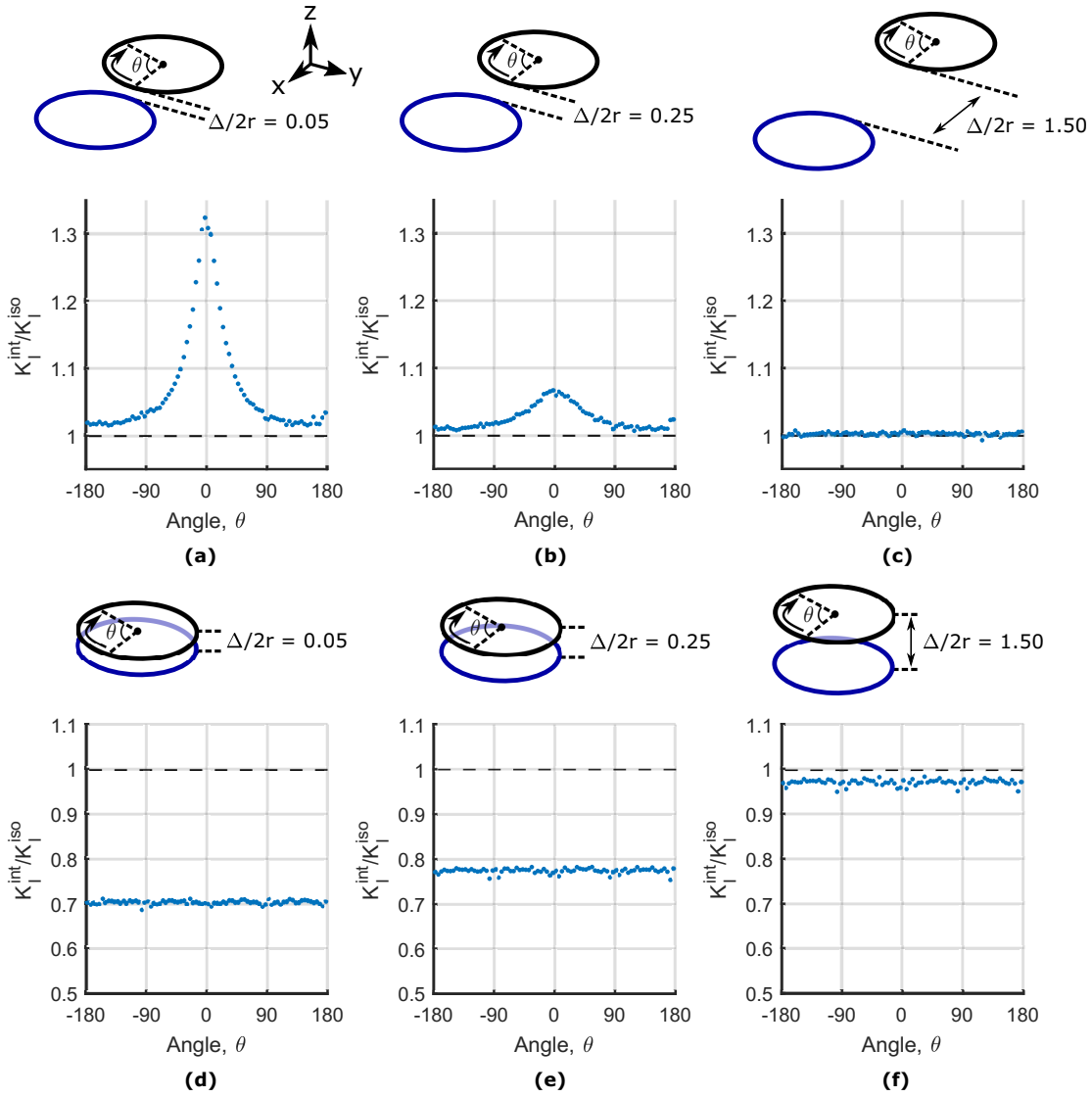



FIGURE 3.4: Change in mode I stress intensity factor resulting from close fracture interaction. (a), (b) and (c) show the case where two fractures are coplanar, *i.e.* on the same $x$ plane, with changing separation along the $y$ axis. At $\theta = 0$, the two fractures are closest to one another, and $K_I$ is amplified. (d), (e) and (f) show a stacked configuration, *i.e.* moving up the $z$ axis. The change in the mode I SIF is represented using $K_I^{int}/K_I^{iso}$. The dashed line in each graph shows the isolated result that would occur if the fractures were isolated, where $K_I^{int}/K_I^{iso} = 1$.

## 3.4 Quantification of interaction

Several measures are proposed to quantify and characterise interaction. These 'measures of interaction' derive from simple relationships similar to $K_i^{int}/K_i^{iso}$. Whilst the ratio $K_i^{int}/K_i^{iso}$ is powerful on its own, it is not well suited to modes II and III for tension, as these modes change sign around the fracture, *e.g.*, Figure 2.10. Therefore, use of $K_i^{iso}$ in the denominator should be avoided, as it approaches zero for certain angles. The

same is true for mode I in certain fracture orientations or stress states. Additionally, $K_i^{int}/K_i^{iso}$ is also only measured on individual tips, with many values per fracture.

It is useful to have a single quantity that captures how the stress state along the tip of a fracture is changed due to interaction. Summarising interaction with one value enables analysis using interaction variation maps, aiding understanding of past and potentially arising fracture geometries. For simulations containing hundreds and thousands of fractures, cheap and local measures of interaction will aid the discretisation and level of detail required at different locations of the mesh. The methods proposed herein for characterising interaction are effective for all deformation modes and boundary conditions.

Three such methods are proposed as follows. The first, 'circumferential SIF perturbation', computes the total area between the $K_i^{int}$ and $K_i^{iso}$ curves, either as the sum of all modes ($C$) or for one specific mode ($C_i$). The second, 'maximum SIF perturbation' ($M_i$), computes the maximum perturbation of $K_i$ for the fracture. Both of these methods are used to quantify the magnitude of the interaction. The third, $\epsilon$, the 'amplification to shielding ratio', quantifies whether the fracture is mostly amplified or shielded. Using either $C$ or $M_i$ along with $\epsilon$ captures the change in the SIFs at its tip as a result of nearby fractures.

### 3.4.1 Definition of circumferential SIF perturbation, $C$

Circumferential SIF perturbation is defined as the absolute area between the interacting and isolated SIF curves, as a modification of Equation 2.33, as follows:

$$C = \frac{\sum_{i=I}^{III} \int_{L_f} \left| K_i^{iso} - K_i^{int} \right| dl}{\sum_{i=I}^{III} \int_{L_f} \left| K_i^{iso} \right| dl} \tag{3.1}$$

where $K_i^A$ is replaced with the SIF for an isolated fracture, $K_i^{iso}$. $K_i^N$ becomes the SIFs for an interacting fracture, $K_i^{int}$. This provides a value that represents the absolute change in stress concentration at the fracture tip as a result of other nearby fractures.

As $C$ is a sum over the entire fracture, it is not directional, *i.e.* it does not identify where the fracture may fail, but instead represents the total interaction a fracture undergoes, which may be the result of more than one interacting fracture. $C$ should also be considered a non-local measure. Because the same tip node locations can be used to calculate $K_i^{iso}$ and $K_i^{int}$, additional errors caused by mesh discretisation can be minimized. $C$ can also be calculated for just one mode of deformation ($i$) rather than the total sum of all

modes,

$$C_i = \frac{\int_{L_f} \left| K_i^{iso} - K_i^{int} \right| dl}{\int_{L_f} \left| K_i^{iso} \right| dl}, i = I, II, III. \tag{3.2}$$

This is useful for calculating how one individual mode is altered by interaction. The use of absolute values for $C$ in the denominator avoids asymptotes when the SIFs are very close to zero.

### 3.4.2 Definition of maximum SIF perturbation, $M_i$

Maximum SIF perturbation is defined as the largest difference between the interacting and isolated SIFs:

$$M_i = \max \left( \left| K_i^{int} - K_i^{iso} \right| \right), \quad i = I, II, III. \tag{3.3}$$

This measure can be related to one specific location on the fracture tip at which the difference was largest. This makes $M_i$ a local measure of fracture interaction. The maximum SIF perturbation is unique between the three deformation modes, as the tip node with the maximum $M_I$ is not necessarily the same as the tip node with maximum $M_{II}$ or $M_{III}$. The magnitude of $M_i$ is tied to $\sigma$. As the method relies on the value at one particular tip, rather than averaging over a group of tips, it may be subject to greater discretisation errors.

An illustration of the differences between $C$ and $M_i$ is shown in Figure 3.5(a). This plots the mode I SIF as a function of the tip angle in the same manner as Figure 2.10. The shaded region shows the area between the interacting and isolated curves ($C_I$), and $M_I$ is shown as the maximum change. Both $C$ and $M_i$ use the absolute values of $K_i^{int}$ and $K_i^{iso}$ in their calculations. Thus, they only provide information on the magnitude of interaction, and not whether it is amplifying or shielding.

### 3.4.3 Definition of the amplification to shielding ratio, $\epsilon_i$

When measuring interaction, it is important to consider whether stress has been amplified or shielded. In the simple cases of coplanar interaction, stress is only amplified, *e.g.* Figure 3.4(a-c). In cases where the fractures are stacked and at least partially overlap, stress is shielded, *e.g.*, Figure 3.4(d-f). The type of interaction, either shielding, amplification, or a mixture of the two, is quantified by the amplification to shielding ratio ($\epsilon_i$), which is formulated as follows. Two lists of values, $\kappa_i^a$ and $\kappa_i^s$, are created from the difference between the interacting and isolated SIFs. The parameter $\kappa_i^a$, contains the

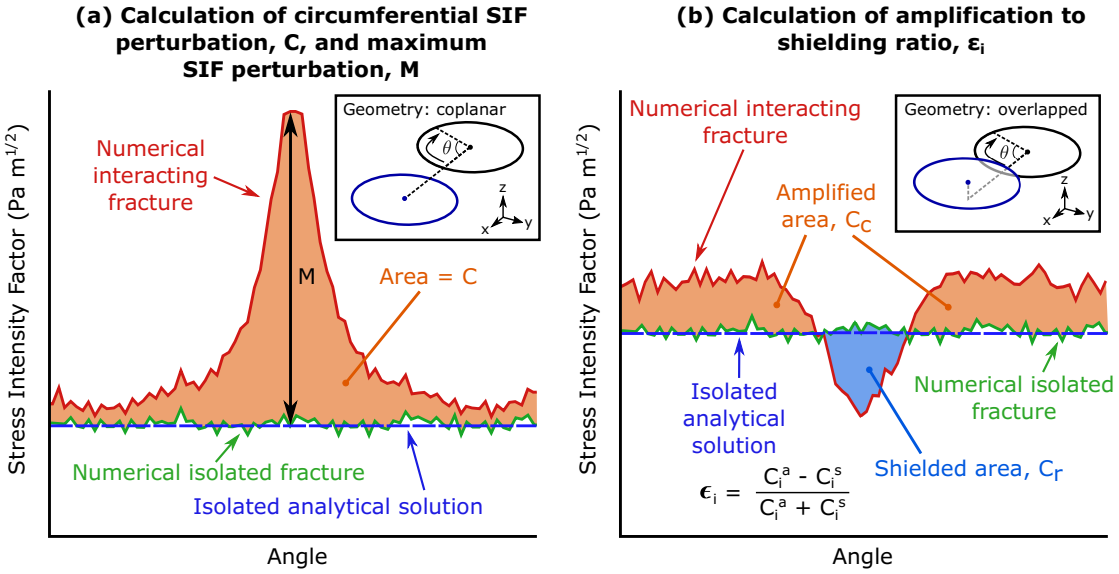



FIGURE 3.5: Methods used to quantify fracture interaction by calculation of $C$, $M_i$, and $\epsilon$. (a) shows $C$ as the area between the two numerically calculated SIF curves for the same coplanar geometry, one isolated and the other interacting with other fractures. $M$ is the maximum difference between the two curves. (b) shows the SIFs for an overlapped fracture geometry, and the calculation of $\epsilon_i$ by comparing the area of the graph that is amplified to the area that is shielded.

values where the SIFs for mode $i$ have been increased, and 0 otherwise,

$$\kappa_i^a = \begin{cases} K_i^{int} - K_i^{iso} > 0, & \kappa_i^a = K_i^{int} - K_i^{iso} \\ K_i^{int} - K_i^{iso} \leq 0, & \kappa_i^a = 0 \end{cases} \tag{3.4}$$

and $\kappa_i^s$ contains values where the SIFs for mode $i$ have been decreased, and 0 otherwise,

$$\kappa_i^s = \begin{cases} K_i^{int} - K_i^{iso} > 0, & \kappa_i^s = 0 \\ K_i^{int} - K_i^{iso} \leq 0, & \kappa_i^s = K_i^{int} - K_i^{iso}. \end{cases} \tag{3.5}$$

These lists therefore contain information for the tips which have been only amplified ($\kappa_i^a$) and only shielded ($\kappa_i^s$). The areas under the curves of $\kappa_i^a$ and $\kappa_i^s$ are then calculated:

$$C_i^a = \int_{L_f} |\kappa_i^a| dl, \tag{3.6}$$

$$C_i^s = \int_{L_f} |\kappa_i^s| dl. \tag{3.7}$$

The balance between amplification and shielding can be found by comparing these two areas. Thus, $\epsilon_i$ is defined as

$$\epsilon_i = \frac{C_i^a - C_i^s}{C_i^a + C_i^s}, \quad i = I, II, III. \tag{3.8}$$

Therefore, $\epsilon_i$ equals 1 when mode $i$ is purely amplified, and equals -1 when purely shielded. When $\epsilon_i > 0$, the SIFs at most of the tips of the fracture are amplified by the presence of another fracture, and when $\epsilon_i < 0$, most of the tips are shielded.

### 3.4.4 Comments on interaction measures

Numerical simulations inevitably produce different results when changes are made in the domain, even if those changes are slight, due to discretisation and numerical errors. This means that there will always be differences between $K_i^{iso}$ and $K_i^{int}$, even when the meshes are identical and fractures are very far apart, although these differences may be very small. Therefore, the measures of magnitude ($C$ and $M$) do not converge to zero when fractures do not interact, but do become very small. This is not a problem for the analysis of $C$ and $M_i$, because the size of this error is small compared to cases when interaction is significant. However, scatter between the values of $K_i^{iso}$ and $K_i^{int}$ will result in $\epsilon_i$ being essentially random when no significant interaction occurs. When analysing a set of $\epsilon_i$ values in space, a threshold should be used to ignore the value of $\epsilon_i$ if either $C_i$ or $M_i$ suggests there is very little interaction. Conveniently, $C_i$ has the same magnitude regardless of the SIF magnitude because it compares the ratio of two areas. A threshold of $C_i = 0.005$ has been used in this work.

The proposed interactivity measures share some commonalities with the transmission factor used as part of Kachanov [1987]'s analytical method. For coplanar fractures, the transmission factor is increased by the presence of the other fracture. In three dimensions, the sign of the transmission factor changes to correspond to cases of fracture interaction either amplifying or shielding stress depending on the geometry. For fracture arrays, the transmission factor concept is extended to an interaction matrix, containing transmission factors which describe the effect of each fracture on one another. The interaction measures suggested here are similar, but are now separated into magnitude and sign of interaction, where $C$ or $M_i$ can be used to show the magnitude of interaction, and $\epsilon_i$ describes the balance of amplification or shielding. These measures are also assigned one per fracture, rather than one per fracture pair.

### 3.4.5 Variation of $C$ and $M$ with separation

Figure 3.6 shows how $C$ and $M_I$ vary in the simple case of increasing fracture separation for three geometries. $C$ is used rather than $C_I$ to highlight the effect of combining the three modes. All graphs (a-c) use the same axes, with $C$ on the left and $M_I$ on the right. In all three geometries, $C$ and $M_I$ demonstrate how, as expected, interaction reduces with separation. Both interaction measures show that shielding interaction when

fractures are stacked (c) has a larger range than coplanar geometries, (a) and (b). The separation at which $C$ falls below 0.005 is marked with a red dashed line, showing that shielding effects have a much longer range than amplification effects.

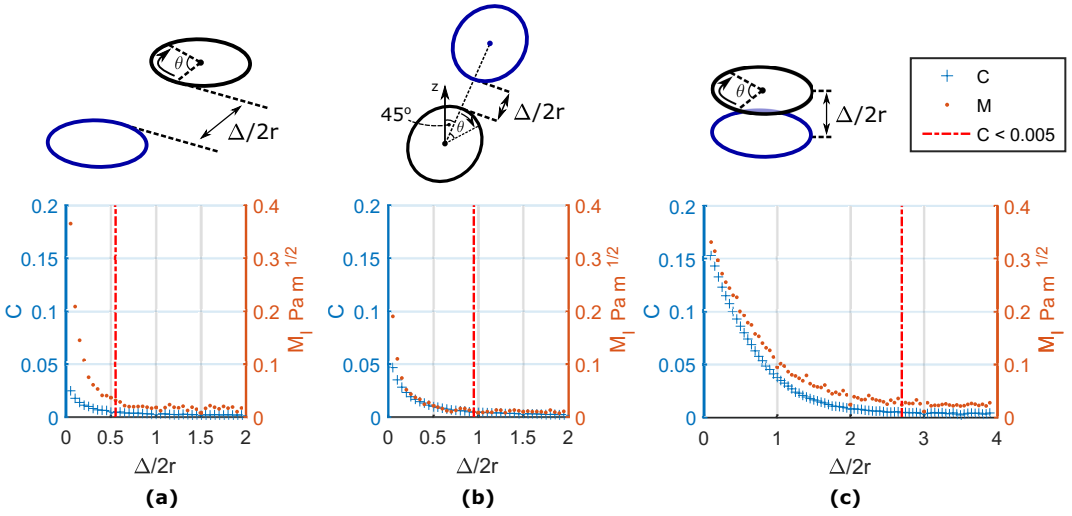



FIGURE 3.6: Variation of $C$ and $M_I$ with fracture separation for three common geometries as a function of increasing fracture separation. In order to highlight the effect of combining modes in interaction measures, $C$ is compared to $M_I$ here. (a) Coplanar geometry, also examined in Figure 3.4(a-c). (b) Inclined coplanar geometry. (c) Stacked geometry, also examined in Figure 3.4(d-f). Fracture separation is measured in terms of $\Delta/2r$, where $r$ is the fracture radius. The dashed red line marks the smallest $\Delta/2r$ where $C < 0.005$, the threshold at which there is considered to be no significant interaction. This is reached at $\Delta/2r = 0.55$ in (a), $\Delta/2r = 0.95$ in (b), and $\Delta/2r = 2.70$ in (c).

For the same variation in the separation of two fractures, their interaction is shown to not only depend on their spacing, but also on their relative positioning with respect to the far-field stresses and their relative positioning with respect to one another. The difference in the behaviour of $C$ and $M_I$ in each case is of particular interest, especially when comparing the two coplanar cases. In Figure 3.6(a), only mode I is changed by interaction, because the fractures are perpendicular to the far field principal stress field and $K_{II}$ and $K_{III}$ are zero. Figure 3.6(b) has the same geometry, but is oriented at 45° to maximum tensile stress, meaning modes II and III are non-zero and are perturbed by the interaction. $M_I$ only relies on mode I, so is higher in (a) where the interaction is confined to one mode, and smaller in (b), when the interaction is shared by three modes. $C$ is the sum of the SIF perturbation for all three modes, so has a higher magnitude in (b) than in (a). Discretisation errors cause small amounts of scatter, and are much higher in $M_I$ than $C$.

In summary, $C$ and $M_i$ are both capable of capturing the decrease in interaction with separation, however, care should be taken to examine which modes are being altered in each case. Separating $C$ into its mode-specific values $C_I$, $C_{II}$, and $C_{III}$ to summarise the change in each mode, using Equation 3.2, may be preferable during interaction analysis,

in order to identify where fractures will become non-planar during growth [Thomas and Pollard, 1993].

For numerically derived values to be useful for analysis, they must not vary strongly as a function of mesh refinement. Figure 3.7 shows, for two fractures with $\Delta/2r = 0.25$ and 80 tip nodes, the value of $C$ and $M_I$, plotted against the number of tip nodes on the fracture. Changes in separation have a much larger effect on $C$ and $M_I$ than do changes in mesh density. The standard deviation of $C$ and $M_I$ across 27 meshes are 0.00038 and 0.0023 respectively. $M_I$ varies more as it is reliant on the value from one node rather than an average across all nodes. The mesh refinement resulting from simulating fractures with 80 tip nodes was considered the best balance between SIF accuracy (see Section 2.5) and simulation time, therefore, 80 tip nodes are used on each fracture throughout the rest of the chapter.

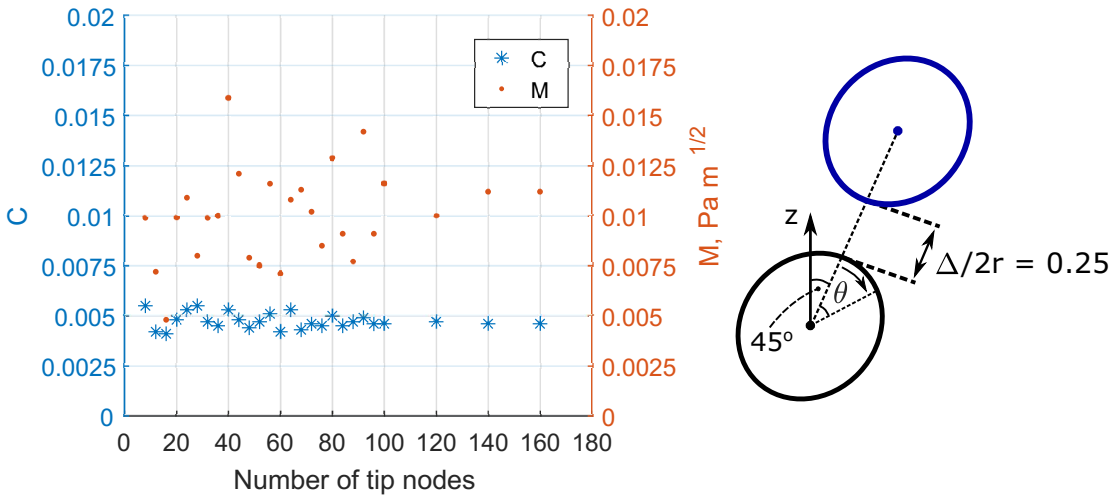



FIGURE 3.7: Sensitivity of interaction measures to mesh refinement. Two fractures have been placed with separation $\Delta/2r = 0.25$ on the same plane inclined 45° to the $z$ axis. $C$ and $M_I$ are measured on one fracture for different mesh refinements, where the density of the mesh is controlled by the number of tips around the fracture.

## 3.5 Interaction maps

In this section, fracture interaction maps are constructed to analyse the effect of one fracture on another, specifically by capturing SIF variations comprising multiple interaction cases, within a single image. They show the variation of $C_i$, $M_i$ and $\epsilon_i$ as the relative position between two fractures changes. A fracture interaction map is constructed by performing simulations in which a base fracture is placed in a fixed position, perpendicular to the direction of stress. A second fracture of equal radius is placed nearby with the same orientation. The values of $C_{I-III}$, $M_{I-III}$, and $\epsilon_{I-III}$ are then measured on the

base fracture in tension. The second fracture is then moved to other locations and the same measurements were made. This creates a grid of values in the ($x$, $z$) plane around the fracture, which is interpolated to create a continuous map of SIF variation around a static fracture. Figure 3.8 demonstrates this process for three locations, alongside the fracture interaction map for $\epsilon_I$ in tension, with a value of $\sigma = 1$ Pa, as a Neumann stress condition at the top boundary).

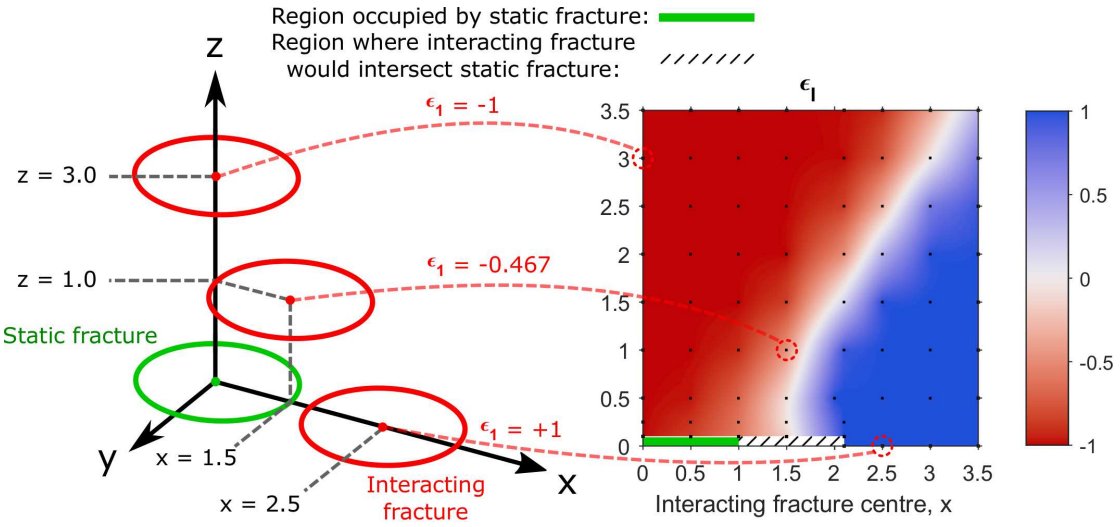



FIGURE 3.8: Schematic demonstrating creation of stress intensity factor variation maps. Maps are built up of the results of many simulations. In each simulation, only two fractures are present at one time: the static fracture (green) remains centred at (0, 0, 0) and the interacting fracture moves around the $x > 0$, $z > 0$ quadrant. The dashed space in the plot shows the region which cannot be sampled, because in this region the fractures intersect. This region changes size based on the orientation and offset of the interacting fracture. An interaction measure ($C_{I-III}$, $M_{I-III}$, and $\epsilon_{I-III}$) is measured on the static fracture, and then is interpolated over the sampled space. Both fractures have a radius of 1 m and 80 tip nodes.

The objective of creating an interaction variation map is to explore the variation of the magnitude and type of interaction, *i.e.*, amplification, shielding, or a mix of the two, depending on relative fracture position and orientation. Compared to plotting the change in stress around a fracture [*e.g.*, Grechka and Kachanov, 2006], interaction maps display the change in the SIFs. Therefore, the impact of interaction is more directly quantified in terms of changes at the fracture tip, and can be examined separately in modes I, II and III. This process could be used to create interaction maps of any interacting fracture orientation or size, as long as the sampled locations do not cause fractures to intersect.

Fracture interaction variation maps are presented in Figures 3.9, 3.10, and 3.11, showing values of $C_{I-III}$, $M_{I-III}$, and $\epsilon_{I-III}$ respectively. Each figure includes maps for four orientations of the interacting fracture. In each figure, (a) shows the interaction map generated from two fractures inclined perpendicular to the direction of tension, (b) shows maps with a 1 m offset along the $y$ axis, (c) shows the map with the interacting fracture

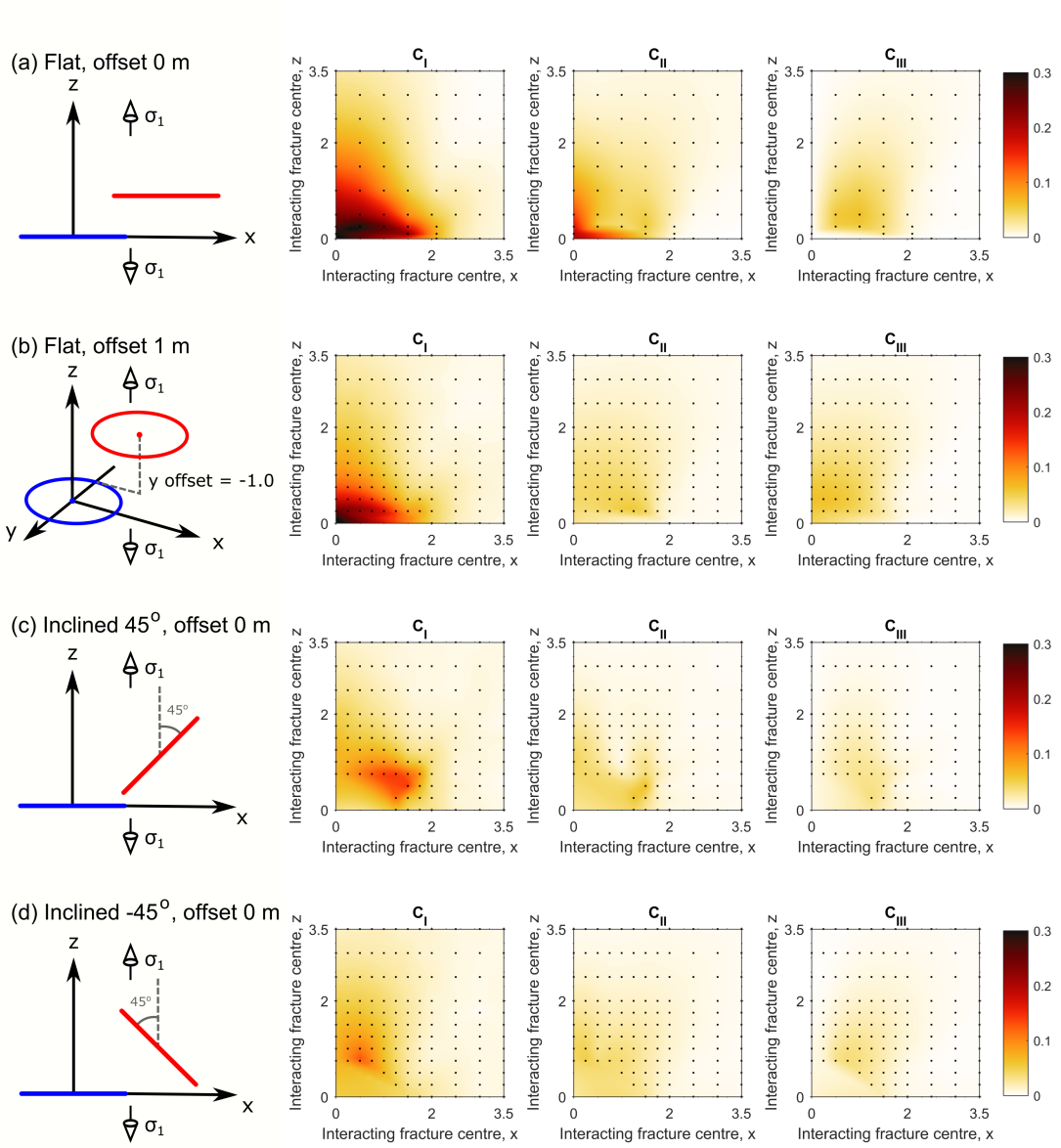



FIGURE 3.9: Stress intensity factor variation maps of $C_I$, $C_{II}$ and $C_{III}$ for four geometries: coplanar (a), coplanar offset by 1 m (b), inclined by 45° (c) and inclined by -45°. Black dots indicate sampled points. Larger values of $C$ indicate higher magnitudes of SIF perturbation and therefore interaction. Both fractures have a radius of 1 m and 80 tip nodes.

inclined at 45°, and (d) shows the map with the interacting fracture inclined at -45°. All simulations are performed in a 20 × 20 × 20 m domain, and the boundary condition is applied as a Neumann stress condition on the top boundary, with a mangnitude of 1 Pa, and direction depending on whether the maps are generated for tension or compression conditions.

### 3.5.1 Interaction variation maps of $C_i$ in tension

Figure 3.9 shows fracture interaction maps of $C_I$, $C_{II}$ and $C_{III}$ for two geometries. The coplanar geometry (a) shows the gradual change between coplanar and stacked geometries. The magnitude of the interaction in the stacked configuration, along $x = 0$ as shown in Figure 3.6(c), was shown to be higher than in the coplanar configuration, along $z = 0$, as shown in Figure 3.6(a) and (c). This behaviour is clear on the interaction variation map of $C_I$, where the extent of the highly perturbed region is much larger when the fractures overlap and enter one another's stress shadow.

In Figure 3.9(a), $C_I$ shows that mode I is the most perturbed interaction mode, particularly when fractures are overlapping. Mode II and III are perturbed at approximately half the magnitude of mode I. Mode II perturbations are not increased uniformly in the overlap region. This is because mode II tends to be perturbed only where fracture tips are close to one another. Otherwise, mode II relatively unperturbed if the tip lies above the fracture surface. This leads to larger magnitudes when more of the fracture tips are lined up vertically, creating a region of lower $C_{II}$ between $x = 0.5$ and 1. These changes in $C_{II}$ highlight the locations at which fractures will undergo non-planar growth as a result of interaction, due to increased mangitudes $K_{II}$ [Cotterell and Rice, 1980], as observed in *en échelon* fracture sets [Delaney and Pollard, 1981]. Mode III is most perturbed when the fractures are partially overlapped, and is unperturbed when the tips are close together. This results in its highest value being in the region of $x = 1$, $z = 0.5$. Outside of this overlapped region, $C_{III}$ is essentially unperturbed, *i.e.*, it falls below the 0.005 threshold discussed in Section 3.4.4.

The coplanar 1 m offset maps (Figure 3.9(b)) essentially show a different plane from the 0 m offset maps. Therefore, they are similar to the coplanar maps in (Figure 3.9(a)), with smaller maximum values and slightly different distributions for $C_{II}$ and $C_{III}$. The map of $C_{II}$ lacks an orientation where fractures are exactly overlapped, making values lower along $x = 0$, and, in the case of $C_{III}$, making values non-zero along $x = 0$.

The inclined geometry in Figure 3.9(c) show much lower magnitudes of $C$. This is due to the fact that the fracture surfaces cannot be placed exactly next to one another, so the highly interacting stacked case cannot be produced at any interacting fracture location. Regions where mode I is more strongly perturbed are present when the interacting fracture's tip is very close to the base fracture plane. In the same manner as in the coplanar case, mode II is larger when the fracture tips are close and overlap in (c), creating a trough along the line $z = 0.75$ for the 45° inclination. When the fracture is rotated by -45° (Figure 3.9(d)), the maximum value of $C_I$ is lower, because there are fewer locations where the fracture tips are very close.

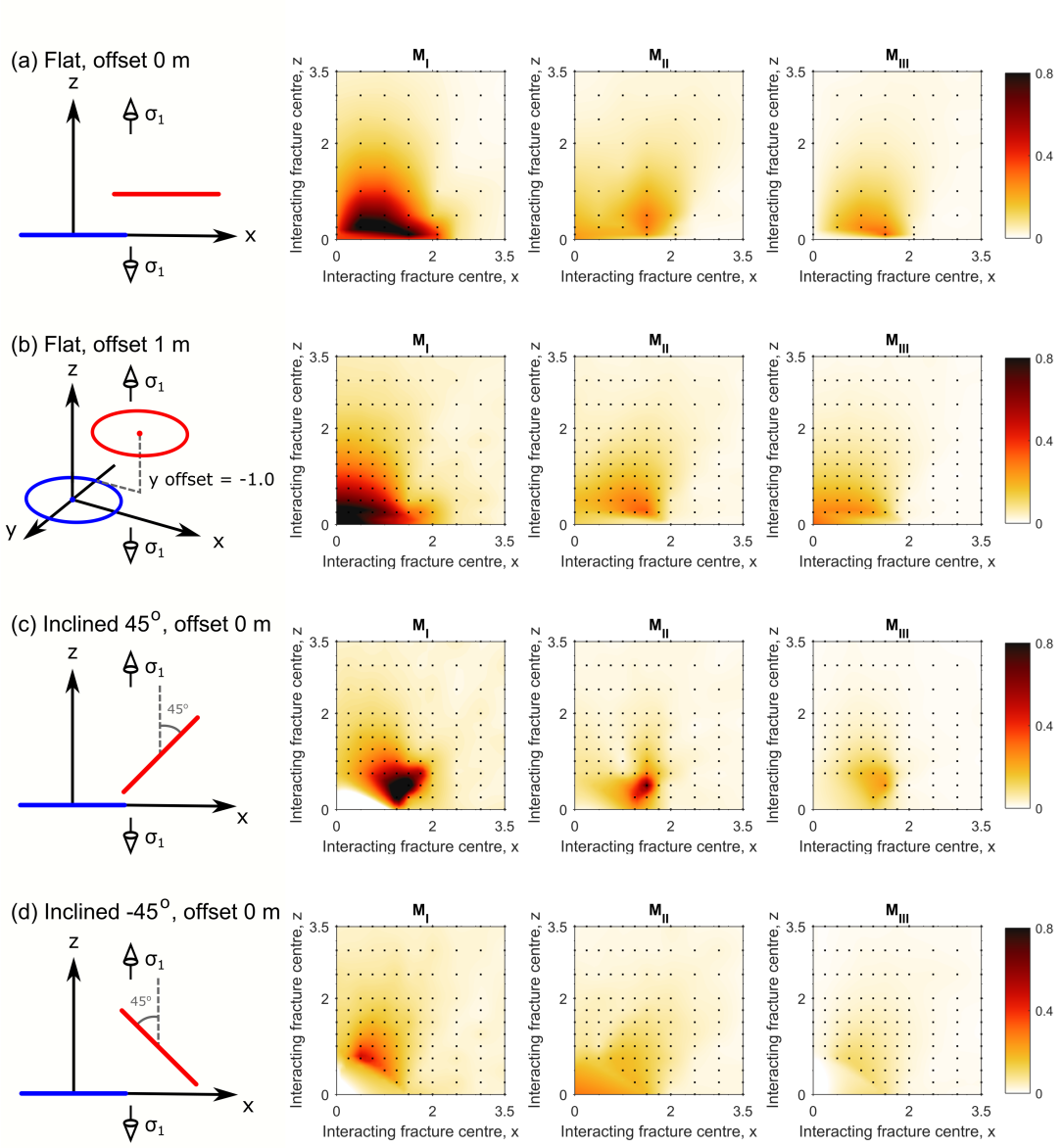



FIGURE 3.10: Stress intensity factor variation maps of $M_I$, $M_{II}$, and $M_{III}$ for four geometries: coplanar (a), coplanar offset by 1 m (b), inclined by 45° (c) and inclined by -45°. Higher values of $M_I$, $M_{II}$, and $M_{III}$ show where that mode changed most significantly from their isolated state. Both fractures have a radius of 1 m and 80 tip nodes.

### 3.5.2 Interaction variation maps of $M_i$ in tension

The interaction maps of $M_i$ in Figure 3.10 show that $M_i$ changes in a similar manner to $C_i$, particularly in (c). The major difference is in the stacked case in Figure 3.10(a), where the highest $M_I$ is found when fractures are partially overlapped rather than fully stacked. When fractures are partially overlapped, the most significant shielding occurs at the centre of the overlapped tips, resulting in a high value for $M_I$. When fully overlapped, the shielding is instead uniform around the whole tip, but lower, resulting

in an intermediate value for $M_I$. By measuring the area instead, $C_I$ considers the interaction magnitude to be higher in the fully stacked case and intermediate in the overlapped case, as observed in Figure 3.6.

### 3.5.3 Interaction variation maps of $\epsilon_i$ in tension

Figure 3.11 shows interaction maps that plot $\epsilon_I$, $\epsilon_{II}$ and $\epsilon_{III}$ for the same geometries as shown in Figure 3.9. In the coplanar geometry in Figure 3.11(a) $\epsilon_I$ demonstrates the transition between stress amplification and shielding very well. Coplanar orientations result in amplification where $\epsilon_I = 1$, and stacked orientations result in shielding where $\epsilon_I = -1$. The transition zone is well resolved even at the coarse resolution of the grid. Maps of $\epsilon_I$ are presented without altering values where $C_I$ is below the threshold of interaction, because the few locations where it is below 0.005 do not cause the distribution of $\epsilon_I$ to be less uniform. The extent of the shielded zone changes significantly in the inclined cases in Figure 3.11(c) and (d), demonstrating the impact of fracture orientation on interaction behaviour. When the interacting fracture is inclined at 45°, the extent of the shielded zone is much smaller because the region of stress amplification at the fracture tip is closest to the other fracture. At -45°, the shielded zone is much larger, because the surface of the fractures face one another in this orientation, combining two stress shielding regions. The coplanar non-offset case of $\epsilon_I$ in Figure 3.11(a) can be seen as being intermediate between these two states.

The parameter $\epsilon_{II}$ has the most complex distribution of the three modes. In (a), $\epsilon_{II}$ is amplified, but a zone of shielding is found on the line $x = 1$ where the fractures are partially overlapped, contrasting the pure amplification when the fractures are fully overlapped. A second small zone of shielding is found when the fractures are very close. These shielding zones also arise in (c) and (d). The complex distribution of $\epsilon_{II}$ reflects the significant changes to fracture propagation angles when fractures are *en échelon*, because the fracture growth angle depends on a combination of all three modes. It also corresponds to the region of lower magnitude $C_{II}$ in Figure 3.9(a).

In all four geometries there is generally very little variation in $\epsilon_{III}$. Typically, $\epsilon_{III}$ is near 0 when the fractures are close ($x$ and $z < 2$), and elsewhere the magnitude of $C_{III}$ is below the threshold (0.005). $K_{III}$ is therefore always equally shielded and amplified if it is altered due to interaction. The threshold of $C_i > 0.005$ is effective at removing misleading values where there is no interaction in modes II and III.

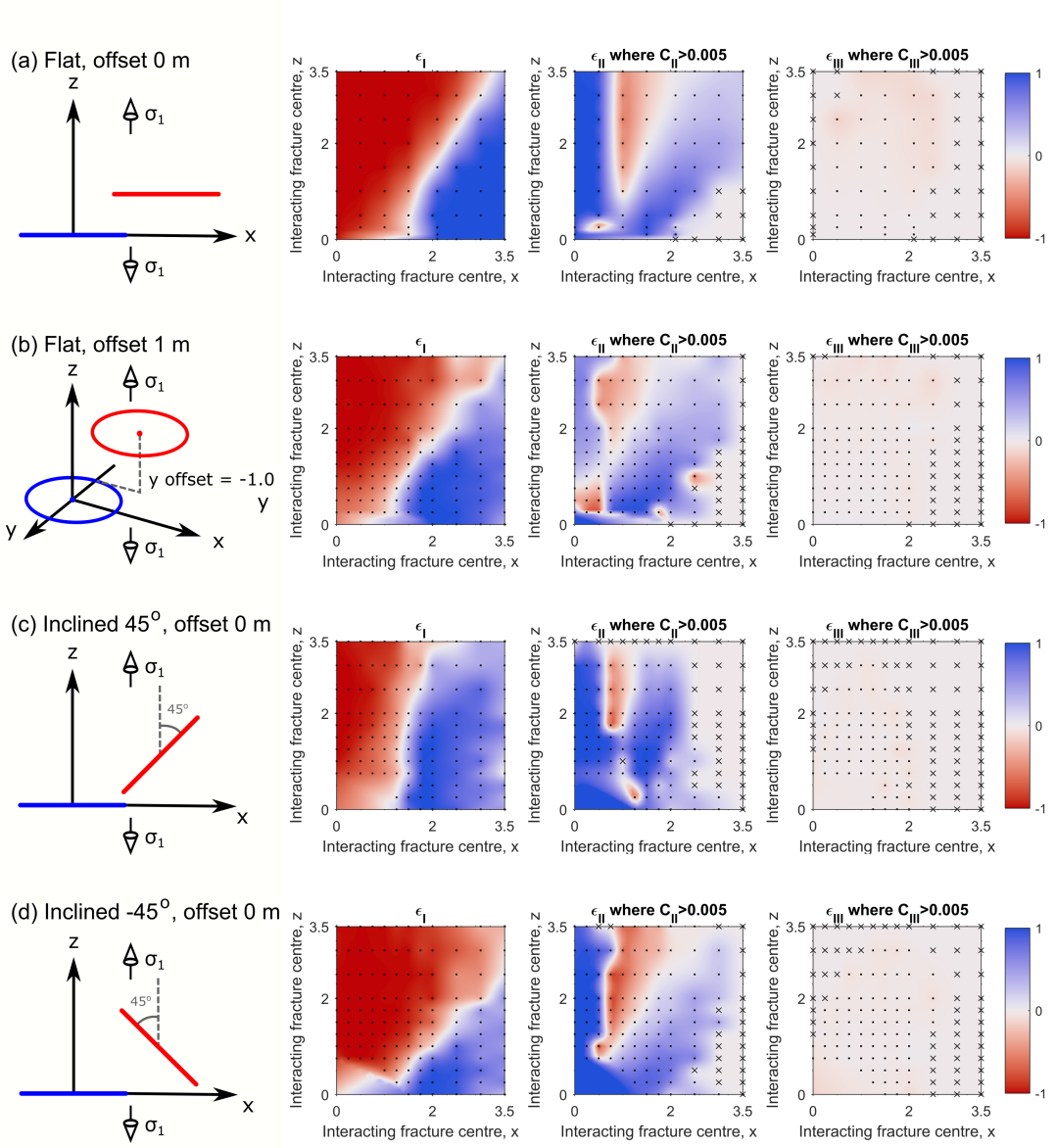



FIGURE 3.11: Stress intensity factor variation maps of $\epsilon_I$, $\epsilon_{II}$, and $\epsilon_{III}$ for four geometries: coplanar (a), coplanar offset by 1 m (b), inclined by 45° (c) and inclined by -45°. $\epsilon_I = 1$ indicates that the SIFs around the fracture are amplified all the way around the tip and $\epsilon_I = -1$ indicates that they are shielded. Intermediate values indicate that the fracture is partially amplified on one side and shielded on the other. Black dots indicate sampled points, and crosses indicate points where $C_i$ is less than a threshold amount (0.005). At these points, $\epsilon_i$ is set to 0, because $\epsilon_i$ produces scattered values when the SIFs in the isolated and interacting cases are very close. Both fractures have a radius of 1 m and 80 tip nodes.

### 3.5.4 Interaction during compression

The SIF interaction results in Sections 3.4 and 3.5 show results for fractures under tension. When fractures are compressed, friction between the two sides of the fracture perturbs the SIFs [Liu and Borja, 2008]. This additional force is important for geological

| | $C$ | $C_I$ | $C_{II}$ | $C_{III}$ | $M_I$ | $M_{II}$ | $M_{III}$ | $\epsilon_I$ | $\epsilon_{II}$ | $\epsilon_{III}$ |
|---|---|---|---|---|---|---|---|---|---|---|
| Tension | 0.06 | 0.11 | 0.02 | 0.03 | 0.35 | 0.07 | 0.10 | -0.65 | 0.62 | -0.04 |
| Compression | 75.01 | 0.46 | 117.11 | 107.46 | 0.0004 | 0.048 | 0.07 | -0.64 | 0.17 | -0.009 |

TABLE 3.1: $C_i$, $M_i$, and $\epsilon_i$ values from the two boundary conditions, tension and compression, on the geometry shown in Figure 3.12.

fractures, where compressive stress regimes are common and the surfaces of fractures will have significant roughness, or brecciated material if they are open. In order to incorporate fracture surface friction, the gap-based Augmented-Lagrangian contact resolution method is used (Section 2.3.5). Initially, fractures have zero aperture, and the stick or slip condition at each fracture surface node is an emerging property of the simulation. During compression the fractures close, and may either stick or slip, rendering the mode I SIFs negative until contact is resolved. This section demonstrates the difference between interaction in tension and compression (Figure 3.12) and shows maps under compression (Figure 3.13).

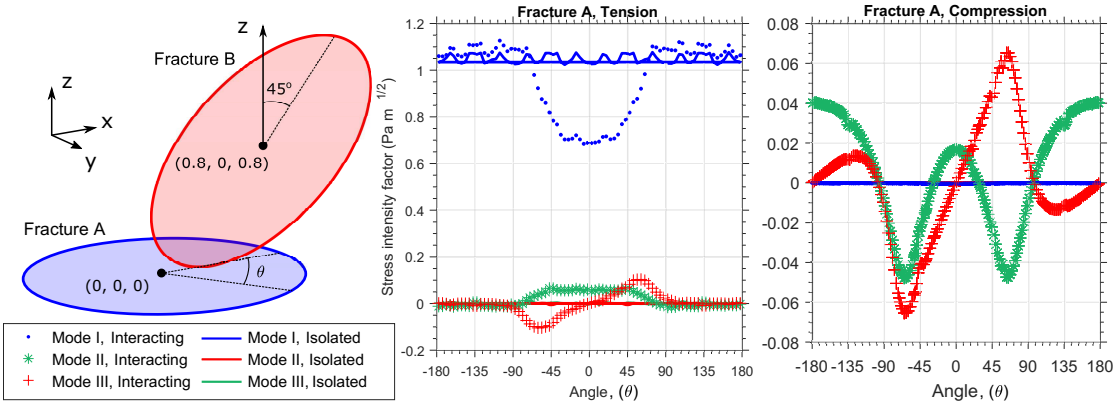



FIGURE 3.12: Geometry of two interacting fractures (a), and the resulting effect on the stress intensity factors for both tension (b) and compression (c). In (c) all modes of SIFs are collapsed to zero for the isolated fracture case. Interaction affects the horizontal fracture in tension, by reducing $K_I$, and under compression, by inducing non-zero $K_{II}$ and $K_{III}$, consistent with slipping of the fracture surface. The analytical solution for mode I is also visible as the flat blue line in (b). Table 3.1

The values of SIFs depend on the friction coefficient assumed for the fracture surface. For stick conditions, SIFs are reduced to zero in most cases, as the fracture does not display in-plane deformation. For slip cases, the deformation of the fracture leads to non-zero stress intensity factors. Figure 3.12 illustrates the behaviour of two interacting fractures under tension and under compression. In the compressive case, the friction coefficient is assumed to be zero, in order to highlight the slip mode and accentuate interaction. Specific values of $C$, $M_i$ and $\epsilon_i$ for these cases are show in Table 3.1.

SIFs are plotted for the horizontal fracture. In the case of tension, $K_I$ values are higher than the other SIFs, but under compression $K_I$ values are instead reduced to zero,

and $K_{II}$ and $K_{III}$ values become dominant. Interaction can be summarised using the same quantities as before. For tension, values of $C$, $M_i$, and $\epsilon$ are consistent with low interaction. In contrast, under compression, values of $C_{II}$ and $C_{III}$ highlight the effect of the interacting sliding fracture. In the isolated compression case, SIF values of the isolated fracture case $k_i^{iso}$, are close to zero. Therefore, the normalised area between SIF curves is much smaller, and the resulting C values are larger. This highlights that interaction measures can be significantly different if the independent variable is not the geometry, but is instead the boundary condition. $M_i$ captures accurately the interaction effect between the two fractures, even if the isolated case has very low SIFs. For both tension and compression, $M_i$ yields similar values of interaction between the fractures, with the exception of mode I which is non-interactive in the compression case. It follows that the same variational maps demonstrated in previous sections can be employed to analyse the present case.

Figure 3.13 shows interaction maps for all the interaction measures in a coplanar geometry. The boundary condition is compression of the top boundary of 1 Pa, an initial fluid pressure of 1 Pa over the fracture surface, and the domain has properties $E = 1$ Pa and $\nu = 0.25$. Measures of magnitude vary with proximity much like in the tension maps. Between the two measures of magnitude ($C_i$ and $M_i$) there are significant differences in the pattern of interaction. $C_I$ suggests the interaction magnitude is high wherever the fractures are close, whereas $M_I$ suggests that stacked geometries are less interacting. Between $C_{II}$ and $M_{II}$, $C_{II}$ is highest when fractures are completely overlapped, and $M_{II}$ is highest during partial overlap. These patterns suggest that stacked geometries lead to uniform changes on each fracture, providing the peak $C_i$ values, and overlapped positions have higher $M_i$ peaks where the fracture tips are close.

Because the fractures were initially opened by the uniform fluid pressure, $K_I$ has a negative value when calculated under compression as the fracture is closing. This inverts the meaning of the sign of $\epsilon_I$, with positive values now indicating most of the fracture has an increased $K_I$ value, *i.e.*, a reduction in the amount of closure and therefore a shadow zone. Two plots of $\epsilon_I$ are shown in Figure 3.13 to demonstrate this effect. The left plot of $\epsilon_I$ shows the result if a negative value of $K_I$ is permitted. Compared to the tension maps of $\epsilon_I$, the sign is flipped but the distribution is similar. The right plot of $\epsilon_I$ uses an absolute value of $K_I$, and closely resembles the tension version. The compression maps of $\epsilon_{II}$ and $\epsilon_{III}$ have similar features to the tension case, including the overlap and stacked zones.

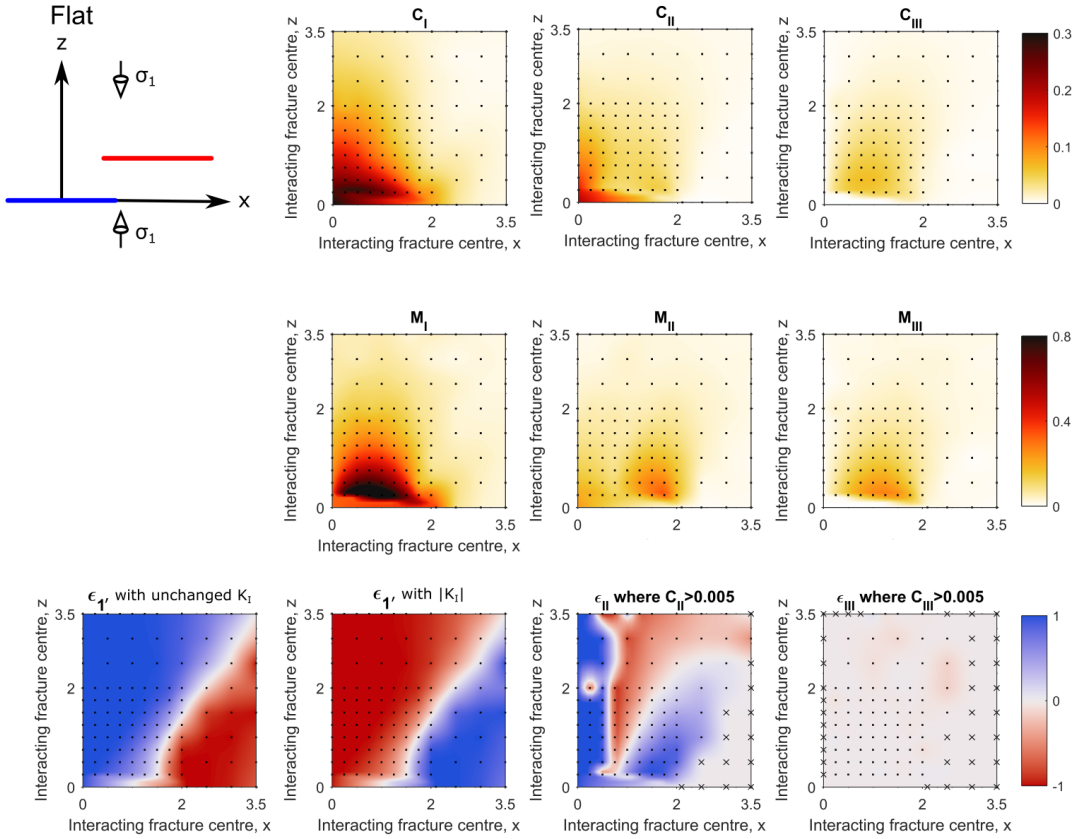



FIGURE 3.13: Stress intensity factor variation maps for coplanar fractures under compression. All the interaction measures are shown, with the same scales as the tension maps in Figures 3.9, 3.10, and 3.11.

## 3.6 Discussion

### 3.6.1 Geological context

Fracture interaction maps provide a useful tool for analysing how a system of fractures will behave. Since the geometry of many fracture systems is well constrained through field and geophysical data, the state of interaction can be explored for a variety of boundary conditions. The interaction measures $C$ and $M_i$ provide a quantitative way to establish whether fractures are interacting, by comparing the values to a threshold, as shown by their change with separation in Figure 3.6. For the fractures that are considered to be interacting, maps of $\epsilon_i$ show whether that interaction will amplify or shield potential growth. This workflow could provide a quantitative assessment as to how a network of joints or dykes will behave, for example, during coalescence into a fault, or ahead of the tip of a fault with a damage zone. In particular, the amount of curvature expected when *en échelon* fracture pairs grow can also be analysed using the

interaction maps. Fractures growing when centred in regions where $C_{II,III}$ and $M_{II,III}$ are high will deflect significantly towards the other fracture. These regions arise when the fractures are overlapped, as found in experiments [*e.g.*, Thomas and Pollard, 1993].

Whilst the methods proposed do not vary with the scale of the fractures being studied, it should be noted that SIFs require that the fractures have distinct tips. Large faults have significant damage zones ahead of their tips, reducing how readily they can be compared to an idealised flaw. Estimations of interaction measures for faults may have to take into account the significant shear strength of faults resulting from brecciated rock inside the fault. The traction-free surface of the Earth also provides an additional stress perturbation if the size of the fractures are comparable to their depth [Roering et al., 1997].

SIF perturbations also occur as a result of heterogeneity in the medium [Yu et al., 2009]. Heterogeneity is a key aspect of geological materials, which can be easily incorporated into mechanical models by variation of material properties such as Young's modulus or Poisson's ratio. This effect could be quantified using interaction measures as more general tools to study the way SIFs are perturbed. Care must be taken in order to differentiate between perturbations induced by heterogeneity, and perturbations induced by fracture interaction, because $K_i^{int}$ will include both of these effects. This can be accomplished by calculating $K_i^{int}$ in a volume containing all the fractures and material property variations, then calculating two versions of $K_i^{iso}$ per fracture - one with the material property variations and one without. Then, separate values of $C$, $M_i$, and $\epsilon_i$ can be found, each one describing the SIF perturbation arising from either heterogeneity and interaction. Such an analysis would facilitate understanding of the competing effects of interaction and heterogeneity on growth.

### 3.6.2 Computational considerations

The number of simulations needed to acquire a full dataset with $n$ fixed fractures in a volume is $n + 1$, because the system must be simulated with all fractures present, providing values for $K_{I-III}^{int}$, then once for each fracture, where that fracture is the only one in the volume, providing values for $K_{I-III}^{iso}$. Only one mesh is required for the domain, as the same mesh can be used for all calculations. The mesh does not need to be particularly refined, as the interaction measures have been shown to remain accurate for coarse meshes (Figure 3.7). Very dense fracture interaction maps are relatively expensive to generate as each location of the interacting fracture requires a new mesh around the moving fracture. The method is also not restricted to using the disk-shaped domain integral method for calculating SIFs; any three-dimensional SIF computation

method, such as displacement correlation [Branco et al., 2015] or displacement discontinuity [Thomas and Pollard, 1993], would also be effective. Variation maps can be generated using any numerical method that generates SIFs, and can be also adapted to other fields.

Three-dimensional growth simulations are an additional method with potential for exploring interaction, and are explored in Chapter 4 and 6. However, SIF variation maps may be more convenient for several reasons. Sparsely sampled interaction maps are reasonably computationally cheap to calculate compared to full fracture growth simulations, that may require re-meshing at every step to track the propagation of the fracture. Growth simulations rely on many non-physical parameters arising as a result of the particular modelling technique, such as the extension increment per step, which has a large effect on the final geometry of the fracture. Additionally, the geometry from each possible initial separation is difficult to summarise in a 2D plot, unlike interaction measures which provide one numerical value per location.

### 3.6.3 Recommended use of interaction measures

The interaction measures and maps described in this work can be used to better understand the behaviour of fractures. For an outcrop or subsurface system where fracture geometries are known, examining the SIFs and interaction measures on each fracture provides a straightforward method for summarising their behaviour. Interaction maps are more useful when the locations of fractures are either variable or unknown, such as when fractures are blind, or across large outcrops where a particular relative fracture orientation arises frequently (*e.g.*, between two fracture populations). Maps shown in this work demonstrate their effectiveness at highlighting geometries that result in enhanced, reduced, or non-planar growth. They can also be created for any pair of fractures with different geometries and orientations. Therefore, rather than referring to a catalog of maps, they should be created to fit the relative fracture orientations which are frequently encountered in a specific geological setting, following the steps outlined in Section 3.5.

It should be noted that $C$ and $M$ do not directly determine the increased likelihood of propagation without additional context, such as material toughness. This can instead be approached by using a critical stress intensity factor for the material, which, if reached by $K_I$, results in fracture propagation [Atkinson, 1984]. This value can be used to scale the results of the output, or in the place of $K_i^{iso}$ to show when fractures are close enough to cause propagation. However, those results will be dependent on the properties of the medium, unlike the maps presented here.

### 3.6.4 Contrasting $C$ and $M_i$

$C$ and $M_i$ both characterise the magnitude of interaction experienced by a fracture. $C$ yields consistent quantifications of interaction across different levels of mesh refinement. Because it is derived from comparing the area beneath two curves, its magnitude is independent of the magnitude of stress. This makes $C$ the most convenient measure for assessing whether interaction occurs using a threshold. The benefits of using $M_i$ are that the calculation is simple, *i.e.*, it does not require numerical integration and can be found graphically, and it also provides a location on the fracture at which the SIF perturbation is highest. Either method provides similar results for the way in which interaction changes around a fracture. In particular, the interaction map for $C_I$ in Figure 3.9 is almost identical to $M_I$ in Figure 3.10.

The benefit of using $C$ will be seen when a system contains multiple close fractures. A complex geometrical arrangement of multiple interacting fractures will create a complex distribution of SIFs around the tip, with multiple peaks and troughs. This would be fully captured by $C$, but only one peak would be selected for $M_i$. Looking at the modes individually is also important because, in overlapped geometries, there may be multiple peaks and troughs in all three modes. Therefore, in most cases, $C$ is the recommended measure.

## 3.7 Conclusions

This work provides several contributions towards analysing and understanding fracture interaction processes through the study of the stress intensity factor (SIF) perturbations. These perturbations occur when two or more fractures are close enough to alter the state of stress at one another's tips. Using a three-dimensional finite element based fracture mechanics model simulating pairs of fractures, these perturbations have been demonstrated and quantified. Three measures of interaction have been proposed to quantify how the SIFs are altered; 'circumferential SIF perturbation' ($C$), 'maximum SIF perturbation' ($M_i$) 'amplification to shielding ratio' ($\epsilon$). $C$ and $M_i$ can be used to quantify the magnitude of the interaction, and $\epsilon$ can be used to describe whether the stress at the tip of a fracture is mostly amplified or shielded. These measures have been used to study the interaction occurring around pairs of fractures of equal size in several orientations. This is accomplished by creating interaction maps, which plot measures of interaction in space according to the location of an interacting fracture. The analysis outlined in this work, and the interaction measures that are proposed, are applicable

to any stress state or fracture population. This provides a new and powerful way to understand how fractures affect one another.

# Chapter 4

# Growth of multiple fractures under tension and compression

## 4.1 Introduction

Modelling and prediction of realistic fracture growth in geological materials has been a long term challenge [Jing and Hudson, 2002]. Many properties of a rock mass are highly dependent on small differences in the geometry of fractures. The linkage of fractures in arrays and networks may have a significant impact on hydraulic properties, including whether the network will percolate and provide a significant increase in permeability for a relatively small change in fracture density [Thovert et al., 2017]. Macroscopic failure occurs when a network of cracks become fully connected throughout a sample [Martin and Chandler, 1994], or form large fault-scale structures in the subsurface [McGill et al., 2000]. This chapter describes the methods implemented in ICGT to grow fractures in three dimensions. This introduction comments on the important features of geological fractures and how propagation is modelled in the ICGT and other numerical models.

### 4.1.1 Fracture interaction in geological media

Fracture arrays in rock outcrops demonstrate the complexity arising when fractures mutually interact, with two examples shown in Figure 4.1. Figure 4.1A shows an array of drying cracks in concrete, where fractures have initially grown horizontally, and later begun to interact. Despite the straightforward stress history of the array, the competition between growing fractures produces a complex pattern. Fractures in Figure 4.1B have undergone a more complex deformation history, where an older fracture array is propped open by mineral fill and crosscut by later fractures. The array shows hooking (curving

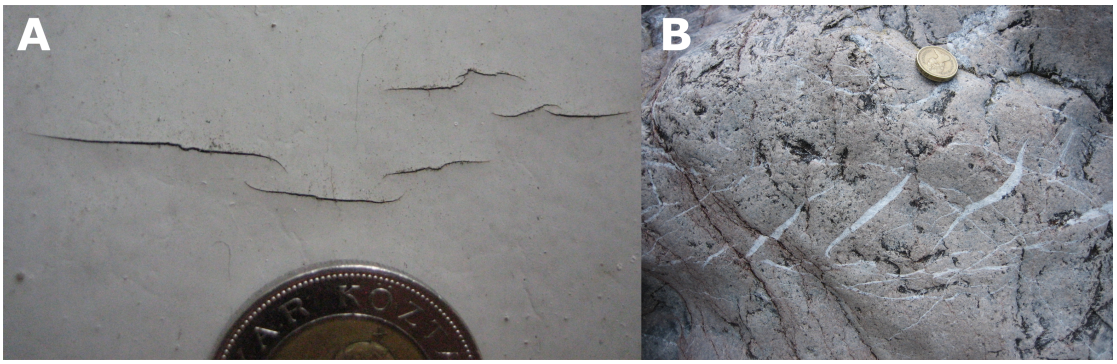



FIGURE 4.1: Fracture arrays observed in outcrops. A: Drying cracks outcropping at the surface of the concrete. B: Fractures from multiple stages of deformation in East Cowes, Isle of Wight, where some fractures are mineralised, then cross cut by other fractures created during other phases of deformation.

of a fracture in the vicinity of another fracture) at the tips of its fractures, which may be attributed to both ductile deformation of the rock mass or interaction. In both examples, the outcrop provides a roughly planar view of the fractures, but within the rock, they may intersect and their tip curvature may vary. Olson [1993] considered the onset of fracture hooking as a balance between whether far-field stress or interacting forces are dominant. Curved paths suggest that remote stresses are nearly isotropic relative to the stresses induced by fractures. Detailed studies of fracture pairs and arrays quantify the onset of intersection through measurements of spacing and fracture length, across a wide range of size magnitudes [Ghosh et al., 2019, Lamarche et al., 2017]. Figure 4.2 shows three further examples of pairs of fractures interacting, reproduced from Pollard et al. [1982]. Hooking at the tips of the fractures is observed at both the laboratory (A) and field (B and C) scales, with similar overall curvatures emerging despite the significantly different scales of observation.

### 4.1.2 Modelling of three-dimensional fracture propagation

Discretely modelling the full process of microfracture activation and linkage to form macrofractures would require significant resolution over several orders of magnitude, making discretisation of the domain very challenging. Smeared fracture models can be used to reproduce this process, because each point where the material which represents weaker material can further concentrate stress [Zhou et al., 2017]. As discussed in Section 2.4.1.1, these models have limited scope for flow simulation, because these smeared fractures do not have apertures and damage is not directly linked to increased permeability. In discrete fracture growth models, only fractures which are on similar length scales are represented. The ICGT upscales the coalesence of microfractures ahead of the tip,

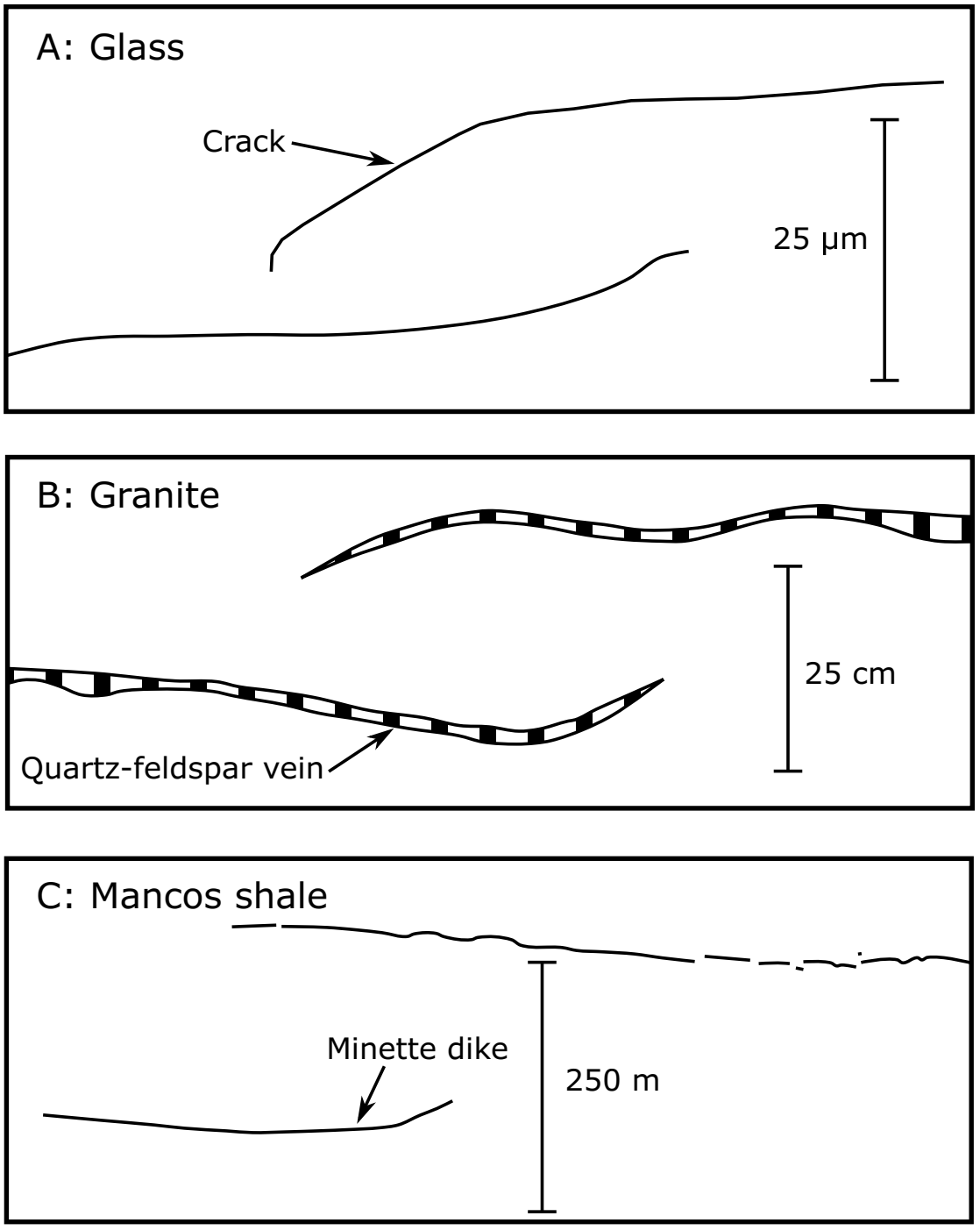



FIGURE 4.2: Examples of fractures interacting across scales, reproduced from Pollard et al. [1982]. A: Two small-scale cracks in a laboratory specimen of glass. B: Two veins in Cottonwood stock, Utah. C: Two igneous dikes near Ship Rock, New Mexico.

simplifying linkage of many existing surfaces to the addition of one surface. Other discrete fracture methods adopt a similar approach [*e.g.*, Gupta and Duarte, 2014, O'Hara et al., 2016]. This still results in a realistic behaviour, because evidence suggests fracture propagation is controlled by the macroscopic stress regime, rather than microfracture properties such as density or orientation [Nasseri et al., 2006]. Microfracture properties

can still be included in growth models by using a reduced value of the critical SIF, or by making the domain heterogeneous or anisotropic.

Variable rates of fracture growth are a further detail of LEFM which are challenging to model. Methods where fractures do not follow the pre-existing discretisation in the domain (*e.g.*, FEM or XFEM) must either remesh or have sufficient mesh density where fractures may propagate, in order to retain accuracy in the fracture tip region. Remeshing requires a numerical method which advances fractures in the domain by a small amount, then updates the discretisation of the domain to match the new fracture tips. A direct link between the discretisation step and the time increment (*e.g.,* fatigue growth with a defined time per load cycle) is not directly available for all boundary conditions, and may not be feasible in any case due to the computational cost of each step.

Mutual fracture growth adds a further complication to time-based schemes. Most analyses of fracture growth have focused on individual fractures, whereas geological fractures are known to grow mutually in the subsurface [Segall, 1984]. In these cases, one fracture will grow more than others, in a process that is difficult to document accurately and validate in three dimensions. This work adopts a straightforward approach is used which does not provide an explicit time increment per growth step[1]. This allows the deformation algorithm to consider a steady state for each growth step, avoiding the significant additional computational cost of a time-integrated scheme. This still enables mutual growth of fractures based on the relative energy release rate across each fracture's tip, handled by a Paris-type fracture growth law.

Section 2.3.7 introduces the methods used to grow fractures in the ICGT, building on the methods established in Chapter 2. After the stress and displacement are solved throughout the domain using either the standard deformation or Augmented Lagrangian contact method, stress intensity factors (SIFs) are calculated using the virtual disk method, providing $K_I$, $K_{II}$, and $K_{III}$ at points along the fracture tip. These three values are used to predict when a fracture tip fails, at what angle it propagates at, and the length of its extension. Mixed mode criteria are implemented to enable fractures to grow under any stress conditions [Richard et al., 2014].

Following the presentation of the growth method, fracture growth is demonstrated and validated under tension and compression. The influence of the fracture growth rate exponent ($\beta$) is explored to quantify how it effects the development of isolated fractures and interacting fracture arrays. The impacts of fracture interaction, quantified in

[1] In other ICGT applications incorporating poroelasticity, viscous fluid flow provides a timescale for fluid growth. For example, Salimzadeh et al. [2017a] compare the radius and aperture of hydraulically fractures with analytical solutions.

Chapter 3 for static fractures, are expanded here to multiple fractures which compete to grow.

## 4.2 Modified two-step Paris-type extension criterion

The most important part of the growth algorithm is assigning the extension length at each tip in each step, as this controls the competitive process of growth during interaction. The other two growth criteria (failure and angle) are introduced in Sections 2.3.7.1 and 2.3.7.2 respectively. Two-dimensional numerical studies show that within a group of cracks, in order to reproduce patterns found in growth experiments, crack fronts must grow at different speeds [Renshaw and Pollard, 1994]. In three-dimensional techniques such as the present method, this means that each point along the fracture tip may have a different growth extent.

Both the Paris and sub-critical crack growth methods both take the form of a power law [Anderson and Anderson, 2005, Ko and Kemeny, 2013, Pugno et al., 2006], of the form:

$$\frac{\mathrm{d}a}{\mathrm{d}N} = c\left(\frac{\mathcal{G}_n}{\mathcal{G}_{max}}\right)^{\beta} \tag{4.1}$$

where $\mathrm{d}a/\mathrm{d}N$ is the advance (in metres) of the fracture tip $n$ per load cycle $N$, $c$ is a material constant, $\mathcal{G}_n$ is the value of $\mathcal{G}$ (the local fracture tip energy release rate) at tip $n$, $\mathcal{G}_{max}$ is the largest value of $\mathcal{G}$ among present fractures, and $\beta$ is the fracture growth rate exponent. In the sub-critical crack growth formulation, $\mathcal{G}$ is often exchanged for $K_I$, as most analyses consider only mode I, and $\mathrm{d}a/\mathrm{d}N$ is exchanged for growth velocity [Kemeny, 1991]. The terms in Equation 4.1 can be seen on the schematic graph in Figure 2.2, including $\beta$, which is the slope of the line in the fatigue growth region (II). The units of the constant $c$ differ between Paris and sub-critical crack growth laws [Vieira et al., 2008].

The value of the exponent $\beta$ controls the extent to which growth is concentrated at tips with higher energy. Lazarus [2003] notes that the Paris law can be applied to both brittle and fatigue propagation. For fatigue fracture growth, $\beta \approx 1$, and, for brittle fracture growth, $\beta >> 1$. Lazarus [2003] shows that, for three-dimensional single fracture growth, this exponent defines the relative extension of the tip nodes of a single fracture. However, a wide range of estimates are made for the value of the fracture propagation exponent. Renshaw and Pollard [1994] estimated that $\beta = 0.35$, based on outcrop observations and two-dimensional laboratory experiments in brittle rocks. It was later shown that this exponent affects the type of ensuing fracture pattern [Olson, 1993], with higher values increasing the localisation of fracture patterns [Lei et al., 2017a]. On individual fractures

propagating in one plane, the final geometry is highly influenced by the value of $\beta$, whilst still converging on circular shapes [Favier et al., 2006, Lazarus, 2003]. In sub-critical growth experiments with few fractures, the value of the exponent is found to be much higher, between 30 and 60 [Ko and Kemeny, 2013]. In the present case, where multiple fractures grow together in three dimensions, high values of $\beta$ reduce the extent to which fractures grow mutually, enhancing interaction effects. In outcrops (*e.g.*, Figure 4.1), multiple fractures are seen to have grown together, demonstrating that lower values of $\beta$ are applicable to slow, fatigue-like growth of arrays.

This work introduces a novel formulation based on Equation 4.1 for handling propagation in domains containing multiple three-dimensional fractures. Rather than defining a single value of $\beta$, two values are defined, $\beta_f$ and $\beta_n$. For each fracture, $\Delta a_f$ is scaled from $\Delta a_v$ based on the ratio between the maximum $\mathcal{G}_n$ on the fracture, and maximum $\mathcal{G}_n$ in the volume:

$$\Delta a_f = \Delta a_v \left( \frac{\mathcal{G}_f}{\mathcal{G}_v} \right)^{\beta_f} \tag{4.2}$$

where $\Delta a_f$ is the maximum extension of fracture $f$, $\Delta a_v$ is the maximum fracture extension length per step for the volume, $\mathcal{G}_f$ is the largest value of $\mathcal{G}_n$ amongst fracture $f$'s tips, $\mathcal{G}_v$ is the largest value of $\mathcal{G}_n$ amongst all the tips in the volume, and $\beta_f$ is the fracture growth rate exponent. Second, the local tip extension $\Delta a_n$ for a tip $n$ on fracture $f$ is given by

$$\Delta a_n = \Delta a_f \left( \frac{\mathcal{G}_n}{\mathcal{G}_f} \right)^{\beta_n} \tag{4.3}$$

where $\beta_n$ is the tip growth rate exponent. The amount of growth in each step can be controlled through $\Delta a_v$, as this sets the maximum growth amount, and in a domain with multiple fractures and varied values of $\mathcal{G}_n$ along their tip nodes, $\Delta a_n \leq \Delta a_f \leq \Delta a_v$.

This approach essentially applies the Paris-type criterion twice: once to define a maximum extension per fracture (Equation 4.2), and a second time to define the variation in extension along the fracture tip (Equation 4.3). In a domain with one fracture, the method is equivalent to a standard Paris law (Equation 4.1), because that fracture will always have $\mathcal{G}_f$ at a node on its tip, and therefore $\Delta a_f$ will be the same as $\mathcal{G}_v$. Additionally, either step can be skipped by setting its respective value of $\beta$ to zero, allowing a single step Paris-type law to be tested without changing the approach. In a domain with multiple fractures, $\mathcal{G}_n$ varies widely across many tips. It may be the case, particularly due fracture interaction, that one value of $\mathcal{G}_n$ is much larger than the others. The present formulation ensures that growth can be distributed across multiple fractures whilst still weighted towards tips with the highest $\mathcal{G}_n$. Separating $\beta$ into two variables is a new approach to modeling quasi-static growth, meaning the approach has the drawback of

obscuring the physical meaning of $\beta$. The implications for use of a modified two-step Paris-type are examined in Sections 4.4, 4.5.1, and 4.6.

## 4.3 Growth of isolated fractures

The error in the SIF and propagation angle accuracy can be quantified in first step, if the fracture starts from a flaw with a shape for which an analytical solution exists (*e.g.*, circle or disk shaped fractures). Beyond the first step, no analytical solutions are available for fractures with three-dimensional surfaces. Instead, fracture geometries can be compared to those observed in experiments. This section investigates growth under tension and compression over multiple growth steps. A circular flaw is inclined at 45° to the principal stress direction, at the centre of a 20 × 20 × 20 m cube. The fracture is discretised using 40 tip nodes, selected based on balancing simulation time and SIF accuracy. A principal stress of $\pm 1 \times 10^7$ Pa is applied in each step in the vertical axis for tension and compression respectively. In each step, $\Delta a_v = 0.1$ m and $\beta_n = 2$. With only one fracture in the domain, $\mathcal{G}_f = \mathcal{G}_v$ and Equation 4.2 simplifies to $\Delta a_f = \Delta a_v$. Therefore, for a simulation containing one fracture, and the value of $\beta_f$ is irrelevant, and the modified two step Paris-type law simplifies to be equivalent to a normal Paris-type law.

### 4.3.1 Tension

Figure 4.3 shows a schematic diagram of the volume containing the fracture, and the geometry of the fracture from two angles, over 31 simulation steps. In the first step, the fracture grows sharply away from its initial plane. The propagation angle changes smoothly along the tip, pointing in opposite directions at the very top and bottom. Over the following steps, the fracture grows at a similar angle to each previous step, with a smaller change in angle over time, converging towards an angle perpendicular to the direction of stress. After 31 steps, the fracture has maintained its circular shape, growing evenly in all directions in each step, because $\mathcal{G}_n$ is uniform around the tip. As growth continues, the fracture orients itself perpendicular to the principal stress direction. In turn, $\mathcal{G}_n$ is also larger when the fracture is larger. This manner of growth matches the widely observed wing crack [*e.g.*, Lee and Olson, 2017].

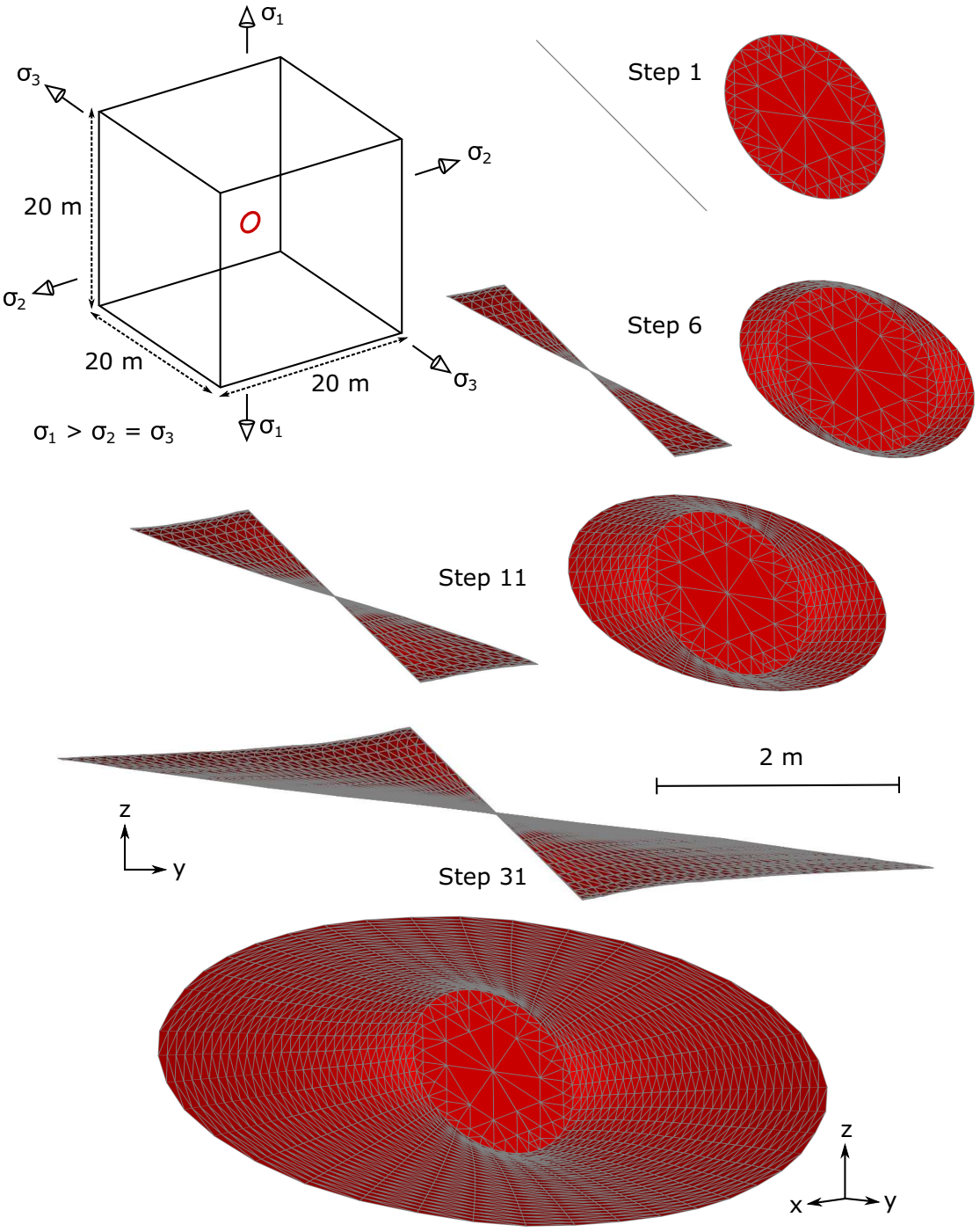



FIGURE 4.3: Growth of an isolated fracture growth under tension. The fracture has 40 tip nodes and initial radius 1 m. The maximum extension in each step ($\Delta a_v$) is 0.1 m. The three stresses in the schematic in the top left are $\sigma_1 = \pm 1 \times 10^7$ Pa, and $\sigma_2 = \sigma_3 = 0$ Pa.

### 4.3.2 Compression

Figure 4.4 shows the progressive growth of a fracture under compression, over 31 steps. Similar to the tension case, the compressed fracture grows as a wing crack, except that it orients itself parallel to the maximum compressive principal stress direction. Similar

wing cracks are widely observed in compression experiments, [*e.g.*, Cao et al., 2015, Dyskin et al., 1999, Germanovich et al., 1994]. Even when rocks are under uniaxial compression, fractures still prefer to grow in the opening mode, curving towards an orientation parallel to the direction of compression [Nemat-Nasser and Horii, 1982]. In the first step, the fracture changes angle significantly away from its initial plane, with a smaller change in angle with each subsequent step. The fracture initially grows uniformly in all directions until the top and bottom tips of the fracture have become vertical. Once vertical, the top and bottom of the fracture grow much less, and the sides propagate instead, creating a horizontally elongated fracture.

In the later stages of growth, the top and bottom of the fracture experience high in-plane shear, leading to $K_{II}$ being much larger than $K_I$ and $K_{III}$. This causes the propagation angle to alternate between two extremes, resulting in an alternating path of growth. In the limit where $\Delta a_n$ tends towards zero, the path tends to be straighter. This effect can be attenuated by reducing the magnitude of $K_{II}$ by half when evaluating the angle criterion. Figure 4.5 demonstrates this with comparison between two fractures, one with $K_{II}$ attenuated (also shown in Figure 4.4) and one without attenuation. The former has a smooth surface throughout growth, and the latter case (B) has a stepped surface on its top and bottom. The macroscopic geometry in both cases is very similar as they converge to the same fracture shape. Minor changes in the attenuated case include a slightly shallower initial angle at the top and bottom, and at the sides of the fracture the surface remains straight throughout growth. Similar adjustments to $K$ values have been used in other models to ensure smooth fracture growth, *e.g.*, moving averages [Gupta et al., 2017].

It should be noted that there are many parameters which influence fracture growth. The figures shown in this section show typical growth for the cases of tension and compression, for relatively small $\Delta a_v$ values, in order to validate growth over many steps. If $\mathcal{G}_n$ varies significantly along the tip, such as in the compression case, differences in $\Delta a_v$ and $N_f$ result in different fracture shapes. For example, if $\Delta a_v$ is large, tips with lower values of $\mathcal{G}_n$ grow much less, leading to a more elongated fracture in the $y$ axis.

### 4.3.3 Comparison with experimental results

Figure 4.6 shows a further validation of the growth. Material failure experiments are mostly performed on through-going fractures, intersecting with the side of the sample. To simplify the final three-dimensional geometries shown in Figures 4.3 and 4.4, a curve is created from the intersection between the fracture and a plane through the $x$-$z$ axes ($x = 0$, $z = 0$). Figure 4.6 compares these curves to experimental two-dimensional wing

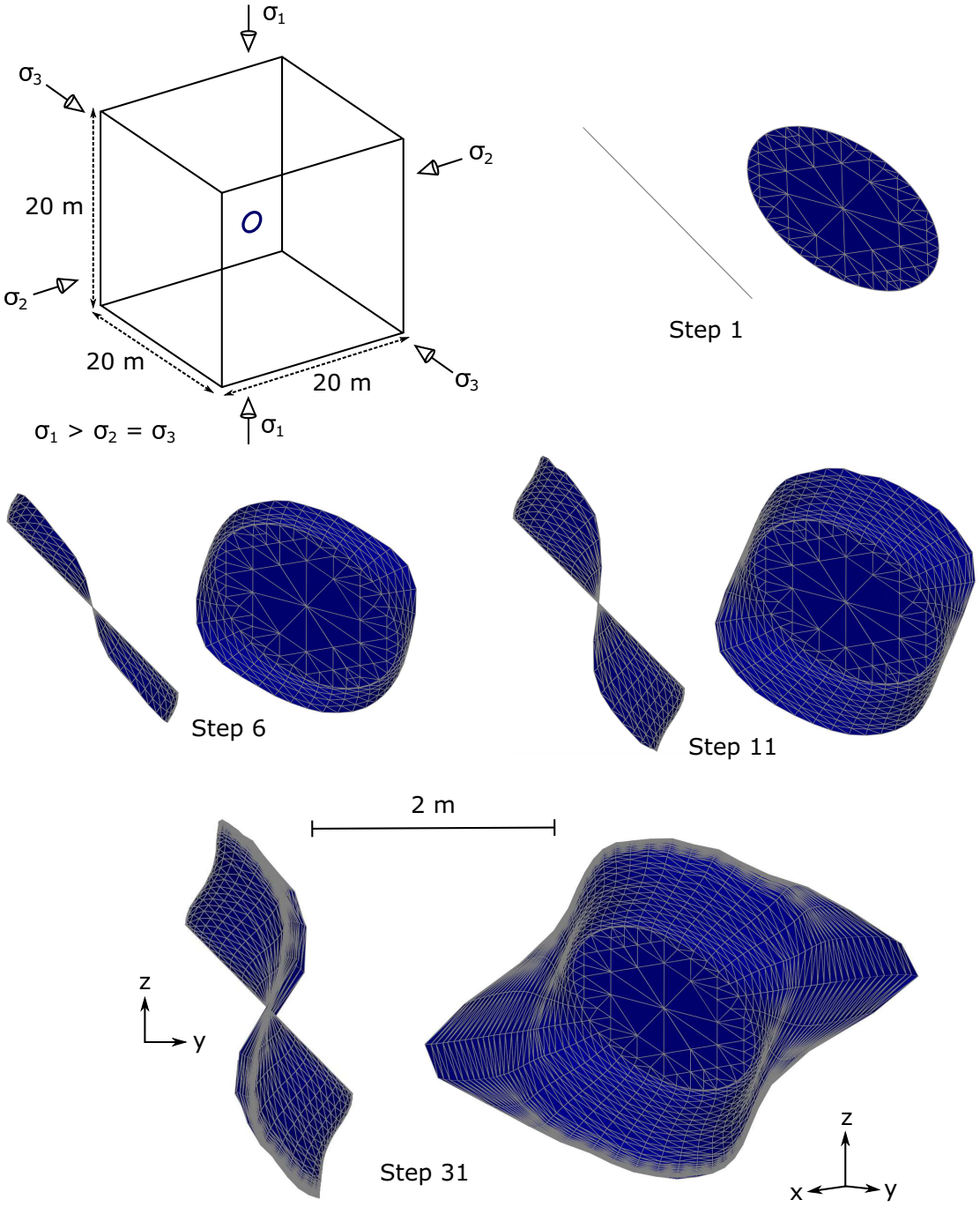



FIGURE 4.4: Growth of an isolated fracture growth under compression. The fracture has 40 tip nodes and initial radius 1 m. The maximum extension in each step ($\Delta a_v$) is 0.1 m. The three stresses in the schematic in the top left are $\sigma_1 = \pm 1 \times 10^7$ Pa, and $\sigma_2 = \sigma_3 = 0$ Pa. The friction coefficient between the fracture surfaces is 0, making $K_I$ non-zero and allowing the faces of the fracture to slide past one another.

crack paths, produced under tension and compression, documented by Olson [1993] and Germanovich et al. [1994]. These experimental results are not taken from unique experiments, rather, they are interpreted from field and experimental results of rock fracturing, including Nemat-Nasser and Horii [1982] and Pollard et al. [1982]. Therefore, Figure 4.6 is not a direct comparison calibrated to the same material properties, but a

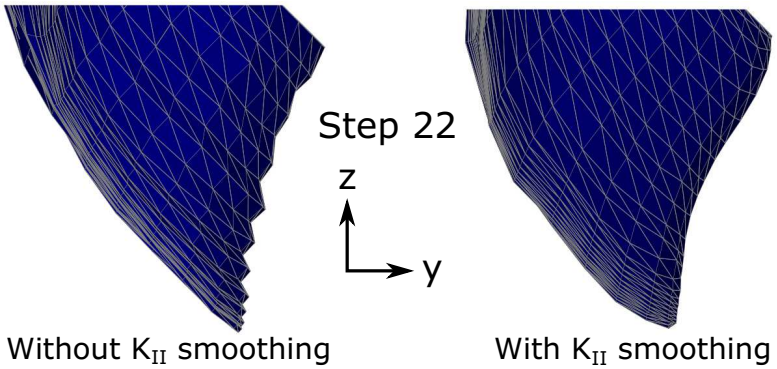



FIGURE 4.5: Effect of attenuating $K_{II}$ on the fracture geometry in growth under compression. A: Side view of a fracture (also shown in Figure 4.4 with $K_{II}/2$ for the growth angle. B: The same initial geometry and boundary conditions as A, but without attenuation of $K_{II}$.

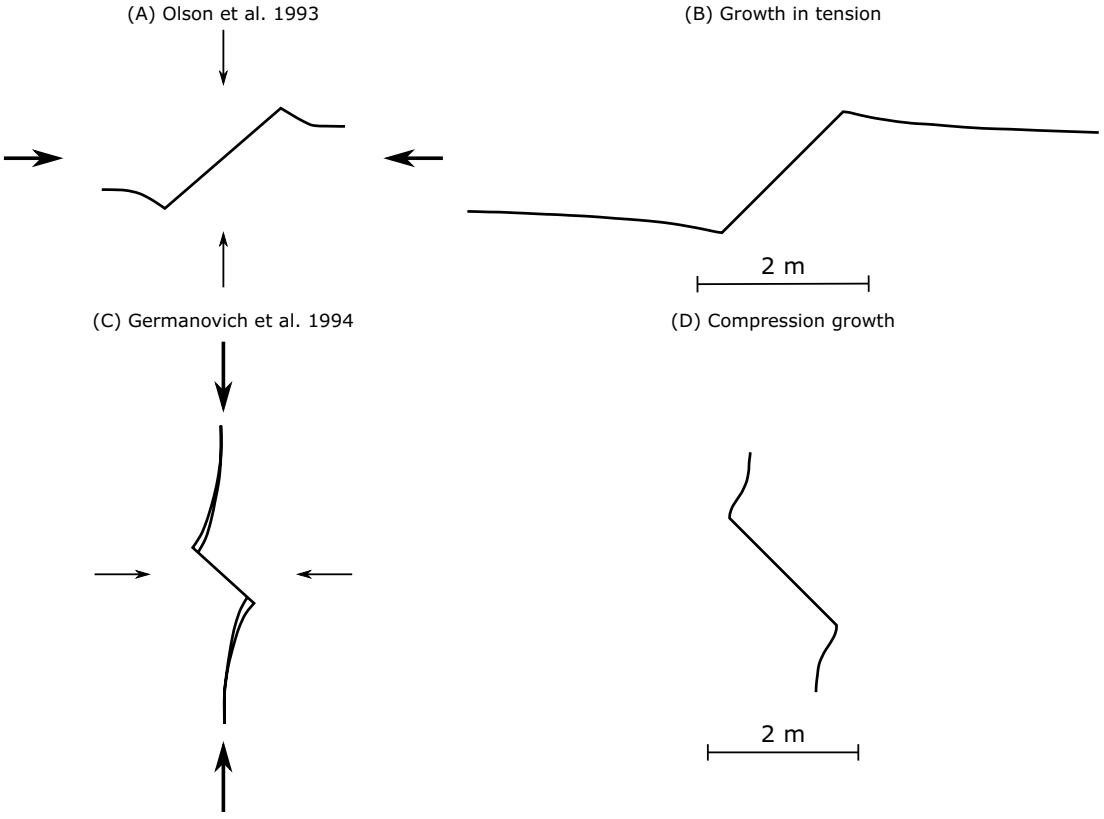



FIGURE 4.6: Comparison between experimental wing cracks and simulated inclined flaws under tension and compression. A: Figure 2A from Olson [1993], demonstrating typical wing crack growth under tension. B: Tension fracture from Figure 4.3 in step 31, visualised as the intersection of a plane in the $x$-$z$ axes. C: Figure 1A from Germanovich et al. [1994], showing a fracture growing from an inclined flaw under uniaxial compression. D: Compression fracture from Figure 4.4 in step 31, visualised as the intersection of a plane in the $x$-$z$ axes.

demonstration that the three-dimensional geometries created by the ICGT are a close match to those found in experiments.

These results show one of many possible vertical cut-planes, as any cut-plane on the $x$-$z$ plane could be visualised. Offsetting the plane would result in smaller initial flaw and different curvature. The orientation of stress shown by arrows in Figure 4.6A and C demonstrates that wing cracks orient themselves perpendicular to the direction of the minimum compressive stress. There are many differences in the mechanics of the growth between the cases. Compression requires a progressively larger load to continue propagation, whereas a tensile crack requires no additional stress, because a larger fracture acquires larger SIFs in tension as long as the stress magnitude remains the same. The location of maximum aperture also differs, with the whole fracture opening in tension [*e.g.*, Pollard et al., 1982], and only the most curved wings opening under compression [Germanovich et al., 1994]. Both of these properties are arise in the present simulations, and mechanical fracture apertures are explored further in Chapter 6.

## 4.4 Effect of fracture propagation exponent on growth

In this section, the growth rate exponents $\beta_f$ and $\beta_n$, introduced in Section 4.2 as part of the Paris-type length criterion, are varied to demonstrate the types of growth that can be resolved under tension. Two values of $\beta_n$ are used, 2 and 20, exploring low velocity (fatigue) and high velocity (brittle) growth, respectively [Lazarus, 2003]. When multiple fractures are present, $\beta_f$ is set at a constant value of 0.35 throughout all examples in this section, matching the value suggested by Renshaw and Pollard [1994]. Setting $\beta_f$ to a value less than 1 ensures that many fractures can grow simultaneously, whilst using $\beta_n > 1$ ensures that, if $\mathcal{G}_n$ varies significantly on one fracture, propagation across its tips will be more varied. The resulting growth is visualized using the fracture tip loop at each growth step. To focus on the effects of fracture extension, $K_{IC}$ is set to a low value, such that $K_v < K_{IC}$ at every node. Therefore, extension lengths are controlled by the local value of $\mathcal{G}_n$, rather than by the failure criterion. Throughout this section, a tension boundary condition is used, applied at the top of the domain, of $1 \times 10^9$ Pa.

### 4.4.1 Low growth rate exponents

Figure 4.7 shows the growth of two inclined fractures, grown in separate models, with $\beta_n = 2$ and $\Delta a_v = 0.1$ m. This is close to the range of fatigue-based growth where $\beta_n \approx 1$. This value means that the fracture will tend to grow more where $\mathcal{G}_n$ is higher, and growth is non-negligible even for lower values of $\mathcal{G}_n/\mathcal{G}_{max}$ (*e.g.*, 0.1 to 0.5). The initially disk-shaped fracture in Figure 4.7A grows by a uniform length at every step. The tips show the re-orientation of the fracture to be perpendicular to the stress field,

as shown in Figure 4.3. It maintains its circular shape throughout growth. On a flat or inclined disk, $\mathcal{G}_n$ is constant around the tip, leading to uniform growth.

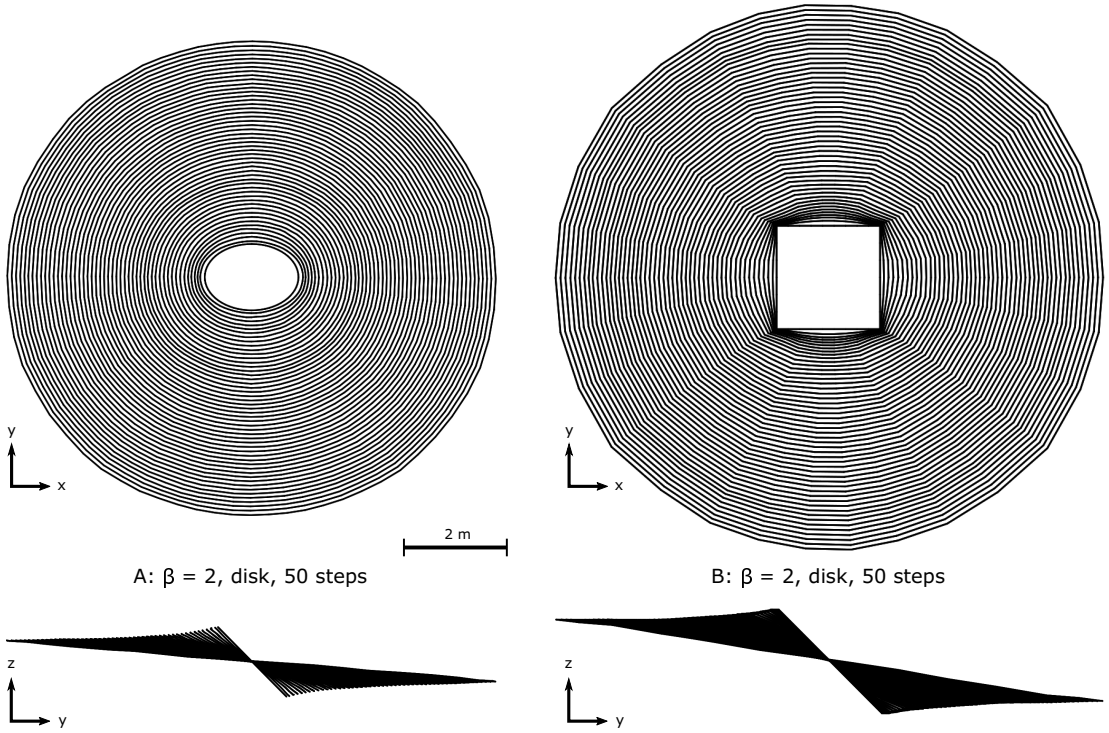



FIGURE 4.7: Fracture tips of isolated fractures grown in tension with growth rate exponent $\beta_n = 2$. The fracture on the left is grown from a disk, with a 1 m initial radius, inclined 45° to the extension direction. In the top left image, the initial fracture appears non-circular due to its inclination relative to the viewpoint. The fracture rectangle is also inclined at 45°, and has dimensions $2 \times 2\sqrt{2}$ m with normal (1, 0, 1). Each fracture is grown in a $20 \times 20 \times 20$ m cube.

A rectangular fracture is shown in Figure 4.7B to illustrate the behaviour of the fracture when $\mathcal{G}_n$ varies and $\beta_n$ is low. The rectangular flaw grows to a very similar wing crack shape as the disk, despite the different initial shapes. In the first steps of growth, the largest extension occurs at the sides furthest from the corners, and no extension occurs at the corners. This continues for several steps until the tip becomes circular, at which point the extension becomes uniform across the tip. This process of 'correcting' the shape of the initial flaw into a circle was also demonstrated in other numerical growth approaches by Lazarus [2003] and Sukumar et al. [2003] for rectangular and non-uniform ellipse-shaped flaws.

### 4.4.2 High growth rate exponents

Figure 4.8 shows penny-shaped fractures growing at $\beta_n = 20$ with $\Delta a_v = 0.1$ m. At this value of $\beta_n$, only tip nodes where $\mathcal{G}_n \approx \mathcal{G}_v$ extend, resulting in less surface extension at each step, on tips where the highest values of $\mathcal{G}_n$ are located. Figure 4.8A shows a

fracture with 32 tip nodes. In the first steps of growth, only the top and the bottom of the fracture extend, with no growth on the sides of the fracture. This non-uniform growth corrects itself towards a more circular fracture, taking many more steps to do so than the $\beta_n = 2$ case. At the last step, the fracture has grown more in the -$x$ direction, despite material properties being isotropic, suggesting the fracture is still in the process of converging towards a uniform shape.

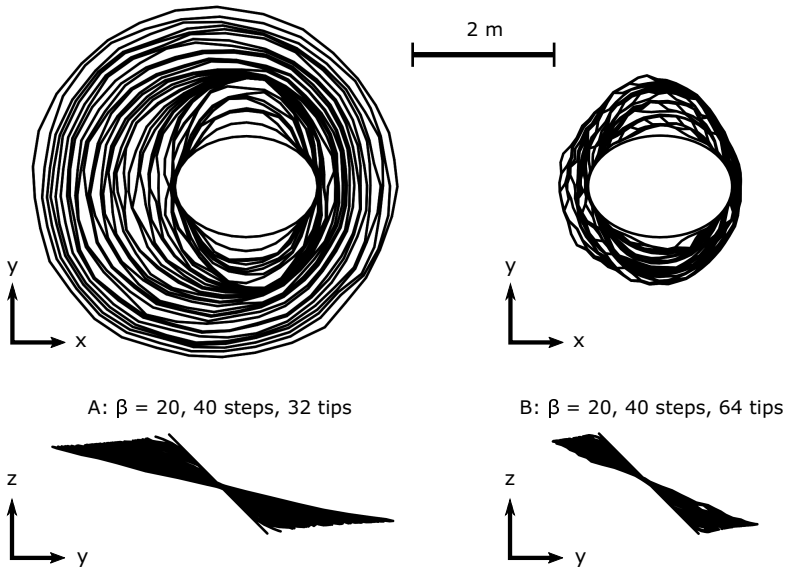



FIGURE 4.8: Fracture tips of isolated fractures grown in tension with growth rate exponent $\beta_n = 20$. Both fractures grow from initial flaws with 1 m radius, inclined 45° to the extension direction. The left fracture was grown with 32 tips, whilst the right was grown with 64 tips. Each fracture is grown in a 20 × 20 × 20 m cube.

Figure 4.8B shows the same initial flaw growing with high $\beta_n$ with 64 instead of 32 tips. This higher refinement will provide more accurate SIFs, but also more values of $\mathcal{G}_n$ along the tip. This makes it more likely for a tip to have a slightly large value of $\mathcal{G}_n$ against which the other tips are scaled. Therefore, very few tips extend in each step in this case. Like the 32 tip case, the result is initially asymmetric. A large $\beta_n$ enhances small variations in the SIFs, which go on to dominate over the geometric effects of the fracture and its interaction with the displacement field. As growth progresses, these errors are corrected, ultimately resulting in a fairly symmetric shape.

### 4.4.3 Effects due to maximum extension lengths

When fracture extension is scaled by $\Delta a_v$ (see Equation 4.2), fractures in models with relatively high $\beta_n$ will only experience a small increase in surface area. This means that, to achieve the same fracture surface area, models with high $\beta_n$ will require many more steps than those with low $\beta_n$. An example of this effect is shown in Figure 4.9. Two inclined fractures grown with the same $\Delta a_v$ and different $\beta_n$ are shown at the point at

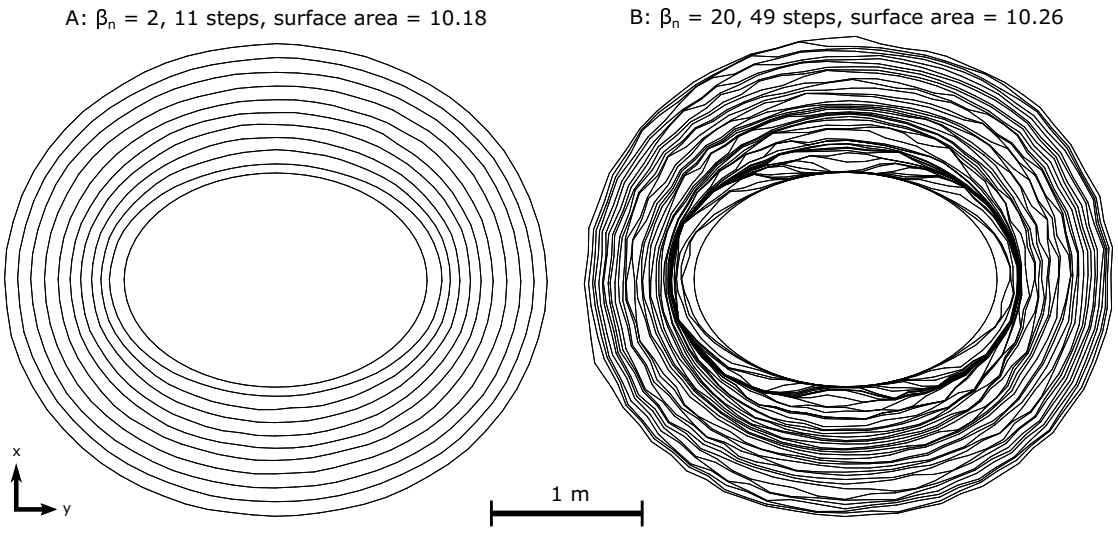



FIGURE 4.9: Fracture tips for two inclined fractures grown in tension in separate models with different values of $\beta_n$. The initial fractures are visible as the innermost loop. Each simulation step results in growth, represented by the next loop outwards. The $\beta_n = 2$ and $\beta_n = 20$ fractures have similar surface areas at steps 10 and 49 respectively. Because both fractures are grown as the only fracture in the volume, the value of $\beta_f$ does not affect their growth. Both fractures have 64 tips, initial radius 1 m and $\Delta a_v = 0.1$ m. Both fractures have 64 tip nodes. Each fracture is grown isolated in a $20 \times 20 \times 20$ m cube.

which they have the same surface area. This requires 49 steps in the $\beta_n = 20$ case, but only 11 steps in the $\beta = 2$ case. The final fracture shape at this point is very similar, despite the $\beta_n = 20$ fracture growing highly asymmetrically in each step.

Further differences can be found for individual fractures if the number of tip nodes is varied. The more tips there are from which to select $\mathcal{G}_{max}$ in each step, the more likely it is that one tip has a much higher value than the others. Figure 4.8 shows an example of this, where two fractures are grown in separate models with different numbers of tips. The final result after 40 steps is that the fracture with more tips acquires a much lower surface area, as at each growth step, typically only one tip extends by a significant amount. These differences have implications for quasi-static growth schemes using different values of the fracture growth exponent. Early numerical experiments which use Paris-type propagation laws find that patterns generated with higher fracture growth exponents can take extremely long times to simulate [Olson, 1993]. This can be mitigated in part by increasing $\Delta a_v$, such that the largest extension is much longer. Other more complex scaling methods can be used to scale $\Delta a_v$, such as ensuring the surface area of the fractures to increases by the same amount in each step.

## 4.5 Growth of multiple fractures

In this section, a fracture array is grown in tension from five fractures, separated by 1 m in the $x$ and $z$ axes. The fractures have an initially circular shape, with a radius of 1 m, and are aligned perpendicular to the direction of tension, meaning they would grow as flat uniform disks similar to Figure 4.7 if they do not experience any interaction effects. The effects of changing the values of $\beta_n$ and $\beta_f$ on the ensuing fracture patterns are demonstrated. The arrays are grown in cubic domains with sides of length 20 m. The boundary condition is applied to the top $(+Z)$ boundary as a Neumann stress condition with magnitude $8 \times 10^7$ Pa. The domain has a Young's modulus of 20 GPa, Poisson's ratio of 0.213, $K_{IC}$ of $10^6$ Pa m$^{1/2}$. These conditions are selected such that all the fracture tips are activated by the relatively high stress. The Young's modulus and Poission's ratio are selected to be in the same range as those of rocks [*e.g.*, Wei et al., 2016].

Interaction maps shown in Section 3.5 include this separation for the case of two fractures, providing a prediction to how the array will behave during growth. The amplification to shielding ratio $\epsilon_I = -0.5$ shows that the fractures are located in one another's shadow, with most of the tips experiencing a reduction in stress, and some outside of the stress shadow experiencing increased stress in mode I. The circumferential SIF perturbation $C_I = 0.09$ indicates the fractures cause a significant change in the stress state at one another's tip, compared to cases where interaction is negligible ($C_I = 0.005$). The difference in the case simulated in this section is that five fractures are used rather than two. Therefore, fractures in the middle of the array would experience a more significant stress shadow, and only the fractures at the end would have tips outside other fracture's stress shadows. A detailed analysis of how growth patterns change depending on fracture separation, in the context of fracture interaction measures and maps, is a promising avenue for further research.

Figure 4.10A shows the fracture array after 34 steps of growth. The array is visualised by showing the tip loop at every other step, in order to improve visual clarity and show the initial array configuration with the inner five loops. Growth of the array is significantly affected by interaction, with very little extension occurring where the fractures were overlapped. Most growth occurs on the top and bottom fractures of the array, which grow out along the $x$ direction where the tips are unaffected by the other fracture's shadow zones. All fractures grow in the $y$ direction where there is more space for part of the tip to grow outside of the other fracture's shadows. This makes the central three fractures highly elongated. The array is shown just before the top and bottom fractures intersect the domain boundaries, at which point the fractures have not intersected. Where the fractures are closest, they begin to curve towards one another at

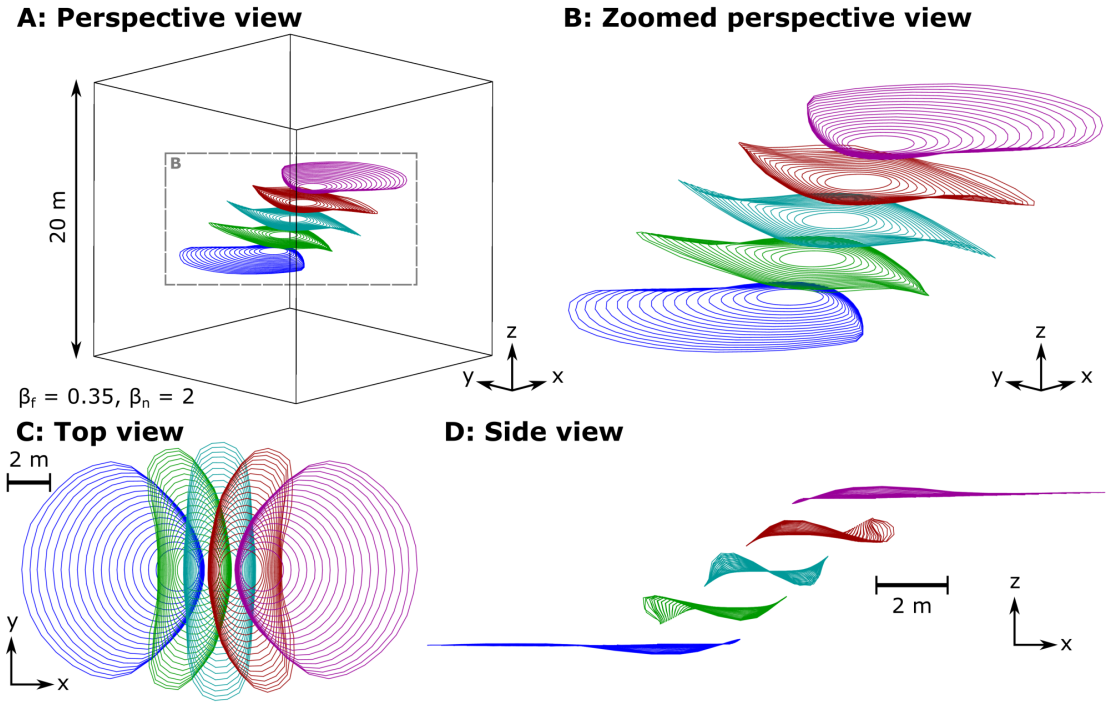



FIGURE 4.10: A fracture array after 34 growth steps under tension. Four perspectives are used to show the array (A: isometric perspective including volume boundaries, B: zoomed isometric perspective, C: top view, and D: side view). The smallest circles show the initial flaws, and each loop surrounding these flaws is the tip of the fracture at every other step. This simulation uses $\beta_f = 0.35$ and $\beta_n = 2$.

different places along their tips. The three inner fractures acquire significant curvature along the $y$ axis, both curving towards and away from one another. The intermediate value of $\beta_n$ means the local variation in $\mathcal{G}_n$ has a relatively large control on the growth at each tip.

### 4.5.1 Fracture growth exponent effects on arrays

The relationship between the fracture growth exponent and interaction patterns has been noted by other authors [*e.g.*, Lei et al., 2017a, Olson, 1993, Renshaw and Pollard, 1994]. Figure 4.11 demonstrates the effect of the exponents in the modified two step Paris-type law introduced in Section 4.2 on growth. The same initial array of fractures in grown in Figure 4.10 is used again, with $\beta_f$ and $\beta_n$ values of 0 and 5 respectively. Setting either $\beta_f$ and $\beta_n$ to 0 means the associated step in the modified two step Paris-type growth law does not affect the growth extent. An exponent of 5 in a power law creates a steep curve, where only fractures or tips with the highest values of $\mathcal{G}_n$ will propagate, as shown by Thomas et al. [2018b].

In Figures 4.10A and B, $\beta_f = 5$ and $\beta_n = 0$, in which case the highest value of $\mathcal{G}_n$ on each fracture determines its extension length, and the local variation in the value

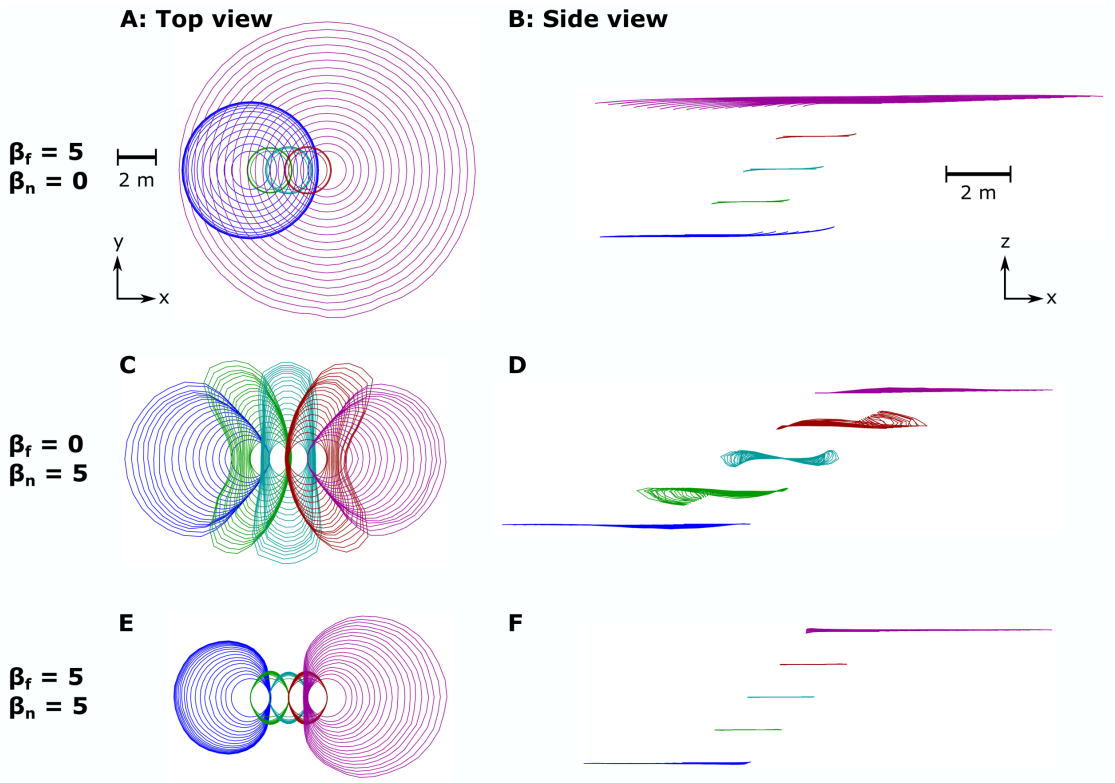



FIGURE 4.11: Three fracture arrays, grown from the same initial flaws in tension with different values of $\beta_f$ and $\beta_n$, viewed from the top and side. Every other step is shown by showing the curve of the fracture tip, up to the 34$^{\text{th}}$ step. A and B use $\beta_f = 5$ and $\beta_n = 0$, A and B use $\beta_f$ =0 and $\beta_n = 5$ and E and F use $\beta_f = 5$ and $\beta_n = 5$. A value of 0 means the associated step in the modified two step Paris-type growth law (Section 4.2) does not affect the growth extent.

of $\mathcal{G}_n$ on each tip does not change the extension length ($\Delta a_f = \Delta a_n$). Therefore, the extension in each step is a fixed value on each fracture. This produces a significantly different growth pattern to Figure 4.10, with much less activation of the inner fractures. The top fracture (purple) grows at the maximum extension length value throughout the 34 growth steps, eventually overlapping the other fractures. This fracture acquires a slightly higher value of $\mathcal{G}_n$ compared to the others, because it does not overlap with as many other fractures initially, and because the boundary condition (extension on the top boundary) results in slightly higher values of displacement closer to the top of the domain (see Section 2.6). The other fractures stop growing when this larger fracture begins to overlap them. This extinction of growth is particularly clear on the bottom (blue) fracture, which initially has similar growth to the top fracture, but after 16 steps (when the top fracture begins to overlap it), grows with a smaller extension length per step and eventually stops. Very little curvature develops, except in the bottom and top fractures which curve vertically at one side.

In Figure 4.10C and D the values are changed to $\beta_f = 0$ and $\beta_n = 5$, making only the second step of the Paris-type law affect growth. This results in growth occurring more

evenly across the five fractures, with their surface areas being similar in the final step. As in the first example of array growth (Figure 4.10), the perspective from the top of the fracture set shows that the local variation in the extension of each fracture tip means the fractures can grow into the space where they do not overlap. More vertical curvature arises than in the $\beta_f = 5$, $\beta_n = 0$ case, but less than in Figure 4.10.

The last case (Figure 4.10C and D) considers $\beta_f = \beta_n = 5$, in which case both steps of the modified Paris-type law have a significant effect on growth, and extension is strongly concentrated on fractures and fracture tips with the highest $\mathcal{G}_n$. The results show an array with much less growth, in terms of total additional surface area added per step, for the same number of growth steps as the other cases. Furthermore, the strong preference for growth to only occur where $\mathcal{G}_n$ is very close to $\mathcal{G}_v$ leads to very little growth on the middle fractures, even when these fractures do not overlap as much as the other cases. Most of the growth happens on the top fracture, as in Figure 4.10A and B.

Figure 4.10 shows that the effect of the growth rate exponent on growth during interaction is significant. The key interaction effects in the growth of these arrays are the shadow zone effects, reducing the extent of each fracture's growth, and the curving of fractures towards or away from one another. Higher values of the exponent tend to increase the shadow zone effect, and decrease the curvature which arises. Higher values of the growth exponent (*e.g.,* 30 and 60 [Ko and Kemeny, 2013]) would therefore concentrate growth significantly towards the most critically stressed fractures and fracture tips.

### 4.5.2 Outcrop visualisation of arrays

The three-dimensional non-planar fracture surfaces shown in Figures 4.10 and 4.11 cannot be readily compared to fractures in outcrops and experiments. Figure 4.12 shows the process and results of visualising the array from Figure 4.10, using a set of four planes which cut through the array. The intersection between the plane and each fracture is shown as a curve, coloured corresponding to the fracture. The traces from each plane are viewed perpendicular to that plane to simulate how the array would be seen in an outcrop. This method of visualizing the array on a two-dimensional plane as a set of curves shows the array strongly resembles the results of two-dimensional numerical simulations [Paluszny and Matthäi, 2009] as well as outcrops (*e.g.,* Figure 4.1, Figure 4.2, Pollard et al. [1982], and Lamarche et al. [2017]).

The four resulting sets of fracture curves have slight differences. Figures 4.12C and E are the most similar to one another, showing how the fractures begin to grow towards one another at their tips. The most curvature is observed on the middle fractures. The

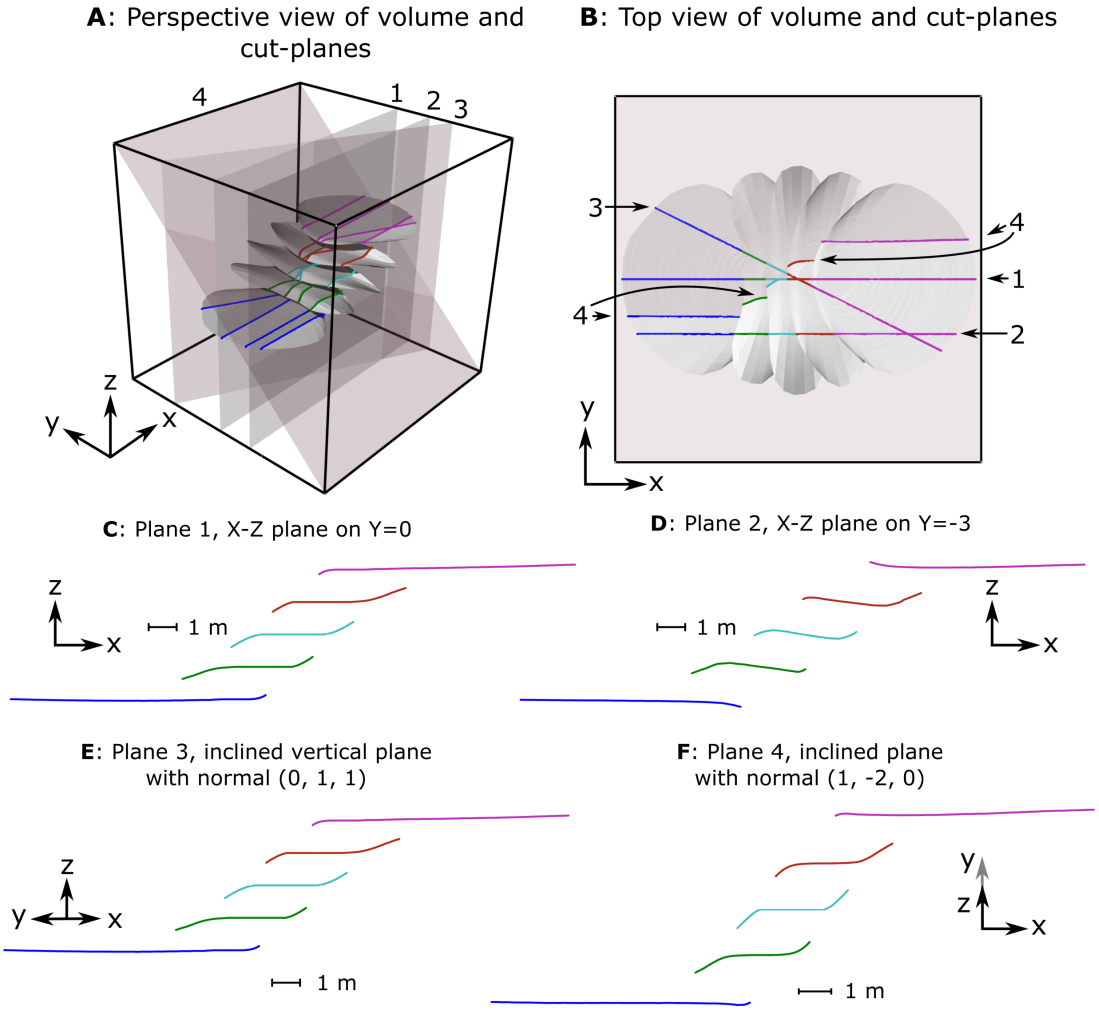



FIGURE 4.12: Cut-plane visualisations of a three-dimensional fracture array, also shown in Figure 4.10, demonstrating the variety of possible ways a fracture array could outcrop. A and B show perspective and top-down views of the volume, including both the visualisation planes as transparent surfaces, and the fractures as opaque surfaces. The trace of each fracture is also included and coloured using the colour scheme from Figure 4.10. C, D, E and F show the traces from each of the intersection planes. Cut-plane traces are shown from a perspective perpendicular to the plane, *i.e.*, as they would appear in outcrop without perspective distortion.

apparent curvature of the fractures is different in D, whose plane is offset from the central line where the initial flaws were placed. Therefore, the middle three fractures appear to be more curved. Additionally, the top and bottom fractures now curve away from the middle fractures. The plane which creates Figure 4.12F is inclined, causing the apparent separation between the fractures to be more significant. These small differences could lead to different interpretations of fracture behaviour in outcrops or experiments, despite all the cut-planes originating from the same three-dimensional array.

### 4.5.3 Non-uniform arrays

Figure 4.13 uses the same combinations of values of $\beta_n$ and $\beta_f$ tested in Figures 4.10 and 4.11 on a different initial array. This array has the same vertical separation, but the initial flaws are arranged in an arc around the centre of the domain. The fracture colours and their respective centres are blue (-2, 0, -2), green (-1.414, 1.414, -1), teal (0, 2, 0), red (1.414, 1.414, 1), and pink (2, 0, 2). This leads to different fracture patterns, where each fracture has some overlap with the others, but has most of its side in a non-overlapped state. Several features of the patterns shown previously emerge when the same $\beta_f$ and $\beta_n$ values are used, including more curvature at low $\beta_f$ and $\beta_n$ (Figure 4.13A), and less overall growth when both values are high (Figure 4.13D). The largest fracture at step 34 varies in each case: in Figure 4.13A, the upper and lower fractures finish at an equal size because they have the least overlap, and therefore have more space to grow without being shielded by others.

When $\beta_n = 0$ (Figure 4.13B), each fracture's tips grow at the same length in each step, as in Figures 4.10A and B. Previously, the top fracture in the array grew the most, due to the slightly higher values of displacement at the top of the fracture set. Here, the middle fracture becomes the dominant fracture, shielding the others after about 16 steps. In the first step, growth is similar on each fracture. From the second step onwards, the middle fracture has a slightly higher $\mathcal{G}_f$, and therefore acquires the highest extension length. Because the fracture remains the largest, it continues to acquire the largest SIFs in subsequent steps, maintaining its lead in fracture size and further suppressing growth on the other fractures. Therefore, the early steps of growth are demonstrated to be the most important for competitive fracture growth utilising a Paris-type propagation law.

Figure 4.14 shows cut-planes through the volume containing the fracture set in Figure 4.13A, using the same approach as in Figure 4.12. These cut-planes show the variety of curvature emerging. Plane 1 does not intersect the initial flaw surfaces of the middle three fractures, leading to slanted traces. This could be interpreted as a rotation of the material between the larger two fractures, as identified in relay ramps in outcrop [Cartwright et al., 1996]. Plane 4 (Figure 4.14F) does not intersect the green fracture, but its presence could be inferred due to the curvature on the blue and teal fractures.

## 4.6 Discussion

The present growth algorithm produces highly realistic growth in three dimensions, demonstrated by the comparisons to experimental cases in Section 4.3 and interaction

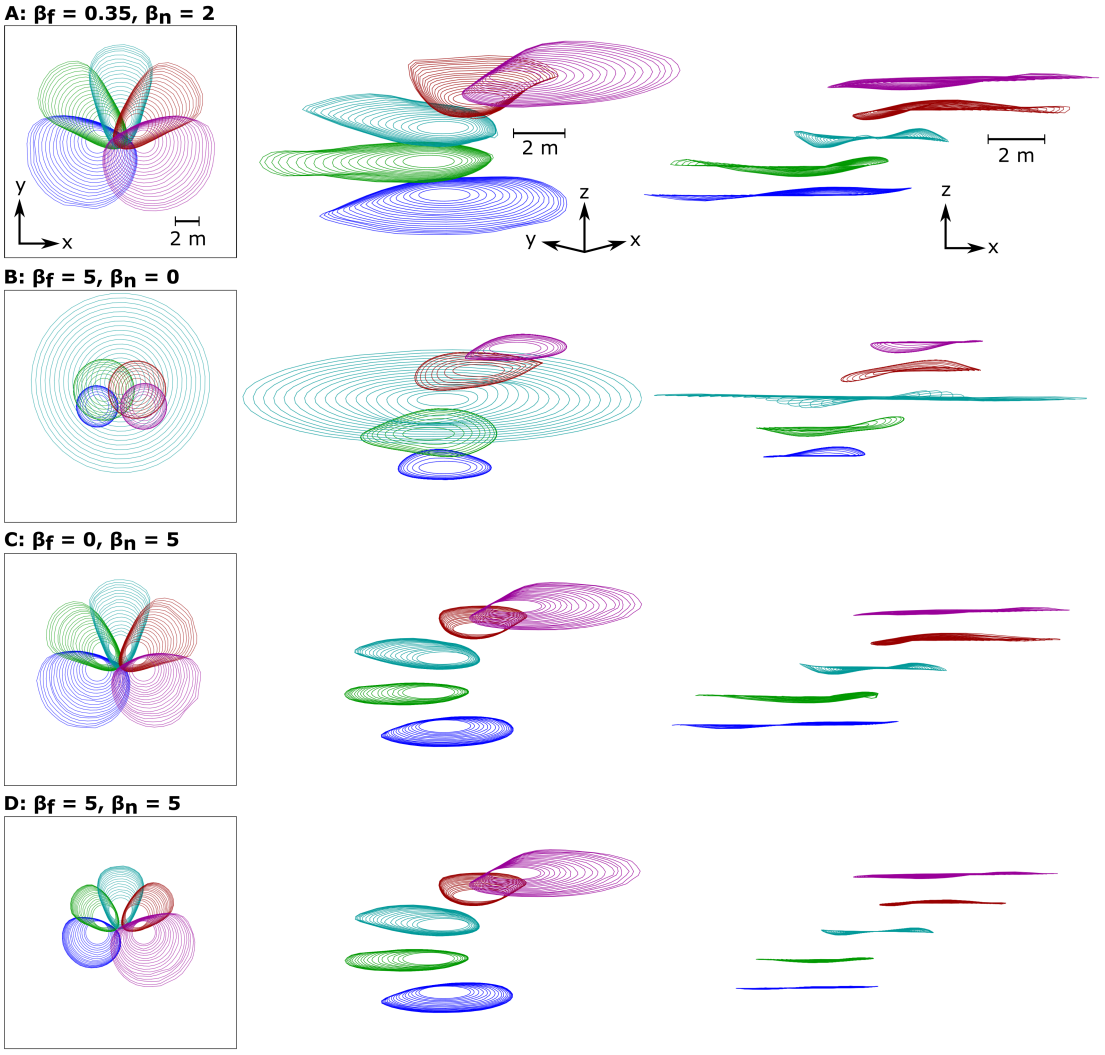



FIGURE 4.13: Four fracture arrays, grown in tension from the same initial flaw set, arranged in a spiral. Different values of $\beta_f$ and $\beta_n$ are used, matching Figures 4.10 and 4.11. Fractures are visualised with the tip loop from each even step of growth, up to the $34^{\text{th}}$ step. A uses $\beta_f = 0.35$ and $\beta_n = 2$, B uses $\beta_f = 5$ and $\beta_n = 0$, C uses $\beta_f = 0$ and $\beta_n = 5$, and D uses $\beta_f = 5$ and $\beta_n = 5$.

patterns in Section 4.5. The process of accurately reproducing specific growth experiments with calibrated material properties would be extremely challenging, due to the significant impact of sample heterogeneity. Fractures growing mutually in this work tend to activate together, whereas in a real experiment, only one fracture may activate amongst a set of interacting fractures [*e.g.*, Thomas and Pollard, 1993]. Fracture activation will depend on the values of the fracture growth exponents $\beta_f$ and $\beta_n$, therefore, if larger values are used than those given here, fewer fractures will activate in domains containing multiple fractures under a variety of stress conditions (*e.g.*, caused by their relative orientations to the direction of principal stress). Furthermore, a numerical approach allows the full geometry of a fracture to be seen, whereas imaging an experimental three-dimensional fracture in great detail is difficult, with experimental results presented

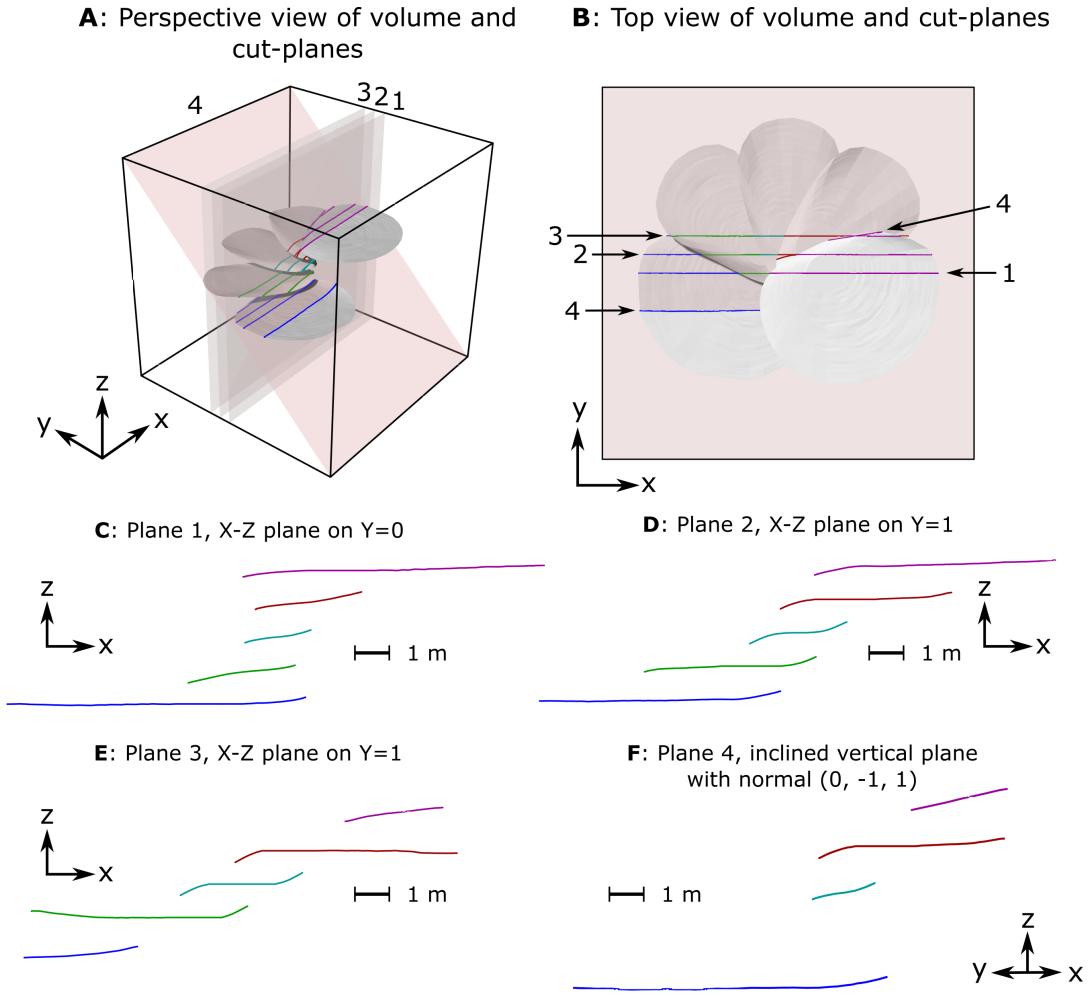



FIGURE 4.14: Cut-plane visualisations of a three-dimensional fracture array, initially grown from a spiral array, also shown in Figure 4.13A. A and B show perspective and top-down views of the volume, including both the visualisation planes as transparent surfaces, and the fractures as opaque surfaces. The trace of each fracture is also included and coloured using the colour scheme from Figure 4.10. C, D, E and F show the traces from each of the intersection planes. Cut-plane traces are shown from a perspective perpendicular to the plane, *i.e.*, as they would appear in outcrop without perspective distortion.

as the trace of a fracture at the edge of a specimen. Therefore, whilst validation of a complex process such as fracture growth is not straightforward, the body of results presented in this Chapter, along with the validation of the SIFs in Section 2.5, provides confidence in the realism of fractures grown in ICGT.

The implications of using a two step modified Paris-type law to govern mutual fracture growth have been examined in detail. The implementation of this approach is motivated by the need to ensure multiple fractures activate during the same growth step, as it is widely observed that, in the subsurface, fractures must have grown concurrently in order to create the patterns that are observed in outcrops (*e.g.*, Segall [1984], Lamarche et al. [2017], and Figure 4.1). Higher values of $\beta_n$ and $\beta_f$ generate fracture patterns where

growth is much more concentrated on fewer fractures (see Figures 4.11 and 4.13). In practice, if a single step Paris-type law was used in a complex domain, fractures would be unlikely to activate widely, and growth would be highly focused on relatively few critically stressed fracture tips. For a domain in tension, this bias towards the most energetic tips would become more significant when these fractures become larger, and would make generating densely fractured domains highly computationally expensive. By separately setting a maximum extension per fracture with the first step of the modified Paris-type law, fractures can grow mutually and competitively, experiencing interaction effects during growth, as is required to grow certain fracture geometries such as mutually hooked tips [Lamarche et al., 2017]. By approximating the growth into quasi-static steps, the produced patterns in fracture arrays are realistic, without incorporating a fully time-based scheme growth scheme. A fully time-based scheme would require significantly more computational recourses in order to resample stress and displacement in very small time increments.

Several features could be added to the growth in order to reproduce more features observed in rock fracturing. Fracture tip fragmentation as a result of $K_{III}$ is included in other numerical methods [*e.g.*, Cambonie and Lazarus, 2014, Leblond et al., 2015], and could improve the realism in fracture geometries where fracture tip twisting is significant. Fractures in the present method are always truncated upon intersection. Cross cutting criteria [*e.g.*, Cheng et al., 2014] could introduce X-intersections alongside present T-intersections in generated fracture networks, which could change flow patterns and connectivity of the network [Sanderson and Nixon, 2015].

A key detail of fracture interaction during growth is the manner in which two fractures curve towards or away from one another [Lamarche et al., 2017, Thomas and Pollard, 1993]. The examples shown in this chapter demonstrate that three-dimensional growth experiments are a promising method for investigating hooking. Different initial separations and radii of *en échelon* fractures will change hooking behaviour. In addition, change in the curvature of hooking fracture depending $\beta_f$ and $\beta_n$ is a key detail which must be constrained before considering fracture interaction in detail. Alternatively, varying the fracture growth exponents in hooking tests could be used to better estimate what the correct value must be in subsurface rocks. Furthermore, as shown in Figure 4.12, the pattern of hooking can vary along the full length of a three-dimensional fracture array.

## 4.7 Conclusion

Following on from the methodology described in Chapter 2, this chapter has demonstrated the growth of fractures in ICGT. The Paris-type criterion governing the extension

of mixed mode fractures is detailed. The fractures grown in this chapter demonstrate highly complex three-dimensional fracture geometries, matching the stress state in the initial steps (see Section 2.5) and after many steps of growth. The importance of the fracture growth rate exponents $\beta_n$ and $\beta_f$, introduced in a novel two step modified Paris-type law, is highlighted in several examples of growth. The impact of variations in fracture tip energy on the relative growth rate of different fracture tips in the domain is highlighted in both single and multiple fracture growth cases. The novel Paris-type law provides an effective scheme for growing fractures in a quasi-static manner, and for exploring how fracture advance and interaction changes over time in geological fracture networks.

# Chapter 5

# Permeability analysis of fractured media

## 5.1 Introduction

Quantification of the effective permeability of inhomogeneous media is a routine part of subsurface flow analysis [Neuman, 2005]. Permeability is frequently a key parameter in large scale models in which small features, such as individual fractures, are too small to be discretised. Reservoir models typically contain grid blocks on the order of several to a hundred metres, whereas rock heterogeneity varies significantly on the scale of centimetres [King, 1989]. The permeability of a smaller region of the full scale model can be calculated, including the effect of small scale heterogeneities, then used in the large scale model, in a process known as permeability upscaling [Bisdom et al., 2015, Renard and de Marsily, 1997]. Other physical properties and processes are upscaled for numerical simulation, including the influence of microfractures on macrofracture growth (see Section 2.2.4) and local damage [*e.g.*, Defoort et al., 2016]. Permeability is a key term in Darcy's law, the experimentally verified constitutive equation for macroscopic groundwater flow [Darcy, 1856]. Darcy's law significantly simplifies the complexity of macroscale flow in rocks, as it can be show to upscale the Navier-Stokes flow which occurs in microscale pores [Narsilio et al., 2009].

Renard and de Marsily [1997] formally define the differences between equivalent, effective, and block permeabilities. 'Equivalent' permeability, $\mathbf{k}_{eq}$, is a constant permeability tensor representing a heterogeneous system, applicable when both systems have the same boundary conditions. 'Effective' permeability, $\mathbf{k}_{ef}$, is used for a medium which is statistically homogeneous on a large scale. Effective permeability $\mathbf{k}_{ef}$ is different from $\mathbf{k}_{eq}$ because it has an intrinsic physical magnitude which is independent of macroscopic

boundary conditions. Effective permeability $\mathbf{k}_{ef}$ is a second order, symmetric, positive definite tensor with terms

$$\mathbf{k}_{ef} = \begin{bmatrix} k_{xx} & k_{xy} & k_{xz} \\ k_{yx} & k_{yy} & k_{yz} \\ k_{zx} & k_{zy} & k_{zz} \end{bmatrix} \tag{5.1}$$

where $x$, $y$ and $z$ are the Cartesian coordinate axes of the medium. Statistically homogeneous conditions are rarely satisfied in subsurface rock environments, therefore a further term, 'block' or 'upscaled' permeability, is the equivalent permeability of a finite block. In practice, block permeability is often used interchangeably with $\mathbf{k}_{ef}$, as the typical use of effective or equivalent permeability is to upscale local properties for large scale models.

Transmissivity is another term arising in the study of fractured media, which refers to the ability of fluid to flow across a fracture plane. It is commonly given as a two-dimensional tensor when flow within a fracture is anisotropic [*e.g.*, Lang et al., 2015, Zou et al., 2017]. In the present work, modelled fractures are often non-planar, meaning their hydraulic properties are not well represented in two-dimensions. Therefore, analysis is focused on the full three-dimensional block permeabilities of entire domains. The influence of fracture geometry and variable apertures on individual fracture transmissivity may be explored in future work.

### 5.1.1 Representative element volumes for fractured systems

A central concept for continuum modelling is the assumption that, for a given medium with a property that varies on a small scale, there exists a sample size exists above which the measured values of the property do not vary between samples, or change further if the size of the sample is increased. This sample size is known as a Representative Element Volume (REV) [Bear, 1989]. In numerical approaches, simulation of detailed pore-scale flow, which would require a complex Navier-Stokes based method, is avoided by assuming an REV and basing the material properties on measurements at or above this scale. Darcy's law subsequently provides a more straightforward expression to describe porous flow [Narsilio et al., 2009]. REVs are also relevant for a variety of materials and properties, and different material properties may have different REV sizes within the same material [Al-Raoush and Papadopoulos, 2010, Azizmohammadi and Matthäi, 2017].

Fractured rocks pose a challenge for the conventional REV concept, as an REV cannot be formally defined for a fracture network. Fracture systems which exhibit scaling behaviour (*i.e.*, power law distributions of fracture and fault length [Cowie, 1998]) do

not possess an homogenization scale [Berkowitz, 2002]. Fracture-related heterogeneities including apertures, spacing, and orientations occur at all length scales. Early examinations of REV scales in fracture networks include Long and Witherspoon [1985], showing that the observation scale significantly influenced the permeability of variably sized, two-dimensional DFNs. They quantified the extent to which a DFN behaves like a porous medium by comparing the anisotropic permeability tensor to a simple directional permeability. Networks with short fractures behaved less like a porous medium than those with longer fractures, with larger observation regions leading to somewhat closer resemblance. In two-dimensional random networks with uniform apertures, Baghbanan and Jing [2007] found that fracture network parameters such as length-aperture scaling also affect the REV scaling. Azizmohammadi and Matthäi [2017] simulated flow on mapped two-dimensional datasets with stress-induced apertures, observing that the REV for permeability anisotropy is larger than for permeability magnitude. However, permeability did not increase with REV size. Furthermore, the variation in the anisotropy of $\mathbf{k}_{ef}$ correlates poorly with the bulk density of fractures.

The permeabilities calculated in this work are equivalent or block permeabilities, following the definitions given by Renard and de Marsily [1997]. Therefore, it should be assumed that they are highly dependent on the scale at which they are calculated. The scale dependence of geomechanical networks is not explored in this work. In the example of a Uranium pellet (Section 5.3) the size and structure of the sample are exact. In the analysis of geomechanical networks in Chapter 6, the results may vary significantly with scale, which could be explored in future work.

### 5.1.2 Analytical methods for calculating effective permeability

A wide variety of methods are available for estimating effective permeability, many of which can be readily applied to complex datasets given their statistics, implemented in numerical methods, or applied analytically to an idealised system. A thorough early review is provided by Renard and de Marsily [1997], focused on upscaling structured grids containing heterogeneities. Since this review, representation of discrete fractures and computing capabilities have significantly improved, so this section focuses on techniques suited to unstructured domains.

Snow [1969] established the first analytical method for calculating the permeability tensor of a fractured rock, which has been used by many subsequent methods as a starting point for analysis. The method assumes the matrix is impermeable and that the fracture pattern is anisotropic with evenly spaced parallel fractures. Oda [1985] extended Snow's method to include a permeable matrix. Oda also introduced a crack tensor which

depends on the geometry of the fractures (apertures, lengths, and orientations). For a block containing several fractures with different orientations, a normal vector describing the ensemble's orientation is found by integrating all normals in the block. Oda's method remains a popular method in reservoir engineering [Decroux and Gosselin, 2013], and is implemented in commercial software such as Petrel, Eclipse, and FracMan [Ghahfarokhi, 2017].

Other semi-analytical methods for finding $\mathbf{k}_{ef}$ in fractured domains include percolation theory, effective medium techniques, and heuristic methods. Percolation theory assumes that, in domains containing either permeable or impermeable units or structures, flow is mostly controlled by the connectivity of permeable regions. Subsequently, a probability-based approach is used to determine whether or not permeable blocks or structures connect across the medium. Geological media departs significantly from assumptions made by percolation theory, including high aspect ratio structures (including bedding planes and fractures), and a variety of individual unit permeabilities rather than binary units which are either permeable or impermeable [Masihi et al., 2016].

Effective medium techniques are a general approach for predicting macroscopic conductivity of a heterogeneous medium, also used extensively to characterise electrical conductivity [Kirkpatrick, 1973]. They are based on the idea of replacing an inhomogeneous medium with an effective homogeneous medium with a permeability of $\mathbf{k}_{ef}$ [King, 1989, Saevik et al., 2014] *i.e.*, they provide a formal method for upscaling inhomogeneous properties. A key property of this new medium is that, if an additional inclusion of a different permeability is added to this homogeneous domain, the resulting mean pressure fluctuation is zero. Therefore, pressure fluctuations have been averaged out over a sufficiently large region. Effective medium theories can are applied to anisotropic fracture networks by separately handling each set of fractures (*e.g.*, sets with different orientations or apertures) as a different material phase. Saevik et al. [2014] examined the use of effective medium methods on three-dimensional DFNs containing fractures in orientated sets. Ebigbo et al. [2016] compared additional effective medium methods against numerically computed permeabilities on three-dimensional dense stochastic fracture networks with random orientations. Saevik et al. and Ebigbo et al. found that several of the techniques gave good predictions.

Heuristic methods use numerical results to find a relationship between fracture network properties and $\mathbf{k}_{ef}$. These equations are based on stochastic numerical simulations and theoretical arguments. A prominent example is that of Mourzenko et al. [2011], who established an equation for calculating $\mathbf{k}_{ef}$ in polydisperse, isotropic networks, where fractures are represented as disks in a permeable medium. The equation combines the matrix permeability, Snow's original permeability, and a term with parameters derived

from the fracture network, including known percolation thresholds, apertures, surface areas, and shape-specific fitting parameters. Ebigbo et al. [2016] found that this heuristic method is a good predictor of $\mathbf{k}_{ef}$ compared to numerically calculated values, matching the accuracy of effective medium methods.

### 5.1.3 Numerical methods for calculating porous flow and permeability

Numerical methods are now widely used to calculate effective permeabilities in complex domains. Berkowitz [2002], Šimůnek et al. [2003], and Neuman [2005] provide detailed reviews of the early work, with key methods and recent developments highlighted in this section. Effective permeability can be calculated by any method which solves for flow and pressure in a heterogeneous domain, therefore, a wide range of methods are considered here, not just those that are directly applied to calculating effective permeability. Methods that do not incorporate fractures in a discrete or inferred way are not highlighted, including commercial reservoir simulation suites such as Eclipse [Schlumberger Geoquest, 2009], which uses the finite-difference method to solve flow [Karimi-Fard and Firoozabadi, 2003]. Such tools should be noted, as they represent the industry standard for large scale flow analyses, and in which effective permeability values are routinely used to solve transport problems [Christie and Blunt, 2001]. Many flow simulation methods can simulate the flow of multiple thermodynamic phases, typically two or three, which is highly important to accurately predicting the behaviour of these phases in a reservoir (*e.g.*, water and oil [Kazemi et al., 1976]; $CO_2$ and water [March et al., 2018]; oil, water, and gas [Li and Lee, 2008]).

#### 5.1.3.1 Dual-porosity methods

Early approaches for solving flow in reservoirs include dual-porosity models [Warren and Root, 1963]. These models idealise a fractured rock as a lattice of fully connected fractures, using average properties such as fracture spacing and aperture to reproduce flow in real rocks [Šimůnek et al., 2003]. This periodic arrangement of fractures separates them from other models. Dual-porosity models have subsequently been refined in many ways, particularly by improving the accuracy of the interaction functions which link the flow and mass transfer between fracture and matrix blocks [Kazemi et al., 1976, Zimmerman et al., 1993], incorporating gradations in pore scales, with separate regions and interaction terms linking progressively smaller pores [Gwo et al., 1995], and variable block sizes [Abbasi et al., 2018].

The simplified geometries used in dual-porosity models have made them unsuited to examining properties such as connectivity, anisotropy, and mechanics on fracture permeability. Furthermore, the models rely on a significant number of parameters which require significant calibration, many of which cannot be easily found in real outcrops, including consistency in fracture spacing [Šimůnek et al., 2003]. Therefore, their usage is uncommon in DFN studies, but they remain popular for porous media simulation, particularly when transfer and storage between different regions of the medium is of great interest, for large (*e.g.*, reservoir or repository) scales, and when fractures do not require discrete representation. Recent applications include micro- and nano-pore systems in shale reservoirs [Yan et al., 2016], $CO_2$ storage [March et al., 2018], and radionuclide transport [Bianchi et al., 2015].

#### 5.1.3.2 Discrete fracture network approaches to porous flow and permeability

Two primary approaches to incorporating discrete fractures in flow simulations are discussed in the literature. The first of these, embedded discrete fracture models (EDFMs), incorporate discrete fractures in a hierarchal manner. Medium and large fracture planes are inserted into a Cartesian grid. The influence of fractures smaller than those which are discretely represented is included by upscaling their effect and using an effective permeability for the matrix. Elements cut by discrete fractures are split to create unstructured segments [Shakiba et al., 2018]. In three dimensions, the connectivity of grid blocks to fractures is handled using two-dimensional arrays. The flow problem can be solved with a variety of approaches, including the finite volume method [Li and Lee, 2008]. Ren et al. [2016] incorporate the extended finite element method (XFEM) alongside the EDFM method to handle more complex geomechanical conditions.

Discrete fracture-matrix (DFM) models are a broader category, distinguished by a discrete representation of all fractures in the domain. A variety of different numerical methods can be employed to find the flow field when a domain including fractures is meshed. These include finite element [Ebigbo et al., 2016, Lang et al., 2014], mixed-hybrid finite element [Maillot et al., 2016a], finite volume [Keilegavlen et al., 2017, Stefansson et al., 2017, Ucar et al., 2018], and finite difference [Karimi-Fard et al., 2004] methods. DFM approaches require sophisticated meshing strategies which are frequently automated to simulate many different realizations of stochastic volumes. Furthermore, these numerical methods may need to be modified to investigate detailed processes along fractures (*e.g.*, coupled processes or leak-off) [Salimzadeh et al., 2017b, Stefansson et al., 2017]. All methods that rely on discretisation will be subject to errors which depend on mesh density and refinement, particularly at fracture intersections. For complex fracture

networks generated using the present method, the influence of this effect is analysed in Section 6.4.4. Due to the complexity of dense fracture networks, some research into fractured rock permeability avoids explicit simulation of flow. For example, Thovert et al. [2017] investigate the percolation threshold on stochastic fracture networks, and how percolation correlates with fracture density, depending on the shapes of the fractures. A thorough review of DFN analyses can be found in Chapter 6.

Following an evaluation of effective medium methods on stochastically generated fracture networks, Ebigbo et al. [2016] characterised the flow properties of the investigated networks using two parameters: the fracture aspect ratio (fracture aperture divided by fracture length) and the fracture-matrix permeability ratio. The ratio of these two parameters was very effective at characterising the flow properties of the stochastic domains. When the fracture aspect ratio was higher than the fracture-matrix permeability ratio, a distinct percolation threshold occurs, and the vast majority of flow occurs in the fractures. When the fracture-matrix permeability ratio is higher than the fracture aspect ratio, the matrix is sufficiently conductive such that the percolation threshold is not significant, and flow takes place in both the fractures and the matrix. Importantly, these two statistics are independent of the fracture intensity, and therefore quantify how the network will behave over a range of possible fracture intensities.

### 5.1.4 Chapter summary

This chapter introduces the methodology used to simulate single phase fluid flow over domains made up of multiple fractures and a rock matrix. This method, first proposed and validated by Lang et al. [2014], is used to find the effective permeability tensor. The method is re-validated in Section 5.2.4 as part of the fracture growth workflow. An application of the flow method to spent Uranium Dioxide fuel is given in Section 5.3, demonstrating the method's use on static fractures in non-cubic domains. This study quantifies the impact of fractures on the fuel's permeability created during irradiation, with the goal of quantifying the properties of spent fuel prior to final storage. The effective permeability calculation method is also used extensively in Chapter 6 to quantitatively explore the hydraulic properties of geomechanical DFNs.

## 5.2 Flow methodology

The key goal of this work is to simulate flow in geomechanical fracture networks, in particular, flow in networks relevant to radioactive waste disposal, such as low permeability igneous or metamorphic rocks [Radioactive Waste Management, 2016a]. The

method of Lang et al. [2014] is well suited to this application for several reasons. It uses a simple basis for flow, as only a straightforward Laplace-type equation is solved for flow, requiring no special treatment between (fracture surface elements) and volumetric (rock matrix) elements, which are frequently required in other models [*e.g.*, Berrone et al., 2017, Liu et al., 2018]. This makes the method computationally cheap, which is particularly important given that three flow experiments must be performed to find the effective permeability. After minor changes to the fracture surfaces, the method can re-use the mesh created for mechanical deformation.

Finite difference methods are not suited to unstructured meshes, and the finite volume method would add a stenciling step to the meshing to create explicit volumes for flow. Flow around a GDF (Geological Disposal Facility) is described as being single phase, where only one fluid phase (*i.e.*, liquid water) is present. In low matrix permeability rocks, poroelastic, leak-off, and thermal effects are unlikely to change the effective permeability of a fracture network significantly. Nevertheless, these effects can be incorporated within ICGT using the fully monolithically coupled poroelasticity method developed separately from the present flow method [Salimzadeh et al., 2018, 2017b].

### 5.2.1 Element-wise permeability

The cubic law describes fluid flow through an idealized open fracture between two parallel smooth plates, and is derived from the Navier-Stokes equations. Witherspoon et al. [1980] demonstrated that the relationship is valid for rock fractures. When the plates are separated by a distance or aperture $h$, the horizontal volumetric flux $Q$ is

$$Q = \frac{-\left|\overline{\nabla p}\right| w h^3}{12\eta} \tag{5.2}$$

where $\left|\overline{\nabla p}\right|$ is the magnitude of the permeability gradient, $w$ is the fracture width, normal to the flow direction [Zimmerman and Bodvarsson, 1996], and $\eta$ is the fluid viscosity. Using Darcy's law to relate this flux to an average velocity shows the fracture permeability is

$$k_f = h^2/12. \tag{5.3}$$

This allows definition of the transmissivity, $T$, of the fracture as the product of permeability and area $A$:

$$T \equiv k_f A = \frac{w h^3}{12} \tag{5.4}$$

Zimmerman and Bodvarsson [1996] took the study of the cubic law further by accounting for deviations arising from some of its assumptions. Real fractures have rough walls and

apertures that vary such that, at some points, the walls may be in contact. A simple modification is to replace $h$ with some form of average aperture, $\langle h \rangle$.

Equation 5.4 is derived assuming laminar flow for low Reynolds numbers. In subsurface conditions, flow in fractures is generally laminar, but exceptions may occur when fluid flow rates are high, or when flow paths are tortuous [Zimmerman and Bodvarsson, 1996]. In the case of deep flows on long timescales, *i.e.*, those particularly relevant for radioactive waste disposal, flow rates are small and aperture variations can be assumed to be gradual, enabling use of a simplified form of the Reynolds 'lubrication' approximation. This is confirmed by flow imaging experiments in rough walled fractures, where the Reynolds number is sufficiently low for laminar flow (less than 0.1) [Lee et al., 2014].

In the present method, Equation 5.3 is used to assign local permeabilities to the elements discretising each fracture's surface. Apertures are defined at fracture nodes, because nodes are a discrete point where a single aperture (*i.e.*, the distance from one fracture node to the equivalent node pair on the other surface) can be defined. Therefore, when calculating permeabilities using Equation 5.3, the average of each of the element's node apertures is used. Fracture apertures can be either a uniform, fixed value, or can inherit the aperture resulting from a displacement field calculated during the mechanical deformation step. The way deformation is modelled is detailed in Section 2.2.1, and the method by which apertures are extracted from the deformation field is described and applied in Chapter 6. In this chapter, fracture apertures are set to a uniform value to validate the method and simulate flow in spent fuel pins. Volumetric elements in the rock matrix are assigned a homogeneous matrix permeability $k_m$.

### 5.2.2 Governing equations for flow

The method solves for Darcy flow within matrix and fractures using the finite element method. To calculate the equivalent permeability of a volume containing discrete fractures, three separate single phase flow problems are solved in the domain, using the finite element method [Lang, 2016]. Each problem simulates flow from one boundary of the domain to the opposite boundary. The boundary conditions of each of the three flow experiments set opposite boundaries as the source and sink. At the source boundary the fluid pressure is set to 100 Pa, and at the sink the fluid pressure is set to 10 Pa. These are Dirichlet boundary conditions which will result in flow going from the source boundary to the sink. The remaining four boundaries allow no flow through them, which is handled by setting the permeability on boundary surface elements to zero.

The Laplace problem models the flow of an incompressible, irrotational, single-phase flow.

$$\nabla \cdot (k^e \nabla p) = 0 \tag{5.5}$$

where $\nabla p$ is the pressure gradient, and $k^e$ is the element permeability. For each flow experiment, element-volume weighted averages of the pressure gradients ($\left\langle \frac{\partial p_f}{\partial x_i} \right\rangle$) and fluxes ($\langle U_i \rangle$) are computed over a sub-domain [Durlofsky, 2005]:

$$\left\langle \frac{\partial p_f}{\partial x_i} \right\rangle = \frac{1}{V_\Omega} \sum_e \int_{V_e} \frac{\partial p_f^e}{\partial x_i} \mathrm{d}V_e \tag{5.6}$$

$$\langle U_i \rangle = \frac{1}{V_\Omega} \sum_e \int_{V_e} U_i^e \mathrm{d}V_e \tag{5.7}$$

where $V_\Omega$ is the volume of the domain, $e$ is a finite element, $V_e$ is the volume of element $e$, $i$ is one of the three coordinate axes ($x$, $y$, or $z$). Surface elements on fractures have zero volume, so a local thickness is assigned from the aperture of each fracture's element. Thus, for each of the three flow experiments, three flux averages and three pressure gradient averages are computed, one for each coordinate axis. These eighteen values are brought forward to compute the anisotropic permeability tensor for the full volume.

The quantities in Equation 5.5 are related to permeability by Darcy's law for porous media,

$$\mathbf{U} = -\frac{1}{\eta} \mathbf{k} \nabla p \tag{5.8}$$

where $\mathbf{k}$ is the permeability tensor, with eigenvalues $k_1$, $k_2$, and $k_3$, and $\eta$ is the viscosity ($1 \times 10^{-3}$ Pa·s throughout this work) [Durlofsky, 2005]. Equation 5.8 provides a linear equation of the form $\mathbf{Ax} = \mathbf{b}$, where $\mathbf{A}$ is a matrix of the average pressure gradients, $\mathbf{x}$ is the effective permeability tensor $\mathbf{k}_{ef}$ (in vertical form as a $1 \times 9$ vector), and $\mathbf{b}$ is a vector of the average flow velocities. The terms in the matrices $\mathbf{A}$ and $\mathbf{b}$ are provided in full by Lang et al. [2014] and contain the eighteen values computed from Equations 5.7 and 5.6. The terms in $\mathbf{A}$ are divided by the fluid viscosity, and then the over-constrained linear equation is solved for $\mathbf{x}$ using LU decomposition, thus providing the permeability tensor of the fractured domain.

### 5.2.3 Finite element domain configuration

During the mechanics portion of the model workflow (computation of stress, displacement, and SIFs; see Chapter 2) the mesh is 'split' along the fractures, with fractures consisting of two co-incident sets of 2D triangular elements, without edges connecting the two sides (see Figure 2.3). For flow, the lack of cross-fracture connections would

cause flow to behave unrealistically on fracture elements, without intervention via another method. Therefore, to ensure fractures respond to flow correctly, the mesh is modified and fractures are 'un-split' before flow is computed. The two meshes will be identical, except that the mesh for flow creates one set of surface elements per fracture rather than two. Figure 5.1 shows two-dimensional schematics which compare an example mesh generated for mechanical deformation (A) to a mesh generated for flow (B). In A, the separation between each side of the fracture is exaggerated to demonstrate how surface elements are connected on fractures during mechanical deformation.

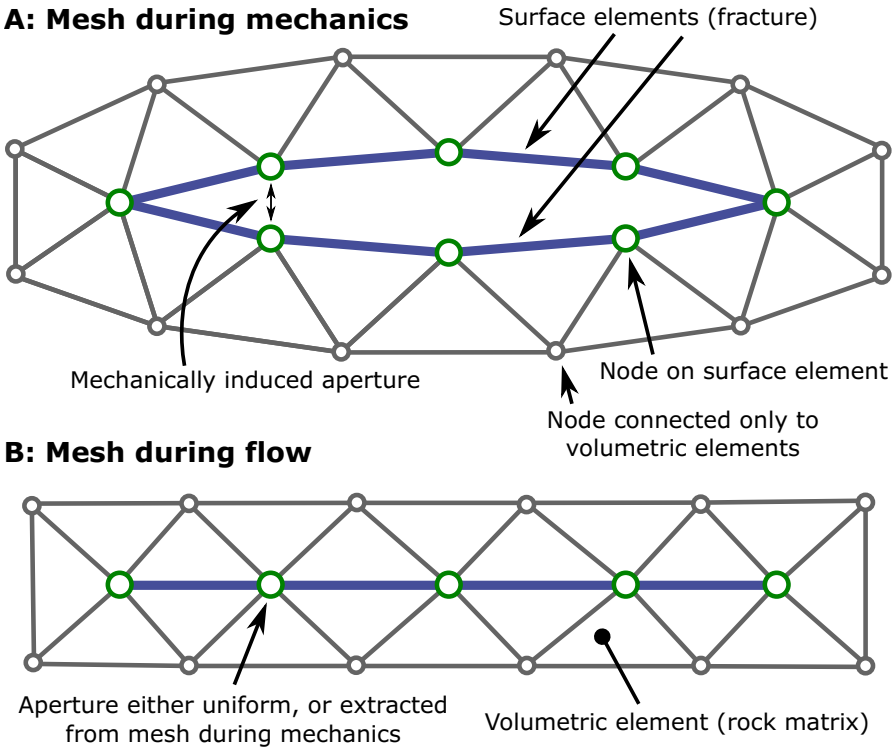



FIGURE 5.1: Schematic comparing meshes on fractures generated for mechanical deformation (A) and flow simulation (B). The mesh during mechanics gives each fracture two sides which begin the simulation overlapped (coincident). Mechanical deformation results in a separation between the two sets of fracture surface elements. This separation is exaggerated in the image to show how the surface elements are connected during deformation. For flow simulations, fractures are instead meshed as one single surface. Elements are shown in two-dimensions for clarity, whereas all simulations in this work are performed in three-dimensions. Elements shown are quadratic, with mid-side nodes are excluded for clarity.

In order to avoid boundary effects, averages for Equations 5.7 and 5.6 are computed only on elements with centres located within the central 90% of the domain. An exception is the validation in Figure 5.2, where the whole domain is sampled in order to match the volume size terms in the analytical equation. This approach has been referred to as undersampling [Lang et al., 2014], and produces results which better reflect the overall connectivity of the domain [Lang et al., 2018].

### 5.2.4 Validation

The analytical method of Snow [1969] is used to validate the effective permeability calculation in ICGT. A standard "sugar cube" model is constructed from periodic, planar fractures with equal spacing (*e.g.*, Figure 5.2). In a cubic sugar cube domain containing $n_f$ fractures, the volume occupied by fractures is $n_f a_f$, where $a_f$ is the fracture aperture. In turn, the volume occupied by rock is $h_{cube} - n_f a_f$, where $h_{cube}$ is the length of the side of the domain. The contribution of the fractures and the matrix in the domain to flow can be found by multiplying these regions by their permeability ($k_f$ and $k_m$, respectively). Then, the average permeability can be found by dividing this value by $h_{cube}$. Thus, the effective permeability of an anisotropic sugar cube in the direction as a set of periodic fractures is

$$k_{\mathrm{w}} = \frac{\left(h_{\mathrm{cube}} - n_f a_f\right) k_m + n_f a_f k_f}{h_{\mathrm{cube}}} \tag{5.9}$$

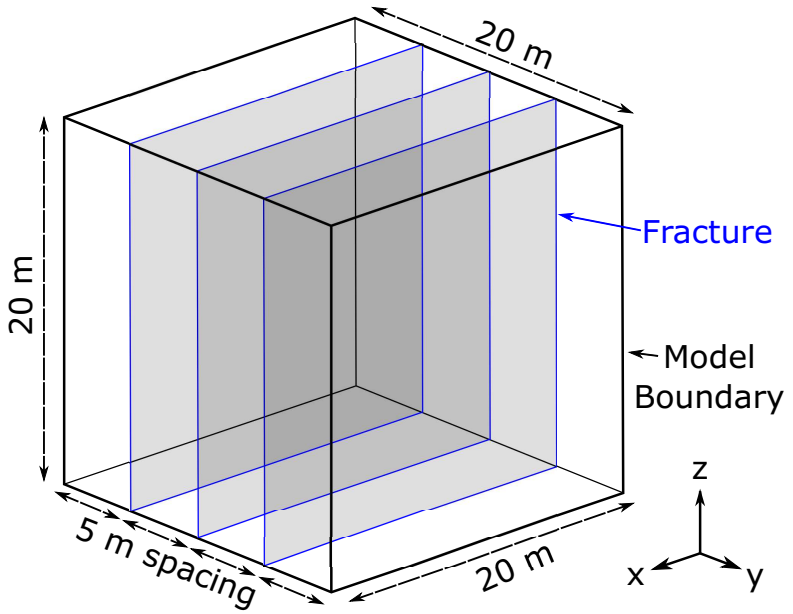
where $h_{\mathrm{cube}}$ is the length of one side of the cube, $n_f$ is the number of fractures, and $a_f$ is the aperture of the fractures (a uniform value across their whole surface) [Lang et al., 2014, Snow, 1969]. The permeability normal to these fractures ($k_{\mathrm{h}}$) is equal to the matrix permeability. Figure 5.2 shows the geometry of an anisotropic sugar cube with $n_f = 3$, $k_m = 1 \times 10^{-15}$, $a_f = 0.0001$. The percentage error is negligible in the $k_{\mathrm{h}}$ direction, and very low in the $k_{\mathrm{w}}$ direction.

## 5.3 Flow in a static fracture network: spent $UO_2$ fuel study

This section describes an example application of ICGT's effective permeability solver to an observed fracture network in spent Uranium dioxide ($UO_2$) fuel. The full study (Thomas et al. [2018a]) includes additional contextual details on the structure and use of the fuel.

### 5.3.1 Spent $UO_2$ fuel background

The UK's Advanced Gas-cooled Reactors (AGRs) are graphite moderated, $CO_2$ cooled reactors operating at pressures of about 4 MPa and gas temperatures in the range 300-675°C [Cordall et al., 1992]. In an AGR reactor, eight fuel elements are stacked vertically in a stringer; each element contains 36 fuel pins, arranged in three concentric circles, shown in Figure 5.3. Elements are numbered 1 to 8, beginning at the bottom of the stringer and working upwards. The operating conditions experienced by fuel pins in different elements varies considerably, with average fuel cladding temperatures ranging




| | Numerical ($m^2$) | Analytical ($m^2$) | Error (%) |
|---|---|---|---|
| $k_w$ | 1.34998e-14 | 1.3500e-14 | 0.0014 |
| $k_h$ | 1e-15 | 1e-15 | 0 |

FIGURE 5.2: Periodic fracture model used to validate the $\mathbf{k}_{ef}$ computation method. $k_w$ is the permeability in the $x$ and $z$ direction, and $k_h$ is the permeability in the $y$ direction. The geometry was simulated using $a_f = 0.0001$ and $k_m = 1 \times 10^{-15}$. Permeability $k_w$ is calculated using Equations 5.9, and $k_h = k_m$.

between around 350°C in element 1 fuel pins to a maximum of 800-850°C in element 7. Fuel pins contain approximately sixty-four $UO_2$ fuel pellets stacked vertically inside a ribbed austenitic stainless steel cladding, as illustrated in Figure 5.3B [Barrable et al., 1997]. Ribs are machined onto the outer cladding surface to improve heat transfer [Hewitt and Collier, 2000]. In service and during subsequent storage and transport, the cladding provides the primary containment for radioactivity generated within the fuel during irradiation.

During irradiation, the ceramic $UO_2$ fuel pellets experience high thermal gradients, initially causing densification, then swelling due to the production of fission products. Degassing also occurs, altering the porosity of the $UO_2$. These processes lead to the formation of fractures in the fuel [Morgan et al., 2012]. In fuel elements that experience higher operating temperatures, the fuel and cladding form a bond, which leads to additional fracture formation as the fuel cools after discharge from the reactor [Morgan et al., 2015].

After discharge from the reactor, individual fuel elements are separated from each other and stored in cooling ponds prior to shipment to Sellafield, UK for interim wet storage. If the fuel cladding suffers corrosion, or any damage that penetrates through the entirety

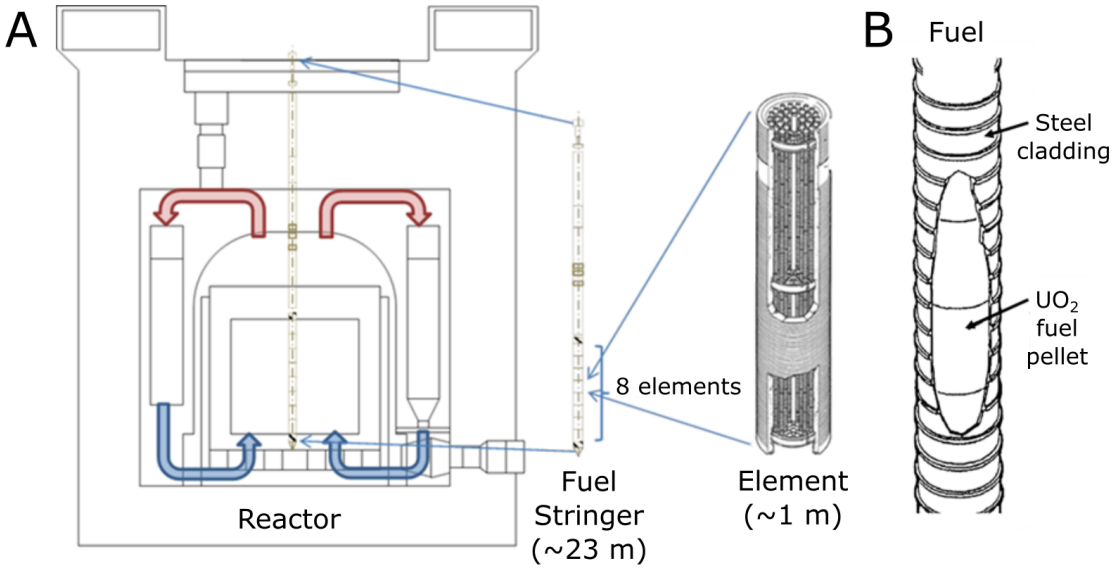



FIGURE 5.3: Schematic of the $UO_2$ fuel pellet and cladding in the context of AGR reactors. A: AGR fuel element, in the context of the reactor. B: AGR fuel pin. After Barrable et al. [1997].

of the cladding, pond water can enter the fuel pin and migrate into the fuel matrix. This may lead to corrosion of the fuel and release of radioactivity into the pond water. In the event that fuel is to enter a period of dry storage, or be consigned for geological disposal, it is important that water from inside failed fuel pins is removed to prevent corrosion or pressurisation of the dry storage/disposal container [Anwyl et al., 2016]. Therefore, it is essential that the permeability of the fuel matrix is understood, as this will affect both saturation and drying of the fuel. Of these, the drying behaviour is particularly important given the potentially long time periods over which outgassing of water vapour can continue [Kholi et al., 1985].

### 5.3.2 Fuel assembly and structure

AGR fuel pins consist of a ribbed stainless steel cladding tube that provides the primary containment for the fuel and the fission and activation products generated during irradiation. The ends of the fuel tube are enclosed by end caps that are seam-welded to provide a continuous and robust containment boundary and are separated from the fuel by insulating aluminium oxide pellets that reduce the operating temperature of the end caps in service. The overall length of a fuel pin is approximately 1 m.

AGR fuel pellets are fabricated from sintered $UO_2$ with a theoretical density greater than 97.2% [Inglis et al., 1982]. The annular (hollow) fuel pellets reduce the fuel centreline temperature, and the central void space provides a reservoir for containment of fission gases released from the fuel during irradiation. The fuel pellets are approximately 15

mm long with an external diameter of 14.5 mm and an internal diameter of 6.35 mm [Cordall et al., 1992]. Figure 5.3B shows a schematic of a fuel pin including the cladding and internal structure. One in six fuel pellets have a groove in the centre of the pellet, known as an anti-stacking groove (not shown in Figure 5.3B). The fuel cladding is compressed into the groove during manufacture to ensure that the cladding strain is evenly distributed along the fuel pin during irradiation.

#### 5.3.2.1 Fracturing of fuel pins

Understanding of fuel pellet fracturing has been driven by the need to understand pellet-clad interaction failures. These fractures occur where the fuel and cladding have bonded, and cladding opposite a fuel crack, which is not bonded to fuel, experiences enhanced strain as the fuel crack opens during irradiation [Mella and Wenman, 2013]. Important aspects of fuel pin behaviour that affect the fracturing include:

- Densification of the fuel during the initial phase of irradiation [Cordall et al., 1992]
- Fuel swelling due to fission gas production [Inglis et al., 1982]
- Clad creep down to contact the fuel [Cordall et al., 1992]
- Clad-fuel bonding [Cordall et al., 1992]
- Differential thermal expansion due to high thermal gradients in the fuel pellets.

The general condition of AGR fuel pellets after discharge is shown in cross- and axial-sections in Figure 5.4. In both examples, there are gaps between the fuel pellets. Although these are a result of manufacturing and therefore within expectations, they have a similar dimension to some of the fuel fractures, and may therefore have a similar impact on drying of the fuel. In the element 1 fuel, there is evidence of a gap between the fuel pellet and cladding, with larger voids around the grooved pellets. Shrinkage cracks may provide a preferential flow path similar to the pellet-clad gap in lower element fuels and may limit the volume of fuel matrix that is remote from a connected flow path. Both shrinkage fractures and pellet-clad gaps may therefore increase the volume of fuel that is connected to a flow path. In both cases, the fuel matrix displays a range of fractures that have large variations in orientation and width. It is therefore concluded that three-dimensional information on the fracture network is required to adequately characterise the fuel fracturing.

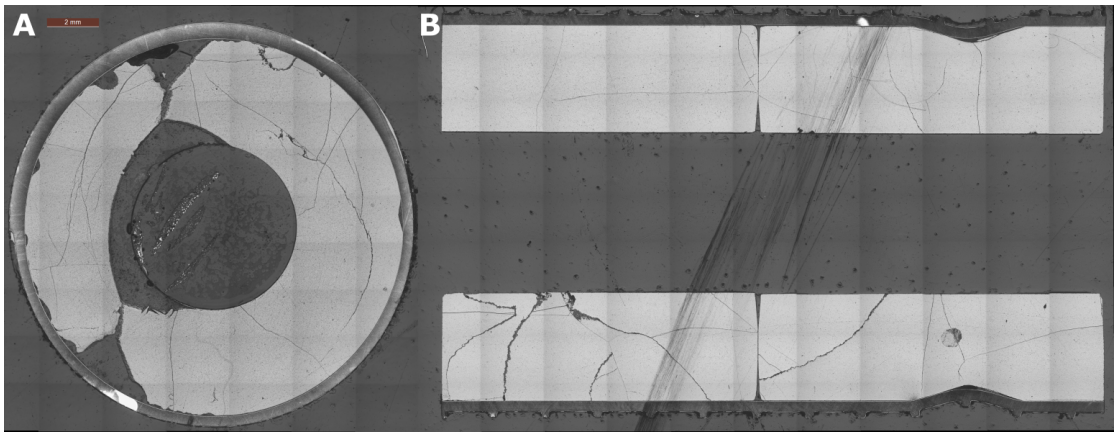



FIGURE 5.4: Cross section (A) and axial section (B) of element 1 fuel pins. The anti-stacking groove is visible on the right hand side in B. The scale is shown on the top left with a horizontal white line of 2 mm.

### 5.3.3 AGR fuel fracture analysis

The following fracture network study has been undertaken using an element 2 fuel pellet. To create a three-dimensional model of the fracture network in the pellet, the end of the pellet was imaged, ground, and polished in five stages. Subsequently, the fractures were traced and interpreted in three dimensions. The numerical approach detailed in Section 5.2 is used to simulate the flow of coolant fluid through the pellet. The equivalent permeability of the network was quantified, summarising the flow properties of the whole pellet, taking into account flow in the fractures and in the $UO_2$ matrix. This work provides an important understanding of AGR pellet permeability, as higher or lower values could influence the disposal procedures necessary for handling spent fuel.

#### 5.3.3.1 Imaging

Imaging of the spent uranium dioxide pellet was performed at the UK National Nuclear Laboratory by David Hambley and Frazer M. Hawthorne, the full details of which are provided in Thomas et al. [2018a]. The observed element 2 fuel pellet had been irradiated for approximately 6 years in the 1980s to a burn-up of 20.5 $GWd.teU^{-1}$, with a cladding temperature in the range 450-520°C. The sample was selected from a position near the centre of the zone where the fuel cladding becomes sensitised to localised corrosion as a result of radiation induced segregation [Hambley, 2013, Marwick, 1978]. Therefore, it represents the type of fuel most likely to be exposed to water.

The initial sampling location was at the interface between the stacked pellets, and sequential grinding was undertaken to remove approximately 0.5 mm of pellet between examinations. Between grinding stages, the remaining thickness was measured using a

calibrated micrometer to determine the section depth from the starting pellet surface. The final images and height of material removed between stages are shown in Figure 5.5. This work examines the top 2 mm of a pellet in 5 images. A full examination of a 15 mm pellet would require approximately 25 sections in total, with an interval of greater than 0.5 mm in some parts due to the occasional need to re-prepare samples.

Fuel sections are cut from the pin using a precision diamond cutting wheel around a position of interest and impregnated with resin to ensure that fuel geometry was retained during subsequent preparation. Sub-samples are then extracted and mounted in traceable mount rings using an epoxy resin. The mounted samples were polished using a variety of diamond-based lubricants to achieve a "mirror" finish for examination using an optical microscope. The degree of polishing undertaken was varied in order to make best use of equipment availability. The difference in the appearance of the cladding in Figure 5.5A and B arises from the variable polishing of different pellet planes. At each imaging step, around sixty high-resolution images of the surface are taken (1088 $\times$ 816 pixels), which are subsequently stitched together into a single high resolution image.

#### 5.3.3.2 Fracture analysis

Figure 5.5 shows the five images corresponding to the progressive grinding of the pellet. These images show a series of fractures, many of which were present in all images. Fractures were traced using Non-Uniform Rational B-Spline (NURBS) curves, to construct delineated models that trace fracture paths within each pellet image. NURBS are smooth parametric surfaces that exactly match the observed characteristics of the fracture, while smoothly interpolating geometry elsewhere. The traces of two of the grinding stages are shown in Figure 5.6, sorted into three fracture sets described in this section. Figure 5.6 also shows two further grinding stages below E, at 5.22 mm and 7.24 mm, to demonstrate how the fracture pattern changes through the pellet. Curves extracted from each image were connected to obtain NURBS surfaces for each fracture within the pellet. Fractures were traced using Computer Aided Design (CAD) software, to construct delineated models that trace fracture paths within each pellet image.

Fractures in the cross sections are sorted into three major sets. Fractures in set one are termed radial fractures, comprised of six fractures which are generally vertical and visible in all of the grinding stages. The even spacing of this group suggests they formed due to thermal stresses during rod heating [Mella and Wenman, 2015]. Five of these fractures connect the central void to the cladding. On the top right of the sample, another fracture intersects one of the five radial fractures in the set, potentially arising due to asymmetry in the heat distribution, or as a result of a secondary thermal gradient.

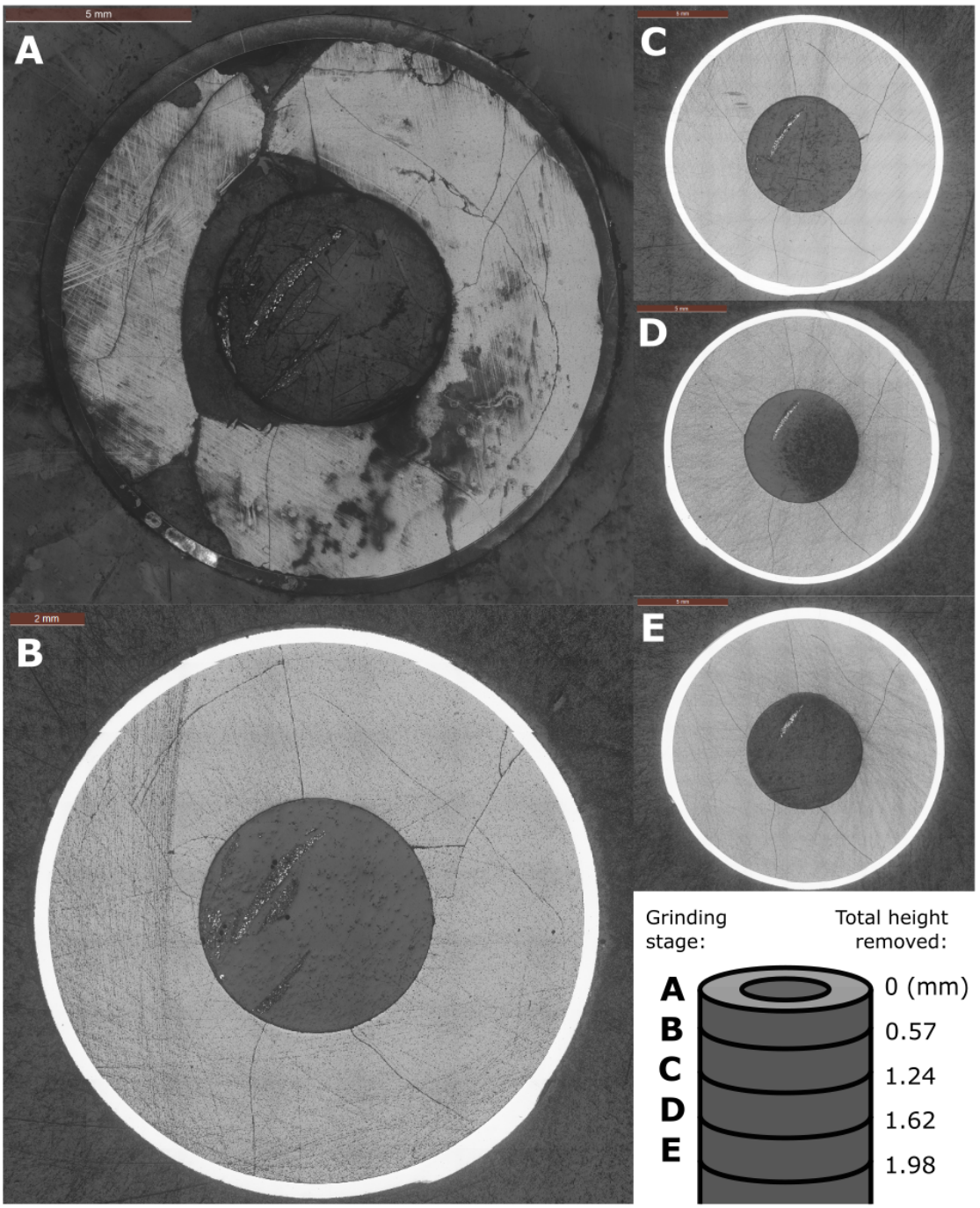



FIGURE 5.5: Optical microscope images of cross section scans of spent AGR fuel after successive grinding and polishing stages. A shows the unpolished surface of the intact pellet. B, C, D, and E show the top of the pellet after grinding and polishing. The lower right schematic shows the height removed by grinding between each image.

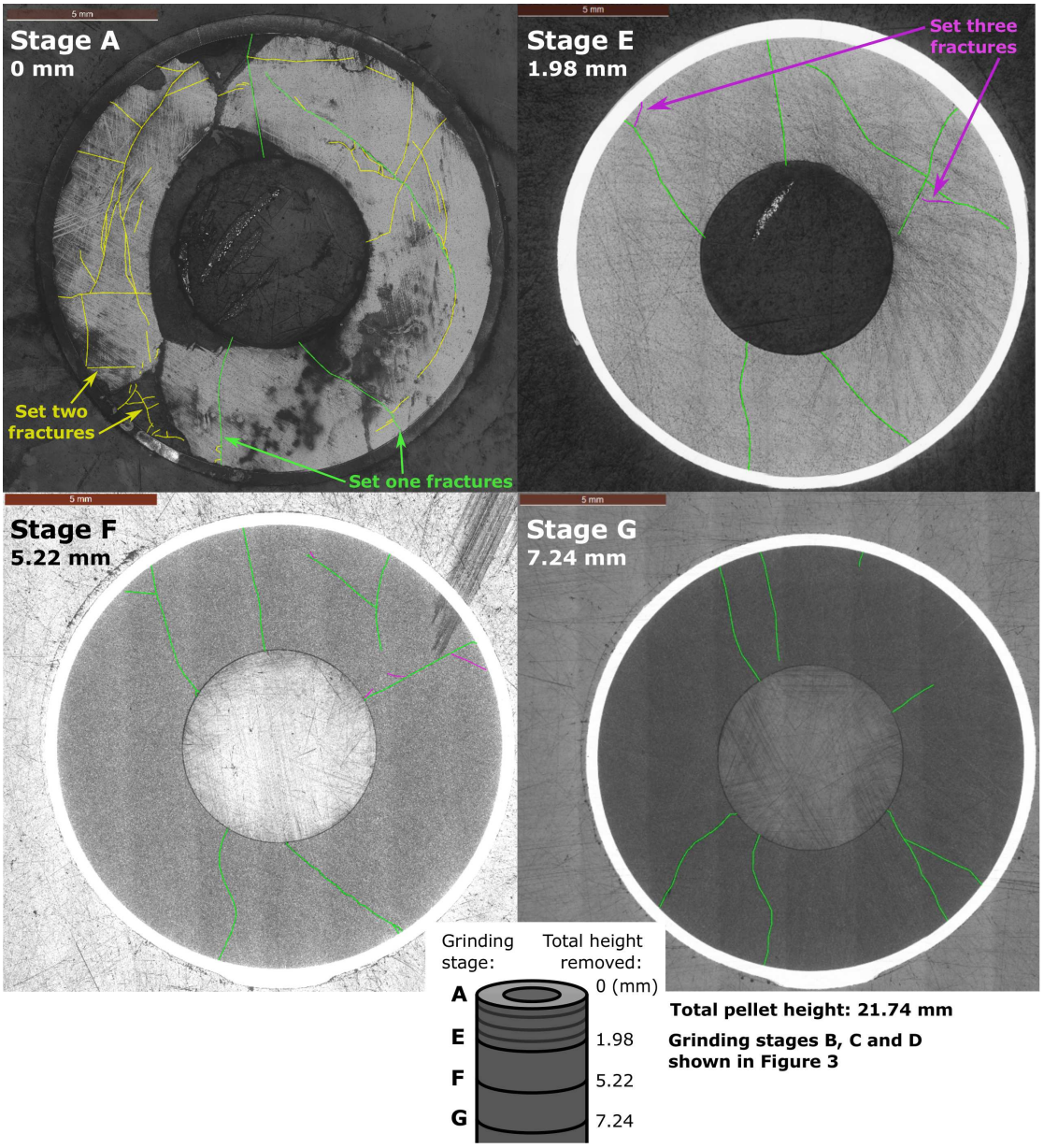



FIGURE 5.6: Examples of tracing fractures on pellet images from grinding stage (A and E, shown in Figure 5.5) and two further stages (F and G). Lines show the traces which were used to construct the full three-dimensional model (Figure 5.7), and are coloured based on the fracture set they were assigned to. The colours of the images have been re-adjusted from the original images to highlight traces.

Fractures in this set do not always intersect the internal or external edge of the pellet at every grinding stage, but each one intersects in at least one of the images, suggesting that these fractures will almost always provide significant connectivity between the sides and centre of the pellet, across its full length.

Fracture set two is visible only at the end of the pellet. These surface fractures are prevalent particularly on the right side of the pellet, and have higher densities in the region of radial fractures. These fractures arise due to flattening against adjacent pellets

during heating, as can be seen in Figure 5.4B, where two pellets touch. These fractures are assumed to be shallow, as they generally do not appear in the scan below stage B. Their clustering has some correlation with radial fractures, in particular, around the left-most radial fracture, which does not intersect with the top of the pellet. Rather, surface fractures are more dense at the left side of stage A, visible in the traced image (Figure 5.6A).

Fracture set three comprises all other fractures which did not fall into the radial or surface groups. These fractures are found in the interior stages (B through E) and appear close to the radial fractures. They tend to be short, close to relatively few features in the volume, and do not always intersect neighbouring fractures, and hence their impact on permeability is limited. The intense surface fracturing in the left of the sample correlates with a larger number of group three fractures connecting to the radial fracture in this region. Therefore, it is likely that there is a connection between the surface fractures and the radial fracture in this location, through the fractures in set three. The origin of fractures in this set is most likely to be local damage associated with the formation of the main (set one) fracture set. Two fractures from set three are visible in stage E in Figure 5.6E.

Further grinding was undertaken to analyse the rest of the pellet in order to ensure that the analysed section was representative of the full pellet. Figure 5.6 shows two more cross sections (stage F and G) closer to the middle of the of the pellet. The radial fractures in set one are present in both additional stages, with five fractures connecting the edge to the centre of the pellet. Between stages E and F, the concentric fracture in the top right of the pellet reduces in extent and splits into two. In stage G, this concentric fracture is not present, and instead, an additional fracture is present in the bottom right of the pellet. Overall, whilst the positions of the radial fractures change slightly, the number of radial fractures is fairly constant in the pellet. Additionally, the radial fractures are mostly found on the top and bottom of the pellet images, and not on the left and right sides. Although using a smaller grinding stage interval would provide frequently spaced images for analysis, the continuity across all the stages, even when the interval was larger in stage F and G, suggests that the interval of 0.5 mm is sufficient for characterising the vertical fractures in the pellet.

#### 5.3.3.3 Fracture network reconstruction

Figure 5.7 shows the discrete fracture network created from the interpreted images. The three sets of fractures are labelled, as well as the names for the different boundaries (front, right, back, left, top, bottom, and middle).

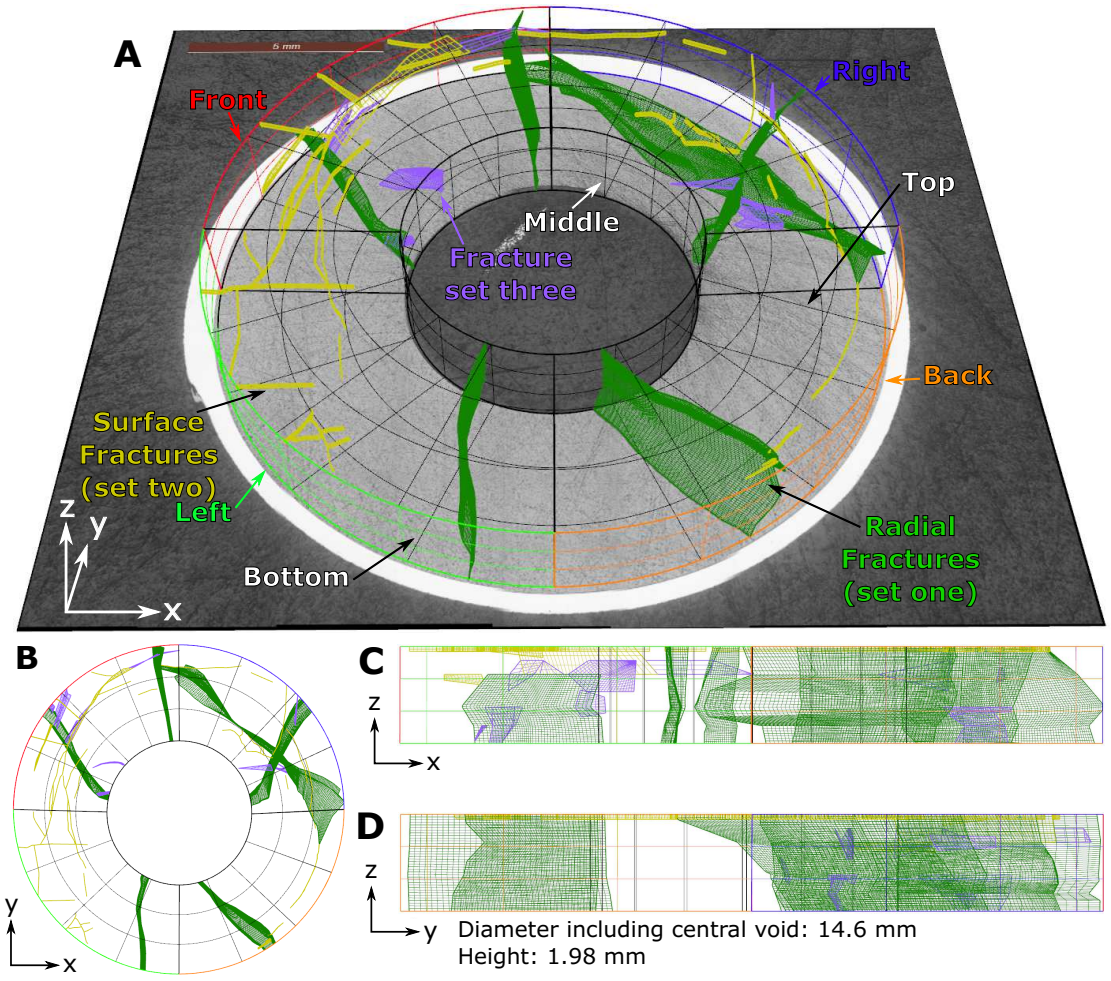



FIGURE 5.7: Three-dimensional discrete fracture network reconstructed from five images of spent fuel. A: Domain boundaries and fractures from an isometric viewpoint, with the stage 5 grinding image placed at the bottom. All objects in the volumetric domain are surfaces, represented using hashed grids providing transparency. B-D: Top and side views.

The height of surface fractures was assumed to be 0.1 mm, unless they are present on the layer below. Fractures only present on one layer were given a height of approximately half a layer either side of the layer they are present on. This is relevant for fractures in set three, which usually do not recur in every layer, so it is necessary to assume a height for the fractures. In some places it is ambiguous whether fractures connect or not, particularly when set three fractures are near the surface. In these cases, the region was examined and, if fractures are densely packed, they were assumed to connect between imaged layers. When intersections between fractures or boundaries were found in only a single grinding stage, the vertical extent of the intersection was assumed to be approximately half the layer height on either side.

#### 5.3.3.4 $UO_2$ porosity and permeability

The porosity of the $UO_2$ was approximated using an additional high resolution images of pellets. Porosities are modified after irradiation due to the release of fission gasses, increasing from 1.9 - 7.2% to up to 10 - 12% [Roque et al., 2000]. Assuming that the porosity is mainly driven by the release of fission gasses that occurs due to thermal loading, a gradient in the porosity is expected to form, reflecting the thermal gradient to which the sample is subjected during service. Analysis was performed by extracting and filtering subsections of pellet images. Images were segmented into domains using the Otsu method, a binning algorithm based on grey level histograms [Otsu, 1979].

Two examples of porosity analysis are shown in Figure 5.8A, a subset of the top of the mapped pellet before grinding (for which the full image is shown in Figure 5.5). This region was binned into two areas, shown in Figure 5.8C as white and grey. The grey area represents visible pores and occupies 4% of the image. Pore sizes were also measured, with an average of $6 \times 10^{-6}$ m, and some large pores of up to $25 \times 10^{-6}$ m, which are comparable in size to the observed fracture apertures.

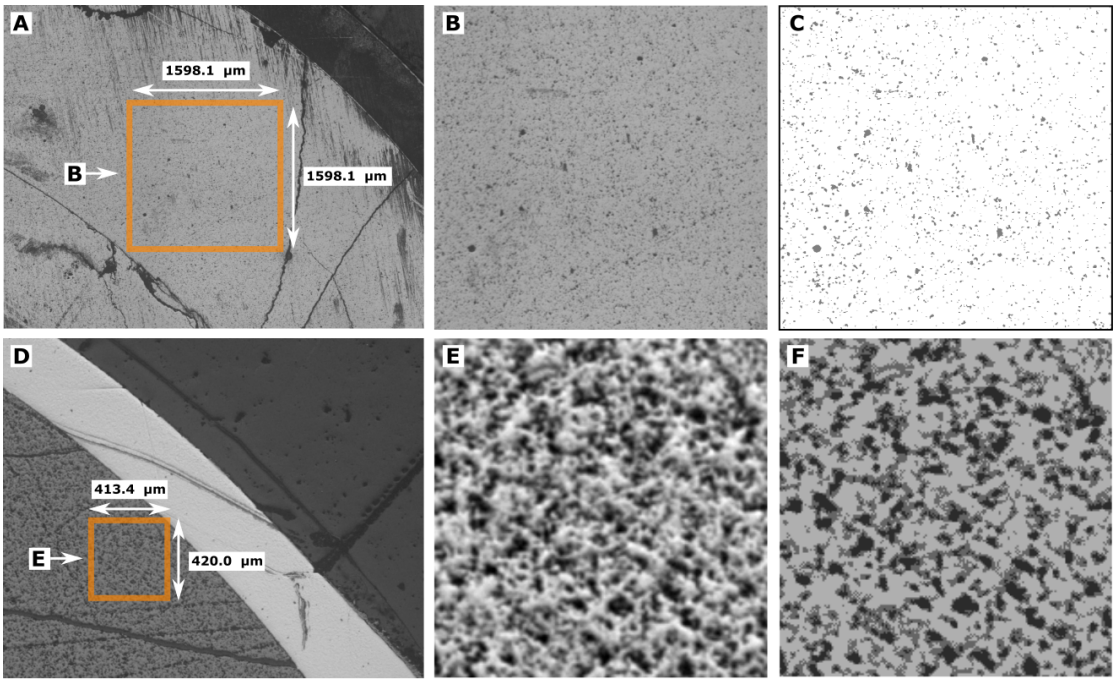



FIGURE 5.8: Subsections of high resolution $UO_2$ optical microscopy images for porosity analysis. A, B and C show a subset of the top of the mapped pellet (pre-grinding, stage A, Figure 5.5), and D, E and F are from a different sample. A and D: Area of image used for analysis. B and E: Enlarged sub-section E has been filtered to increase the contrasts and make pore boundaries more distinct. C and F: Result of binning into domains. In F, these regions are named g1 (light grey), g2 (dark grey), and g3 (black).

The second sample analysed in Figure 5.8 is an image of a different pellet with a visibly more porous surface. Three domains were extracted in Figure 5.8: g1 (light grey), g2

(dark grey), g3 (black). The distributed percentages are as follows: g1 occupies 54.4% of the sample, g2 represents 31.7% of the sample, and g3 represents 14%. The black domain (g3) can be used to estimate the absolute porosity, and the g2 domain can be partially attributed to sample porosity. Larger pore sizes were also measured, with an average of $14 \times 10^{-6}$ m.

The subsection in Figure 5.8D is taken near the boundary of the pellet next to the cladding. Subsections taken from near the inner void have higher g3 proportions of up to 30%. This analysis demonstrates the significant increase in porosity of $UO_2$ pellets after de-gassing, and the significant variations in porosity which may arise between samples.

An estimation for the $UO_2$ matrix permeability, based on porosity and average pore size measurements, was found from [Zimmerman, 2018]

$$k_{UO_2} = \frac{\phi d^2}{96} \tag{5.10}$$

where $\phi$ is the porosity and $d$ is the average pore size. The two regions sampled in Figure 5.8 provide $k_{UO_2}$ estimates for low and high porosity pellets, of $1.5 \times 10^{-14}$ $m^2$ and $5.6 \times 10^{-13}$ $m^2$ respectively. Although porosity estimates from interpreted images can be affected by the imaging technique, these porosity estimates are similar to acoustic measurements of spent fuel [Roque et al., 2000]. These porosity estimates are an approximation for the porosity of the real pellet. Future work may simulate pellets with more realistic anisotropic distributions of permeability.

#### 5.3.3.5 Fracture permeability

Fracture apertures were measured most accurately on the top of the pellet (Figure 5.5A) as this region has the highest resolution. Larger voids along fractures have apertures of up to 0.077 mm. Most apertures are in the range of 0.01 - 0.025 mm. Images B-E have lower resolutions meaning fractures have sub-pixel apertures. There are no significant differences between the apertures in each fracture group, or between polished and unpolished images.

Two uniform aperture values were tested in order to explore the potential impact of fractures on permeability. Fracture apertures are assumed to be either 20 or 10 microns across all fractures in flow simulations, where 20 microns is close to the mean aperture and is therefore the most realistic estimate. The lower value is also considered to explore the potential variation within the pellet, where the fracture may be constrained by the pellet body. This results in fracture permeabilities of $8.3 \times 10^{-12}$ or $3.3 \times 10^{-11}$ $m^2$

respectively, approximately three orders of magnitude higher than $k_{UO_2}$. To enable flow across the central void of the domain, its boundary (middle) is assigned the same properties as the fractures. Therefore, fractures which intersect the central void are connected, and the permeability is representative of the $UO_2$ material, rather than the void space in the centre. The cladding around the $UO_2$ is also excluded for the same reason. With the present method, assigning variable fracture apertures is possible, but sampling the variable apertures was too time consuming for the present work. Instead, two aperture estimates were investigated to gain some insight into different possible fracture apertures. Future work may consider how the variability in apertures observed in the pellets changes pellet permeability.

#### 5.3.3.6 Flow and equivalent permeability

The method described in Section 5.2 is applied to find $\mathbf{k}_{ef}$ for the pellet. For each porosity and fracture aperture considered, three numerical flow experiments are performed to study the hydraulic properties of the pellet, and calculate its equivalent permeability tensor, $\mathbf{k}_{ef}$, following the method detailed in Section 5.2 [Lang et al., 2014]. Experiment 1 used the 'left' as the source and 'right' as the sink, and experiments 2 and 3 used the 'front' and 'back', and 'top' and 'bottom' respectively. The locations of these boundaries were selected such that they intersected some fractures and therefore created percolating flow paths, such that flow experiments would match real cases where flow enters the pellet near a fracture. Flow entering the pellet in a region where no fractures intersect the boundary is also considered (see the discussion of the rotated case Section 5.3.4). The boundary definitions are shown in the reconstructed fracture network in Figure 5.7.

A further flow case considers the radial permeability of the pellet when fluid enters from the inner void and radially flows outwards through the sides. This case is relevant for when cooling fluid breaches the rod in another pellet, and flow is able to fill the central void. Subsequently, the fluid would fill the pellet from the inner void. To compute the radial permeability, a flow simulation is performed with the central void's boundary as the inlet, and the pellet's outer edge as the outlet. The element-wise sums of the radial pressure gradient ($\nabla p_r$) and radial velocity ($\mathbf{U}_r$) are found in the direction from the model's centre to the each element. The radial permeability is then found by rearranging Equation 5.8:

$$K_r = \frac{\mathbf{U}_r}{\nabla p_r}\eta \tag{5.11}$$

where $k_r$ is radial permeability. Because the direction varies depending on the element location, the right hand side is taken to be positive.

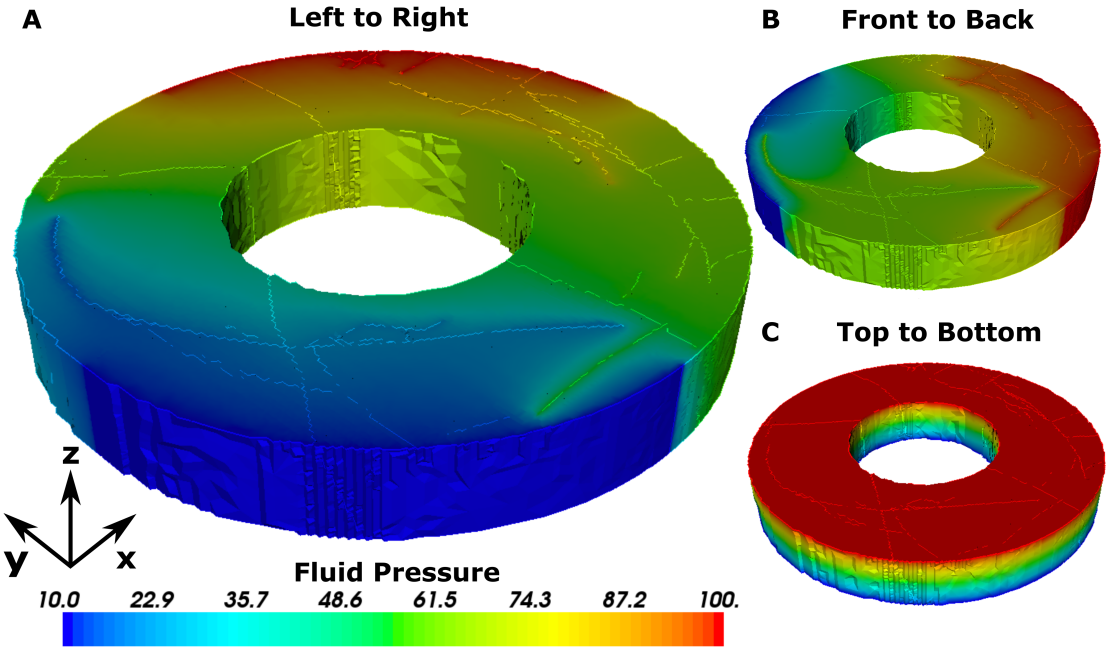



FIGURE 5.9: Distributions of fluid pressure (Pa) in the pellet for the three flow simulations (left to right, front to back, and top to bottom). The porosity in the simulations is 4% and the fractures have apertures of 20 $\mu$m.

### 5.3.4 Results and discussion

Flow through the simulated pellet is visualised in Figures 5.9 and 5.10, showing the fluid pressure distribution and fluid velocity respectively. The three principal directions of flow in the pellet and their relative magnitudes are given for several aperture and flow conditions in Table 5.1.

The pressure distribution demonstrates the organization of flow in the pellet. In the absence of fractures (*i.e.*, in the unfractured $UO_2$) the pressure drop from source to sink is linear and gradual. Fractures which do not provide a flow conduit from source to sink tend to equilibrate fluid pressure along their length. This is particularly visible for the poorly connected surface fractures (set two), where the fractures that connect to the inlet and outlet boundaries are at high and low pressure respectively. Fractures which connect to the centre (set one) have the same gradual change in fluid pressure along them.

Flow vectors in Figure 5.10 show a significant increase in fluid velocities in fractures. The majority of flow in the horizontal experiments occurs on fractures in set one, which connect the boundaries to the centre. In Figure 5.10A, flow enters either on the set two fracture which intersects the right side of the inlet boundary, or enters along one of the surface fractures (set two). Flow through surface fractures connects to set one and three fractures near the front boundary. In the front to back experiment (Figure 5.10B), flow

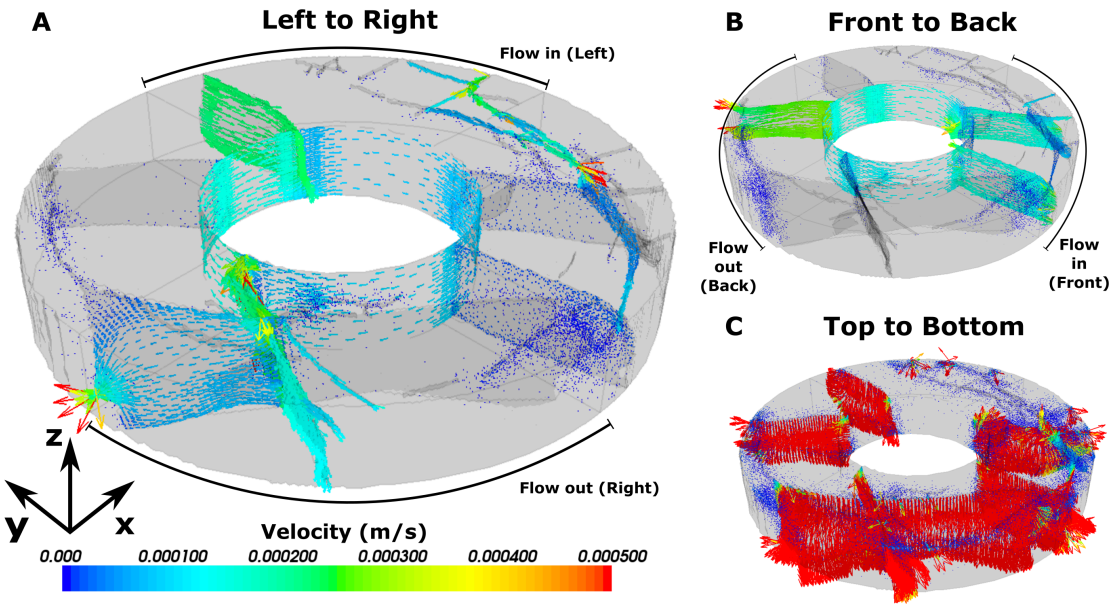



FIGURE 5.10: A, B, and C: Fluid velocity vectors in the three flow experiments. Flow vectors are colored and scaled by magnitude. Vectors are present throughout the domain, but much more flow occurs through the fractures. Flow in the $UO_2$ has magnitudes of $10^{-6}$ to $10^{-8}$ $ms^{-1}$, with higher values nearer fractures and boundaries. One vector is placed for each element in the mesh, therefore higher densities of vectors do not indicate more flow. Rather, the colour of the vector indicates the speed of the flow at that point. The porosity in the simulations is 4% and the fractures have apertures of 20 $\mu$m. The top to bottom (C) simulation has velocities in set one fractures of 0.0015 $ms^{-1}$.

enters the volume mostly along two set one fractures. The outlet is one fracture, in which the fluid velocities are higher in order to transport more fluid through one rather than two fractures. In the vertical flow simulation (Figure 5.10C), fluid velocities are much higher due to the direct connections between the inlet and outlets provided by set one fractures and the central void.

The equivalent permeability tensors of the pellet, calculated for several boundary conditions and fracture apertures, are given in Table 5.1. The eigenvectors of the tensor ($k_1$, $k_2$, and $k_3$), showing the principal directions of permeability in the pellet, are not the same as the directions of flow in each experiment. Instead, they show the minimum, intermediate and maximum direction of permeability in the pellet respectively, and are aligned in similar directions in each case. The exception to these orientations is the case without fractures. The radial permeability, $k_r$, is calculated using the method in Equation 5.11. The $UO_2$ matrix porosity and fracture apertures are varied between high and low values discussed in Section 5.3.3.4, demonstrating how permeability may vary in fuel with higher operating temperatures. High and low porosities are 4% and 15% respectively, and high and low apertures are $20 \times 10^{-6}$ m and $10 \times 10^{-6}$ m respectively. Each of the simulations with fractures is compared to the final case in Table 5.1, which

| | $k_i$ | $k$ (m$^2$) | $k_i/k_{u,i}$ | $x$ | $y$ | $z$ |
|---|---|---|---|---|---|---|
| High porosity, high aperture | $k_1$ | 6.10E-13 | 1.090 | 0.99 | 0.15 | -0.03 |
| | $k_2$ | 6.57E-13 | 1.174 | 0.13 | -0.91 | -0.38 |
| | $k_3$ | 7.03E-13 | 1.255 | -0.08 | 0.38 | -0.92 |
| | $k_r$ | 6.74E-13 | 1.204 | - | - | - |
| High porosity, low aperture | $k_1$ | 5.66E-13 | 1.011 | 0.99 | 0.15 | -0.03 |
| | $k_2$ | 5.72E-13 | 1.021 | 0.13 | -0.91 | -0.38 |
| | $k_3$ | 5.77E-13 | 1.030 | -0.08 | 0.37 | -0.92 |
| | $k_r$ | 5.73E-13 | 1.024 | - | - | - |
| Low porosity, high aperture | $k_1$ | 6.61E-14 | 4.407 | 0.99 | 0.15 | -0.03 |
| | $k_2$ | 1.14E-13 | 7.601 | 0.13 | -0.91 | -0.38 |
| | $k_3$ | 1.60E-13 | 10.667 | -0.08 | 0.38 | -0.92 |
| | $k_r$ | 1.30E-13 | 8.692 | - | - | - |
| Low porosity, low aperture | $k_1$ | 2.14E-14 | 1.426 | 0.99 | 0.15 | -0.03 |
| | $k_2$ | 2.74E-14 | 1.825 | 0.13 | -0.91 | -0.38 |
| | $k_3$ | 3.31E-14 | 2.209 | -0.08 | 0.38 | -0.92 |
| | $k_r$ | 2.94E-14 | 1.962 | - | - | - |
| Low porosity, high aperture, rotated | $k_1$ | 2.27E-14 | 1.515 | 0.95 | 0.32 | -0.01 |
| | $k_2$ | 1.24E-13 | 8.246 | 0.28 | -0.83 | -0.48 |
| | $k_3$ | 1.63E-13 | 10.844 | 0.16 | -0.45 | 0.88 |
| | $k_r$ | 1.30E-13 | 8.667 | - | - | - |
| No fractures, high porosity | $k_1$ | 5.60E-13 | 1.000 | 0.00 | 0.00 | -1.00 |
| | $k_2$ | 5.60E-13 | 1.000 | 0.75 | -0.66 | 0.00 |
| | $k_3$ | 5.60E-13 | 1.000 | 0.66 | 0.75 | 0.00 |
| | $k_r$ | 5.60E-13 | 1.000 | - | - | - |
| No fractures, low porosity | $k_1$ | 1.50E-14 | 1.000 | 0.00 | 0.00 | -1.00 |
| | $k_2$ | 1.50E-14 | 1.000 | 0.75 | -0.66 | 0.00 |
| | $k_3$ | 1.50E-14 | 1.000 | 0.66 | 0.75 | 0.00 |
| | $k_r$ | 1.50E-14 | 1.000 | - | - | - |

TABLE 5.1: Equivalent permeability tensors of seven flow simulations. For each simulation, three eigenvalues ($k_i$) are given in three directions ($i = 1$, 2 and 3), along with the radial permeability ($k_r$). Associated eigenvectors are given in the $x$, $y$, and $z$ column with unit normal of 1, rounded to three significant figures. $k_i/k_{i,u}$, is the ratio between the fractured and unfractured pellet (with a fixed permeability of $k_m$), or the increase in permeability due to the presence of fractures.

has no fractures, and no increased permeability around the central void (*i.e.*, only flow through the $UO_2$ matrix is considered).

The vertical eigenvector ($k_3$) is the largest in all the cases with fractures. The permeability in this direction is increased by up to one order of magnitude. This demonstrates the anisotropy arising from the alignment of the set one fractures. In the horizontal plane, the self-organisation of the set one fractures (*i.e.*, their even spacing) causes the permeability difference to be smaller. However, the set one fractures are more aligned with the $y$ direction (see Figure 5.7A), providing twice as much permeability than the $x$ direction. As shown in Figure 5.6, the preference for radial fractures to be aligned along

the $y$ direction persists throughout the pellet, therefore this anisotropy is likely to apply throughout the pellet.

The highest overall permeabilities are found in cases with high porosity. These cases are found to have smaller $k_i/k_{u,i}$, due to the smaller difference between the $UO_2$ matrix and fracture permeabilities. If the contrast between the fracture and matrix permeabilities is small, such as the high porosity, low aperture case, or if the fractures have wide spacing, then fractures can have only a small impact on flow. Therefore, pellets with high fission gas release may have permeabilities which depend much less on the fracture network present. For the pellet mapped in this work, the most relevant case is the low porosity, high aperture case. This result is similar to permeability measurements of similar spent fuel rods, measured through gas flow experiments where the central void is closed, which are of the order of $2 \times 10^{-13}$ m$^2$ [Rondinella et al., 2015]. In all cases, the radial permeabilities are higher than the horizontal permeabilities, because all the radial fractures have a direct path to the outlet, rather than only those which line up across the pellet in the $k_1$ and $k_2$ directions. Because cladding failures are likely to enable fluid to fill the central void, the radial permeability is likely to be the best estimate for the lateral permeability of the pellet.

Depending on the extent of the failure of the cladding, it is possible that flow may enter the fuel pin on one side, but find no connecting fracture to the central void. Therefore, a case of poor connectivity (*i.e.*, where the inlet does not connect to a fracture) is tested by rotating the boundaries by 30°. In this case, when the left boundary is the inlet, no fracture touches the inflow region. The resulting permeability tensor is the 'low connectivity' case in Table 5.1. Compared to the equivalent case, where both horizontal flow experiments have connectivity across the domain, the permeability in the direction with no fractures ($k_1$) increases much less. This provides a lower bound for the permeability enhancement horizontally across the pellet, due to fracturing AGR spent fuel, in the case when flow does not percolate fully.

### 5.3.5 Conclusion

This chapter has introduced important theory relevant to flow in fractured media, including defining effective permeability, analytical and numerical methods for calculating permeability, representative element volumes, and percolation. Within this context, the permeability calculation method of Lang et al. [2014] is described and validated. Thus, this method is used in Chapter 6 on domains containing geomechanical fracture networks, in order to understand how the mechanics of fracture growth influence network permeability.

An application of this method is demonstrated, where the effective permeability of fractured spent nuclear fuel is estimated. In the studied uranium dioxide pellet, both the porosity and the apertures of fractures are shown to significantly change pellet permeability. If the contrast between the $UO_2$ matrix permeability and the fracture permeability is small, *i.e.*, in high fission gas release fuel, the fracture network may have a relatively small effect on pellet permeability. The three-dimensional system is in essence an extruded 2D system, however, it differs from observations at the surface of the pellet, and several grinding steps should be used to ensure that mapped fractures are not surface artefacts.

Many of the features of the pellet imaged for this study are typical of other pellets, such as the radial fractures providing direct connections from the outer to inner boundaries. A key feature arising in other pellet cross sections are concentric fractures which circle the central void (*e.g.*, Figure 5.4A). Fracturing parallel to the grinding surfaces maybe under-represented in the network examined, which can be observed in axial images Figure 5.4B. Different fracturing patterns are also observed in pins which underwent higher operating temperatures, where bonding layers often form between the fuel and the cladding [Morgan et al., 2015]. During cooling, the region becomes fractured as the reactor cools faster than the cladding. These fractures are not present in the studied pellet, and would result in a higher permeabilities than those found in this study. Similar analyses of pellets across the 500°C temperature range in AGRs will provide a further understanding of the permeability range of spent fuel. Furthermore, a gap is not always present between the pellet and the cladding due to bonding, which would reduce the ability of fluids to reach all the fuel surface. Separate analysis of this case would demonstrate how permeability may be reduced if no fuel-clad gap is assumed.

# Chapter 6

# Growth and flow in geomechanical fracture networks

## 6.1 Introduction

Discrete fracture network (DFN) models provide an effective method for simulating and studying features of fractured rock. A DFN model explicitly defines the shapes and intersections of fractures inside the modeling domain. They are widely applied to improve understanding of several geological applications, including radioactive waste disposal [Baek et al., 2017, Cvetkovic et al., 2004, Follin et al., 2014, Tsang et al., 2015], petroleum production [Cottereau et al., 2010, Kim and Deo, 2000, Shokri et al., 2016], hydraulic fracturing [Fu et al., 2013, McClure et al., 2016], and geothermal energy production [Kolditz, 1995]. The methods by which physical properties are calculated on these networks varies widely between implementations, including boundary element [Tuckwell et al., 2003], discrete element [Lisjak and Grasselli, 2014], finite difference [Karimi-Fard et al., 2004], finite element [Kim and Deo, 2000], finite volume [Koudina et al., 1998], and virtual element methods [Benedetto et al., 2017].

The requirement to explicitly define and discretize fractures makes DFNs generally unsuitable for applications where fractures are present across many length scales, due to the computational demand of such a detailed model [Hernández et al., 2015, Karamnejad and Sluys, 2014, Oliver et al., 2016]. On reservoir or repository scales, model dimensions can be tens to hundreds of metres or more in size [Berkowitz, 2002], despite fractures a metre or less in size providing important connectivity. This is reconciled either by representing relatively few fractures for large scales [*e.g.*, den Boer and Sayers, 2017, Fang et al., 2017, Hardebol et al., 2015], or more commonly, by upscaling parameters such as effective permeability from smaller DFN models for use in large scale continuum

models [Ahmed Elfeel and Geiger, 2012]. The latter approach is routine in industry applications of DFNs. Therefore, much recent work has focused on methods for generating 'kinematic' DFNs which have realistic properties [Bonneau et al., 2016, Maillot et al., 2016b]. Because the detail of real networks is usually unknown, approaches are often stochastic in order to find average properties, or to evaluate analytical methods for calculating effective permeability [Ebigbo et al., 2016, Leung and Zimmerman, 2012, Mourzenko et al., 2011, Sævik et al., 2013].

DFNs are often generated by randomly inserting planar fractures in a domain using Poisson point processes, often referred to as "Poisson DFN models" [Maillot et al., 2016b]. Real fracture networks have many features which are not well reproduced by such a technique, including:

- Orientation: subsurface fracture networks form as a result of discrete deformational phases associated with tectonic events [Gillespie et al., 1993] or local disturbances such as tunnel excavation [Baek et al., 2017]. These states of stress are almost never isotropic. This results in sets of fractures with similar orientations whereas many DFN studies have focused on isotropic networks [*e.g.*, Ebigbo et al., 2016, Mourzenko et al., 2011, Thovert et al., 2017].

- Shape: whilst fractures are typically planar, non-planar geometries frequently arise during mixed mode growth, particularly as a result of interaction [Olson and Pollard, 1991]. Additionally, fractures do not have uniform shapes, unlike the ellipses which are frequently used in three-dimensional DFNs.

- Spacing: the presence of fractures in a rock has a large impact on where further fractures can nucleate and form. Fractures reduce stress along their strike and increase stress at their tips (see Chapters 2 and 3) [Kachanov, 1987], which has been shown to have significant influence on the density of fractures in networks [Davy et al., 2010]. In layered rocks, fracture spacing is also controlled by layer thickness [Olson, 2004].

- Aperture: fractures have complex walls and can be filled with different materials, resulting in extremely heterogeneous apertures and flow distributions across large fractures [Black et al., 2016, Tsang and Neretnieks, 1998], particularly at intersections [Leckenby et al., 2005]. DFN models typically have fixed apertures [Mourzenko et al., 2011] or simplified relationships between fracture properties and aperture [Baghbanan and Jing, 2007, Ebigbo et al., 2016].

- Length: the distribution of fracture lengths in a population is usually described using power laws [Bonnet et al., 2001, Davy et al., 2010, Gillespie et al., 1993].

Fracture length also correlates with fracture aperture [Olson, 2003, Renshaw and Park, 1997]. This means larger fractures generally have much more impact on flow than smaller ones. Distributions of length are incorporated into Poisson DFNs more frequently than other features mentioned in this section, particularly normal [Leung and Zimmerman, 2012, Ren et al., 2017] and lognormal [Fereshtenejad et al., 2016, Ji and Koh, 2016, Lang et al., 2018] distributions.

- Intersections: stochastic networks have fundamentally different topological properties compared to real networks [Sanderson and Nixon, 2015]. In Poisson DFNs, intersecting fractures will always cross one another, whereas in real networks, both crossing and abutting are possible.

Many DFN studies recognise the importance of these realistic features to network flow properties, and have made progress towards increased realism in several ways. Contemporary studies incorporate heuristic or kinematic rules for inserting fractures into their networks [*e.g.*, Bonneau et al., 2016, Davy et al., 2013]. Alternative fracture shapes to ellipses have also been explored, including regular and irregular polygons [Cvetkovic et al., 2004, Thovert et al., 2017]. Power law distributions of fracture lengths are already widely used in stochastic DFN studies [*e.g.*, Bonneau et al., 2016, Thovert et al., 2017], and in some studies, fracture apertures scale as a function of their length [Ebigbo et al., 2016]. These rule-based approaches to DFN generation have generated networks with some realistic properties, but do not contain all the features described in the previous paragraph. In particular, incorporating interaction effects during concurrent fracture growth requires a fully mechanical approach, and gives rise to many fracture network properties, including spacing, size (or length) distributions, non-planar surfaces, and intersections.

Fracture networks generated geomechanically (*i.e.*, using the physical laws of fracturing) have been successful at reproducing realistic network features, but so far, have seen limited use. Examples of two-dimensional fracture growth have demonstrated the potential for grown fracture networks to reproduce realistic network properties [Olson, 2004, Philip et al., 2005, Renshaw and Pollard, 1994]. Paluszny and Matthäi [2010] introduced a FEM approach where automatic meshing of discrete fractures allows growth in any direction. This method also enables stress-dependent apertures to be found for fracture apertures, showing that uniform apertures on fractures in DFNs may cause an over-prediction of effective permeability.

This chapter makes significant progress towards realistic fracture network generation through the use of the ICGT based fracture growth simulator [Paluszny et al., 2013, Paluszny and Zimmerman, 2011]. Geomechanical fracture growth, as described the

linear elastic fracture mechanics (LEFM) theory, is used for the first time to create three-dimensional networks where realistic features arise as a result of the stress state in the volume. Many of the realistic features of networks discussed in this section arise as a result of the interaction between fractures. The hydraulic properties of the generated geomechanical networks are quantified using the effective permeability computation method [Lang et al., 2014] with uniform fracture apertures, and compared to a suite of stochastic DFNs. A new method for extracting fracture apertures from the displacement discontinuity either side of the fracture surfaces is also outlined in this work. This means the hydraulic properties of fractures are the result of the deformation in the domain, and that apertures are altered by fracture interaction. The effective permeability of geomechanically grown networks are compared to the permeabilities of stochastic DFNs with a range of densities and fracture insertion rules. This work evaluates the benefits of incorporating geomechanics into DFNs and provides practical suggestions for improving how subsurface fracture systems can be modelled.

### 6.1.1 Review of discrete fracture network permeability studies

In this section, recent DFN studies which examine permeability are reviewed. The most recent review of this topic is by Lei et al. [2017a] including discussion on the influence of geomechanics and coupled effects. They sort DFN studies into three groups: geological (using datasets derived from real outcrops), stochastic (using random insertion of fractures to create datasets), and geomechanical (using physically based or inspired processes to create datasets). Davy et al. [2018] also provide a short review of the present issues arising in the use of DFNs, highlighting qualities length scaling of fractures, fracture density, intersections, and clustering.

#### 6.1.1.1 Discrete fracture networks with uniform apertures

Stochastic DFN studies began in the 1980s to investigate two major topics: percolation theory and hydrogeology. Stochastic networks were used extensively to study percolation, starting with the work of Balberg et al. [1984], who examined distributions of capped cylinders in three dimensions. Before this, the percolation of spheres had also been studied, but capped cylinders provided a closer approximation of fracture geometries. The influential aspect of the study was the random placement of objects into a domain, and the testing of a large number of these domains with Monte Carlo methodology. Checking for percolation in a system is a relatively simple calculation compared to permeability. Robinson [1983] used the term ‘fracture’ to describe the objects being

tested, first in two dimensions (lines) and then in three dimensions (planes) [Robinson, 1984].

In the context of fractured rock, Baecher et al. [1977] was the first to conceptualise a fractured rock as a three-dimensional domain containing two-dimensional disks. The term 'joint system model' was used to describe these types of models before DFN nomenclature became standard [Dershowitz and Einstein, 1988]. Baecher et al.'s study was motivated by the need to extrapolate two-dimensional outcrop data (*i.e.*, traces of fractures) to three-dimensional volumetric rock and fracture properties. Barton [1978] performed a similar study, placing cut-planes through volumes containing disks and analysing the resulting populations of traces. Dershowitz and Einstein [1988] review various types of early DFNs, which expanded to include intersections and terminations, disks with arbitrary orientations, and tesselated domains where various geometric units fractures are repeated. Dershowitz and Einstein highlighted the need to motivate DFN generation towards reproducing realistic fracture networks.

Long et al. [1982] performed the first study where flow and permeability were calculated using results of FEM simulations on two-dimensional networks. The results included rose-plots which quantified permeability in many radial directions. At the time, understanding the REV concept and how fracture networks disrupted it was a topic of great interest. Long et al. [1982] examined how differently sized fracture networks, concluding that the size of an REV must be large compared to the fracture lengths in order to provide a good statistical sample of the bulk rock. They also separately studied how interconnection correlates with permeability, and also highlighted the potential level of uncertainty arising from borehole analysis [Long and Witherspoon, 1985].

Long et al. extended their study method to three-dimensions [Long et al., 1985], generating networks as orthogonal sets of circles. Long et al. [1985]'s move to three dimensions was motivated by the fact that a two-dimensional cut-plane will underestimate the permeability of a full three-dimensional network. Lang et al. [2014] demonstrated and quantified this effect, showing that in domains near the percolation threshold, a cut-plane can underestimate permeability by up to three orders of magnitude.

Three-dimensional stochastic networks have been the standard for examining DFN behaviour since the work of Long et al. [1982]. It was quickly recognised that random networks would not reproduce realistic network features [Long and Billaux, 1987]. Some work has continued on two-dimensional networks, particularly on mapped fracture outcrops. Two-dimensional models also simplify the implementation of numerical models, therefore, the influence of mechanics has been explored further in two dimensions. Lei et al. [2014b] compared stochastic DFN realisations to a fracture network mapped from rock outcrops in Kilve (UK). Stochastic DFNs had significantly mean different hydraulic

properties to the analogue network. Differences were more pronounced if mechanical conditions were varied. This analysis was also extended to a semi-three-dimensional case, by extruding the fractures seen at the surface [Lei et al., 2017b]. These numerical experiments also predicted the formation of new fractures, and demonstrated that a two-dimensional analysis would neglect out-of-plane stress effects on permeability.

#### 6.1.1.2 Discrete fracture networks with mechanical apertures

Bisdom et al. [2015] incorporate stress-dependent apertures to flow simulations, using outcrops from the Gafsa basin (Tunisia) for their datasets. They found that, under minor amounts of shear, apertures become highly heterogeneous, and only a small fraction of the network contributed to permeability. Furthermore, the equivalent permeability did not depend on the fracture intensity. Instead, the orientations of fractures relative to the applied stress had a much greater control on the network's effective permeability. This resulted in the two-dimensional DFN with the lowest intensity having the highest permeability. Further work found that averaging apertures for upscaling of permeability results in an underestimation of network permeability [Bisdom et al., 2016].

Hyman et al. [2018] explored how the increase in effective permeability scales with volume properties, including the contrast between fracture and matrix permeabilities. They used a static DFN, matching statistical properties derived from a fractured shale. They identify a power-law relationship between the size of the jump and the difference between the fracture and matrix permeabilities, in both two-dimensional growth simulations and stochastic DFNs. Garipov et al. [2016] provide a further example of a psuedo-three-dimensional DFN incorporating coupled poroelasticity and mechanics to calculate fracture apertures.

Lang et al. [2018] consider the effect of the stress tensor on the orientation of maximum permeability in discrete fracture networks, using a multi-scale approach to computing each fracture's hydraulic properties. At the rock mass scale (*i.e.*, the scale of the full DFN), contact stresses are calculated using the gap-based Augmented Lagrangian method [Nejati et al., 2016]. These stresses are then used to compute stiffness and transmissivity for each fracture individually, representing the roughness of the fracture surface using a power spectrum. This results in an anisotropic permeability on each fracture at the rock mass scale. Study of 265 three-dimensional DFNs, each containing eight fractures subjected to anisotropic stress, showed that the direction of maximum permeability is along the same direction as the intermediate principal stress. This is due to fractures acquiring the most slip in the plane of the maximum and minimum principal stresses, which, for individual fractures, results in highest transmissivities in

the direction perpendicular to this slip. This is a different result from two-dimensional studies which do not consider an anisotropic stress tensor, which find that the maximum permeability is aligned with the maximum principal stress direction [Baghbanan and Jing, 2008, Jing et al., 2013]. This further highlights the importance of studying fracture networks in three dimensions, and incorporating the effect of mechanics on fracture hydraulic properties.

#### 6.1.1.3 Geomechanical discrete fracture networks

Modifications to simple Poisson DFN generators to improve realism include accounting for fracture spacing and clustering [Long and Billaux, 1987], alternative fracture shapes [Cvetkovic et al., 2004, Thovert et al., 2017, Wettstein et al., 2012], anisotropy [Vu et al., 2018], and varied fracture apertures [Ebigbo et al., 2016]. Methods to improve realism which incorporate mechanics of growth are the subject of this section.

In the context of DFNs, the term 'geomechanical' has been used to describe DFNs which are, to some extent, created using mechanical rules and laws. Lei et al. [2017a]'s definition of a GDFN (Geomechanical Discrete Fracture Network) is one where fracture patterns are created using LEFM-based physics describing fracture growth. This definition is adopted in this work, to separate them from other terms which have been used to describe DFNs generated with rules inspired by mechanics, rather than fully simulating the mechanics of growth (*e.g.*, kinematic [Maillot et al., 2016a]). Stochastic qualities will arise in all types of simulated DFN, due to the requirement in any DFN generation method to have some initial flaw or heterogeneity distribution from which the fracture network grows. In this work, it is demonstrated that, whilst this initial flaw distribution has an effect on the final network, most of the properties of the domain result instead from the remote stress conditions, and the self-organisation of fractures during competitive growth.

Renshaw and Pollard [1994] introduced the first two-dimensional LEFM-based simulator designed to grow fracture arrays. Fractures were represented as flat lines which grow parallel to one another. At the two tips of each fracture, $K_I$ is calculated using the method of Kachanov [1987], thereby incorporating fracture interaction into the tip energy state. Two criteria are used to control growth. A sub-critical crack growth criterion controls failure, and the fracture growth rate is controlled by a Paris-type law. Through the mechanical interaction of fractures, localized zones of more intense fracturing formed where larger fractures exerted a stronger influence on other nearby fractures, concentrating stress near their tips. Renshaw and Pollard [1994] also considered the influence of

the fracture growth rate exponent in the Paris-type growth law on the resulting network, as discussed in Section 4.2.

Renshaw and Pollard's method has many similarities to ICGT's growth method (*e.g.*, LFEM basis, growth criteria). Similar models have been used to investigate the clustering of fractures [Olson, 2004] and the impact of fractures on permeability [Philip et al., 2005]. Tuckwell et al. [2003] extended a Renshaw and Pollard-type model to include the in-plane shear (mode II) SIF, enabling simulation curved fracture geometries and more complex deformation. Cowie et al. [1993] examined a similar domain in two dimensions, using a damage model rather than an LEFM based method, and observed similar localisation intense fracturing, shadow zone formation, and self-organisation. These results were later examined in terms of the displacement between the two sides of the developing fractures, providing context for the results which was directly applicable to fault and basin development [Cowie et al., 2000].

Josnin et al. [2002] generated the first three-dimensional geomechanical network informed by statistical and mechanical rules, and can be seen as the first kinematic DFN, before the term was coined by Maillot et al. [2016a]. In Josnin et al.'s method, the domain begins with bedding planes representing stratification, and fractures are grown symmetrically in the other two perpendicular planes, where the largest fractures in the final network had begun propagating the earliest. The effect of stress shadow zones were incorporated and scaled based on fracture size. Fracture intersections are handled to create a mix of terminations and cross-cutting fractures. Vertical propagation through bedding planes is controlled three factors: by a probability (as a function of the layer's strength), the height of the fracture (justified by correlating a fracture's height to its potential energy), and shadow zones of other fractures in the layer above. Josnin et al.'s method therefore provides many different psuedo-mechanical rules which work together to generate stratified, three-dimensional DFNs. They found that the resulting networks had various realistic features, including a linear relationship between layer thickness and fracture spacing, and log-normal distributions of fracture lengths. Jourde et al. [2007] used Josnin et al.'s method to generate stratified DFNs, and quantified their permeabilities. Flow was solved by assuming an all the flow takes place in the fractures, where permeability is governed by a parallel plate cubic law. They found that certain geometric and physical parameters had significant impacts on effective permeability. Fracture spacing within layers, and the stopping capacity of bedding planes, were found to significantly impact permeability by several orders of magnitude. Fracture lengths were found to have relatively less impact on permeability.

Davy et al. [2013] proposed a framework for generating DFNs which simplifies the rules of fracturing, including arresting propagating fractures upon intersection with larger

ones. Maillot et al. [2016a] continued this work and use the term 'kinematic' DFN to describe DFNS created using mechanically-inspired rules. The method is capable of producing networks with realistic power law length distributions and can produce both 'T' and 'X' intersections between fractures. Networks generated using this method are found to have significantly smaller permeabilities than equivalent Poisson DFN models with the same statistical properties (fracture density, length, and orientation) [Maillot et al., 2016b]. Maillot et al. [2016a] compare the permeability of Poisson DFNs to kinematic DFNs. They found that, for equivalent geometrical characteristics (fracture intensity, length, and orientation distributions), kinematic DFNs had systematically smaller permeabilities and more significant flow channeling. Bonneau et al. [2016] also generate DFNs using mechanically inspired rules focused on fracture interaction and shadow zones. They use a heuristic Poisson point process to select the locations at which fractures are inserted into a network, favoring locations at the tips of fractures where stress would be concentrated, and avoiding locations along the fracture sides where stress would be reduced. The resulting networks were more likely to be clustered, meaning networks percolate at a reduced threshold.

Masihi and King [2007] developed a novel fracture model based on the elastic free energy due to fracture density, which is known to follow a Boltzmann distribution. The model calculates the statistical distribution of the fractures using an expression for the spatial correlation of the fractures as an objective function. Therefore, the resulting statistics of the domain are not derived directly from the flaw seeding process, rather, they are a result of the mechanics of the system. The model reproduces fracture interaction effects, where large fractures have neighbors located further away than small fractures. Their first results are for two dimensions, with two perpendicular fracture sets. Extension of Masihi and King's work to three dimensions, where apertures are spatially variable, will provide a further method for dense geomechanical DFN generation.

In most DFN generation methods, including those incorporating mechanics or psuedo-mechanical rules, fractures are planar objects. Non-planar fractures are much less frequently incorporated into DFNs. Motivated to create curved fracture networks which would arise in anticlines, Fereshtenejad et al. [2016] developed a method which folds an initially planar set of disks. Their method by which fractures are folded is geometric, rather than mechanically based, and is therefore only suited to anticline or syncline modelling and cannot handle arbitrary stress distributions.

### 6.1.2 Characterisation of fracture networks

Various statistical measures have been used to characterise discrete fracture networks. Each of these statistics may also be split between different fracture sets in the network [*e.g.*, Cvetkovic et al., 2004]. An important statistic is the number of fractures present, scaled by some dimension of the observation. This is referred to as fracture intensity or frequency, and the exact measures used depend on the sampling dimension. An example of a formal description of the system in literature is by Dershowitz and Herda [1992], known as the $P_{xy}$ system, where x refers to the feature dimension and y refers to the sampling region dimension. Table 6.1 summarises the eight possible measures of frequency and intensity. The term 'fracture density' is often used interchangeably with frequency or intensity [*e.g.*, Ebigbo et al., 2016], which some authors suggest should be phased out in order to standardise terminology [Sanderson and Nixon, 2015].

| | Dimension of feature: | 0 | 1 | 2 | 3 |
|---|---|---|---|---|---|
| Dimension of sampling region: | | Number | Length | Area | Volume |
| 1 | Line | $P_{10}$ Fracture intensity, 1D frequency | $P_{11}$ Dimensionless intensity | | |
| 2 | Area | $P_{20}$ 2D frequency | $P_{21}$ Fracture intensity | $P_{22}$ Dimensionless intensity | |
| 3 | Volume | $P_{30}$ 3D frequency | | $P_{32}$ Fracture intensity | $P_{33}$ Dimensionless intensity |

TABLE 6.1: $P_{xy}$ system used for definition of fracture frequency, intensity, and density, based on the dimensions of features and observation. Reproduced from Sanderson and Nixon [2015].

Fractures can be observed in boreholes (one-dimensional, providing the number of fractures present), outcrops (two-dimensional, providing the lengths of the fractures present), or in a volume (three-dimensional, providing the surface areas of the fractures present). In order to compare two different samples, the length, volume or area must be considered in some way. The 'number' column in Table 6.1 shows the most straightforward way to do this, which is to divide the number of fractures observed by the volume sampled.

This yields the terms $P_{10}$, $P_{20}$, and $P_{30}$ for line, area, and volume sampling regions respectively. This statistic is straightforward to calculate, but ignores fracture size.

Fracture intensity is more widely used in DFN studies than frequency, and either has dimensions [$L^{-1}$] or is dimensionless. Intensity includes fracture size in its calculation. With dimensions [$L^{-1}$], the quantifiable size of the fractures in the given sampling region is divided by the size of the sampling region. For two-dimensional systems, this means the total length of fractures is divided by the area ($P_{21}$), and in three-dimensional systems, the surface area of fractures is divided by the volume ($P_{32}$). One-dimensional fracture intensity is equivalent to one-dimensional frequency ($P_{10}$). $P_{32}$ is the best suited intensity statistic for three-dimensional analysis of DFNs, because surface area is straightforward to measure [Pan et al., 2010]. However, it is uncommon to find it defined for real fractured networks, because full fracture surface areas are mostly unknown, therefore $P_{21}$ and $P_{10}$ values are more commonly reported, with some exceptions [*e.g.*, Cvetkovic et al., 2004, Gonzalez-Garcia et al., 2000].

Procter and Sanderson [2018] contrast the three measures of intensity. They demonstrate on real fracture outcrops datasets that reported $P_{10}$ values have a strong linear correlation with $P_{21}$, with a slope of one and intercept close to zero, suggesting that $P_{10}$ values are a good estimate for $P_{21}$ values. $P_{10}$ has a further benefit of being very quick to estimate. In situations where it can be calculated, the main benefit of $P_{32}$ is that the whole network is examined, whereas a one-dimensional line or two-dimensional plane may not intersect all fracture sets. Dershowitz et al. [2000] consider the scaling relationships between $P_{10}$, $P_{21}$ and $P_{32}$, for example data from Äspö, Sweden. They found that $P_{10}$ values could be multiplied by 2 to scale them to $P_{32}$ values. This scale factor will be site specific, and depends significantly on the borehole orientation.

Dimensionless intensity is also used in DFN studies as it is independent of absolute fracture and domain size. The first use of a dimensionless intensity was by Balberg et al. [1984], for quantifying the percolation threshold of a three-dimensional domain containing random sticks. Balberg et al. [1984] used the excluded volume of an object, defined as the volume surrounding an object in which the centre of another must be situated for the two to intersect, to calculate dimensionless intensity. Adler et al. [2012] define this dimensionless intensity (or in their terminology, density) as the the intensity (*i.e.*, $P_{32}$) multiplied by the excluded volume. The benefit of this measure is that it relates the density to the connectivity of the domain, as it equals the average number of intersections per fracture. However, for fractures with complex non-planar surfaces, excluded volume is difficult to estimate. There are various other methods of calculating dimensionless density, for example, multiplying by a characteristic length or aperture

[Sanderson and Nixon, 2015], but Balberg et al. [1984]'s method using an excluded volume is most common in DFN studies [*e.g.*, Ebigbo et al., 2016, Lang et al., 2014].

The number of fracture intersections in a dataset is also of great interest, as more intersections increase the chance that flow percolates [Thovert et al., 2017]. Intersection measures are subject to dimensional considerations, with intersections per unit length, or length of intersections per surface area being common measures for two and three-dimensions respectively [Sanderson and Nixon, 2015]. One-dimensional borehole analysis is not suited to considering intersections, as it cannot provide certainty that fractures are intersected, and a single borehole is unlikely to cross an intersection point. The type of intersection can also be characterised, with some fractures terminating ('T') and others carrying on ('X'). Shokri et al. [2016] provide an example of intersection analysis on two-dimensional DFNs, investigating the relationship between fractal dimension, permeability, and the onset of intersection. They find that the connectivity index of a network (total number of intersection points divided by the number of fracture lines, *i.e.*, a dimensionless intersection intensity) is a more useful parameter for estimating permeability, particularly when the fracture intensity falls under the percolation threshold.

Additional statistics used to characterise networks are average properties of each fracture set, including length, aperture, and orientation. The hydraulic response of real fractures can also be found using packer and tracer testing. Some literature which uses datasets from underground research laboratories, with individual fracture hydraulic measurements, include Ji and Koh [2016] for the Korean Underground Research Tunnel (KURT), and Cvetkovic et al. [2004] for the Äspö hard rock laboratory in Sweden.

#### 6.1.2.1 Real networks

Where possible, a real fracture network is best understood through outcrop analyses (*e.g.*, in the field or in the walls of a tunnel). This methods offers only a two-dimensional view of a network, showing the traces of the fractures and their orientations. Imaging of fractures and faults using seismic methods can produce three-dimensional images of fractures, but typically has too coarse a resolution to detect micro to meso-scale fractures which significantly contribute to subsurface flow [Jackson and Rotevatn, 2013]. In rocks where all sides can be imaged, a better idea of the internal arrangement of fractures can be constructed. Surface analyses will also include additional fractures due to excavation damage zones or unloading fractures which are more frequent near the Earth's surface. Furthermore, the apertures of these fractures may be altered due to enhanced weathering.

A detailed example of a real three-dimensional fracture network is Gonzalez-Garcia et al. [2000], who construct the network inside a Herycnian granite block from La Peyratte, France. The DFN is created from nine parallel trace maps [Ledésert et al., 1993]. The trace maps, resulting DFN, and histograms showing fracture surface area frequency in the DFN are reproduced in Figure 6.1. The block contained about 240 fractures in two sets of fractures oriented between $\pm 30^{o}$ inclination from the vertical axis. Six of the fractures could be traced through each section. Constructing the DFN from these traces required the fractures to curve and twist between the planes. The method of reconstructing a fracture network from traces observed in cut-planes was also used in Section 5.3 [Thomas et al., 2018a]. An early example, and methodology for creating networks from core samples, is demonstrated by Gertsch [1995], but no statistics of the resulting three-dimensional fracture network are given.

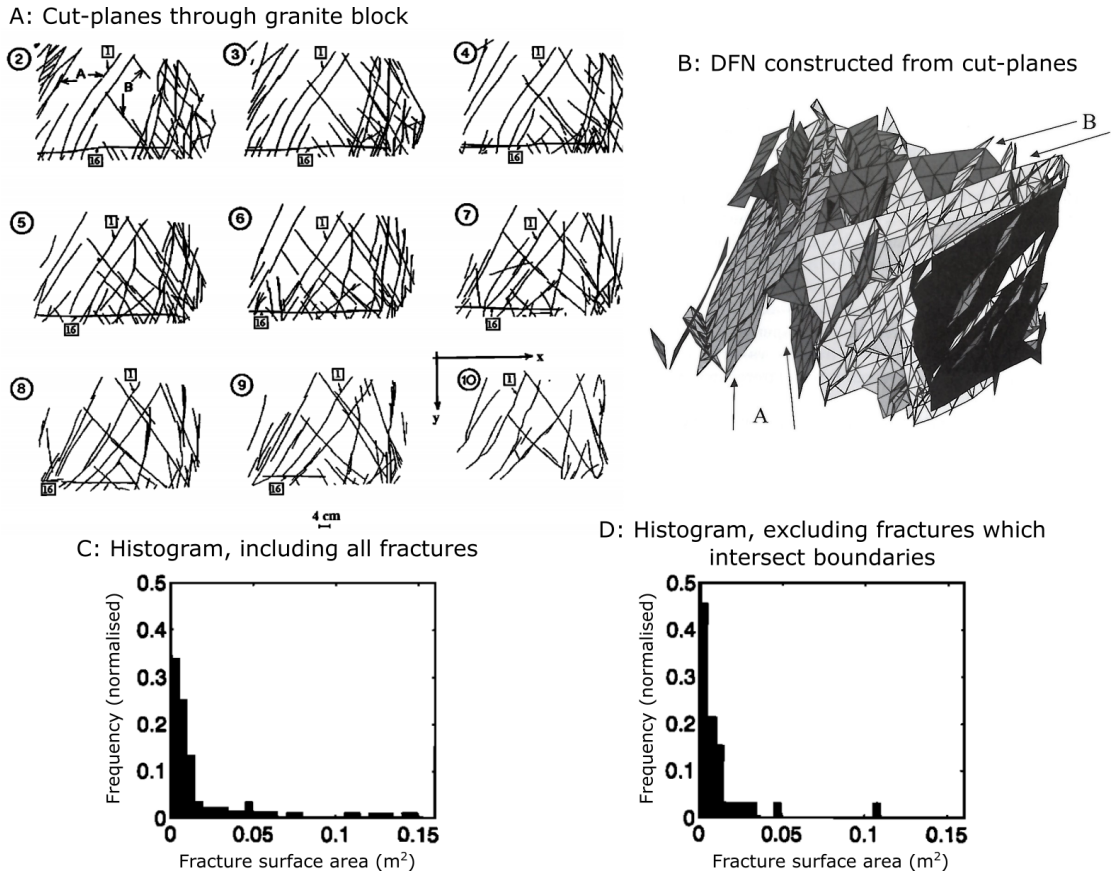



FIGURE 6.1: Three-dimensional DFN from cut-planes through a granite block, from Gonzalez-Garcia et al. [2000]. A: Traces of fractures on nine trace maps through the volume. The annotation '16' marks a horizontal fracture. B: DFN created from traces. The original dimensions of the granite block were $52 \times 35 \times 36$ cm$^2$. Annotations 'A' and 'B' identify the directions of the two major sets of fractures. C: Histogram of fracture surface areas in the final DFN. D: Histogram of fracture surface areas in final DFN, with fractures that intersect the boundaries excluded. Both histograms have frequency values normalised. From Ledésert et al. [1993] and Adler et al. [2012].

The total surface area of fractures was estimated from the trace maps as 2.6 m$^2$ by

Ledésert et al. [1993], and the block volume was 0.066 $m^3$ [Adler et al., 2012]. When the DFN was constructed from the network, the triangulated fracture surface area was slightly lower (2.05 $m^2$) [Gonzalez-Garcia et al., 2000]. This gives the constructed DFN a $P_{32}$ value of 31.06 $m^{-1}$. The histograms (Figure 6.1C and D) suggest that the majority of fractures in the network were small. These measures will still underestimate the number of small fractures present, as some are be missed by the nine cut-planes. Fracture surface areas are difficult to measure on real datasets, but it is notable that plots of fracture lengths against frequency also have peaks at the minimum observed length [*e.g.*, Hardebol et al., 2015].

Cvetkovic et al. [2004] present a DFN study on a thoroughly characterised rock network at the Äspö hard rock laboratory, situated in Sweden, 460 m below the surface. The properties of the fracture network in the crystalline rock surrounding the laboratory were characterised using boreholes, tunnels and pump testing. Fractures were present in three sets, each with significantly different dip, strike, and length. The $P_{32}$ densities for the three sets were 0.26, 0.85 and 0.18 $m^{-1}$, giving a total density of 1.29 $m^{-1}$. DFNs used for subsequent radionuclide transport simulations were stochastically generated based on these data.

Some field measurements of fracture intensity consider whether fractures are closed, open, or flowing. Follin et al. [2014] review the results of twelve borehole studies in Forsmark, Sweden. Across all the fractures identified in boreholes, an average of 23.8 % of fractures were open, 1.7 % were flowing, and the rest were sealed. This demonstrates that the stress state of the host rock will result in relatively few optimally inclined, open fractures, corroborating with results from the DFNs under stress discussed in Section 6.1.1.3. This leads to different measures of fracture intensity for each type of fracture. Follin et al. also separated their results between different depth zones, with intervals of 0 to 200 m, 200 to 400 m, and greater than 400 m. Shallow open fractures (above 200 m) had $P_{10}$ densities in the range of 1.13 to 3.17 $m^{-1}$, and deep open fractures ranged between 0.535 to 0.77 $m^{-1}$. Flowing fractures had much lower densities, at 0.153 to 0.33 $m^{-1}$ for shallow fractures and 0.005 to 0.05 $m^{-1}$ for deep fractures. Munier [2004] gives further examples of borehole data from Forsmark, demonstrating how $P_{10}$ varies with depth for one borehole (Figure 3-23).

### 6.1.3 Synthetic networks

Results from psuedo-mechanical DFNs also provide estimates for the fracture intensity of real rocks. The kinematic networks generated by Maillot et al. [2016a] developed different $P_{32}$ values depending on the rules used to generate the network. Two rules

for fracture growth and two rules for fracture arrest give rise to four possible kinematic growth methods. Fractures grow uniformly as circles until they touch another fracture's surface. The growth mode is determined by the relative speed of growth compared to the rate at which new fracture nucleation points are added. Mode S (sequential) models will grow a fracture much faster than a new fracture is added, and mode C (competitive) will add new fractures whilst others grow. In arrest mode A, a fracture will stop at this point. In arrest mode B, growth continues, maintaining a circular shape and leaving the intersected point as a fixed location on the fracture tip [Davy et al., 2013]. Maillot et al. [2016a] generates DFNs with a range of densities ($P_{32}$ = 1.59 to 2.68 $m^{-1}$) using these methods, comparing them to equivalent stochastic (Poisson) DFNs.

The present method does not have separate nucleation or arrest modes, as it begins each DFN with an initial array which does not have fractures added to it, and fracture tips arrest upon intersections with other surfaces (see Section 2.3.7.5). The closest comparison to Maillot et al. [2016a]'s kinematic models is growth mode C and arrest mode B, as all the fractures compete and grow together, and if one tip is intersected, the rest of the fracture can continue to grow. In this case, Maillot et al. [2016a]'s networks with C and B rules lead relatively dense networks with an average $P_{32}$ = 2.68 $m^{-1}$, for networks containing on the order of 1146 ± 24 fractures. A significant difference here is that fracture interaction will tend to suppress the growth of other fractures, meaning competitive growth entails very different growth patterns.

## 6.2 Challenges in growing dense fracture networks

This section introduces several aspects of the ICGT which are optimised in order to generate GDFNs efficiently and realistically. The SIF calculation method displacement correlation (DC) is used in GDFN generation in this chapter. Compared to using the disk-shaped domain integral method (see Section 2.5), for a small reduction in SIF accuracy, computational time is saved by reducing sampling to only two points. Additionally, in terms of the error in the propagation angle around the tip (Figure 2.11D), both DC and the disk-shaped domain integral yield similar results. Further changes introduced and considered in this section are SIF smoothing, discretisation of large datasets, handling of fracture intersections, and conditions for ending simulations.

### 6.2.1 Stress intensity factor smoothing

This chapter uses a different method for smoothing SIFs, compared to the method in Section 4.3.2, where only one SIF mode (II) is smoothed. In a growing network, variations may arise in any one of the three SIF modes for several reasons. Mesh refinement reduces over time as tips become further apart, or when adjacent tips intersect another fracture or boundary. As explored in Chapter 4, small variations in the SIFs will lead to changes in growth that, over many steps, converge (*i.e.*, self-correct) towards a uniform fracture tip, because parts of the fracture tip that advance more in one step will advance relatively less in subsequent steps. This will produce a uniform fracture when the full simulation is considered. However, in a domain containing many other fractures, growth changes due to interaction are more significant and persistent than the slight variations which balance non-uniform growth in cases where growth should be uniform. This provides further motivation for ensuring smoothing happens in each step.

A novel NURBS-based smoothing method is developed to smooth small variations in the $K_I$, $K_{II}$, and $K_{III}$ fields. A two-dimensional second degree rational B-spline curve approximates each modal stress intensity factor, whereby each point of the spline is defined as $(x, K_i)$, where $x$ is the one-dimensional distance along the tip curve, and $K_i$ is the modal stress intensity value. The result is a curve which is smooth, and is defined to smoothly approximate through all the original SIF values, for each modality in an independent manner. The curve is defined by a low number of control points, so as to reduce variability in the SIF prediction. The smoothing is not employed in any of the validation exercises and only aids complex simulations with large amounts of fractures.

Figure 6.2 compares unsmoothed and smoothed SIF values around an inclined, penny shaped, 1 m radius fracture. The unsmoothed results have small variations, most clear in the $K_I$ curve, and the smoothed curve effectively removes these variations. Modes $K_{II}$ and $K_{III}$ are also smoothed, particularly noticeable at their peaks ($0^o$ and $90^o$, respectively). A small offset also arises with increasing angle in these modes, however, which may have a small effect on the growth angle of one side of the fracture.

### 6.2.2 Discretisation in late-stage GDFNs

Dense growth simulations must be performed at lower mesh refinements to provide faster computation times, providing less accurate SIFs as discussed in Section 2.5. Furthermore, as fracture tips spread out in the later stages, and deactivate when they intersect other fractures or boundaries, fewer fracture tips are present in the domain. This results in larger minimum finite element sizes, as the sizes are set by the distance between tip

nodes, and therefore fewer total elements are present in late stage meshes. This is beneficial for reducing the overall simulation time, as smaller matrix inversions and fewer SIF calculations are required in later steps.

Fixed numbers of fracture tips are used to generate the present GDFNs. Dynamically adding additional fracture tips to increase refinement in later simulation stages was tested during GDFN growth tests. This did not lead to significant differences between late step geometries. However, if fracture tips are added based on a minimum size for each fracture tip, many fracture tips will tend to reach this size at the same time, rapidly increasing the refinement and slowing the simulation significantly. Therefore, dynamic addition of new tip nodes is not included in the present work, but could be used in the future to improve the detail of late stage network geometries, particularly where fracture tip loops become angular.

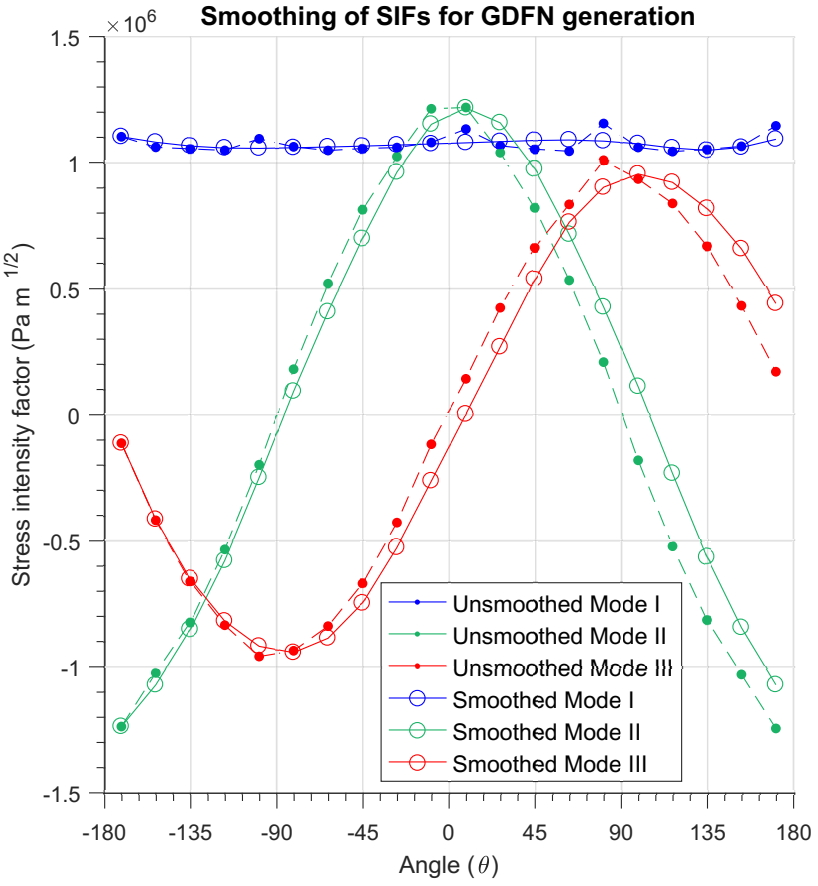



FIGURE 6.2: Effect of smoothing on SIFs. Both fractures are isolated, at the centre of a 20 × 20 × 20 m cube, with a radius of 1 m. The material properties and boundary condition used match those used to generate GDFNs (Section 6.3).

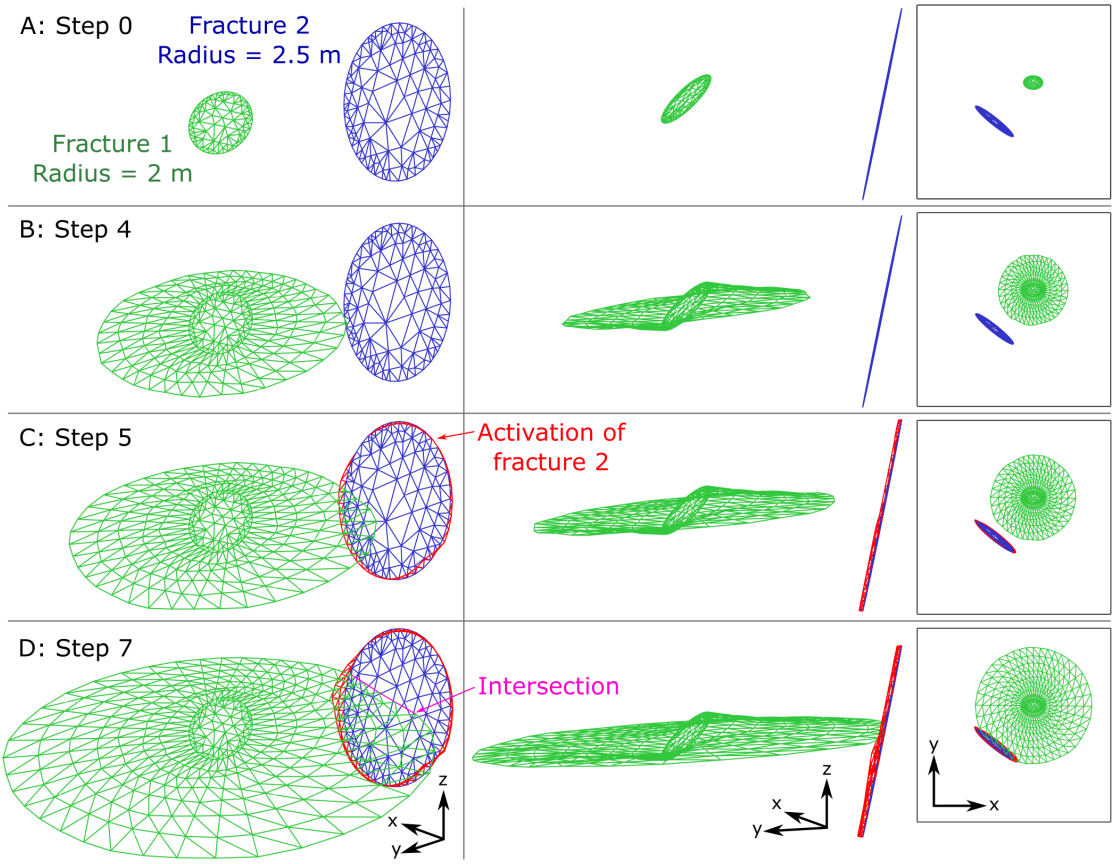



FIGURE 6.3: Geometry of two fractures at four growth steps, shown in three orientations: two isometric views (left and centre) and viewed from the top with volume boundaries shown (right). From the initial state (A, step 0), fracture 1 (green) activates first, with fracture 2 (blue) activating from step 5 (C) onwards. In step 7, the fractures become intersected. Red lines show geometry added to fracture 2 by growth, and the pink line shows the intersection between fracture 1 and 2 in step 7. Fracture 1 is centred at (2, 2, 0), has normal (0, 1, 1), and a radius of 1 m. Fracture 2 has centre (-2, -2, 0), normal (4, 5, 1), and a radius of 2.5 m. The geometry of step 10 is shown in Figure 6.4.

### 6.2.3 Fracture intersection example

The rules governing intersection of fractures are detailed in Section 2.3.7.5. Fracture interaction, activation, and intersection are demonstrated for growing fractures in Figures 6.3 and 6.4. Two fractures are grown under tension, using material properties shown in Table 6.2, with 40 fracture tip nodes rather than 20. Therefore, the boundary conditions and material properties used to grow GDFNs in this chapter are also used to grow this fracture pair. Fracture 1 is centred at (2, 2, 0), has normal (0, 1, 1), and a radius of 1 m. Fracture 2 has centre (-2, -2, 0), normal (4, 5, 1), and a radius of 2.5 m. The initial inclinations of these fractures mean that, in the first step, fracture 1 activates but fracture 2 does not. Fracture 2's tips do not have sufficient magnitude SIFs to meet the mixed mode failure criterion. However, this changes after several growth steps due to fracture interaction.

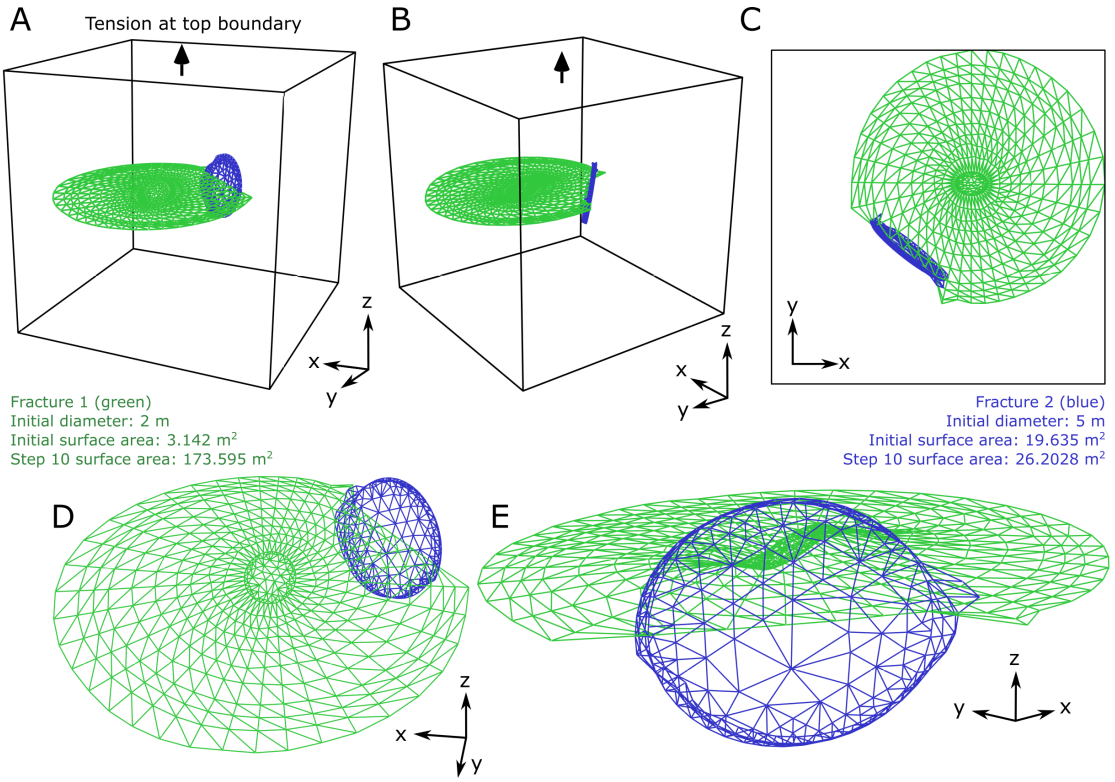



FIGURE 6.4: Geometry of two intersected fractures. The same geometry is shown in five perspectives: isometric (A and B) and viewed from the top (C) with volume boundaries shown, and isometric views without volume boundaries (D and E). The geometry shown is at growth step 10, when fracture 1 (green) has grown whilst intersected, and now intersects the outer boundary. Steps 0, 4, 5, and 7 of this dataset are shown in Figure 6.3. Red surfaces show new growth around fracture 2 from step 5 onwards. The pink curve in D shows the line along which the two fractures become intersected.

Fracture 1 begins by propagating radially, approaching fracture 2. Figure 6.3C shows step 4, which is the point before fracture 2 becomes active. In step 5, a small amount of growth occurs on fracture 2 (highlighted with red lines), because the stress state at fracture 2's tips becomes sufficient for growth. This activation demonstrates stress amplification prompting growth in otherwise inactive fractures. This activation is not uniform, and is largest just below the plane of fracture 1. The direction of growth on fracture 2 is perpendicular to the stress field, *i.e.*, reactivation prompts growth along the direction dictated by the regional stress, rather than growth in other planes, such as its original inclination.

Growth on both fractures continues in a similar way in step 7 (Figure 6.3D), where the fractures become intersected. At the intersection, several tips on fracture 1 are truncated against fracture 2. Figure 6.4 shows the geometry after three further steps, where fracture 1 has continued to grow at the tips where it has not been truncated. Stress concentration where the two fracture tips are close result in enhanced growth of both fracture 1 and 2. Fracture 1 intersects the outer boundary in this step, visible from

above in Figure 6.4C. A small overlap occurs, most clearly visible in Figure 6.4E at the right of the intersected part, which is the result of the growth vectors not intersecting fracture 1's surfaces.

### 6.2.4 Flow channeling through fracture intersections

Fracture intersections are of fundamental importance to fracture network permeability. Figure 6.5 shows the geometry and flow results for a simulation in which nine fractures grow to become intersected and create a percolating channel. Material properties used for the growth and flow simulations are shown in Table 6.2. The initial domain contains five small, inclined fractures and four large, evenly spaced, vertical fractures. These vertical fractures mostly do not grow, instead acting as permeable interfaces between the active fractures. The results show step 8, where each of the inclined fractures have grown enough to intersect the adjacent vertical fractures or volume boundaries. Similar to the previous example, small sections on the vertical fractures are activated due to the proximity of the smaller inclined fractures. This can be seen most clearly in Figure 6.5A and B, on the vertical fracture furthest to the right of each image.

Figure 6.5E and F compare the flow velocity patterns in the initial state and the final state. Flow simulations use apertures of 0.001 m on the fractures and matrix permeabilities of $1 \times 10^{-15}$ m$^2$. The images show flow from the $-y$ boundary (front right) to the $+y$ boundary (back left). Fast flow in step 0 is fully concentrated on the inclined fractures due to their alignment with the flow direction. The vertical fractures do not enhance flow in this case, as they are oriented perpendicular to this flow direction.

In step 8, flow is highly concentrated along the connected pathway created by the fracture intersections. Flow velocity magnitudes are similar on both the inclined and vertical fractures. All of the inclined fractures are fully activated by the flow, whereas flow on the vertical fractures is restricted to the shortest path between the other intersection. This demonstrates that flow channeling is an emergent property that arises in ICGT simulations depending on the geometry of networks and flow boundary conditions. Flow channeling observed here arises in both uniform aperture and mechanical aperture cases, however, it is enhanced when apertures are derived from the displacement field (see Section 6.5).

## 6.3 Generated geomechanical discrete fracture networks

Towards the goal of analysing the permeability of grown fracture networks, six GDFNs are generated to provide a suite of different test cases. Material properties for hard

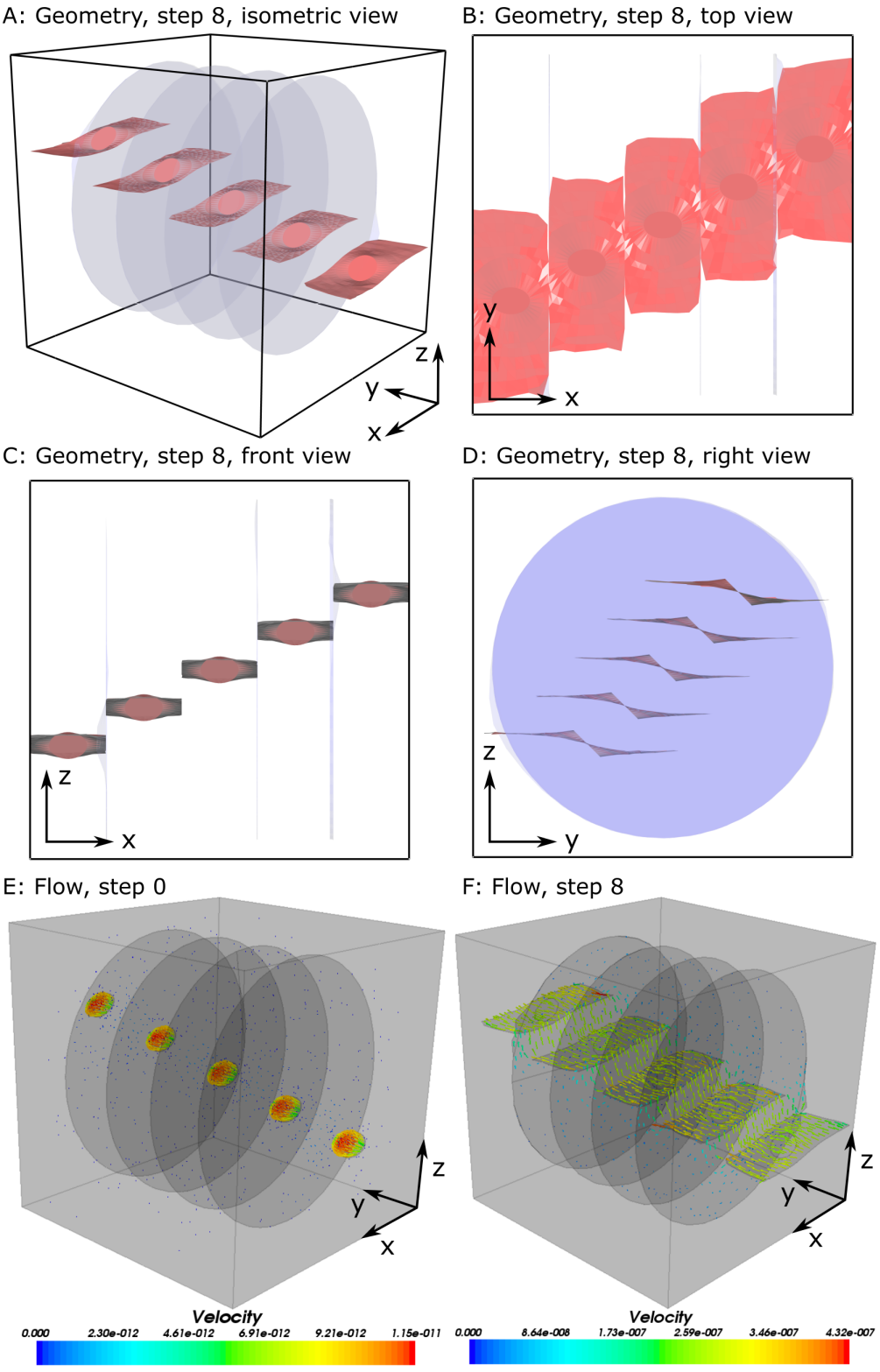



FIGURE 6.5: Effect of fracture intersections on flow in a connected dataset containing nine fractures grown under tension. Initially, four of the large vertical fractures (blue, 9 m radius) start as disks parallel to the direction of tension, and five of the small fractures (red, 1 m radius) start as disks with small inclinations, spaced between the four vertical fractures. A, B, C, and D show the geometry of fractures in the volume at step 8, in isometric, top, front, and right views respectively. E shows the flow vectors resulting from flow from the -$y$ to the +$y$ boundaries.

| **Parameter** | **Value** |
|---|---|
| Young's modulus | $20 \times 10^9$ Pa [Krech et al., 1974] |
| Poisson's ratio | 0.2 [Krech et al., 1974] |
| Critical stress intensity factor | $1 \times 10^6$ Pa $m^{1/2}$ [Wei et al., 2016] |
| Tensile stress at top boundary (Neumann condition) | $2 \times 10^6$ Pa |
| Displacement at bottom boundary (Dirichlet condition) | 0 m |
| Flow boundary condition | 100 Pa at source boundary, 10 Pa at sink boundary |
| Matrix permeability | $10^{-15}$ $m^2$ |
| Fracture aperture (uniform) | 0.001 m (for Section 6.4) |
| Fracture aperture (mechanical) | Variable (see Section 6.5) |
| Initial fracture radius | 0.5 and 2.5 m (see Table 6.3) |
| Number of fractures | 30, 60, and 90 (see Table 6.3) |
| $K_{IC}/K_{IIC}$ | 0.7540 [Chang et al., 2002] |
| $K_{IC}/K_{IIIC}$ | 1.5881 [Aliha et al., 2015] |
| Maximum fracture extension per step | 2 m |
| Minimum fracture extension per step | 0 m |
| Fracture growth exponent $\beta_f$ | 0.35 [Renshaw and Pollard, 1994] |
| Fracture growth exponent $\beta_n$ | 2 |
| Fracture tip nodes | 20 |
| Size of domain | $20 \times 20 \times 20$ m |

TABLE 6.2: Parameters used during generation of GDFNs.

rocks (*e.g.*, granite, granodiorite) are chosen to make results particularly relevant to radioactive waste disposal and other deep rock applications. Table 6.2 shows the material properties, numerical parameters, and boundary conditions chosen to grow geomechanical datasets.

Understanding gained from growth simulations in Chapter 4 informed the initial conditions for the GDFNs. In particular, it was assumed that, under a tensile boundary condition, fractures that are perpendicular to the direction of maximum stress will grow the most. If a fracture is inclined, it will to grow at a slower rate compared to fully perpendicular fractures. Therefore, by seeding a domain with two sets of fractures, flat and inclined respectively, a more complex dataset could be created with greater vertical connectivity. The vertical fractures can be thought of as originating from an earlier phase of deformation. The simulated phase then grows a set of fractures with new orientations, and potentially activates the pre-existing fractures. An example of this in an isolated case is shown in Figure 6.3.

| GDFN | Total fractures ($n_{f,\text{initial}}$) | Horizontal fractures (Set one) | Inclined fractures (Set two) | Final step | Initial $P_{32}$ | Final $P_{32}$ | Equivalent $n_{f,\text{final}}$ |
|---|---|---|---|---|---|---|---|
| A | 30 | 25 | 5 | 31 | 0.015 | 0.28 | 588 |
| B | 30 | 25 | 5 | 55 | 0.015 | 0.37 | 749 |
| C | 60 | 50 | 10 | 34 | 0.029 | 0.43 | 881 |
| D | 60 | 50 | 10 | 42 | 0.029 | 0.48 | 986 |
| E | 90 | 75 | 15 | 19 | 0.044 | 0.43 | 867 |
| F | 90 | 75 | 15 | 12 | 0.044 | 0.37 | 757 |

TABLE 6.3: Summary of generated geomechanical fracture networks (GDFNs). Horizontal fractures have normal (0, 0, 1) and initial radii of 0.5 m, and inclined fractures have normal (4, 5, 1) and initial radii of 2.5 m. The final column ($n_{f,\text{final}}$) gives the equivalent number of fractures, with average radii equal to the initial state, that volume would need to contain to have the same $P_{32}$ as the final state (see Equation 6.1). Values in the sixth and seventh columns are rounded to two significant figures, and the eighth column to three significant figures.

Each GDFN is generated with the same material properties and numerical parameters, with only the initial number of fractures changing in each case. Fractures are placed such that fracture centres are at least 1 m apart, but can still initially intersect (*i.e.*, vertical fractures can initially intersect horizontal fractures). Each GDFN is named with a letter (A-F) and the initial fractures, final growth step, and final $P_{32}$ are shown in Table 6.3. The datasets are in three pairs which each have the same number of initial fractures, but between each pair, there are significant differences in final step number and $P_{32}$.

The smaller GDFNs (A and B) started with 30 fractures, and grew for a relatively large number of steps. The stopping criterion (when no fracture tips grow further) is met at steps 31 and 55 respectively. The random placement of fractures in each domain leads to different growth paths, with fractures arresting against other fractures or boundaries at different growth steps. Therefore, the final fracture density in GDFN A and B is different, despite the same number of initial flaws being used in both volumes. The same trend can be observed in the other GDFNs. GDFN B reaches a much higher density than A due to taking many more steps for growth to finish. GDFNs seeded with the most fractures tend to grow for fewer steps, but reach fracture densities similar to other GDFNs with fewer initial fractures. This suggests that, as more initial fractures are added, a critical density is reached. At this point, fractures in the present GDFN have fully intersected boundaries, other fractures, or are shadowed such that they no longer meet the mixed mode failure criterion anywhere.

Because the number of fractures in each GDFN during growth does not vary, these DFNs are not straightforward to compare to stochastic datasets. A simple comparison would

be to assume that, for each GDFN, an equivalent DFN could be created which used the same fracture properties as its initial state, with enough fractures to reach the fracture intensity of the final growth step. This equivalent number of initial fractures in the final step (equivalent $n_{f,\text{final}}$) is calculated as follows,

$$n_{f,\text{final}} = \text{P}_{32,\text{final}} \frac{\text{P}_{32,\text{initial}}}{n_{f,\text{initial}}} \tag{6.1}$$

where $\text{P}_{32,\text{final}}$ is the $\text{P}_{32}$ of the final step, $\text{P}_{32,\text{initial}}$ is the $\text{P}_{32}$ of the initial step, and $n_{f,\text{initial}}$ is the initial number of fractures in the dataset. This is given as the last column in Table 6.3, and demonstrates the significant increase in the density of the dataset. During growth, the equivalent of between one to two orders of magnitude more fractures are added to the dataset. GDFN A observes the smallest increase, from 30 to 558.34 fractures, and GDFN D observes the largest, from 60 to 985, *i.e.*, $n_{f,\text{final}}$ is higher when the final $\text{P}_{32}$ of a GDFN is higher. Furthermore, the geometric arrangement of these additional surfaces has significant impacts on the network's flow properties, as examined in Section 6.4.

### 6.3.1 Changes in geometry during growth GDFNs

This section shows the geometry and statistics of the six GDFNs during growth. Different GDFNs are selected for each visualisation and statistical analysis in this section. All six GDFNs are analysed in terms of their effective permeability in Section 6.4. For clarity, DFNs in this section are visualised as opaque planes rather than the individual triangular elements on their surfaces, or the surface meshes which discretise them. Geometries are rendered in CAD software, which is also used for post-processing of intersections in Section 6.4.3. To improve three-dimensional interpretation of the internal structure of the datasets, the rendering process simulates a light source, such that some fractures will cast shadows onto others. This light source's position is relative to the particular viewpoint used to capture each image, offset to the left. Therefore, the shadows move position depending on the viewpoint and can vary between different viewing angles.

The initial and final geometries of the six GDFNs are shown in Figures 6.6, 6.7, and 6.8. Fractures are coloured by set, with horizontal fractures in red and inclined fractures in blue. In all six GDFNs, the initial state is a random cluster of fractures, with clear increases in final fracture intensity with the initial number of fractures present. In the final steps, the fractures have grown to fill the volume, with many horizontal fractures intersecting each of the side boundaries. From the top down view, only in the corners of the domains are there regions in which fractures have not filled the domain fully.

Fractures which intersect along some of their surfaces can become elongated, as growth continues on the rest of the fracture, whilst the intersected tips remain deactivated and stationary. In all GDFNs, the initially inclined fractures have activated and grown surfaces oriented perpendicular to the stress direction, in the same way as the inclined fracture in Figure 6.3 activates.

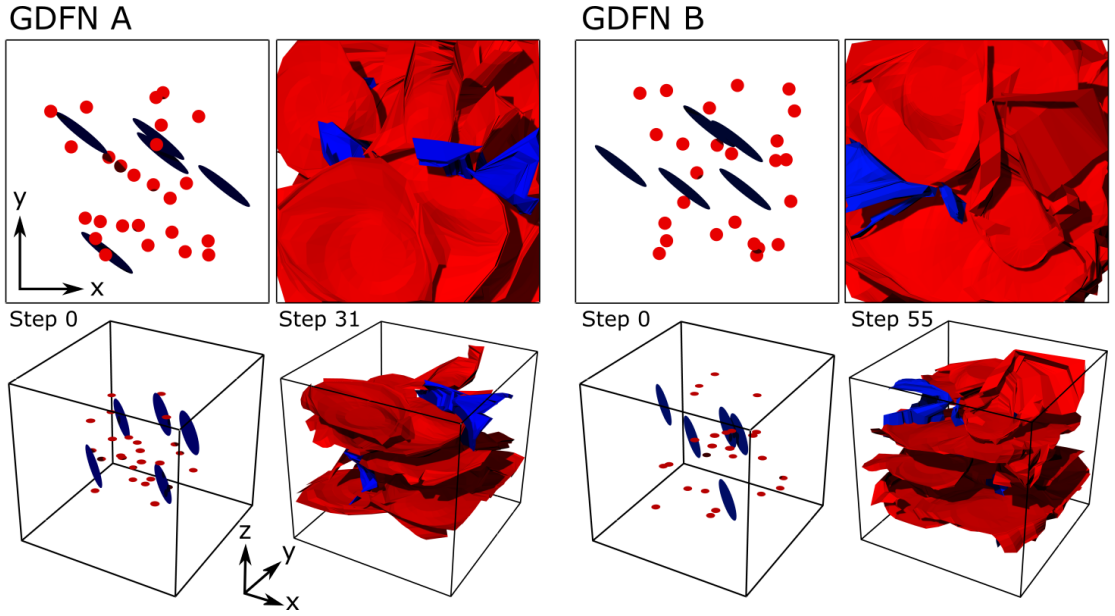



FIGURE 6.6: Initial and final geometries of GDFNs A and B, each containing thirty initial fractures. Each step is shown from above and from an isometric viewpoint. Fractures are coloured based on their initial size and inclination - red fractures are initially horizontal and blue fractures are initially inclined (see Table 6.3). The cubic domain has sides of length 20 m.

The majority of fracture growth in the GDFNs is horizontal (perpendicular to the stress direction), however, there are many fractures whose growth deviates from the horizontal plane. Some fracture surfaces become curved, particularly in later growth stages and near boundaries. There are several reasons for the development of this curvature. In each case, finding an exact reason for the development of curvature is not straightforward, due to the complexity of how fractures interact in very dense domains, which will influence both the magnitude of stress at fracture tips and the angle of growth. Even in GDFN A and B with thirty fractures each, all fractures are shadowed to some extent by others. Overlapping fractures are widely observed to re-orient themselves to grow into space which is further away from other fractures (*e.g.*, Section 4.5). The entire domain experiences fracture overlapping to some extent, therefore, widespread curvature should be expected.

Some curvature is the result of the initial fracture orientations, particularly for the inclined fractures, where growth in perpendicular to the direction of stress results in curvature from their initial inclination. More of the curvature arises closer to the top

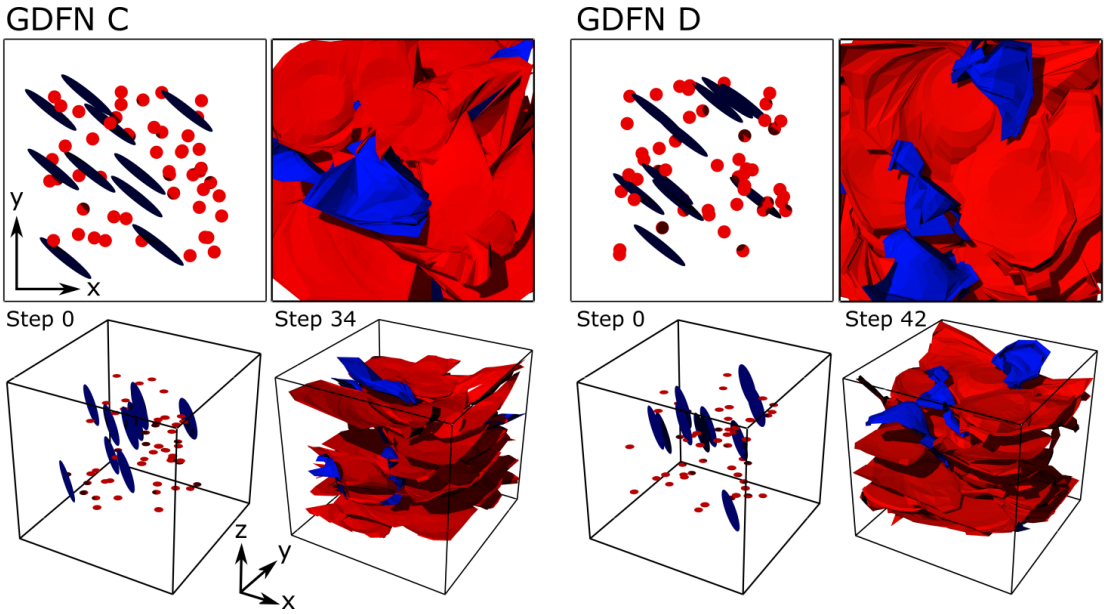



FIGURE 6.7: Initial and final geometries of GDFNs C and D, each containing sixty initial fractures. Each step is shown from above and from an isometric viewpoint. Fractures are coloured based on their initial size and inclination - red fractures are initially horizontal and blue fractures are initially inclined (see Table 6.3). The cubic domain has sides of length 20 m.

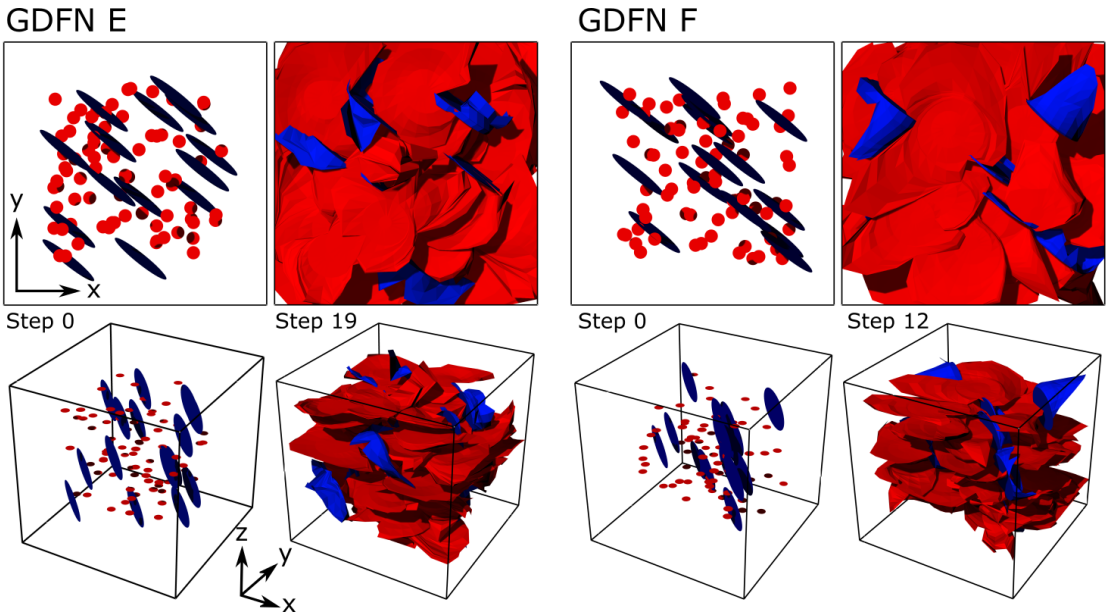



FIGURE 6.8: Initial and final geometries of GDFNs E and F, each containing ninety initial fractures. Each step is shown from above and from an isometric viewpoint. Fractures are coloured based on their initial size and inclination - red fractures are initially horizontal and blue fractures are initially inclined (see Table 6.3). The cubic domain has sides of length 20 m.

of the domains, where the tensile boundary condition is applied. This is a boundary effect on the SIFs, as identified and examined in Section 2.6. Boundary intersections are required to examine percolation between the boundaries, therefore, the influence on the

boundary on the present GDFNs should be considered before they are directly compared to real subsurface networks, which will lack boundary truncation and curvature effects. The influence of boundaries on the present GDFNs is discussed further in Section 6.6.1. Few fractures grow to intersect the top boundary, with only one fracture growing upwards in GDFNs A, D, and E. In comparison, fractures generally do not grow or curve towards the bottom of the domain, due to the asymmetric boundary condition where tensile stress is applied to the top of the volume, and the bottom of the domain is fixed. Therefore, whilst the final domain is well connected horizontally, the fractures do not provide a connected pathway from the top to the bottom of the domain.

#### 6.3.1.1 Changes in geometry of GDFN B in detail

Figures 6.9 and 6.10 shows the growth of GDFN B from its initial state to the final growth step. Figure 6.9 shows the initial state and the first 5 growth steps, and Figure 6.10 shows growth steps in larger intervals. Growth in the initial steps is concentrated on the horizontal fractures, which extend quickly within the first five steps. From a top-down perspective, by step 5 the domain becomes almost completely filled with fractures. Growth is fairly uniformly distributed in step 1, but in step 2, fracture sizes become more varied. For example, at the top of the domain, two fractures at the top grow much less than fractures lower down. This demonstrates stress shielding induced by the larger fractures, and shows that the earliest growth steps are critically important for determining late stage geometries.

In the early steps (Figure 6.9), an inclined fracture (blue) can be seen to activate and grow surfaces which are perpendicular to the stress direction, but only at the tips that are closest to other fractures and the top of the domain. This preferential activation may be due to the higher stress values closer to where the boundary condition is set, or due to the horizontal fractures which grow close to the upper tips of the fractures, or a combination of both.

In the later steps (Figure 6.10), the area of new fracture surfaces added in each step reduces. Most fractures have become intersected, either with the boundary, or against other fractures. The majority of new surfaces that are added are not horizontal, with some fractures acquiring irregular shapes. For example, a fracture at the top of the volume, which was initially smaller in steps 5 and step 10, only grows on one side, and begins to curve upwards in steps 20 to 30. The large fractures which shadow it have mostly stopped growing, or grow slowly in other places. Therefore, as long as its fracture tips meet the failure criterion of the material, this upper fracture can grow preferentially towards regions where the energy at the fracture tip is maximised, *i.e.*, increasing the

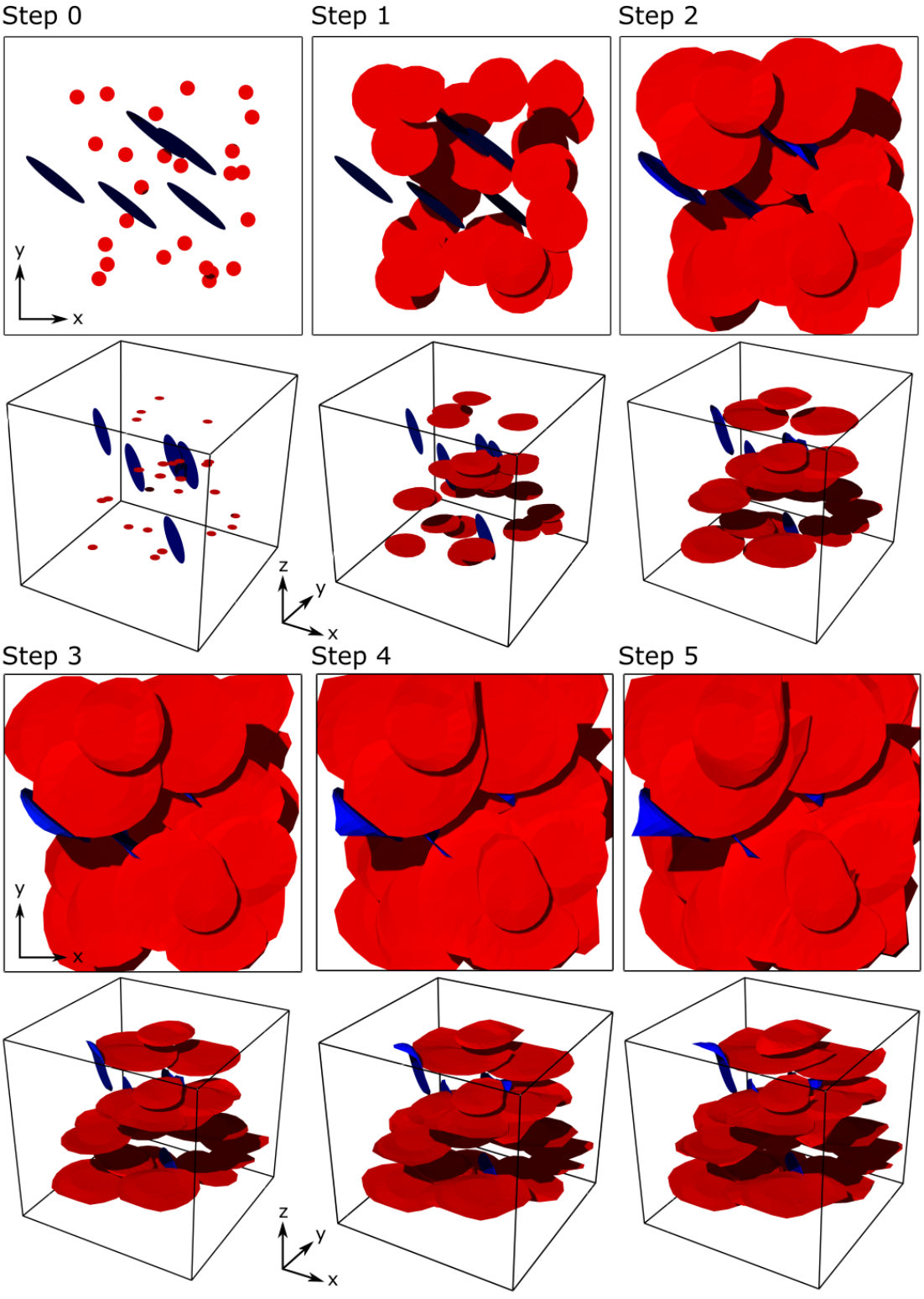



FIGURE 6.9: Growth steps from 0 to 5 for GDFN B, visualised from top-down and perspective viewpoints. Initially horizontal fractures in set one are coloured red, and initially inclined fractures in set two are coloured blue (see Table 6.3). Darker regions are shaded relative to a light source to the upper left of each viewpoint. The cubic domain has sides of length 20 m.

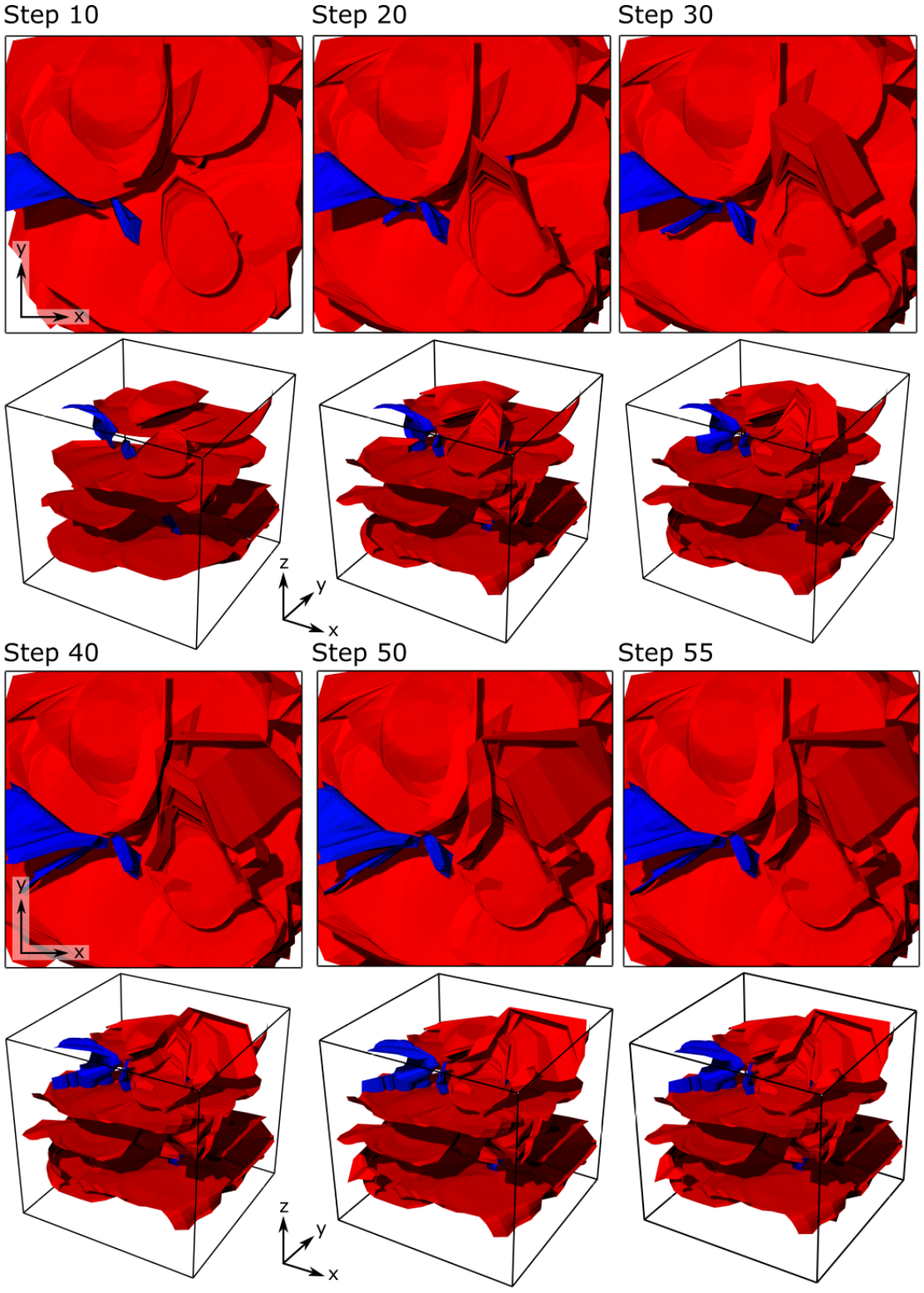



FIGURE 6.10: Selected growth steps from 10 to 55 for GDFN B, visualised from top-down and perspective viewpoints. Fractures in set one are coloured red, and fractures in set two are coloured blue (see Table 6.3). Darker regions are shaded relative to a light source to the upper left of each viewpoint. The cubic domain has sides of length 20 m.

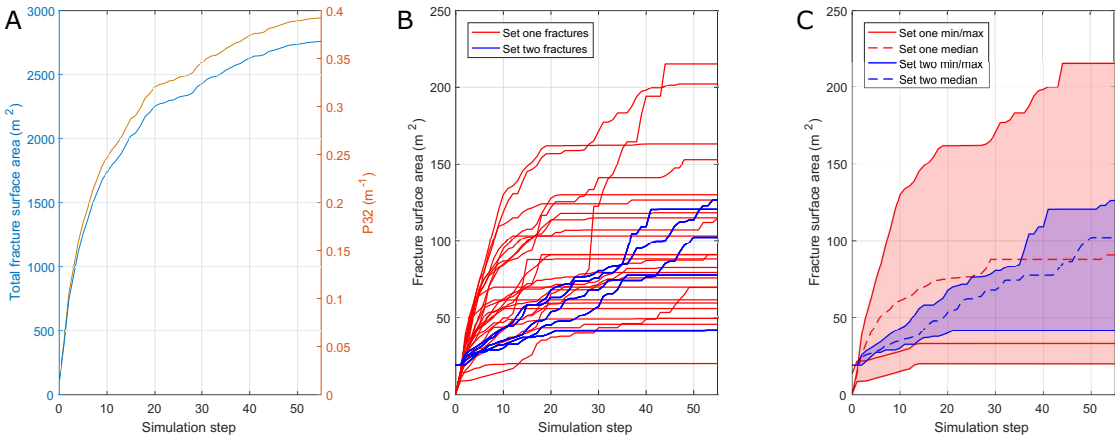



FIGURE 6.11: Fracture surface area statistics from GDFN B (Table 6.3). A: Change in fracture intensity with simulation step, quantified with the total fracture surface area (left axis) and $P_{32}$ (right axis). B: Change in surface area on individual fractures, sorted into the two sets. Set one fractures are initially flat and have radius 0.5 m, and set two fractures are initially inclined and have radius 2.5 m (see Table 6.3). C: Fracture surface areas as shown in B, showing only the minimum, maximum and median fractures in each of the fracture sets.

separation between itself and the shadowing fractures beneath it. In steps 40 to 55, it continues to grow significantly. The initially inclined fractures develop complex surfaces which continue to grow where they do not intersect. In the last steps shown, two different fractures produce the surfaces in the upper left of the isometric views.

### 6.3.2 Statistical analysis of fracture geometry during GDFN growth

The statistics of the GDFN B's geometry are shown in Figure 6.11 in three graphs, illustrating how fracture surface area changes during the growth of GDFN B. To demonstrate the similarities between how growth progresses between different GDFNs, Figure 6.12 shows the same graphs for GDFN C, which starts with 60 rather than 30 fractures. All graphs plot fracture surface areas, either for individual fractures or as a sum for the whole volume, and $P_{32}$, against simulation step.

Figure 6.11A shows the simulation step against two measures of fracture intensity (total fracture surface area and $P_{32}$). These are essentially the same value, where the $P_{32}$ is the total fracture surface area divided by the total volume of rock (8000 $m^3$). These results follow a curve with a reducing gradient during the simulation. In the early steps, the increase in fracture surface area is rapid, with approximately 80% of the surface area being present by the 20th growth step. The curve is not smooth, as the growth rate per step increases around step 30 after falling at step 20. Eventually the curve becomes flat at the final step, where the end condition is met (*i.e.*, no more fractures extend).

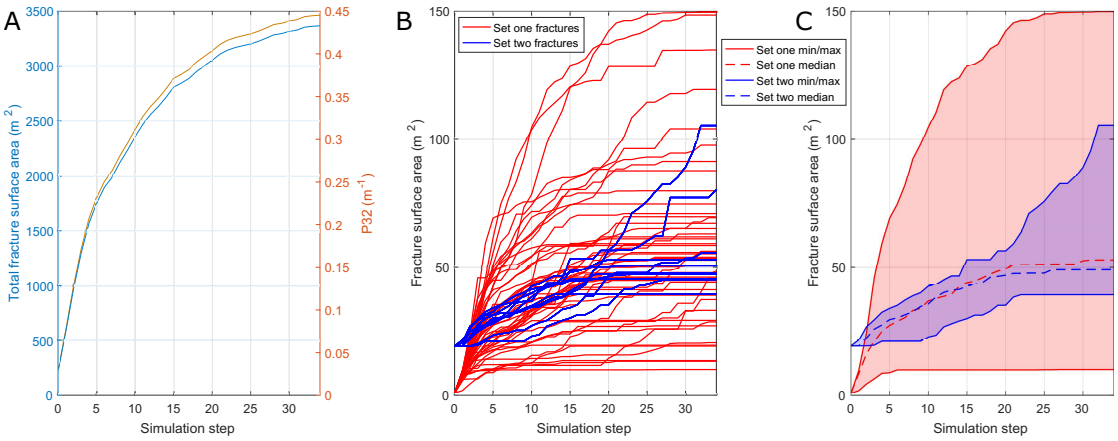



FIGURE 6.12: Fracture surface area statistics from GDFN C (Table 6.3). A: Change in fracture intensity with simulation step, quantified with the total fracture surface area (left axis) and $P_{32}$ (right axis). B: Change in surface area on individual fractures, sorted into the two sets. Set one fractures are initially flat and have radius 0.5 m, and set two fractures are initially inclined and have radius 2.5 m (see Table 6.3). C: Fracture surface areas as shown in B, showing only the minimum, maximum and median fractures in each of the fracture sets.

Changes in total fracture surface area added per step can be examined in Figure 6.11B, which plots the surface area of each fracture over simulation time. Fractures are coloured by set, and at step 0, the difference in the initial surface areas of each set can be seen. Fractures in set one, which are horizontal and smaller, grow quickly in the first ten steps. They are clearly responsible for the initial sharp rise in $P_{32}$. Fractures in set two grow at a more steady rate throughout the simulation. Each fracture's surface area can be seen to increase, then plateau at a step when all their fracture tips become inactive or no longer fail.

Towards the later growth steps, fractures in the GDFN gradually finish growing. Some fractures finish growing relatively early in the simulation. For example, the set one fracture which ends with the lowest surface area stops growing at step 11. The third largest set one fracture stopped growing in step 19. Other fractures grow more quickly once others become inactive, for example, the largest set one fracture experiences a large increase in growth at step 30. This explains why the $P_{32}$ against simulation step curve was not smooth at this step. This sudden increase in growth rate is the result of the Paris-based growth criterion used throughout this work (Section 4.2). Fracture tips with the largest stress intensity factors grow the most. If tips that were previously the most energetic in the volume grow towards regions of stress reduction, or if they become inactive due to intersections, new tips in the domain will become the most energetic in their place. Therefore, fractures can experience increases in growth due to the deactivation or shielding of others in the volume.

Figure 6.11C shows the same data as in Figure 6.11B, but instead plots the maximum,

minimum, and median of each of the fracture sets. Set one fractures have a much wider range of final surface areas than those in set two. Whilst set one fractures are optimally inclined for growth, there are many more of them, and their initial small size means that if they deactivate early in the simulation, they remain small until the final step. Set two fractures start slightly larger than set one fractures, and grow at a slower rate, but eventually have a higher median fracture size than fractures in set one. Once a set two fracture propagates, new surfaces are added which are generally oriented in the same plane as set one fractures. Therefore, in this extended state, the flat part of the fracture is more optimally inclined for growth, leading to a similar median fracture size between the two sets.

By comparing the statistics of GDFN B and C (Figure 6.12), it is clear that growth occurs in a similar manner in both datasets. The main difference between the GDFNs is that, when there are more initial fractures, final step fracture surfaces areas are smaller (see Figure 6.12C, where the median fracture surface areas are lower). The curve of $P_{32}$ against simulation step is smoother, as no fractures experience significant additional growth in the later steps, unlike GDFN B. Despite the total number of steps being lower in GDFN C, the same surface area over simulation time relationship occurs in both cases. Therefore, by their final step, fractures in both of the GDFNs have made use of the available space for growth. All six GDFNs behave similarly in terms of $P_{32}$ and individual fracture surface area changes during growth.

### 6.3.3 Outcrop visualisation of GDFNs

Cut-planes provide a method for visualising the internal geometry of the fracture network, as used in Section 4.5.2. Figure 6.13 shows GDFN C in its 33$^{rd}$ growth step, and visualises the fractures on ten different cut-planes. The cut-planes are arranged uniformly around the central region of the domain, therefore, they include the regions where initial flaws were inserted, and where the domain has the highest fracture density. The cut-planes reveal the highly complex geometries of the fractures, and each share some similar properties.

Most of the fractures are horizontal set one fractures that have grown to cross about half of the domain. Inclined set two fractures are present all in the cut-planes. Set two fractures undergo significant changes in their propagation angle, sharply deviating from their initial planes. In some cut-planes, there are fractures which curve back onto themselves and terminate, both from set one and set two (*e.g.*, planes 1 and 7). Some of these unusual fracture paths may be the result of cut-planes intersecting fractures at

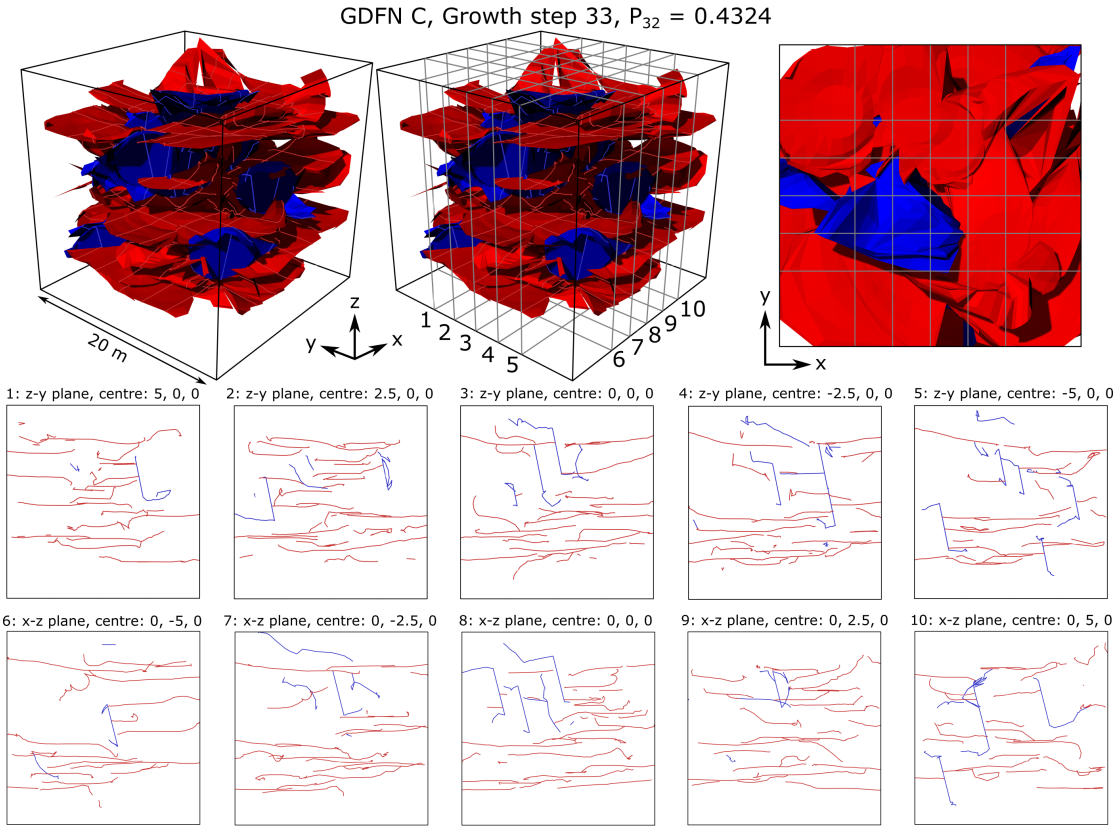



FIGURE 6.13: Ten cut-planes through GDFN C at growth step 33 (see Table 6.3). In the three-dimensional images, fractures are coloured by set (red fractures are in set one, blue fractures are in set two), and darker regions are shaded relative to a light source to the upper left of each viewpoint. The intersection of the cut-planes with the domain boundaries are shown in grey. In the cut-planes, the traces are coloured by the fracture set the fracture belongs to.

angles which enhance the curvature. In most cases, these paths are the results of fractures continually re-orienting themselves towards the direction which maximises stress at their tips, *i.e.*, avoiding regions of stress shielding.

Hydraulic properties can be inferred from the observed cut-planes. Many fracture intersections can be observed, and in other places fractures are very close but do not touch. Relatively few fractures cross-cut one another, with some exceptions visible in cut-planes 3, 9, and 10. All the cut-planes feature some fracture traces which are curved, and some traces are jagged with sharp changes in direction. From studying the cut-planes, it is clear that the domain percolates. Planes 3, 7, and 8 have explicit percolation paths, and it is reasonable to conclude that fractures that are close to intersecting would likely intersect in other possible cut-planes.

### 6.3.4 Fracture surface area frequency analysis

Fracture populations are often analysed using histograms [*e.g.*, Gonzalez-Garcia et al., 2000], or in graphs which compare frequency-length distributions [Hardebol et al., 2015]. The present fractures cannot be assigned a characteristic length, therefore, their surface areas are used to create histograms in Figure 6.14. Histograms at steps 0, 9, and 32 are shown, presenting the surface area data of GDFN C in a slightly different way to Figure 6.12. In step 0, the initial sizes of the fractures are clear, with set one fractures being the smallest, and set two being the largest. In step 9, almost all fractures have increased in size, with a single set one fracture remaining below 10 $m^2$. All of the set two fractures have grown as well. Two fractures in set one have grown to almost ten times their initial surface area. In step 32, the domain is near its final state, and the peak has moved further. The final distribution could be described as roughly normal, with a higher tail towards three high surface area set one fractures.

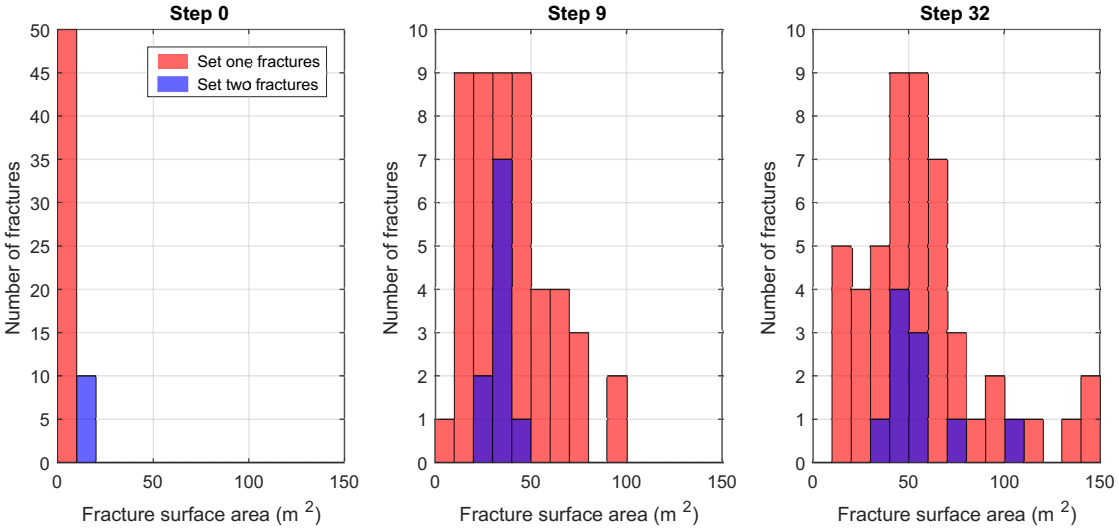



FIGURE 6.14: Histograms of fracture sizes at three steps (0, 9, and 32) and during the generation of the GDFN C. Fracture sets one and two are shown in different colours. Step 0 has a different $y$ axis limit to steps 9 and 32.

Figure 6.14 can be compared to real data, in particular, the example of Gonzalez-Garcia et al. [2000], who created and characterised a DFN inside a natural granite block using cut-plane analysis. As shown previously, Figure 6.1C and D are histograms of fracture surface areas, with and without boundary intersecting fractures. These have a different distribution to the present GDFNs, in particular, the peak observed fracture surface area is the smallest size category, rather than an intermediate value. This suggests that more growth occurs on more fractures in the GDFN than in a real network, or that there are too few fractures present in the GDFN to reproduce the distribution. By utilising additional computational recourses (*i.e.*, more simulation time and memory), the present networks could be grown with many more fractures, including distributions

of much smaller fractures. These small fractures may remain relatively small if they are shielded by other fractures, meaning a large number of fractures remain small in the domain, which would contribute to the lack of small fractures present in the GDFNs, and improve their realism. A similarity is that large fractures in the GDFN develop to a similar relative size as in the granite block, providing the high tail of the distribution. Further discussion on the differences between GDFNs, kinematic networks, and real networks can be found in Section 6.6.3.

## 6.4 Hydraulic properties of geomechanical discrete fracture networks with uniform fracture apertures

For each GDFN (A-F), the permeability calculation method introduced in Chapter 5 was applied to the geometry at each growth step. The medium is assigned a constant matrix permeability of $10^{-15}$ m$^2$, and fractures are assigned constant apertures of 0.001 m, leading to a fracture permeability of $8.33 \times 10^{-11}$ m$^2$. These parameters are chosen to set a high contrast between flow in fractures and flow in the matrix, such that the percolation threshold is clear, and the effects of the fracture network are more significant relative to the background matrix flow. The geometries from each GDFN's growth step are used to generate new meshes at a higher mesh refinement than the mechanics. The influence of mesh refinement on the permeability results is examined for GDFN F in Section 6.4.4.

Ebigbo et al. [2016] provide a method for characterising a fracture network's permeability independently from its fracture intensity. This can be applied to the present GDFNs to estimate their hydraulic properties with uniform apertures, and put their behaviour in context with other flow simulations in literature. Ebigbo et al. use the ratio between two parameters of the network to characterise three-dimensional DFNs containing elliptical fractures. These parameters are the fracture aspect ratio $\alpha$,

$$\alpha = \frac{h}{2a} \tag{6.2}$$

where $h$ is the fracture aperture and $a$ is the fracture radius, and the permeability ratio $\kappa$,

$$\kappa = \frac{k_m}{k_f}. \tag{6.3}$$

The ratio $\alpha/\kappa$ identifies the regime of flow in a fracture network. The properties in these two equations are fixed values in this section, except for the fracture radius, which does not have a simple value after growth of a GDFN's initial state. Representative radii can be chosen for different GDFN growth steps in order to examine the range of the $\alpha/\kappa$

ratio. For both early and late GDFN states, $\alpha/\kappa$ is consistently greater than 1. The highest ratio is found in growth step 0, where $a$ is the average initial fracture radii, and a representative late stage case would be a domain where a typical fracture's radius takes up the whole volume ($a = 10$ m). Both of these values of $a$ result in $\alpha/\kappa >> 1$. Ebigbo et al. demonstrate that, in networks where $\alpha/\kappa >> 1$, the pressure distribution and flow in the domain will be dominated by the fracture network, and distinct percolation thresholds will be observed.

The results of the uniform aperture flow simulations are shown in several figures in this chapter. Tables 6.4 and 6.5 show the numerical results of flow in GDFN E. The eigenvalues and eigenvectors are given in columns 3 to 6, and the permeability along each of the coordinate axes are given in columns 7 to 9. These directional permeabilities are later shown in graph form in Section 6.4.2. In the first step, the volume is unaffected by the presence of fractures, with a relatively isotropic effective permeability tensor, with slightly higher vertical permeability due to the larger set two fractures.

Percolation occurs in GDFN E in step 4, where the horizontal permeabilities ($k_{xx}$ and $k_{yy}$) increase from around $10^{-14}$ to $10^{-12}$ m$^2$. In the later steps, the horizontal permeabilities subsequently increase by an additional order of magnitude to $1.85 \times 10^{-11}$ m$^2$. Slower increases in permeability coincide with the reduced fracture intensity increases in later steps. Furthermore, the volume will approach a limit in the possible maximum permeability, as the overall number of horizontal fractures that connect the boundaries does not change significantly in the later growth stages. In GDFN E, percolation occurs along both axes at the same step, but in other GDFNs (A, C, D, and F), percolation can occur along one horizontal axis before the other (see Figure 6.17).

The vertical permeability ($k_{zz}$) does not experience a similar increase, and instead fluctuates between $10^{-15}$ and $10^{-14}$ m$^2$. Most of the additional fracture surfaces that are added are along the horizontal axis, and because these surfaces do not contribute to flow along the vertical axis, they can create flow paths that lead to lower overall vertical permeability, even when the overall fracture intensity increases. These percolation properties are consistent with conclusions drawn from analysis of GDFN cut-planes in Figure 6.13, where connected horizontal flow paths are widely observed, but no fractures intersect the bottom or the top of the domain.

### 6.4.1 Visualisation of GDFN effective permeability using ellipsoids

Figure 6.15 visualises the effective permeability tensors of GDFN E as ellipsoids, alongside the geometry at each step. Three vectors are created by multiplying the eigenvectors by their respective eigenvalues. The ellipsoid is formed by using the eigenvectors as its

| Step | $k_i$ | $k$ (m$^2$) | $x$ | $y$ | $z$ | $k_{xx}$ (m$^2$) | $k_{yy}$ (m$^2$) | $k_{zz}$ (m$^2$) |
|---|---|---|---|---|---|---|---|---|
| 0 | $k_1$ | 1.01E-15 | 0.62 | 0.77 | 0.16 | 1.17E-15 | 1.11E-15 | 1.21E-15 |
| | $k_2$ | 1.21E-15 | -0.03 | 0.23 | -0.97 | | | |
| | $k_3$ | 1.26E-15 | 0.79 | -0.60 | -0.17 | | | |
| 1 | $k_1$ | 1.27E-15 | 0.23 | -0.27 | 0.94 | 1.61E-15 | 1.61E-15 | 1.30E-15 |
| | $k_2$ | 1.54E-15 | -0.68 | 0.64 | 0.35 | | | |
| | $k_3$ | 1.71E-15 | 0.70 | 0.72 | 0.04 | | | |
| 2 | $k_1$ | 1.72E-15 | -0.18 | -0.03 | 0.98 | 2.99E-15 | 2.86E-15 | 1.76E-15 |
| | $k_2$ | 2.84E-15 | -0.33 | 0.94 | -0.03 | | | |
| | $k_3$ | 3.05E-15 | 0.93 | 0.33 | 0.18 | | | |
| 3 | $k_1$ | 1.89E-15 | -0.05 | 0.03 | 1.00 | 5.84E-15 | 1.03E-14 | 1.90E-15 |
| | $k_2$ | 5.52E-15 | -0.97 | 0.25 | -0.05 | | | |
| | $k_3$ | 1.06E-14 | 0.25 | 0.97 | -0.02 | | | |
| 4 | $k_1$ | 1.27E-15 | 0.03 | 0.04 | 1.00 | 1.25E-12 | 2.34E-12 | 5.63E-15 |
| | $k_2$ | 1.18E-12 | 0.97 | 0.23 | -0.04 | | | |
| | $k_3$ | 2.41E-12 | 0.23 | -0.97 | 0.03 | | | |
| 5 | $k_1$ | -6.67E-15 | -0.03 | 0.05 | 1.00 | 3.44E-12 | 3.62E-12 | 4.57E-15 |
| | $k_2$ | 3.39E-12 | 0.90 | 0.43 | 0.01 | | | |
| | $k_3$ | 3.68E-12 | 0.43 | -0.90 | 0.05 | | | |
| 6 | $k_1$ | 2.18E-16 | 0.03 | 0.02 | 1.00 | 5.79E-12 | 5.02E-12 | 9.62E-15 |
| | $k_2$ | 4.60E-12 | -0.51 | 0.86 | 0.00 | | | |
| | $k_3$ | 6.21E-12 | 0.86 | 0.51 | -0.04 | | | |
| 7 | $k_1$ | 1.66E-15 | 0.03 | 0.01 | 1.00 | 7.41E-12 | 7.33E-12 | 1.10E-14 |
| | $k_2$ | 6.66E-12 | -0.68 | 0.73 | 0.02 | | | |
| | $k_3$ | 8.08E-12 | 0.73 | 0.68 | -0.03 | | | |
| 8 | $k_1$ | 3.91E-15 | -0.02 | 0.00 | 1.00 | 8.29E-12 | 9.11E-12 | 8.02E-15 |
| | $k_2$ | 8.07E-12 | 0.91 | 0.42 | 0.02 | | | |
| | $k_3$ | 9.34E-12 | 0.42 | -0.91 | 0.01 | | | |
| 9 | $k_1$ | 1.30E-15 | -0.04 | 0.00 | 1.00 | 9.49E-12 | 9.52E-12 | 1.37E-14 |
| | $k_2$ | 9.14E-12 | -0.71 | 0.70 | -0.03 | | | |
| | $k_3$ | 9.89E-12 | 0.70 | 0.71 | 0.03 | | | |

TABLE 6.4: Effective permeability of GDFN E from step 0 (the initial state) to growth step 9. Several permeabilities are given for each step. The permeability tensor is given by its eigenvalues ($k_i$, $i$=1, 2, 3) and eigenvectors (with directions $x$, $y$, and $z$). permeabilities in the $x$, $y$, and $z$ directions ($k_{xx}$, $k_{yy}$, and $k_{zz}$) are given. Steps 10 to 19 are given in Table 6.5.

| Step | $k_i$ | $k$ ($m^2$) | $x$ | $y$ | $z$ | $k_{xx}$ ($m^2$) | $k_{yy}$ ($m^2$) | $k_{zz}$ ($m^2$) |
|---|---|---|---|---|---|---|---|---|
| 10 | $k_1$ | 1.79E-15 | -0.03 | -0.01 | 1.00 | 1.09E-11 | 1.12E-11 | 1.45E-14 |
| | $k_2$ | 1.05E-11 | 0.80 | 0.60 | 0.03 | | | |
| | $k_3$ | 1.16E-11 | 0.60 | -0.80 | 0.01 | | | |
| 11 | $k_1$ | 3.95E-16 | 0.03 | 0.01 | 1.00 | 1.13E-11 | 1.26E-11 | 9.55E-15 |
| | $k_2$ | 1.13E-11 | 0.99 | 0.10 | -0.03 | | | |
| | $k_3$ | 1.26E-11 | 0.10 | -0.99 | 0.01 | | | |
| 12 | $k_1$ | 7.72E-16 | -0.03 | -0.02 | 1.00 | 1.24E-11 | 1.38E-11 | 1.49E-14 |
| | $k_2$ | 1.22E-11 | 0.94 | 0.34 | 0.04 | | | |
| | $k_3$ | 1.40E-11 | 0.34 | -0.94 | -0.01 | | | |
| 13 | $k_1$ | 4.46E-16 | -0.03 | -0.02 | 1.00 | 1.28E-11 | 1.40E-11 | 1.48E-14 |
| | $k_2$ | 1.26E-11 | 0.96 | 0.29 | 0.03 | | | |
| | $k_3$ | 1.41E-11 | 0.29 | -0.96 | -0.01 | | | |
| 14 | $k_1$ | 5.25E-16 | -0.03 | -0.02 | 1.00 | 1.33E-11 | 1.41E-11 | 1.75E-14 |
| | $k_2$ | 1.28E-11 | 0.86 | 0.52 | 0.04 | | | |
| | $k_3$ | 1.46E-11 | 0.52 | -0.86 | 0.00 | | | |
| 15 | $k_1$ | 2.95E-16 | 0.04 | -0.02 | 1.00 | 1.40E-11 | 1.46E-11 | 2.06E-14 |
| | $k_2$ | 1.34E-11 | -0.81 | 0.58 | 0.04 | | | |
| | $k_3$ | 1.51E-11 | 0.58 | 0.81 | -0.01 | | | |
| 16 | $k_1$ | 9.78E-16 | 0.04 | -0.01 | 1.00 | 1.50E-11 | 1.55E-11 | 1.98E-14 |
| | $k_2$ | 1.43E-11 | -0.79 | 0.61 | 0.04 | | | |
| | $k_3$ | 1.62E-11 | 0.61 | 0.79 | -0.01 | | | |
| 17 | $k_1$ | 2.01E-16 | -0.03 | -0.01 | 1.00 | 1.59E-11 | 1.63E-11 | 1.77E-14 |
| | $k_2$ | 1.54E-11 | 0.78 | 0.62 | 0.03 | | | |
| | $k_3$ | 1.69E-11 | 0.62 | -0.78 | 0.01 | | | |
| 18 | $k_1$ | 7.56E-15 | 0.00 | -0.03 | 1.00 | 1.51E-11 | 1.65E-11 | 7.89E-15 |
| | $k_2$ | 1.45E-11 | 0.88 | 0.48 | 0.02 | | | |
| | $k_3$ | 1.71E-11 | 0.48 | -0.88 | -0.03 | | | |
| 19 | $k_1$ | 1.55E-14 | 0.01 | -0.03 | 1.00 | 1.87E-11 | 1.85E-11 | 2.50E-15 |
| | $k_2$ | 1.76E-11 | -0.67 | 0.74 | 0.03 | | | |
| | $k_3$ | 1.96E-11 | 0.74 | 0.67 | 0.01 | | | |

TABLE 6.5: Effective permeability of GDFN E from step 10 (the initial state) to growth step 19. Several permeabilities are given for each step. The permeability tensor is given by its eigenvalues ($k_i$, $i$=1, 2, 3) and eigenvectors (with directions $x$, $y$, and $z$). permeabilities in the $x$, $y$, and $z$ directions ($k_{xx}$, $k_{yy}$, and $k_{zz}$) are given. Steps 0 to 9 are given in Table 6.4.

axes. The ellipsoid therefore does not predict permeability values in all directions, rather, it serves as a way to visualise the tensor in three dimension with respect to the geometry of the domain. The two early growth steps shown (0 and 1) demonstrate that the tensor is initially relatively isotropic, with all three vectors having similar magnitudes.

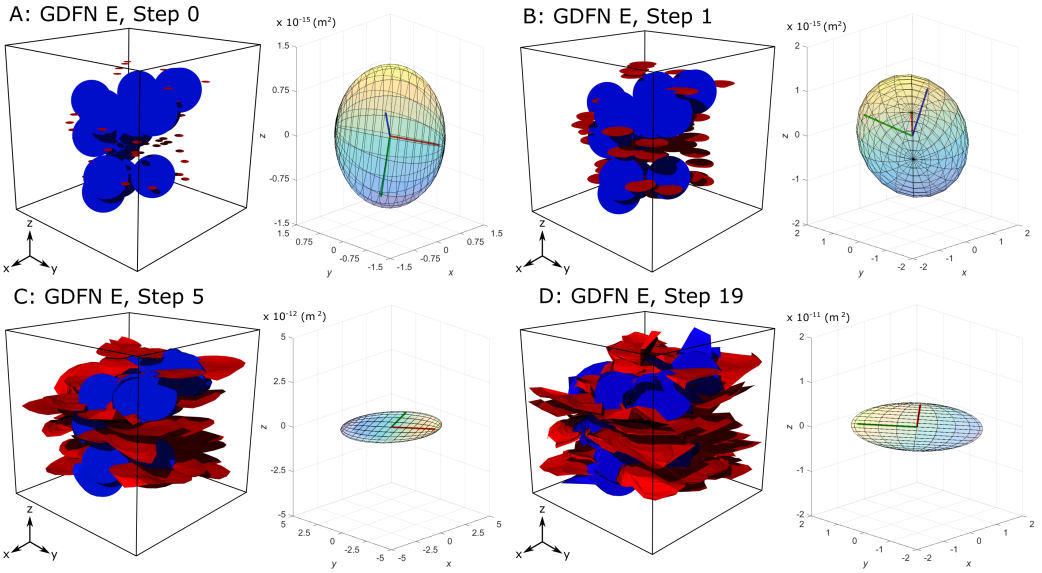



FIGURE 6.15: Geometry and ellipsoid visualisation of the effective permeability tensor from GDFN E at steps 0 (A), 1 (B), 5 (C), and 19 (D). The fractures are coloured by set, with set one fractures being red, and set two fractures being blue. The surface of the ellipsoid are transparent, so when it has significant volume (in step 0 and step 1), the grid on its surface is visible from the other side. The vectors are shown as lines with length equal to their magnitude, and are coloured blue, green, and red in ascending order of magnitude. To visualise the ellipsoids and vectors at similar sizes, the axes limits are different in each plot.

Step 5 shows the network at the point at which it begins to percolate, and because the horizontal permeabilities increase by two orders of magnitude, the tensor and its ellipsoid changes to a flat shape. The directions of the two large eigenvectors changes between steps 5 and 19, and Table 6.5 shows these directions change more gradually in the intermediate steps.

### 6.4.2 Flow comparison with stochastic discrete fracture networks

In this section, the geometric and hydraulic properties of GDFNs are compared to stochastic discrete fracture networks (SDFNs) in order to quantitatively examine how a grown network is similar or is different from a random network.

| SDFN set | Number generated | Fracture radius (m) | Fracture orientation | Fracture insertion boundaries |
|---|---|---|---|---|
| 1 | 81 | Fixed<br>4.2787 | Random | $x = \pm 11$<br>$y = \pm 11$<br>$z = \pm 11$ |
| 2 | 141 | Normal distribution<br>Mean 4.1411<br>SD 1.0854 | Random | $x = \pm 11$<br>$y = \pm 11$<br>$z = \pm 11$ |
| 3 | 114 | Fixed<br>4.2787 | Set one: (0, 0, 1)<br>(5 in 6 fractures)<br>Set two: (4, 5, 1)<br>(1 in 6 fractures) | $x = \pm 11$<br>$y = \pm 11$<br>$z = \pm 8$ |

TABLE 6.6: Description of stochastic discrete fracture networks (SDFNs) generated for comparison with geomechanical DFNs. Standard deviation is abbreviated to SD. Fracture orientations are given as vectors normal to the inserted fracture's plane.

#### 6.4.2.1 Stochastic network generation

Three sets of SDFNs, summarised in Table 6.6, are generated with a range of different set-up parameters to create a range of comparison datasets. Each set uses a different flaw insertion method to provide a range of comparison datasets with different properties. Disks are randomly inserted into the same initial domain used to create GDFNs (an empty 20 × 20 × 20 m cube). Random ($x$, $y$, $z$) coordinates for fracture centres are generated using the uniform random number generator in the C++ standard library. The fracture sizes and limits of the placement of the fracture centres vary between the groups of SDFNs. The number of fractures is varied to provide a range of fracture intensities, up to the highest fracture intensity reached by the GDFNs. The distribution of fractures is made psuedo-random, because fracture centre locations which would be placed less than 1 m away from another fracture's centre are reselected automatically. This avoids fractures overlapping significantly, which would create redundant fracture intensity.

Statistics from the final geometry of GDFN C are used to generate SDFNs, with GDFN C chosen because it reaches a relatively high fracture density in its final steps. Stochastic domains are generated with circular fractures, requiring a representative value for the radius from the GDFNs to create comparable networks. Most of the fractures in the final domains are roughly circular, therefore, fracture surface area values are converted to an approximate radius using the relationship $r = \sqrt{A/\pi}$, where A is the mean fracture surface area. This method results in a median radius of 4.05 m and mean radius of 4.28 m for fractures in GDFN C. SDFNs and GDFNs are compared in terms of $P_{32}$ rather than the number of fractures, because GDFNs have fixed fracture numbers but changing intensities over time.

Datasets in SDFN set one contain fractures with fixed radii of 4.28 m with random orientations. Fracture centres are allowed within a 11 × 11 × 11 m cube, centred at the centre of the domain boundaries, such that fractures can partially intersect the domain. Datasets in SDFN set two use the same generation method as SDFN set 1, but instead of fixed sized fractures, they contain fractures with variable radii, distributed normally around a mean of 4.14 with a standard deviation of 1.09. Datasets in SDFN set three uses the same fixed fracture sizes as set one, but contain fractures in two sub-sets: five out of six fractures are in sub-set one and are horizontal, and one in six fractures in sub-set two are inclined. These orientations match the initial flaw distributions used to create the GDFNs, and therefore SDFN set three provides a more direct comparison to the GDFNs. The $\alpha/\kappa$ in all three SDFN sets is much greater than 1, therefore, a similar flow pattern to the GDFNs can be expected across all densities [Ebigbo et al., 2016].

The geometry of six example SDFNs from each of the three sets are shown in Figure 6.16. Both low fracture intensity (A, C, and E) and a high fracture intensity (B, D, and F) SDFNs are shown. Examining the three-dimensional geometry in the high intensity cases, it is clear the network will percolate, although only one of the cut-planes shown has a percolating path (D). The cut-planes from SDFN set three provides the closest comparison to the GDFN cut-planes (Figure 6.13). SDFN set three reproduces the approximate ratio of horizontal to inclined fractures, with fractures are marginally more clustered together in the stochastic network.

#### 6.4.2.2 Directional permeabilities of geomechanical and stochastic discrete fracture networks

The effective and directional permeabilities of the SDFNs were calculated. Each SDFN set's permeability is compared to the permeability of GDFN individually, producing eighteen graphs, which are grouped by SDFN set in Figures 6.17, 6.18, and 6.19. Each figure contains six subplots with the same SDFN directional permeability values ($k_{xx}$, $k_{yy}$, and $k_{zz}$) as coloured dots. These directional permeabilities are the diagonal terms in the $\mathbf{k}_{ef}$ (Equation 5.1). Each subplot has the permeability results for a single GDFN across all of its growth steps, marked with crosses and connected with lines. The rest of this section analyses these graphs, contrasting the hydraulic properties of the GDFNs and SDFNs in several ways. GDFN and SDFN directional permeabilities are compared in this section, rather than the effective permeabilities, so that the axis along which flow is considered in each case is the same.

The GDFN directional permeability curves (which are the same in Figure 6.17, 6.18, and 6.19) provide the best way to compare the flow progression in the different GDFNs.

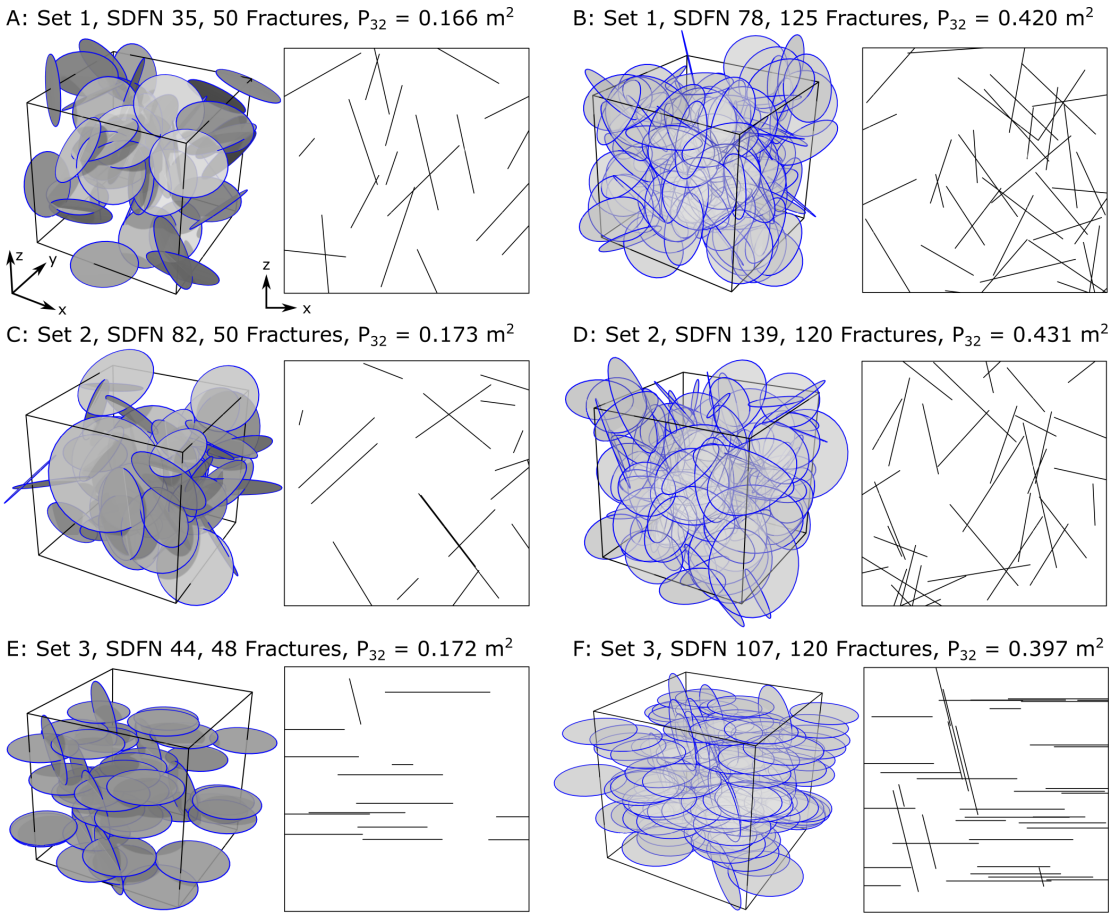



FIGURE 6.16: Geometries of six stochastic discrete fracture networks in perspective and cut-plane view. A and B are in SDFN set one, C and D are in set two, and E and F are in set three. Generation rules for each set shown in Table 6.6. Cut-planes are taken through the $x$-$z$ plane, passing through (0, 0, 0).

Several features are common to all six GDFNs. Step 0 corresponds to the lowest $P_{32}$ value, at which point all GDFNs begin with $k_{xx}$, $k_{yy}$, and $k_{zz}$ close to the matrix permeability ($10^{-15}$ m$^2$). Fracture growth increases the effective permeability in the subsequent steps, particularly the horizontal directions ($k_{xx}$ and $k_{yy}$). After 4 to 5 growth steps, fractures connect to form a percolating flow path from one horizontal boundary to its opposite boundary. This is seen as a large increase in $k_{xx}$, $k_{yy}$, or both $k_{xx}$ and $k_{yy}$ in the same step. Similar to the results for GDFN E analysed in Tables 6.4 and 6.5, percolation increases permeability from between $10^{-15}$ to $10^{-14}$ m$^2$ up to $10^{-12}$ m$^2$. Further growth steps after percolation increase the horizontal permeabilities by approximately one order of magnitude in all GDFNs.

#### 6.4.2.3 Percolation in GDFNs and SDFNs

The vertical axis does not fully percolate in any GDFNs. Instead, changes in $k_{zz}$ with increasing $P_{32}$ are different depending on the GDFN. Most $k_{zz}$ values are scattered,

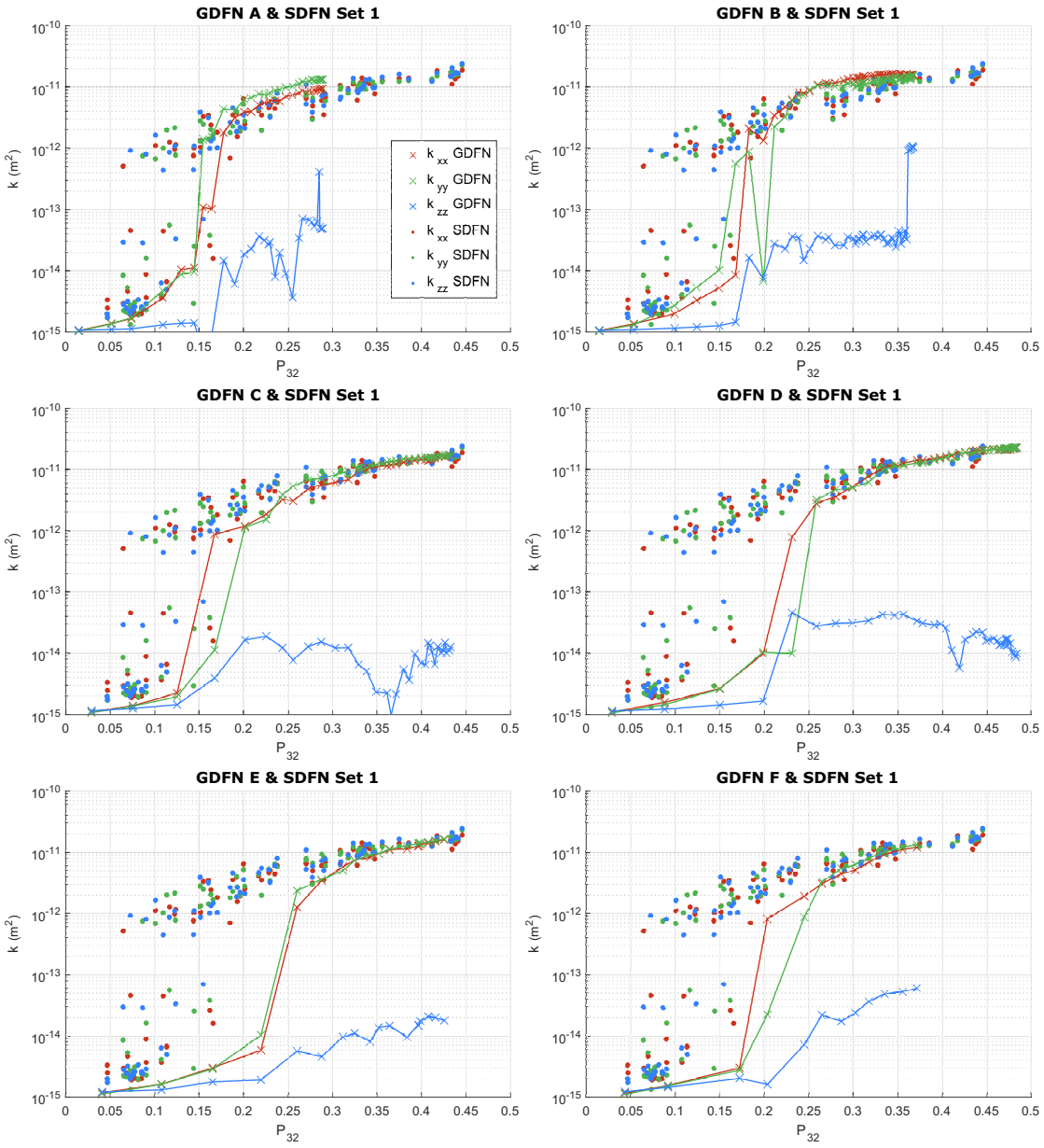



FIGURE 6.17: Permeability along the directional axes ($x$, $y$, and $z$) in the six GDFNs compared to SDFN set one, which contain randomly oriented fractures with a fixed radius of 4.2787 m. Each graph shows one GDFN's directional permeabilities at each growth step, represented with crosses connected by lines, and SDFN permeabilities as coloured dots.

not always increasing with $P_{32}$, particularly in GDFNs A, C, and D. As identified in the permeability progression of GDFN E, additional fracture surfaces may not always increase vertical permeability if they create flow paths perpendicular to the vertical axis.

Unlike the other GDFNs, vertical percolation occurs in GDFN B, with the $k_{zz}$ increasing by an order of magnitude in the final two steps, percolating in a similar way to the horizontal axes. GDFN B's geometry can be examined in Figures 6.9 and 6.10, where, in the final step, a fracture intersects the top boundary after following an upward,

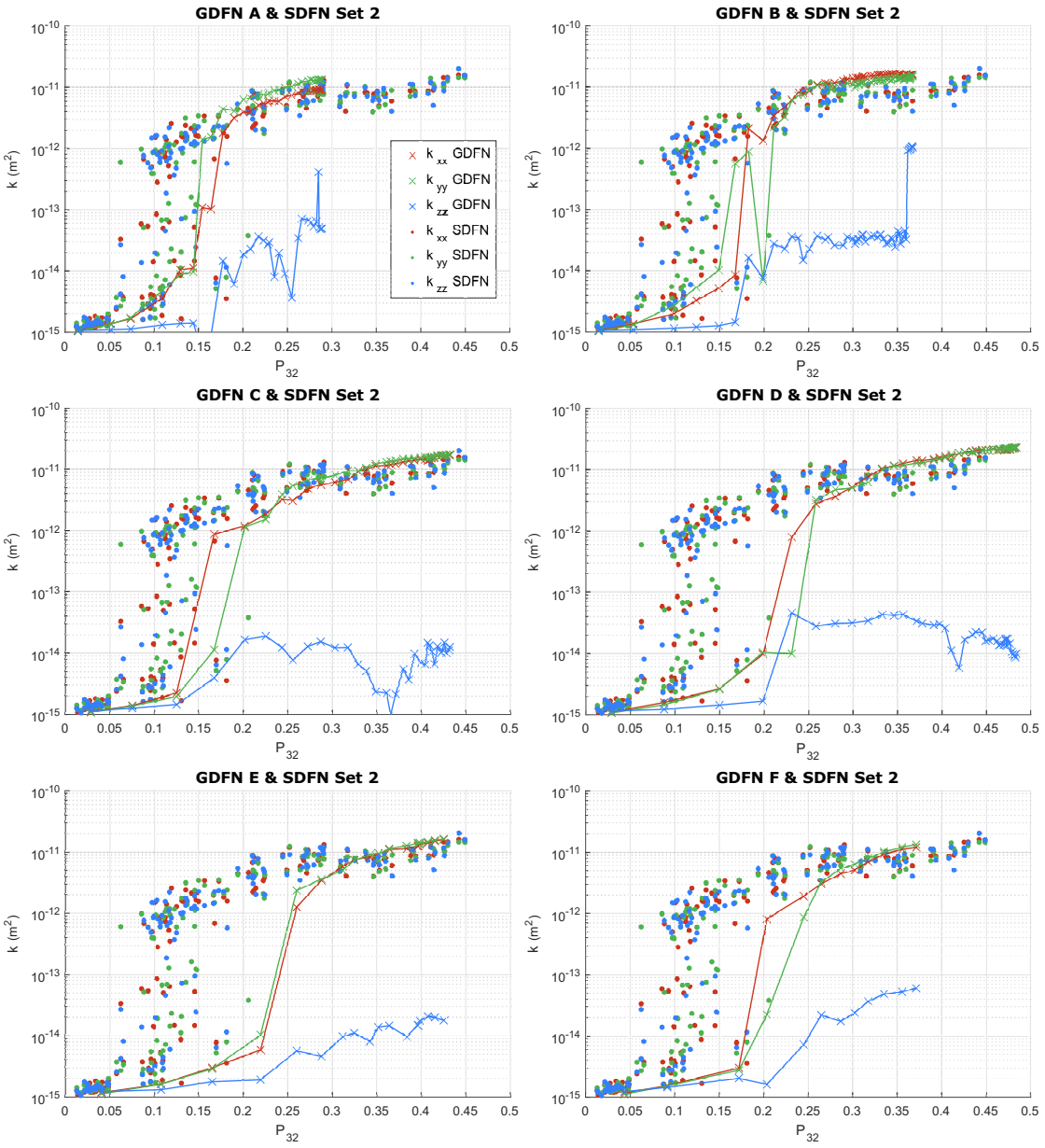



FIGURE 6.18: Permeability along the directional axes ($x$, $y$, and $z$) in the six GDFNs compared to SDFN set two, which contain randomly oriented fractures with normally distributed radii, where the normal distribution has a mean of 4.1411 and a standard deviation of 1.0854. Each graph shows one GDFN's directional permeabilities at each growth step, represented with crosses connected by lines, and SDFN permeabilities as coloured dots.

stepped growth path. A fracture also intersects the bottom boundary at the final step as well, and the well connected fracture network creates a flow path between these fractures. Another exception to the increasing permeabilities in GDFN B is the $7^{\text{th}}$ step, where percolation in the $y$ direction occurs in the $4^{\text{th}}$ step, but in the $6^{\text{th}}$ step, the permeability falls temporarily to non-percolating values. This variability is the result of slight differences in meshing of the flow domain that may affect connectivity between fractures along critical points. At the early steps, the percolation path in GDFN B

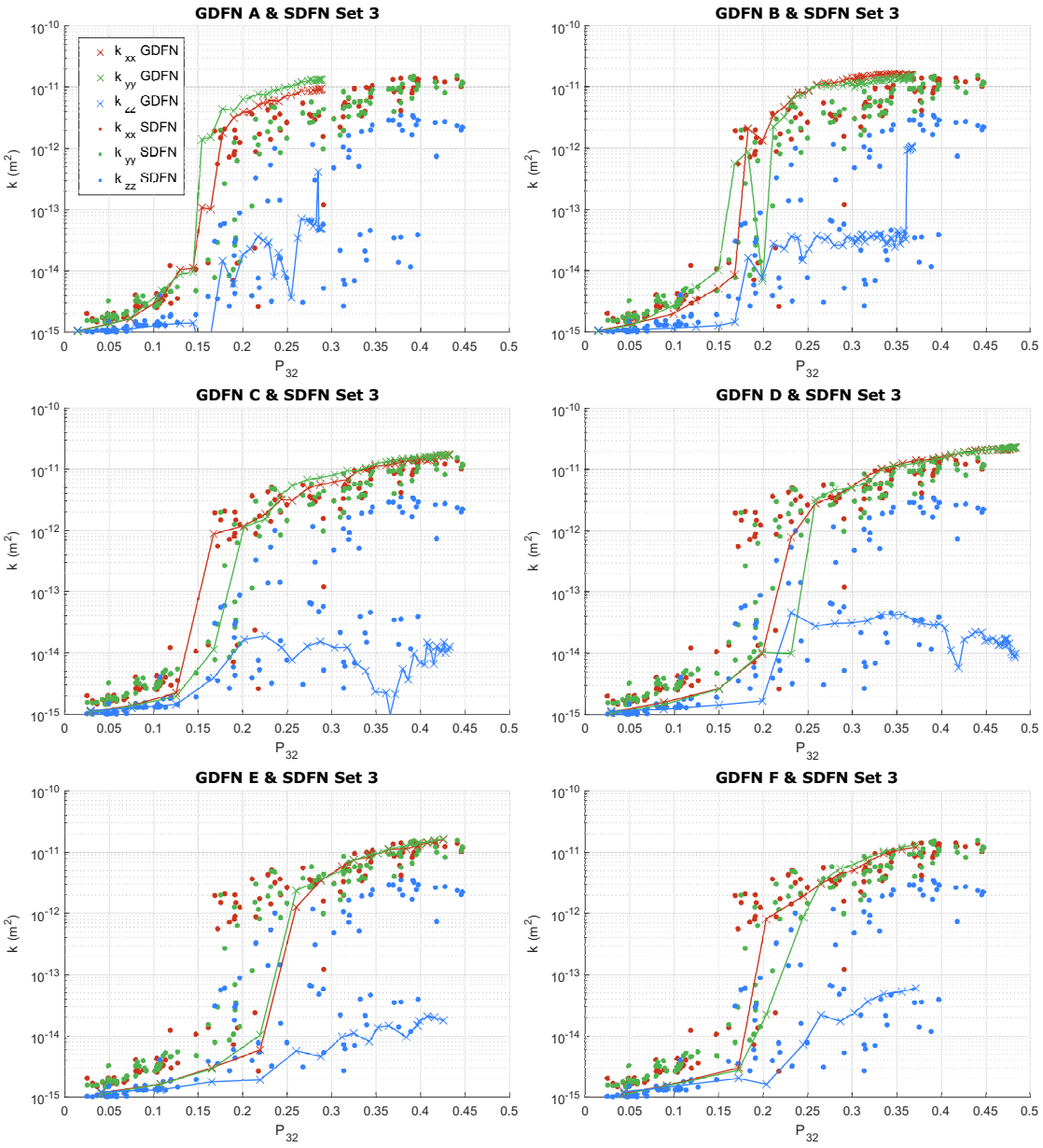



FIGURE 6.19: Permeability along the directional axes ($x$, $y$, and $z$) in the six GDFNs compared to SDFN set three, which contain two sets of fractures, both with fixed radii of 4.2787, with five in six fractures being horizontal, and one in six fractures being inclined (see Table 6.6). Each graph shows one GDFN's directional permeabilities at each growth step, represented with crosses connected by lines, and SDFN set three permeabilities as coloured dots.

along the $y$ direction is dependent on the manner in which small areas are meshed. A slight change to the local region can change whether a flow path exists between two fractures that are close, due to the fixed sizes of tip node elements. The influence of mesh refinement on percolation is considered further in Section 6.4.4.

The $P_{32}$ at which GDFNs percolate varies significantly, between approximately 0.15 (GDFN A) and 0.25 (GDFN E). GDFNs with fewer fractures percolate at lower densities

than GDFNs with more fractures. This is because their initial intensity is lower, whilst the general pattern of fracture growth remains the same regardless of the initial number of fractures. The growth step at which percolation occurs is much more consistent than the $P_{32}$, because all GDFNs start to percolate either at growth step 4 or step 5. This implies that, whilst various factors must influence percolation in GDFNs, the total number of simulation steps (*i.e.*, the accumulated growth over time), and parameters such as maximum tip extension per step, are important to consider alongside the fracture intensity of the full dataset. Further discussion on percolation in GDFNs can be found in Section 6.6.2.

The three SDFNs each have different relationships between directional permeability and $P_{32}$. At low $P_{32}$ values, SDFN $k_{xx}$, $k_{yy}$, and $k_{zz}$ are higher than all the present GDFNs. The SDFN sets percolate at different intensities: SDFN sets one and two percolate at the lowest $P_{32}$ values (0.05 to 0.2), and SDFN set three percolates at higher $P_{32}$ values (0.15 to 0.4). Because SDFN sets one and two are isotropic, all three axes percolate, whereas set three percolates mostly along the $x$ and $y$ axes. Set three percolation in the $z$ axis only occurs consistently at the highest fracture intensities (0.4 to 0.45). Compared to the GDFNs, SDFNs set one and two have very different percolation properties, due to the onset of percolation at low densities and their isotropy. Because of their stochastic generation method, the permeability of SDFNs is scattered, therefore the trends mentioned here are subject to some variability. In particular, SDFN permeabilities vary across 4 orders of magnitude when they are around the density at which percolation can occur, because the stochastic arrangement of fractures does not consistently yield a percolating path at this density.

SDFN set three much more successfully reproduces how percolation occurs in the GDFNs, due to their similar anisotropic properties, and percolation occurring horizontally at approximately the same $P_{32}$ as GDFNs A, B, D, and F. Across all sampled fracture intensities, SDFN set three has more scattered permeabilities than sets one and two, particularly in the $z$ direction. Its highest permeabilities are also lower than the other sets. This is a consequence of the fracture insertion method, because the horizontal fractures are oriented optimally for flow along the $x$ and $y$ directions, but do not form a connected flow path unless a fracture in the inclined set connects them. SDFN set three could be used as a stochastic method for predicting the present GDFN hydraulic properties, but would only be somewhat effective at high densities, and would poorly predict vertical permeability.

#### 6.4.2.4 Permeability magnitudes in GDFNs and SDFNs

Permeability magnitudes also differ between the GDFNs and SDFNs. After a network percolates, additional fracture intensity leads to further permeability increases. In SDFNs, this increase is one order of magnitude, up to a maximum permeability of approximately $1.1 \times 10^{-11}$ m$^2$. In comparison, GDFN permeabilities at the point of percolation are lower than SDFNs of equivalent fracture density. Furthermore, GDFNs increase in horizontal permeability at a faster rate after percolation than SDFNs, evidenced by the steeper $P_{32}$ against $k_{ef}$ trends. This is due to the growth process adding horizontal fracture surfaces which are favourable for horizontal flow, rather than density being added in random directions.

All six GDFNs have different $P_{32}$ values in their final step, however, horizontal permeabilities at this step are similar in all cases, between $1 \times 10^{-11}$ and $1.2 \times 10^{-11}$ m$^2$. This consistency suggests that the number of fractures in the domain and the final density do not affect the maximum possible permeability. Instead, the growth process, boundary condition, and space available for growth control the largest possible permeability a network can achieve.

### 6.4.3 Intersections in geomechanical discrete fracture networks

Intersections are fundamental to the permeability of a network. Other authors have approached DFN effective permeability by analysing the number of intersections per fracture [Shokri et al., 2016, Wettstein et al., 2012]. In this study, intersections are quantified by the total length of fracture intersections. This length is computed by iteratively intersecting all of the surfaces in the geometries of the studied DFNs. This is performed as a post-processing step, due to the significant computational cost of detecting intersections when there are many surfaces present in a volume, particularly in late stage GDFNs. Improvements in computational time are made by skipping fractures which have been compared against each other already, also ensuring intersections are not included more than once. Intersections which go outside of the domain (possible in SDFNs where fractures are seeded partially outside the domain) are excluded from length totals. This post-processing is performed in Rhinoceros 6, a CAD package with Python scripting interface.

Figure 6.20 shows the two-dimensional curves resulting from fracture-fracture intersections in four datasets. The four datasets show both GDFN E and SDFN set one at low and high fracture intensities. In the GDFNs, fracture intersections are constrained to the centre of the domain where the fractures are initially inserted. The intersection

curves are short and often curved. In SDFNs, intersections are much longer and occur throughout the domain. This observation is at odds with the permeability data analysed in Section 6.4.2.2, because at high fracture intensities, SDFNs and GDFNs have similar permeabilities, despite the significantly different intersection properties between these two DFN types. SDFNs have many long intersections, and still create networks in which enable flow as a GDFN of the same fracture intensity with much shorter intersections.

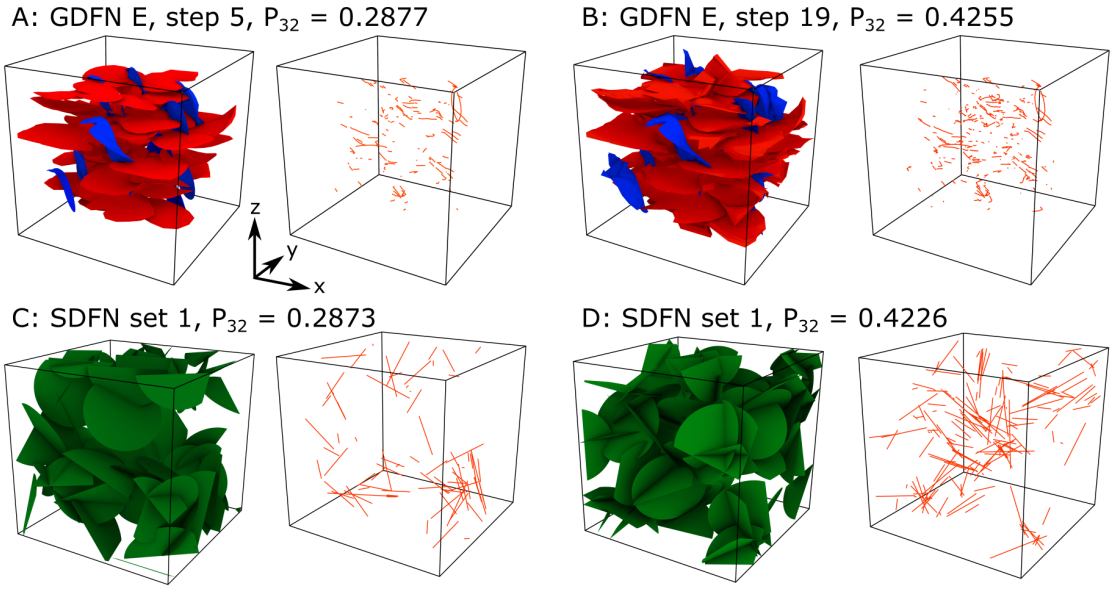



FIGURE 6.20: Intersection patterns in GDFNs (A & B) and SDFNs (C & D). Each DFN is shown in two images: left, with fractures coloured by set (red fractures are initially horizontal, blue fractures are initially inclined, and green fractures are randomly oriented), and right, with curves showing where fractures intersect. A and B show two steps in the growth of GDFN E. C and D show two SDFNs from set one.

The total length of fracture intersections for every growth step of the geometries of two of the GDFNs (A and E) are plotted in Figure 6.21A. The $x$-axis is the $P_{32}$ fracture intensity of the growth step. Figure 6.21B plots the same data, along with fifty five SDFN datasets from set one and fifty five from set three, across a range of $P_{32}$ values. The GDFNs both have a similar trend, where intersection lengths scale approximately linearly with intensity.

The two SDFNs have different intersection length trends, with SDFN set three being similar to the GDFNs. It matches GDFN A's trend closely at low intensities, and GDFN E's trend at high densities. The similarity between SDFN set three and the GDFNs is a result of the generation method for SDFN set three, which contains mostly horizontal fractures with some vertical fractures, such that it resembles the GDFNs (see Figure 6.16). Because the horizontal fractures never intersect, intersections are completely determined by the placement of the vertical fractures, resulting in a less intersected set of DFNs, despite the large fractures they contain. In the GDFNs, horizontal fractures can re-orient themselves and intersect with others growing in the same plane. SDFN

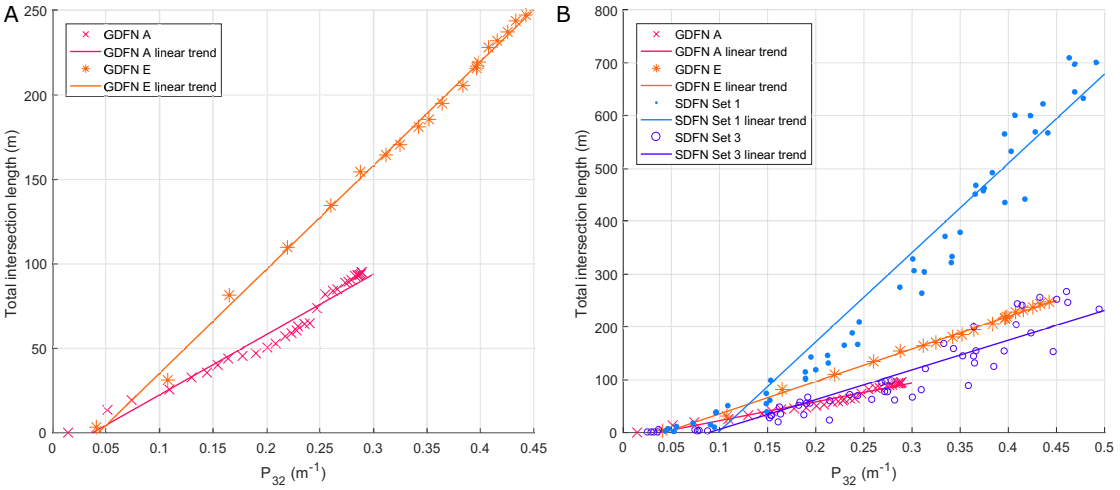



FIGURE 6.21: Total length of fracture intersections (m) plotted against $P_{32}$ ($m^{-1}$) in GDFNs and SDFNs. A: GDFN A and GDFN E. B: GDFN A, GDFN E, 30 DFNs from SDFN set one, and 30 DFNs from SDFN set three. The linear trend for GDFN A has gradient 357.4 and $y$-axis intercept -13.4, GDFN E has gradient 615.2 and $y$-axis intercept -26.3, SDFN set one has gradient 1691.5 and $y$-axis intercept -166.5, and SDFN set three has gradient 562.8 and $y$-axis intercept -50.2.

set one has a significantly different trend, with similar intersection lengths only at low densities (less than 0.2 $m^{-1}$). Randomly oriented, fixed size fracture networks have a significant difference in their intersection properties, because when intersections occur, they tend to be longer. However, from the permeability trends in SDFN set 1 and the GDFNs (Figure 6.17) suggest that longer intersections do not create more flow. Instead, as long as intersections occur, permeability increases regardless of the length of those intersections.

The difference between intersections in GDFNs and SDFNs is further quantified by fitting a linear trend between the fracture intensity ($P_{32}$) and the total length of intersections (see Figure 6.21 caption). At higher densities, the trend becomes non-linear, however, a straightforward linear trend is sufficient to compare the four present trends. The gradient of SDFN set three is intermediate between GDFN A and E, while SDFN set one has a much steeper gradient.

### 6.4.4 Influence of mesh refinement on effective permeability

In domains containing complex geometries, mesh refinement can have some influence on the hydraulic properties of the domain. In particular, the significant fluctuation in vertical permeability may be a result of inconsistent refinement between slightly different geometries. Figure 6.22 shows the directional permeability of GDFN F across its 13 growth steps, using four levels of discretisation on the fractures. As introduced in Section 2.3.3, the number of tip nodes around a fracture sets the minimum size of

the fracture tip elements, and therefore controls global refinement, particularly in high fracture intensity domains. In all cases where flow is solved in this chapter, fracture surfaces are meshed with constant refinement, as shown in Figure 2.3A, to improve detail at fracture intersections.

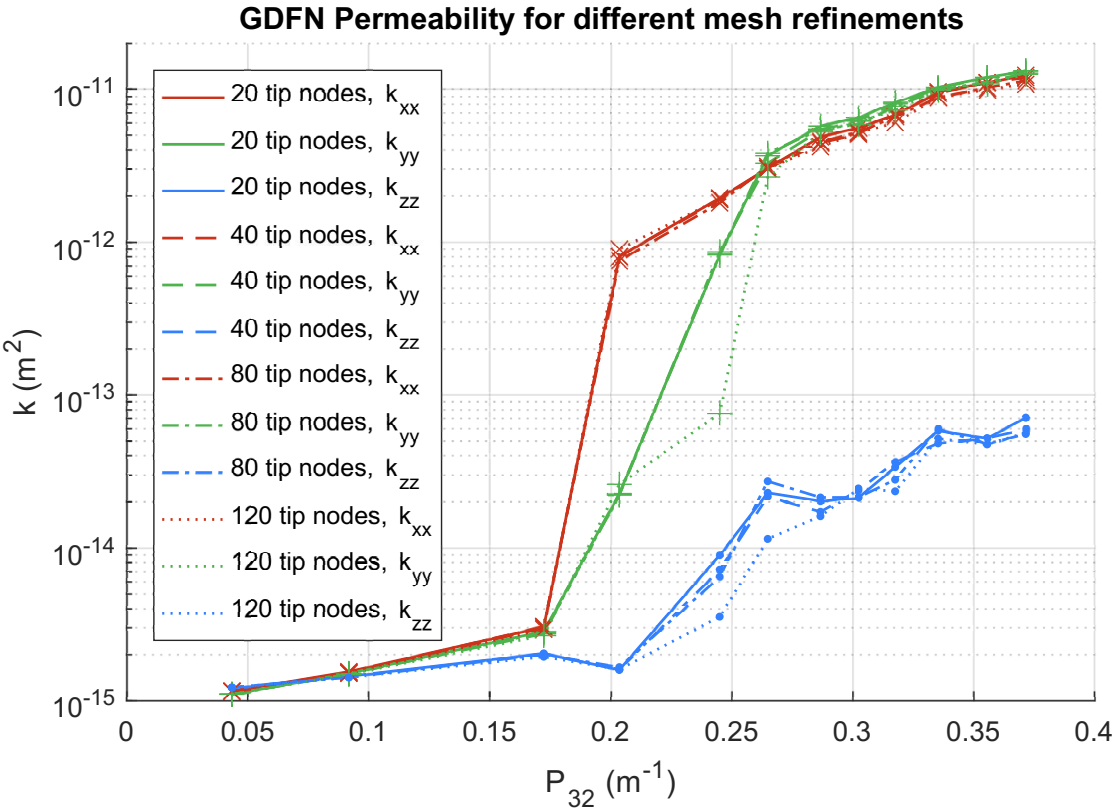



FIGURE 6.22: Permeability in the $x$, $y$, and $z$ axes for the same GDFN growth sequence with different levels of mesh refinement. Refinement is controlled by the number of fracture tip nodes.

The results show a very similar progression of permeability with fracture density, in particular, for results with 20, 40, and 80 fracture tip nodes. Therefore, if any one of these mesh refinements were to be analysed in isolation, similar conclusions would be drawn. Small differences emerge at the highest mesh refinement. When fractures have 120 tip nodes, lower values of $k_{yy}$ and $k_{zz}$ are found in step 4 to step 7. The mesher handles close fractures such that, if the distance between the two fractures is smaller than the local element size (*i.e.*, the size of the closest fracture tip), they are considered touching, as the volumetric element size is too small for this gap. In this high refinement case, the lower permeability arises because fractures are considered more disconnected. Figure 6.22 shows that, if there are differences in the resulting permeability from the discretisation between close fractures, they are relatively minor, and do not significantly influence the final permeability progression with fracture intensity.

## 6.5 Effective permeability of geomechanical discrete fracture networks with variable fracture apertures

The present analysis on DFN permeability assumes that fractures have uniform apertures across their entire surfaces. As discussed in Section 6.1, this is a significant simplification for subsurface networks, where fracture apertures are affected by rough fracture surfaces, infill material, and *in situ* stress states [Black et al., 2016, Leckenby et al., 2005]. These modifications to fracture apertures have been demonstrated to affect network permeability by many other investigators [*e.g.*, Bisdom et al., 2015, Lang et al., 2018, Lei et al., 2017b, Min et al., 2004]. This section presents the methodology and results of flow simulations on GDFNs with mechanically derived apertures.

### 6.5.1 Mechanical fracture aperture calculation

In the GDFNs examined in this section, fracture apertures are computed locally across fractures after the FEM results for displacement are calculated (see Section 2.2.1). The aperture calculation method makes use of the pairing of fracture surface elements on fracture surfaces, where one element is the master and another is the slave, shown in Figure 2.6. If the stress state has caused the two sides of a fracture to no longer be coincident, there will be a discontinuity between the displacements of the master and slave elements. To compute local aperture, the normal gap function ($\mathbf{g}_N$) is calculated for each master-slave node pair using Equation 2.5. The length of vector $\mathbf{g}_N$ is the distance between the two nodes, which is stored at each master node. These apertures are used as part of the flow method, as described in Section 5.2.1.

Figure 6.23 shows an example of mechanical fracture apertures on a growing wing crack in tension. The fracture is visualised as a mesh of triangular surface elements. At each master node, a cubic glyph is placed with colour scaled by the aperture between the two fracture surfaces at that point. The figure shows two steps, step 0 (A) and step 5 (B). At step 0, the distribution of apertures is uniform, with the highest aperture in the centre of the fracture, reducing to zero at the edges. In step 5, the aperture is generally uniform, particularly on the new fracture surfaces created by growth. The highest apertures are no longer on the initial fracture plane. Instead, the peak apertures are at the highest and lowest parts of the fracture with the most curvature, which grew in this step.

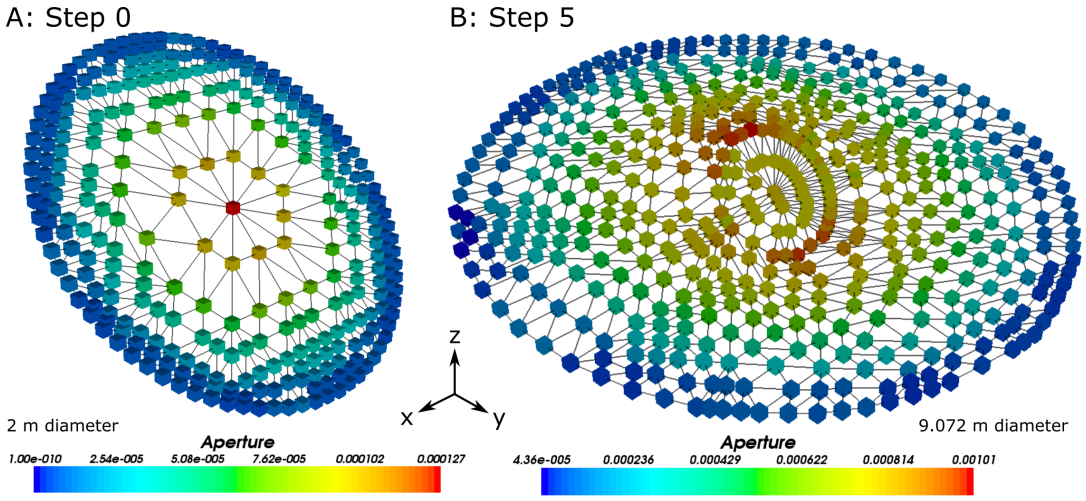



FIGURE 6.23: Example of the mechanical fracture apertures on a growing, isolated, penny shaped fracture. The fracture is initially oriented 45° to the $z$-axis. Its surface elements are shown in two steps, 0 (A) and 5 (B). The computed aperture at each node is shown as a cube, coloured by the magnitude of the aperture. The stress causing the apertures is the same boundary condition used for growth (tension at the top boundary of $2{\times}10^6$ Pa).

### 6.5.2 Permeability of geomechanical discrete fracture networks under different stress magnitudes

This section introduces mechanical apertures to fractures in a GDFN, quantifying the permeability response when all the properties of a DFN are determined geomechanically. Analysis in this section is performed on GDFN E, chosen because it has relatively few growth steps; consequently, the computational cost of computing mechanical apertures and fluid flow is relatively lower compared to the other GDFNs. Three tensile boundary conditions are used of different magnitudes: $1 \times 10^7$ Pa, $0.5 \times 10^7$ Pa, and $0.25 \times 10^7$ Pa, applying the stress on the top boundary of the domain. The lower of these values was selected because it provides overall flow magnitudes in the same range as the uniform aperture cases. The higher stress boundary conditions demonstrate how stress magnitude correlates with permeability magnitudes, which is a non-trivial relationship due to the cubic law. These results are compared to the uniform aperture results from Section 6.4.2, where fractures have apertures of 0.001 m across all their surfaces. Due to the computational cost, not every step has been computed for all stress boundary conditions. Instead, a representative number steps are shown to demonstrate the hydraulic response of the GDFN relative to other boundary conditions and the uniform aperture flow results.

### 6.5.3 Aperture distribution and total fracture void space

Figure 6.24 shows the spatial distribution of the apertures on fracture surfaces in GDFN E in one of its final growth steps (18). Fractures are represented as opaque surfaces, coloured by the aperture on the fracture, interpolated from values at the fracture nodes. The boundary condition ($1 \times 10^7$ Pa at the top boundary) is the largest amongst those tested, and subsequently results in the highest permeability of all DFNs examined in this work (see Figure 6.27). The distribution of apertures has similarities with Figure 6.23, where the highest apertures are found at the centre of flat, large fractures. The highest apertures are also found towards the sides of the domain. At the domain edges, fractures are less densely packed, so less stress shielding takes place here, allowing fractures to acquire large apertures.

The majority of fracture surfaces have apertures much lower than those shown in Figure 6.24. The lowest apertures in the domain are in the range of $10^{-3}$ to $10^{-5}$ m, and occur at the edges of fractures and on the vertically inclined fractures. From the side views (C and D), these fractures are clearly visible, and it can be seen that the majority of the domain has apertures below 0.01 m. When examined at a different scale (between $10^{-3}$ and $10^{-6}$ m), these fractures also have an aperture distribution with higher values at their centre. Percolation in the domain requires the inclined fractures to provide a connecting flow path between the horizontal fractures, therefore, despite their low aperture, fluid must use these pathways in order to percolate.

Figure 6.25 shows a graph comparing $P_{32}$ against the total void space, $\phi$, in the domain, contributed by fractures due to their apertures. Void space is calculated by summing, over all the fractures, the product of each surface element's area and its aperture. With uniform apertures, this results in a linear relationship between $P_{32}$ and $\phi$. When apertures are computed from the stress field, the relationship becomes non-linear, characterised by an initially lower total void space, and an increasing gradient with higher $P_{32}$ values. In later steps, the total area of fracture surfaces added gradually reduces. However, the void space contribution from mechanical apertures continues to increase significantly. The lowest stress state ($0.25 \times 10^7$ Pa) provides a reasonably close match to the uniform aperture case.

Changing fracture apertures mean that the network's $\alpha/\kappa$ ratio is altered, with potential implications for flow patterns in the network [Ebigbo et al., 2016]. In a domain with both non-elliptical fracture shapes and non-uniform apertures, calculation of both $\alpha$ and $\kappa$ is not straightforward (see Equations 6.2 and 6.3). The networks investigated in this chapter have had $\alpha/\kappa$ ratios estimated at being much greater than 1. The similarity between the change in total void space with $P_{32}$ for mechanical and uniform

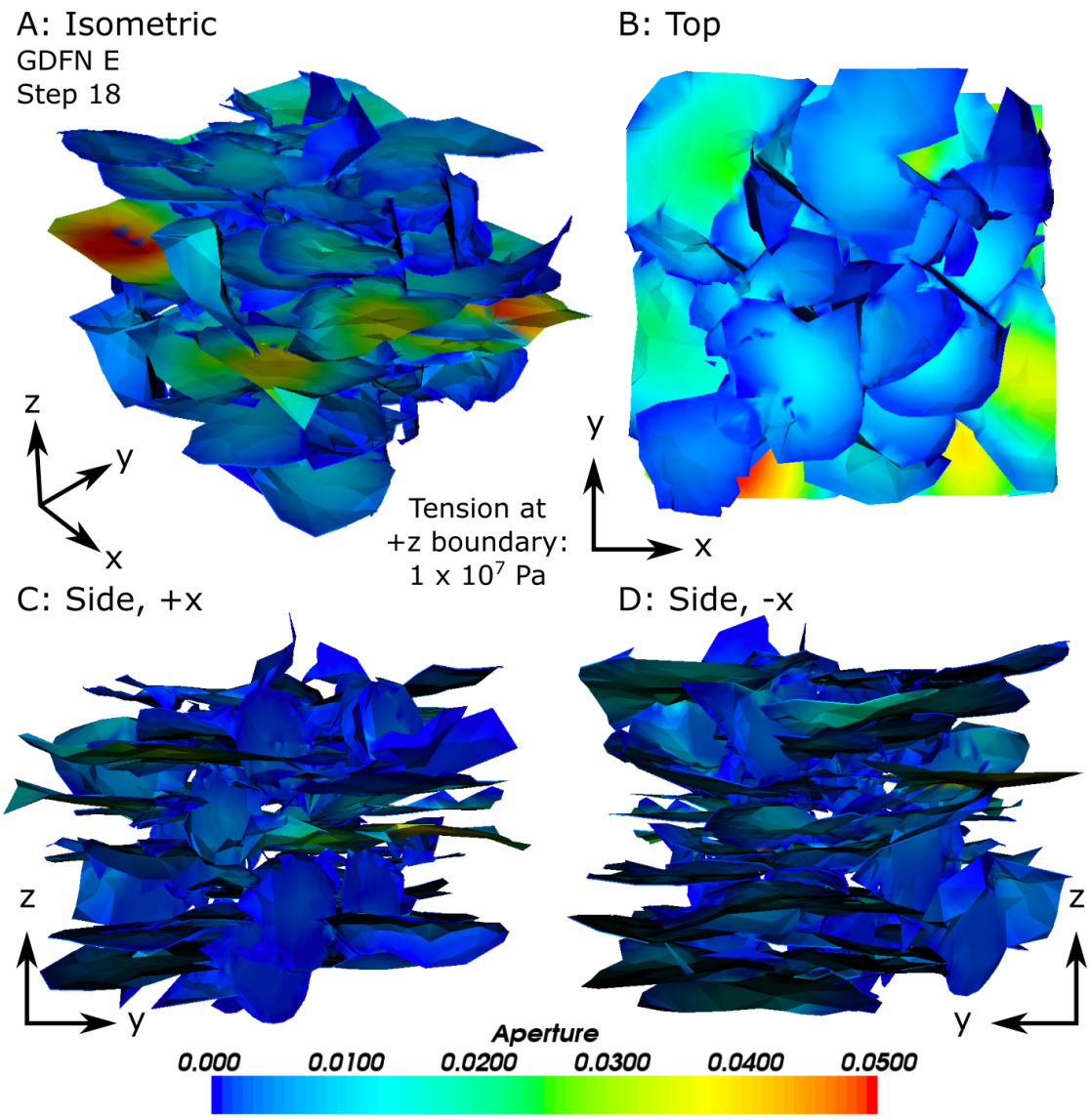



FIGURE 6.24: Four views of apertures of fractures in GDFN E under a tensile stress (1 $\times$ $10^7$ Pa at the top boundary). Fractures are shown as opaque surfaces, and coloured by the aperture at surface element nodes. A continuous colour distribution on surfaces is created by interpolating between the aperture values at nodes. Only elements with apertures above $10^{-10}$ are shown, meaning only the values on the fracture surfaces are shown and the boundaries are excluded.

aperture GDFNs suggest that, in the present mechanical aperture cases, $\alpha/\kappa$ remains much greater than 1. If a lower stress was applied to the network, there would be lower void space and apertures overall. In this case, the $\alpha/\kappa$ ratio may be less than one, which would suggest that the fracture network would have less influence on flow and pressure gradients in the domain.

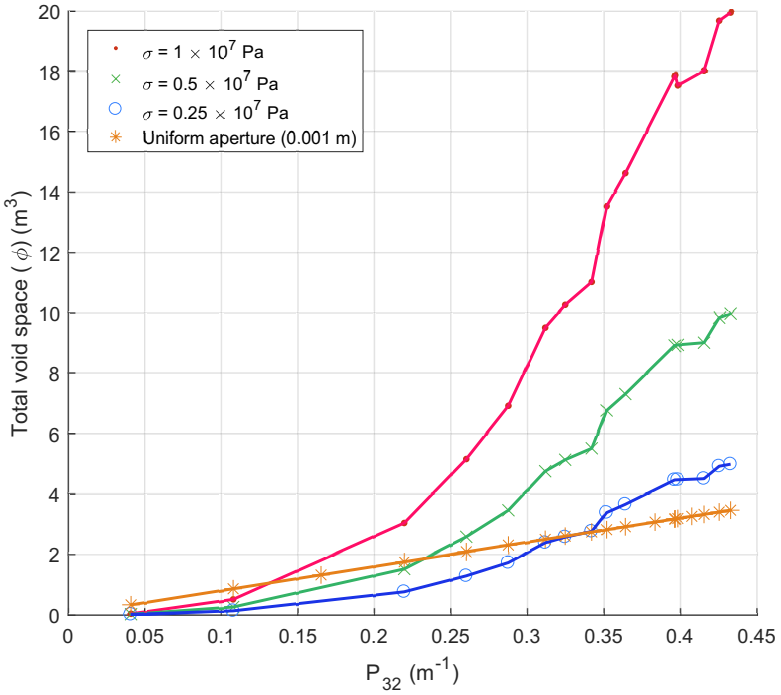
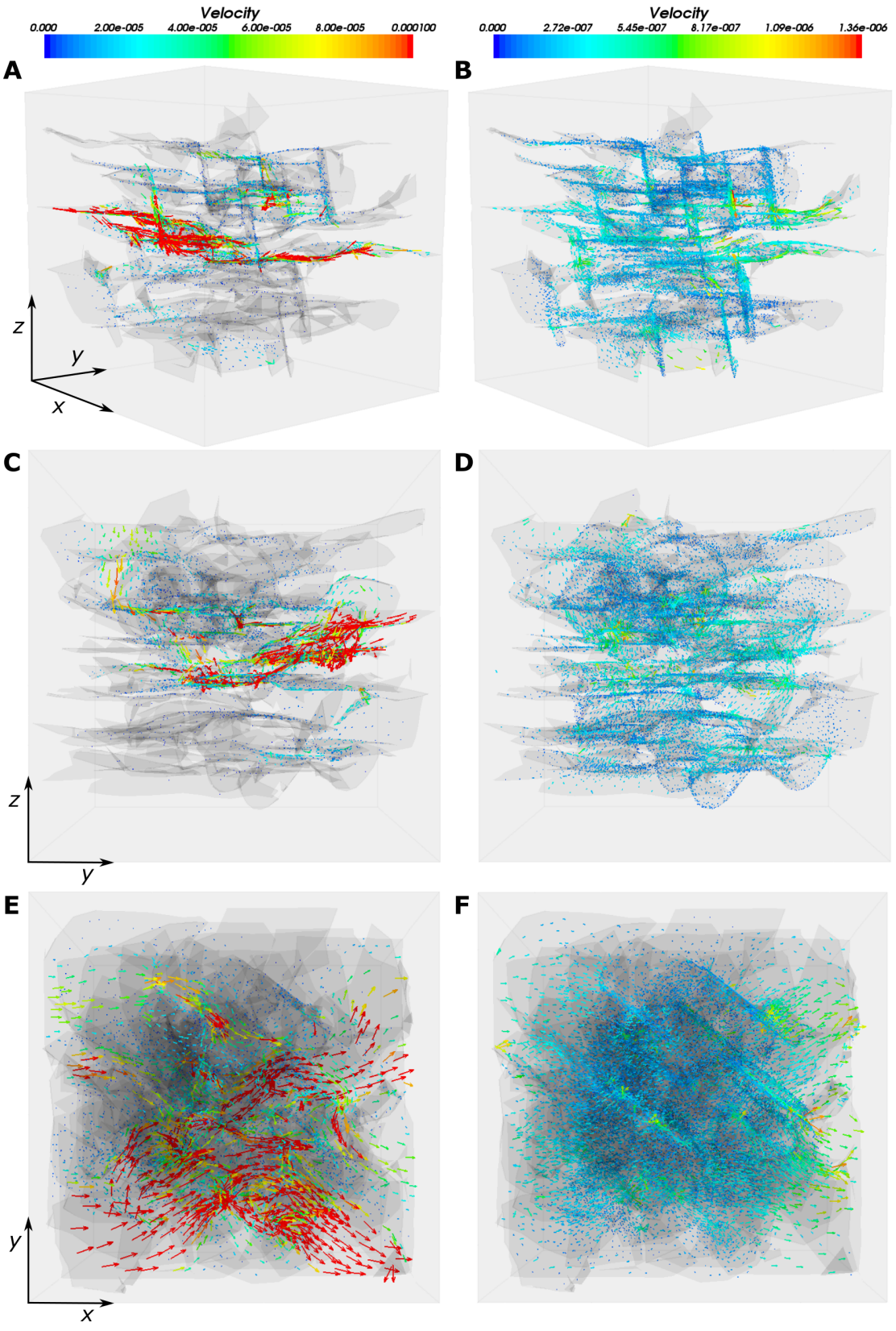



FIGURE 6.25: Total volume of void space due to fracture porosity ($\phi$) in GDFN E resulting from different aperture distributions. Three tensile boundary conditions of different magnitudes are compared to uniform apertures. Three boundary condition magnitudes are shown across most stages of growth in the GDFN.

### 6.5.4 Directional permeability for different tensile stress magnitudes

The effective and directional permeabilities of GDFN E are computed for the three stress magnitudes. Sub-figures A, C, and E in Figure 6.26 show the flow pattern that results from the aperture distribution in Figure 6.24. These are compared to the same results for uniform apertures in sub-figures B, D, and F. Fractures are visualised as transparent surfaces, and the flow at each element is shown with an arrow, scaled and coloured by the magnitude of the flow. Therefore, flow does take place in the rock matrix, but occurs at a much slower rate than fracture flow, thereby focusing the visualisation on flow that takes place on the fractures. Faster flow in the mechanical aperture case is the result of higher maximum aperture values in the mechanical aperture simulation compared to the uniform aperture case. The difference in flow velocities is not the focus of this analysis, as flow magnitudes will scale with aperture, which depends on the magnitude of the stress boundary condition applied, and will not be consistent for all mechanically stressed rock masses.

A significant difference between the two cases is how flow is distributed. In the uniform aperture flow results, flow occurs at similar magnitudes on most of the fractures in the domain. Fractures which are better connected, particularly in the centre of the domain,


Velocity
0.000
2.00e-005
4.00e-005
6.00e-005
8.00e-005
0.000100
A
z
y
x
Velocity
0.000
2.72e-007
5.45e-007
8.17e-007
1.09e-006
1.36e-006
B
C
z
y
D
E
y
x
F

have more flow because they provide a well connected path from source to sink. Inclined fractures also provide flow paths, particularly visible in Figure 6.26B.

In the mechanical aperture flow case, the majority of the network has no significant flow. Most of the flow is concentrated on horizontal fractures which are situated in the vertical middle of the volume. These are the high aperture fractures shown in Figure 6.24, which open most at the sides of the volume. Because they also connect to form a flow path from one side of the volume to the other, and the cubic law results in a large increase of apertures on these fractures, this flow path becomes highly favoured and the rest of the domain is relatively hydraulically inactive. Flow is also concentrated at the centres of fractures, rather than their edges, where apertures are higher. In mechanical aperture flow simulations, if flow takes place on the inclined fractures, it occurs when there is a connected pathway for flow to follow, rather than on all of the inclined fractures at similar magnitudes. When the pressure gradient boundary condition is altered to a different boundary, new channels form, as is widely observed in other models [Moreno and Tsang, 1991, Tsang and Neretnieks, 1998].

The observed flow channeling in GDFN E is consistent with the results of Bisdom et al. [2015], where in networks with stress dependent apertures, only small fraction of the network was found to contribute to permeability. Furthermore, these results match observations of deep subsurface networks, where a minority of fractures provide flow pathways (see Section 6.1.2.1) [Follin et al., 2014, Tsang and Neretnieks, 1998].

The directional permeabilities at the different growth steps of GDFN E are plotted in Figures 6.27 and 6.28 for both mechanical and uniform aperture cases. Each set of three graphs compares $k_{xx}$, $k_{yy}$, and $k_{zz}$ separately, against $P_{32}$ in Figure 6.27, and against void space ($\phi$) in Figure 6.28. Uniform aperture flow results (also shown in Figure 6.17E) provide a comparison to the data in Section 6.4.2. Two $x$ axis values are chosen because the relationship between $P_{32}$ and $\phi$ is demonstrated as being non-linear in Figure 6.25, therefore, characterising a network by its total void space due to fractures may be a better way to compare datasets with significantly different total apertures.

FIGURE 6.26 *(preceding page)*: Fluid velocity from flow along the $x$-axis (from the -$x$ boundary to the +$x$ boundary) in GDFN E, step 18. Local flow is represented with one vector per finite element, and fractures visualised as transparent surfaces. Flow vectors scale in size and colour with velocity. Three viewpoints are shown for two different simulations with different apertures. The left side (A, C, and E) shows results from mechanical apertures, computed under with a tensile stress boundary condition of $1 \times 10^7$ Pa at the top boundary. The right side (B, D, and E) shows results from uniform aperture fractures (0.001 m). The volume is $20 \times 20 \times 20$ m. The variable aperture results use the scale on the upper left scale for velocity, and uniform aperture results use the upper right scale.

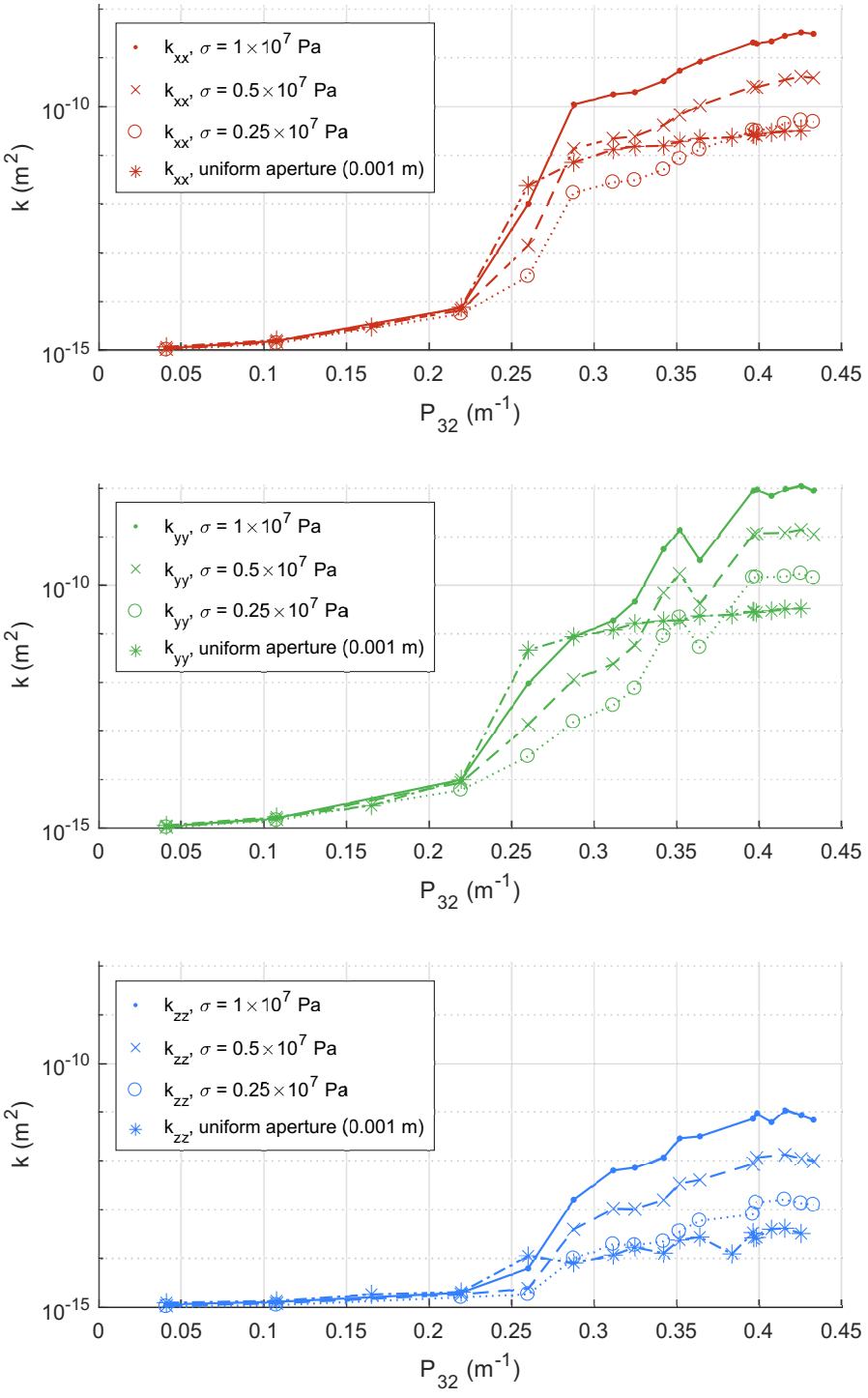



FIGURE 6.27: Directional permeability compared to fracture intensity ($P_{32}$) of GDFN E across its growth steps for three mechanical aperture cases and uniform fracture apertures. The top graph shows results for flow along the $x$ axis ($k_{xx}$), the middle for flow along the $y$ axis ($k_{yy}$), and the bottom for flow along the $z$ axis ($k_{zz}$).

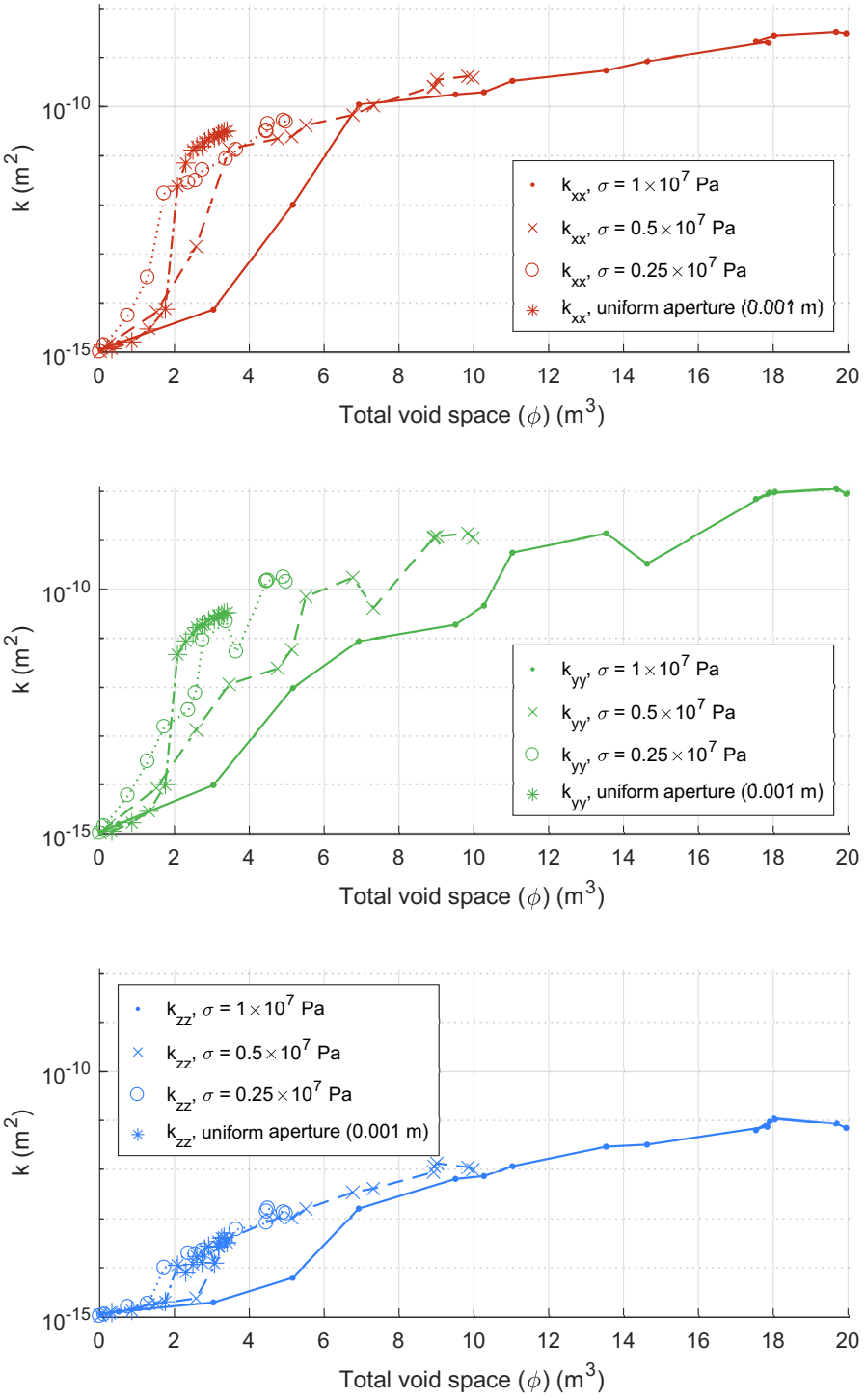



FIGURE 6.28: Directional permeability in compared to total fracture void space ($\phi$, m$^3$) of GDFN E across its growth steps for three mechanical aperture cases and uniform fracture apertures. The top graph shows results for flow along the $x$ axis ($k_{xx}$), the middle for flow along the $y$ axis ($k_{yy}$), and the bottom for flow along the $z$ axis ($k_{zz}$).

Directional permeabilities are higher in all cases for the first two stress states ($1 \times 10^7$ and $0.5 \times 10^7$ Pa). In the $z$ direction, a much larger increase in $k_{zz}$ occurs around the point of percolation. However, because the fracture apertures are variable, there is no characteristic permeability value (or change in value) which would suggest that a percolating path has been established in the network. Therefore, at fracture intensities above the percolation point observed in uniform aperture tests, directional permeability continues to increase significantly in the mechanical apertures tests. This increase is particularly clear in $k_{yy}$, where percolation does not cause a distinct sharp increase for stresses $0.5 \times 10^7$ and $0.25 \times 10^7$ Pa. Only the stress magnitude $1 \times 10^7$ Pa observes a $k_{yy}$ increase at step 4 similar to the uniform aperture case. Subsequently, $k_{yy}$ increases gradually with a steeper gradient, reaching higher values than the uniform aperture case.

As observed in the $P_{32}$ against $\phi$ results (Figure 6.25), the lowest stress boundary condition ($0.25 \times 10^7$ Pa) provides the closest match to uniform apertures. This stress state results in lower permeabilities across most fracture intensities for $k_{xx}$ and $k_{yy}$ than the uniform aperture state. Under this lower stress condition, percolation is delayed by several growth steps ($k_{xx}$), or the threshold is made more gradual ($k_{yy}$, *i.e.*, not characterised by a single jump at one step, but instead by several large increases over multiple growth steps).

By comparing $\phi$ to $k_{xx}$, $k_{yy}$, and $k_{zz}$ (Figure 6.28), some additional trends emerge between the different stress magnitude cases. When plotted against $\phi$ rather than $P_{32}$, in lower void space GDFNs, the different $k$-$\phi$ trends are similar, in terms of their gradients before and after percolation. This is particularly clear for $k_{zz}$, and the lowest of the stress magnitude cases. Linear increases in $\phi$ can lead to order of magnitude increases in $k$, particularly when the percolation threshold is met. Higher total fracture void space datasets have a very different trend due to the significant increases in void space for the high stress case. After the increase in percolation and at relatively high values, the gradients between $\phi$ and $k$ are similar across all three mechanical aperture cases.

## 6.6 Discussion

### 6.6.1 Parameters influencing geomechanical discrete fracture network generation

The six GDFNs examined in this chapter have broadly the same properties, despite containing different numbers of fractures and stochastic initial fracture distributions. There are many parameters which affect the generation of a GDFN, and the numerical and

physical parameters chosen are given in Table 6.2. Numerical parameters which influence growth include the maximum extension per step, which will change the frequency at which stress is sampled in the domain. Changing this sampling frequency may alter fracture growth paths due to mutual growth and interaction effects, which are sensitive to the relative locations of fractures. As explored in Section 4.4, the number of fracture tip nodes will influence refinement mesh refinement, SIF sampling locations, and fracture geometries after growth. Therefore, the relationship between $P_{32}$ and the growth step may be different if these parameters change, but for the same set of material properties and boundary conditions, GDFNs will still converge towards similar properties in their final growth step.

The only stochastic influence on a GDFN's development is the locations of its initial flaws. The particular arrangement of initial flaws does change the number of steps it takes for a network to finish growing, indicating that the point at which no growth occurs depends on the space fractures have available for growth. Despite the influence of model variables on GDFN growth, the statistical and hydraulic properties of the GDFNs are relatively similar between the six datasets explored in this work. This suggests that the formation of fracture networks is primarily the result of the regional stress, and the mechanical process of growth. In terms of the material properties (see Table 6.2), $\beta_n$, $\beta_f$, and $K_{IC}$ have significant implications for growth, as explored in Chapter 4.

Of the three criteria which control fracture growth, the Paris-type extension criterion has the most effect on how the present networks develop, with implications for the distribution of fracture sizes in a GDFN at its final step. A key property of this criterion is that propagation is favoured on fractures which have the most energy ($\mathcal{G}_n$) at their tips. As observed in other models in tension [*e.g.*, Cowie et al., 1993, Renshaw and Pollard, 1994], this means that small fractures become inactive when large fractures form. This effect does occur in the present work, however, the introduction of a boundary at which fractures terminate intervenes in this process. Growth will be initially favoured on the most energetic fracture tips, extending with the maximum extension length $\Delta a_v$. Once these tips terminate, as long as other fracture tips meet the failure criterion in the material, the next most-stressed fracture tips will extend with $\Delta a_v$. Therefore, due to fracture terminations at boundaries, the present models may encourage growth on more fractures than would activate in a real subsurface network. This effect may explain the difference between fracture length (or surface area) frequency histograms for natural networks, and those from the GDFNs (Figure 6.14). If more fractures remained small, the distribution would more closely match the example shown in Figure 6.1 [Gonzalez-Garcia et al., 2000]. Fracture size effects will also be enhanced by the values of $\beta_f$ and $\beta_n$. The values selected (0.35 and 2 respectively, see Table 6.2) will have encouraged

wider activation of fractures with less concentrated growth at relatively high energy fracture tips.

Other features of the networks grown and examined here can be considered boundary effects. In the subsurface, fractures growing in low fracture intensity rock will continue to grow without bounds. Termination of fractures at boundaries changes how stress is distributed, and therefore growth, in the domain. Boundary intersecting fractures also acquire higher apertures on fractures intersecting edges of the domain, which may be a consequence of the lack of stress shielding in less dense regions of the domain. Furthermore, the potential preference for fractures to curve towards the boundary at which stress is applied, as observed in Figure 6.10, could be due to both boundary effects (see Section 2.6), SIF corner effects (see Section 2.3.7.6), and fracture interaction. Boundary intersections are important for examining a network's flow properties, as with a distinct domain boundary, connected paths between source and sink boundaries are possible, and percolation can be observed.

A potential way to explore how impactful boundary effects are on network permeability is to use a smaller flow jacket during the flow analysis. Lang et al. [2018] placed flow boundary conditions over only a small part of the centre of the domain which could intersect fractures. Using less of the network for flow analysis will require the full network to have more total fracture intensity, in order for a sub-region of the domain to provide a reasonably dense flow case.

### 6.6.2 Percolation in geomechanical discrete fracture networks

In Section 6.4.2, for the present set of GDFNs, it is concluded the simulation step number provides a more consistent way to quantify the onset of percolation, compared to the $P_{32}$. Because the requirement for percolation is at least one connected pathway, a dataset containing only a few fractures would percolate once one fracture grew to fill the domain. This would occur at a later growth step than in the present simulations, but at much lower $P_{32}$ than the GDFNs datasets considered in this work. Therefore, analysis of percolation in a GDFN is fundamentally different from stochastic analyses of percolation, because fracture propagation promotes anisotropic percolation without significant dependence on $P_{32}$. In comparison, a stochastic network can only create a percolating path by chance, therefore, fracture intensity correlates much better with percolation in the SDFNs.

A full analysis on the relationship between GDFN properties and percolation is an important avenue for future research. Such a relationship will need to consider a wide

range of factors. Some of these will be physical parameters, such as the stress or deformation boundary condition and material toughness. Numerical parameters, including the growth rate, maximum extension in each step, and number of fracture tip nodes, will also have a significant effect. Additionally, percolation in GDFNs may change significantly if cross cutting of fractures during growth is allowed. Because percolation is a key property of a DFN, understanding what brings about percolation in a GDFN is vital for explaining why they percolate at different densities and growth steps, and the consequences of using them for hydraulic analysis of subsurface networks.

Mechanical apertures also have implications for percolation in GDFNs, due to the wide range of aperture magnitudes observed in the present networks. If mechanical apertures are used rather than uniform apertures, fractures may provide a connected path for flow, but small apertures on certain fractures may render parts of the path inactive. This is an emergent property in the GDFNs presented here, matching how the majority of fractures will be closed in real, deep subsurface networks [Follin et al., 2014]. Such a property will likely be reproduced by a stochastic network which is subjected to similar stress states, but because of the differences in fracture intersection patterns in GDFNs compared to SDFNs (see Section 6.4.3), it is assumed that the influence of mechanical apertures would be more significant in grown networks.

### 6.6.3 Further methods for improving geomechanical network realism

The present networks have been demonstrated as being geometrically and hydraulically different from stochastic networks. Assessing the extent to which the generated GDFNs are similar real subsurface fracture networks is an additional challenge. Significant similarities include the anisotropy of the resulting network, and the influence of fracture interaction on fracture shape, non-planarity, and intersections. When apertures are derived from mechanical deformation, flow becomes focused on the most open and best connected fractures. These features match most of the properties of natural fracture networks identified in Section 6.1.

There are important differences between how a natural domain is seeded with initial stress concentrators and subjected to stress, compared to the equivalent processes in a GDFN. The concept of an initial distribution of flaws does not translate to subsurface environments in a simple way. Stress concentrators and initial flaws are prevalent due to rock heterogeneity, however, the distribution of flaws before the start of growth is difficult to establish from an already grown network. The present method of randomly generating the locations of the initial flaw set does not necessarily match rock mass properties before growth. This state is not straightforward to quantify, therefore, a

stochastic flaw insertion method provides a reasonably unbiased way of generating an initial state. Furthermore, because the final geometric and hydraulic properties of the present GDFNs are similar, even when different numbers of initial flaws are used, final properties of GDFNs are shown to be a product of mechanical process of mutual growth, rather than depending significantly on the initial flaw state.

A real network will have experienced multiple phases of deformation associated with previous tectonic events, whereas in this chapter, only one phase of deformation occurs. By including initially inactive inclined fractures, the influence of a previous phase of deformation on a network has been reproduced in a straightforward way. These initial inclined fractures become significant in flow simulations, providing important paths for flow between horizontal fractures. In mechanical aperture flow experiments, they acquire low apertures due to their orientation, with consequences for flow channelisation and effective permeability. Therefore, despite the single phase of mechanical deformation which is used to grow the network, the network behaves as if a prior phase of deformation had created a previous flaw distribution. Future analysis can grow the fracture network under multiple different phases to examine in detail how fractures may selectively activate and reactivate under different stress states. The tensile boundary condition that drives mechanical processes in the GDFNs can be most directly compared to tectonic conditions associated with unloading, for example, isostatic rebound due to deglaciation.

Fracture spacing in the present networks essentially is the result of the initial seeding process, whereas, in natural networks, it is a consequence of fracture interaction. Fractures which have tips situated in the shadows of others experience reduced growth, and often remain inactive as the energy available for growth is concentrated on the larger fracture [Thomas and Pollard, 1993]. In the present GDFNs, most fractures are activated in the domains regardless of whether they are in another's shadow. There is relatively little influence exerted by fracture interaction on how fractures are spaced. As proposed in Section 6.6.1 for investigating fracture size distributions, the influence of interaction on fracture spacing can be explored through modifying fracture growth velocity exponents ($\beta_n$ and $\beta_f$). In particular, higher values of where growth would be more concentrated on more highly stressed fractures (*e.g.*, Figure 4.11).

Fracture intersections resulting from growth are mostly limited to 'T' intersections in this work. A limited number 'X' intersections occur when some fracture tips are deactivated, and free tips adjacent to these intersected tips continue to grow. Other mechanisms which would enable the formation of 'X' intersections are not explored, as a conservative approach has been taken to handling crossing by terminating fractures against all free surfaces.

Other authors propose empirical criteria for handling fracture-fracture intersections [*e.g.*, Cheng et al., 2014, Renshaw and Pollard, 1995], which may enable a mix of both 'T' and 'X' intersections to arise in GDFNs. As discussed in Section 2.3.7.5, the implementation of such a criteria is not straightforward. In GDFNs, fracture surfaces hare varied and non-planar, meaning a criterion for crossing cannot assume particular relative fracture shapes or orientations. If 'X' intersections were possible, fewer fracture tips would terminate once intersected, meaning fractures could grow to larger sizes, increasing the final growth step's fracture intensity. The fracture network would be better connected, with the prospect that large fractures could cut through the entire domain if 'X' intersections were generally favourable. These changes would not lead to significant (*i.e.*, one or more orders of magnitude) increases in final network densities, and the GDFNs would still have broadly the same hydraulic properties, with a slightly higher final permeability due to both increased maximum fracture intensity and connectivity.

### 6.6.4 Comparing geomechanical networks to subsurface networks

Realistic properties of the GDFNs have been shown to emerge as a result of the mechanical growth processes. A future step towards generating realistic representations of the subsurface will be to directly match the properties of a GDFN with a particular subsurface environment. This can be approached in several ways. A GDFN can be matched statistically to a present network, for example, by matching fracture intensity of the whole network or individual fracture sets. The tectonic stress regimes which formed a subsurface network can be used as boundary conditions to grow fractures. Specific geometric features can be investigated and incorporated into a GDFN, such as the interaction between a previous fracture set and an actively growing set. A bespoke GDFN which matches a specific subsurface setting will provide unparalleled insights to its mechanical and hydraulic properties.

The present GDFNs have $P_{32}$ fracture intensities up to 0.45 $m^{-1}$, which is similar to observed fracture populations in deep subsurface, hard rock environments. Some fracture intensities of deep subsurface networks are given in Section 6.1.2.1. These networks were surveyed towards the goal of radioactive waste disposal in crystalline rocks, so they provide examples of sparsely fractured media. Cvetkovic et al. [2004] calculated $P_{32}$ values of 1.29 $m^{-1}$ for fractures in rock surrounding the Äspö hard rock laboratory in Sweden. Follin et al. [2014] observed $P_{10}$ values between 1.13 and 3.17 $m^{-1}$ in boreholes drilled to characterise the subsurface in Forsmark, Sweden. Fracture intensities in GDFNs presented in this work are in the same range as these values. The fracture intensity of the final GDFN growth steps are within an order of magnitude of at least one to two fracture sets present in deep subsurface networks.

The granite block examined in detail by Ledésert et al. [1993] and Gonzalez-Garcia et al. [2000] has a $P_{32}$ of 31.06 $m^{-1}$, a significantly higher density than the present GDFNs. This high intensity is likely to be influenced by the detailed sampling of the block, and damage associated with being a surface outcrop, where fracture densities are much higher. It is expected that the present GDFNs do not reproduce an equivalent fracture intensity, given the much simpler stress history the network is subject to. Generation of more densely fractured GDFNs can be facilitated by implementing fracture crossing, applying multiple separate deformation phases, seeding of new flaws, and using different physical processes to grow fractures (*e.g.*, fluid injection and thermal effects). Compared to kinematically generated DFNs, the present networks are also less intensely fractured by one order of magnitude [Maillot et al., 2016a].

Expected challenges which are likely to be encountered when matching GDFNs to real networks are considered in the rest of this section. The present GDFNs are grown until no fracture tips are active. Real subsurface fracture networks do not share this concept of a final, 'mature' state, as they may be actively growing under the present stress state. Therefore, it may be preferable to allow a GDFN to grow to fracture intensities higher than the target network's, providing a range of possible fractured states. Because the present networks have relatively low densities compared to some real networks, it is likely that much more growth (*i.e.*, more fractures and more phases of deformation) would be needed to match GDFNs to most subsurface networks.

Using a detailed tectonic history to generate a GDFN would enable analysis of how individual phases of deformation altered network geometries and permeabilities through time. Because the present method is quasi-static, the duration of the tectonic stress conditions which cause the network to grow can only be specified indirectly. Subsequently, the geometric state of each fracture set can be matched to its associated tectonic phase to reproduce a specific stress history.

An additional challenge will be to provide an initial flaw distribution that the present method requires, because such a flaw distribution is difficult to quantify from a final fracture network, even when examined in detail. GDFNs may be able to reproduce the mechanical and hydrological properties of the system without exact knowledge of an initial distribution of micro-flaws, as the final patterns of the present networks depend strongly on the mechanical conditions and deformation history, rather than on the placement of the small defects within the rock.

## 6.7 Conclusions

This chapter has demonstrated a fully mechanically-driven model for generating three-dimensional geomechanical discrete fracture networks (GDFNs). The method is built within the Imperial College Geomechanics Toolkit (ICGT) and utilises significant advancements in fracture growth methodology from Chapters 2 and 4. Six GDFNs are generated and examined in detail, through their geometric and hydraulic properties, and compared to a suite of stochastic discrete fracture networks (SDFNs). The realism of the networks is critically analysed, and implications for future use and development of GDFNs is discussed in detail.

The six GDFNs presented contain realistic features which are absent from standard stochastic networks. During growth, fractures orient themselves with respect to the principal stress direction, leading to significant anisotropy in the final network. Fracture sizes are highly heterogeneous and non-planar due the mechanical process of mutual fracture growth, interaction, and intersection. Stress amplification, validated and quantified for pairs of fractures in Chapter 3, causes initially inactive fractures to grow. Despite GDFNs growing from an initially random set of initial flaws, all six GDFNs converge towards similar final densities, with many geometric similarities between the final domains. This demonstrates that the primary influences on the network's properties are the stress conditions and fracture interaction, rather than stochastic processes which initiated them. The final networks have fracture intensities of the same order of magnitude as deep fracture networks in crystalline rocks [Cvetkovic et al., 2004, Follin et al., 2014].

The equivalent permeabilities of the GDFNs are quantified using the flow method introduced in Chapter 5. Each of the GDFNs has a similar pattern of permeability during their growth, characterised by an initially isotropic permeability tensor, percolation perpendicular to the stress direction after several growth steps, and increasing permeability towards a similar limit, influenced by the final network density. Compared to three sets of SDFNs with different flaw insertion schemes, GDFNs are much more anisotropic, more permeable at higher densities, and generally percolate at higher fracture intensities. A group of SDFNs which mimic the properties of the grown GDFNs more closely match GDFN properties, but lack the important realistic features which emerge during the growth process.

The influence of mechanics on network hydraulic properties is also examined by re-stressing the GDFNs, then extracting mechanical fracture apertures from the displacement discontinuity between fracture surfaces. The resulting flow patterns are significantly different from uniform aperture flow experiments. Aperture distributions are

highly influenced by the stress field and mutual fracture interaction. Flow is significantly more channelled through fewer fractures in the domain, matching observations of other real and simulated networks, where a subset of open, optimally oriented fractures provides the primary pathway for flow in the network [Bisdom et al., 2015, Follin et al., 2014, Tsang and Neretnieks, 1998].

The results presented in this chapter demonstrate a new method for generating fracture networks, and represents a step-change for the field of discrete fracture network engineering. GDFNs can be readily generated and applied to a wide variety of topics, including radioactive waste disposal, reservoir analysis, geothermal energy, $CO_2$ sequestration, and structural geology. Potential avenues for future work to further improve GDFN generation are proposed in Chapter 7.

# Chapter 7

# Conclusions

This thesis demonstrates a methodology for generating networks containing geometrically realistic fracture properties which emerge from geomechanical processes. Developed within the Imperial College Geomechanics Toolkit (ICGT), the method utilises significant advancements in the simulation of three-dimensional fractures to produce a wide range of results. This section summarises the novel results presented in this thesis, their significance in the context of the scientific fields they advance, and future avenues of research that are now possible.

- **The development of a fully three-dimensional, finite element based fracture growth simulator.**
  This thesis brings together functionality from ICGT's long term development to enable the simulation of dense fracture network growth. These developments include methods for computing accurate fracture tip stress intensity factors (SIFs) [Nejati et al., 2015a,b], handling the friction between fracture surfaces [Nejati et al., 2016], accurately resolving fracture interaction [Thomas et al., 2017b], simulating fluid flow, and calculating effective permeability [Lang et al., 2014]. This thesis contains validations for all of these methods in the present implementation of ICGT: stress intensity factor computation (Section 2.5), interaction (Section 3.2.3), growth in tension and compression (Section 4.3), and flow and effective permeability (Section 5.2.4). These validations provide new benchmarks for the accuracy required to simulate accurate fracture growth in dense geomechanical networks.

- **The development of a method for quantifying three-dimensional fracture interaction in space.**
  In Chapter 3, a new method for quantifying the way multiple fractures affect stress at one another's tips is introduced. The method requires the results of only two

simulations of a static fracture: one where the fracture is isolated, and a second where one or more fractures interacts with it. Three 'interaction measures' can then be calculated by comparing the SIFs between these two states. Two of the measures, the circumferential SIF perturbation ($C$) and the maximum SIF perturbation ($M$), quantify how much the SIFs have been affected by the additional fracture. A third measure, the amplification to shielding ratio ($\epsilon$), quantifies whether that change mostly increases or decreases stress along its tip. These measures of interaction aid in calculating the separation at which fractures begin to affect one another, and whether stress changes will suppress or enhance growth. The method is demonstrated in ICGT, but has been designed such that it can be readily applied using any method which can calculate SIFs on fractures which coexist in three dimensions. The variation in these interaction measures are plotted spatially in novel 'fracture interaction maps', which can be generated for any pair of fractures of different shapes, sizes, orientations, or stress states. This thesis extends the work first published in Thomas et al. [2017b] by demonstrating additional interaction maps, including those generated under compression.

- **Simulation of fracture growth under tension and compression.**
  Chapter 4 validates the growth of isolated fractures in ICGT. Fractures growing in tension respond by forming wing cracks, as are widely observed in laboratory tests. Accurate growth of a fracture under compression makes novel use of the Augmented Lagrangian contact resolution method, developed by Nejati et al. [2016]. The method ensures SIFs are influenced by friction between the fracture surfaces, which leads to realistic growth of fractures under compression. Fracture geometries grown in both tension and compression compare very well to the compiled results of experimental wing cracks [Germanovich et al., 1994, Olson, 1993]. A modification of the Paris-type fracture growth criterion, used to set the extension length of each fracture tip, is introduced, and the implications of assuming different values of the fracture growth exponents ($\beta_f$ and $\beta_n$) on growth of single and multiple fractures are examined in detail. Arrays of fractures demonstrate how fractures interact during growth and evolve into complex non-planar surfaces.

- **Permeability analysis of a fractured Uranium Dioxide fuel pellet.**
  The effective permeability calculation method of Lang et al. [2014] is demonstrated within the present implementation of the ICGT by its use in a collaborative study with the UK National Nuclear Laboratory [Thomas et al., 2018a]. During irradiation in Advanced Gas-cooled Reactors, Uranium Dioxide fuel pellets become fractured due to a combination of densification, heating, swelling, creep, and cladding interactions. High quality images of cut-planes through a $UO_2$ fuel pellet are

combined to construct a pellet-scale discrete fracture network. The effective permeability of the pellet is quantified for a range of fracture apertures and $UO_2$ matrix permeabilities. The results demonstrate the significant impact of throughgoing fractures on the pellet's effective permeability. Numerically computed pellet permeabilities are found to closely match experimental results [Rondinella et al., 2015]. This study provides confidence in the use of the effective permeability computation method on geomechanical fracture networks, and advances understanding of the UK's radioactive waste inventory.

- **Generation of the first fully geomechanically grown, three-dimensional discrete fracture networks.**
  Chapter 6 begins by describing the implementation of several techniques which improve the generation of dense geomechanical fracture networks. Six geomechanical fracture networks are then generated and examined in detail, starting from stochastic domains with varying number of initial fractures. Over up to 55 growth steps, the networks grow until no fractures propagate. The final networks contain realistic features which emerge as a result of the stress state in the volume and the competitive process of fracture growth. The networks are inherently anisotropic, with the preferred orientation of fracture growth being perpendicular to the direction of maximum tension. A wide range of fracture shapes are present in the final networks, and fractures become widely intersected and form a well connected network. Initially inactive fractures can be activated when other fractures concentrate stress at their tips. The generated geomechanical fracture networks reach fracture intensities of a similar order of magnitude as deep crystalline fracture networks [Cvetkovic et al., 2004, Follin et al., 2014]. These networks represent a step change for field of discrete fracture network engineering, because they are created using the physics of fracture growth rather than stochastic processes.

- **Hydraulic properties of geomechanically grown fracture networks.**
  The effective permeability method is used to examine the hydraulic properties of the generated geomechancial fracture networks. A suite of stochastic networks are generated to provide a comparison to the geomechanical networks, along with other studies on random networks of disk-shaped fractures [*e.g.*, Ebigbo et al., 2016, Sævik et al., 2013, Thovert et al., 2017]. Patterns of fracture intersections in geomechanical networks are significantly different from stochastic networks, with much shorter total intersection lengths. Despite this, at high densities, geomechanical networks achieve higher permeabilities along the directions of their inherent anisotropy. Geomechanical networks generally percolate at higher densities than stochastic networks. Significantly different flow patterns emerge when fracture apertures are derived from the stress field, with only a small proportion of the

fractures forming a percolating path, due to inclined fractures acquiring much smaller apertures. This intensification of channelling when a network is subjected to mechanical stresses matches observations from other numerical methods [Bisdom et al., 2016, Min et al., 2004], and leads to flow patterns which are closer to those observed in real networks [Tsang and Neretnieks, 1998]. Direct application of geomechanical fracture networks to specific subsurface environments, informed by past and current stress regimes and statistical properties of present networks, will provide a much greater understanding of the effective permeability of fractured rock masses.

## 7.1 Future work

The development of new methods for generating and simulating geomechanically fractured media provide several avenues for further research.

- **Further development of ICGT towards generating denser networks.**
  The present geomechanical discrete fracture networks (GDFNs) have a relatively low density compared to most natural networks which are investigated in subsurface related sciences. Further development of the ICGT will enable denser networks to be generated. Multiple phases of deformation can be applied to the present GDFNs, which would create additional fracture intensity along new orientations. Such networks will contain more features which derive from the mechanics of fracture growth, particularly when fractures grow or reactivate amongst a population of previously grown fractures. Further studying and modelling of fracture intersections will result in an even wider variety of intersections arising in GDFNs.

- **Performance of semi-analytical effective permeability calculation methods on geomechanical discrete fracture networks.**
  Contemporary discrete fracture networks have been used to examine the capabilities of semi-analytical methods to estimate effective permeability [Ebigbo et al., 2016, Sævik et al., 2013, Thovert et al., 2017]. Geomechanical networks have been demonstrated as being fundamentally different from stochastic networks, which methods such as effective medium theory have been shown to work well for. Understanding how well semi-analytical methods work on geomechanical networks will provide further confidence in their use on real rock masses, or potentially demonstrate how they are ineffective and could be improved.

- **Scale dependence on the permeability of GDFNs.**
  Scaling of representative elementary volumes (REVs) in fractured rock has been a

topic of interest for a long time [Azizmohammadi and Matthäi, 2017, Baghbanan and Jing, 2007, Berkowitz, 2002, Long and Witherspoon, 1985]. Geomechanical networks have significantly different internal geometries compared to stochastic networks. A study which investigates how permeability scales with respect to GDFN scale would provide an improved understanding of permeability scaling in the subsurface. Furthermore, the scaling of mechanical processes in fracture network growth can also be considered using a three-dimensional geomechanical methodology (*e.g.*, spacing of fractures in a layered medium [Procter and Sanderson, 2018]).

- **Influence of physical and numerical parameters on the development of geomechanical discrete fracture networks.**
  A wide range of parameters may influence the way GDFNs develop. Many of these properties will have relatively little influence on the final networks. For example, the final state of the present GDFNs were relatively unaffected by the initial number of fractures. Investigations to the impact of the fracture growth exponents $\beta_f$ and $\beta_n$ have shown that fracture shapes and interaction patterns change significantly with different exponent values [Thomas et al., 2018b]. In this thesis, the values of the $\beta_f$ and $\beta_n$ parameters have been chosen based on the findings of other analyses [Lazarus, 2003, Renshaw and Pollard, 1994]. This choice of values has enabled networks to develop into dense domains where fractures activate widely, and ensured final fracture patterns are influenced by interaction. Future work should put examine how realistic these values are by comparing mutual growth in outcrops and experiments to simulated fractures and networks. Reducing the computational time per growth step will also enable simulations with high $\beta_f$ and $\beta_n$ to be tested, as high values reported by other researchers result in smaller growth increments per growth step in the present method [Ko and Kemeny, 2013, Olson, 1993]. Further parameters of interest include material properties (*i.e.*, Young's modulus, Poisson's ratio, and the critical stress intensity factor) and numerical parameters (minimum and maximum fracture extensions lengths per growth step and number of fracture tip nodes). Greater understanding of how these properties influence geomechanical network development will in turn improve understanding of how different subsurface rock properties influence their internal networks.

- **A dimensionless formulation of fracture interaction and growth in the ICGT**
  Fractures have fractal properties in nature, with similar structures arising across many different scales (*e.g.*, Figure 4.2). In the present method, scale does not significantly influence the results of growth simulations. A dimensionless formulation of the present method will make the results of simulations more readily applicable

to a wider range of applications. In particular, the SIF interaction maps in Chapter 3 and fracture arrays in Chapter 4 can be scaled by the radii and separations between interacting fractures.

- **A study of percolation in GDFNs.**
  Percolation is a key property of a connected network and has been examined in detail for the present networks. However, the properties of the networks are influenced by many parameters, including extension lengths in each step, numbers of initial flaws and their distribution, fracture growth rate exponents, and boundary effects. This variability complicates forming a more unified theory on percolation thresholds in geomechanical networks. Additionally, the present GDFNs have properties which are not considered in other fracture network percolation studies, including non-planar fractures and mechanical influences on activation and spacing [*e.g.*, Masihi and King, 2007, Thovert et al., 2017]. Therefore, new insights to percolation in real fracture systems may be available following a detailed study of percolation in growing geomechanical networks.

# Bibliography


Abbasi, M., Madani, M., Sharifi, M., Kazemi, A., 2018. Fluid flow in fractured reservoirs: exact analytical solution for transient dual porosity model with variable rock matrix block size. Journal of Petroleum Science and Engineering 164, 571–583.

Adler, P. M., Thovert, J.-F., Mourzenko, V. V., 2012. Fractured porous media. Oxford University Press.

Ahmed Elfeel, M., Geiger, S., 2012. Static and dynamic assessment of DFN permeability upscaling. Proceedings of SPE Europec/EAGE Annual Conference, 4–7.

Al-Ostaz, A., Jasiuk, I., Lee, M., 1998. Circular inclusion in half-plane: Effect of boundary conditions. Journal of Engineering Mechanics 124 (3), 293–300.

Al-Raoush, R., Papadopoulos, A., 2010. Representative elementary volume analysis of porous media using X-ray computed tomography. Powder Technology 200 (1-2), 69–77.

Alart, P., Curnier, A., 1991. A mixed formulation for frictional contact problems prone to Newton like solution methods. Computer Methods in Applied Mechanics and Engineering 92, 353–375.

Aliha, M. R., Bahmani, A., Akhondi, S., 2015. Determination of mode III fracture toughness for different materials using a new designed test configuration. Materials and Design 86, 863–871.

Anders, M. H., Laubach, S. E., Scholz, C. H., 2014. Microfractures: a review. Journal of Structural Geology 69, 377–394.

Anderson, T. L., Anderson, T., 2005. Fracture mechanics: fundamentals and applications. CRC press.

Ansys, Inc., 2012. ANSYS ICEM CFN User Manual (version 14.5).

Antolovich, S. D., Saxena, A., Gerberich, W. W., 2018. Fracture mechanics – An interpretive technical history. Mechanics Research Communications 91, 46–86.

Anwyl, C., Boxall, C., Wilbraham, R., Hambley, D. I., Padovani, C., 2016. Corrosion of AGR Fuel Pin Steel under Conditions Relevant to Permanent Disposal. Procedia Chemistry 21, 247–254.

Atkinson, B. K., 1984. Subcritical crack growth in geological materials. Journal of Geophysical Research: Solid Earth (1978–2012) 89 (B6), 4077–4114.

Azizmohammadi, S., Matthäi, S. K., 2017. Is the permeability of naturally fractured rocks scale dependent? Water Resources Research 53, 1–23.

Baecher, G., Lanney, N., Einstein, H., 1977. Statistical description of rock properties and sampling. In: The 18th U.S. Symposium on Rock Mechanics (USRMS). pp. 1–8.

Baek, S. H., Kim, S. S., Kwon, J. S., Um, E. S., 2017. Ground penetrating radar for fracture mapping in underground hazardous waste disposal sites: A case study from an underground research tunnel, South Korea. Journal of Applied Geophysics 141, 24–33.

Baghbanan, A., Jing, L., 2007. Hydraulic properties of fractured rock masses with correlated fracture length and aperture. International Journal of Rock Mechanics and Mining Sciences 44 (5), 704–719.

Baghbanan, A., Jing, L., 2008. Stress effects on permeability in a fractured rock mass with correlated fracture length and aperture. International Journal of Rock Mechanics and Mining Sciences 45 (8), 1320–1334.

Balberg, I., Binenbaum, N., Wagner, N., 1984. Percolation thresholds in the three-dimensional sticks system. Physical Review Letters 52 (17), 1465–1468.

Bandis, S. C., Lumsden, A. C., Barton, N. R., 1983. Fundamentals of rock joint deformation. International Journal of Rock Mechanics and Mining Sciences and 20 (6), 249–268.

Banks-Sills, L., 1991. Application of the finite element method to linear elastic fracture mechanics. Applied Mechanics Reviews 44 (10), 447–461.

Banks-Sills, L., Sherman, D., 1986. Comparison of methods for calculating stress intensity factors with quarter-point elements. International Journal of Fracture 32 (2), 127–140.

Barrable, D., Kershaw, J. H., Overton, R. S., Brearley, K., Gray, D. R., 1997. Increasing Fuel Irradiations at Advanced Gas-cooled Reactors in the UK. Vol. 1. Top Fuel.

Barton, C., 1978. Analysis of joint traces. In: The 19th US Symposium on Rock Mechanics (USRMS). pp. 38–41.

Barton, N., Bandis, S., Bakhtar, K., 1985. Strength, deformation and conductivity coupling of rock joints. International Journal of Rock Mechanics and Mining Sciences and 22 (3), 121–140.

Bažant, Z. P., Estenssoro, L. F., 1979. Surface singularity and crack propagation. International Journal of Solids and Structures 15 (5), 405–426.

Bear, J., 1989. Dynamics of fluids in porous media. Dover Publications.

Belytschko, T., Black, T., 1999. Elastic crack growth in finite elements with minimal remeshing. International Journal for Numerical Methods in Engineering 45 (5), 601–620.

Belytschko, T., Gracie, R., Ventura, G., 2009. A review of extended/generalized finite element methods for material modeling. Modelling and Simulation in Materials Science and Engineering 17 (4), 043001.

Benedetto, M., Borio, A., Scialò, S., 2017. Mixed virtual elements for discrete fracture network simulations. Finite Elements in Analysis and Design 134, 55–67.

Benthem, J. P., 1977. State of stress at the vertex of a quarter-infinite crack in a half-space. International Journal of Solids and Structures 13 (5), 479–492.

Benveniste, Y., Dvorak, G. J., Zarzour, J., Wung, E. C. J., 1989. On interacting cracks and complex crack configurations in linear elastic media. International Journal of Solids and Structures 25 (11), 1279–1293.

Berkowitz, B., 2002. Characterizing flow and transport in fractured geological media: a review. Advances in Water Resources 25 (8-12), 861–884.

Berrone, S., Pieraccini, S., Scialò, S., 2017. Flow simulations in porous media with immersed intersecting fractures. Journal of Computational Physics 345, 768–791.

Bianchi, M., Liu, H. H., Birkholzer, J. T., 2015. Radionuclide transport behavior in a generic geological radioactive waste repository. Groundwater 53 (3), 440–451.

Bisdom, K., Bertotti, G., Nick, H. M., 2015. The impact of in-situ stress and outcrop-based fracture geometry on hydraulic aperture and upscaled permeability in fractured reservoirs. Tectonophysics 690, 63–75.

Bisdom, K., Bertotti, G., Nick, H. M., 2016. The impact of different aperture distribution models and critical stress criteria on equivalent permeability in fractured rocks. Journal of Geophysical Research: Solid Earth 121, 4045–4063.

Black, J. H., Woodman, N. D., Barker, J. A., 2016. Groundwater flow into underground openings in fractured crystalline rocks: an interpretation based on long channels. Hydrogeology Journal 25, 445–463.

Bonneau, F., Caumon, G., Renard, P., 2016. Impact of a stochastic sequential initiation of fractures on the spatial correlations and connectivity of discrete fracture networks. Journal of Geophysical Research: Solid Earth 121, 5641–5658.

Bonnet, E., Bour, O., Odling, N. E., Davy, P., Main, I., Cowie, P., Berkowitz, B., 2001. Scaling of Fracture systems in geological media. Reviews of Geophysics 39 (3), 347–383.

Borden, M. J., Hughes, T. J. R., Landis, C. M., Verhoosel, C. V., 2014. A higher-order phase-field model for brittle fracture: Formulation and analysis within the isogeometric analysis framework. Computer Methods in Applied Mechanics and Engineering 273, 100–118.

Borstad, C., McGrath, D., Pope, A., 2017. Fracture propagation and stability of ice shelves governed by ice shelf heterogeneity. Geophysical Research Letters 44 (9), 4186–4194.

Brace, W., 1960. An extension of the Griffith theory of fracture to rocks. Journal of Geophysical Research 65 (10), 3477–3480.

Branco, R., Antunes, F. V., Costa, J. D., 2015. A review on 3D-FE adaptive remeshing techniques for crack growth modelling. Engineering Fracture Mechanics 141, 170–195.

Bratton, T., Canh, D. V., Van Que, N., Duc, N. V., Gillespie, P., Hunt, D., Li, B., Marcinew, R., Ray, S., Montaron, B., et al., 2006. The nature of naturally fractured reservoirs. Oilfield Review 18 (2), 4–23.

Bremberg, D., Faleskog, J., 2015. A numerical procedure for interaction integrals developed for curved cracks of general shape in 3-D. International Journal of Solids and Structures 62, 144–157.

British Geological Survey, 2017. Radioactivity and the Environment research consortia. URL www.bgs.ac.uk/rate/researchConsortia.html

Budzik, M. K., Myhre Jensen, H., 2014. Perturbation analysis of crack front in simple cantilever plate peeling experiment. International Journal of Adhesion and Adhesives 53, 29–33.

Busfield, J. J. C., Jha, V., Liang, H., Papadopoulos, I. C., Thomas, A. G., 2005. Prediction of fatigue crack growth using finite element analysis techniques applied to three-dimensional elastomeric components. Plastics, Rubber and Composites 34 (8), 349–356.

Cambonie, T., Klinger, Y., Lazarus, V., 2019. Similarities between mode III crack growth patterns and strike-slip faults. Philosophical Transactions of the Royal Society A: Mathematical, Physical and Engineering Sciences 377 (2136).

Cambonie, T., Lazarus, V., 2014. Quantification of the crack fragmentation resulting from mode I+III loading. Procedia Materials Science 3, 1816–1821.

Cao, P., Liu, T., Pu, C., Lin, H., 2015. Crack propagation and coalescence of brittle rock-like specimens with pre-existing cracks in compression. Engineering Geology 187, 113–121.

Cartwright, J. A., Mansfield, C., Trudgill, B., 1996. The growth of normal faults by segment linkage. Geological Society, London, Special Publications 99 (1), 163–177.

Chang, S.-h., Lee, C.-i., Jeon, S., 2002. Measurement of rock fracture toughness under modes I and II and mixed-mode conditions by using disc-type specimens. Engineering Geology 66 (1-2), 79–97.

Chapman, N. A., McEwen, T. J., Beale, H., 1986. Geological environments for deep disposal of intermediate level wastes in the United Kingdom. Tech. Rep. IAEA-SM-289/37.

Charles, R., 1958. Static fatigue of glass. I. Journal of Applied Physics 29 (11), 1549–1553.

Chen, F. H. K., Shield, R. T., 1977. Conservation laws in elasticity of the J-integral type. Zeitschrift fär angewandte Mathematik und Physik 28 (1), 1–22.

Cheng, W., Jin, Y., Chen, M., Xu, T., Zhang, Y., Diao, C., 2014. A criterion for identifying hydraulic fractures crossing natural fractures in 3D space. Petroleum Exploration and Development 41 (3), 371–376.

Christie, M., Blunt, M., 2001. Tenth SPE comparative solution project: a comparison of upscaling techniques. SPE Reservoir Evaluation & Engineering 4 (04), 308–317.

Cook, R. D., et al., 2007. Concepts and applications of finite element analysis. John Wiley & Sons.

Cordall, D., Hatton, D., Jackson, P., Hale, C., 1992. Performance of AGR fuel - past, present and future. Nuclear Energy 1 (31), 55–63.

Cottereau, N., Garcia, M. H., Gosselin, O. R., Vigier, L., 2010. Effective fracture network permeability: Comparative study of calculation methods. SPE EUROPEC/EAGE Annual Conference and Exhibition, Barcelona, pp. 1–31.

Cotterell, B., Rice, J. R., 1980. Slightly curved or kinked cracks. International Journal of Fracture 16 (2), 155–169.

Cowie, P. A., 1998. Normal fault growth in three-dimensions in continental and oceanic crust. Faulting and Magmatism at Mid-ocean Ridges, 325–348.

Cowie, P. A., Gupta, S., Dawers, N. H., 2000. Implications of fault array evolution for synrift depocentre development: Insights from a numerical fault growth model. Basin Research 12 (3-4), 241–261.

Cowie, P. A., Vanneste, C., Sornette, D., 1993. Statistical physics model for the spatiotemporal evolution of faults. Journal of Geophysical Research: Solid Earth (1978–2012) 98 (B12), 21809–21821.

Crider, J. G., 2015. The initiation of brittle faults in crystalline rock. Journal of Structural Geology 77, 159–174.

Cvetkovic, V., Painter, S., Outters, N., Selroos, J. O., 2004. Stochastic simulation of radionuclide migration in discretely fractured rock near the Äspö Hard Rock Laboratory. Water Resources Research 40 (2).

Darcy, H., 1856. Les fontaines publiques de la ville de Dijon: exposition et application.

Davy, P., Darcel, C., Le Goc, R., Munier, R., Selroos, J. O., Mas Ivars, D., 2018. DFN, why, how and what for, concepts, theories and issues. 2nd International Discrete Fracture Network Engineering Conference.

Davy, P., Le Goc, R., Darcel, C., 2013. A model of fracture nucleation, growth and arrest, and consequences for fracture density and scaling. Journal of Geophysical Research: Solid Earth 118 (4), 1393–1407.

Davy, P., Le Goc, R., Darcel, C., Bour, O., De Dreuzy, J. R., Munier, R., 2010. A likely universal model of fracture scaling and its consequence for crustal hydromechanics. Journal of Geophysical Research: Solid Earth 115 (10), 1–13.

de Dreuzy, J.-R., 2002. Hydraulic properties of two-dimensional random fracture networks following power law distributions of length and aperture. Water Resources Research 38 (12), 2065–2078.

Decroux, B., Gosselin, O., 2013. Computation of effective dynamic properties of naturally fractured reservoirs - comparison and validation of methods. In: 75th EAGE Conference & Exhibition incorporating SPE EUROPEC 2013. pp. 10–13.

Defoort, T., Paluszny, A., Zimmerman, R., 2016. Comparison of fracture mechanics and damage mechanics approaches to simulate three-point bending and double-notch shear experiments on rock samples. In: 50th U.S. Rock Mechanics/Geomechanics Symposium. American Rock Mechanics Association.

Delaney, P. T., Pollard, D. D., 1981. Deformation of host rocks and flow of magma during growth of minette dikes and breccia-bearing intrusions near Ship Rock, New Mexico. U.S. Geological Survey Professional Paper 12.

den Boer, L. D., Sayers, C. M., 2017. Constructing a discrete fracture network constrained by seismic inversion data. Geophysical Prospecting, 1–17.

Dershowitz, W. S., Einstein, H. H., 1988. Characterizing rock joint geometry with joint system models. Rock Mechanics and Rock Engineering 21 (1), 21–51.

Dershowitz, W. S., Herda, H. H., 1992. Interpretation of fracture spacing and intensity. In: Tillerson, J., Wawersik, W. (Eds.), Proceedings of the 33rd U.S. Symposium on Rock Mechanics. Vol. 40. pp. 342–344.

Dershowitz, W. S., Hermanson, J., Follin, S., Mauldon, M., 2000. Fracture intensity measures in 1-D, 2-D, and 3-D at Aspo, Sweden. In: 4th North American Rock Mechanics Symposium. American Rock Mechanics Association, pp. 849–853.

Dolbow, J., Moës, N., Belytschko, T., 2001. An extended finite element method for modeling crack growth with frictional contact. Computer Methods in Applied Mechanics and Engineering 190 (51-52), 6825–6846.

Duffy, O. B., Bell, R. E., Jackson, C. A. L., Gawthorpe, R. L., Whipp, P. S., 2015. Fault growth and interactions in a multiphase rift fault network: Horda Platform, Norwegian North Sea. Journal of Structural Geology 80, 99–119.

Durlofsky, L., 2005. Upscaling and gridding of fine scale geological models for flow simulation. 8th International Forum on Reservoir Simulation, 1–59.

Dyskin, A. V., Germanovich, L. N., Ustinov, K. B., 1999. A 3-D model of wing crack growth and interaction. Engineering Fracture Mechanics 63 (1), 81–110.

Ebigbo, A., Lang, P. S., Paluszny, A., Zimmerman, R. W., 2016. Inclusion-based effective medium models for the permeability of a 3D fractured rock mass. Transport in Porous Media 113, 137–158.

Fabrikant, V. I., 1987. Close interaction of coplanar circular cracks in an elastic medium. Acta Mechanica 67 (1-4), 39–59.

Fan, Y., Zhu, Z., Kang, J., Fu, Y., 2016. The mutual effects between two unequal collinear cracks under compression. Mathematics and Mechanics of Solids, 1–14.

Fang, J., Zhou, F., Tang, Z., 2017. Discrete fracture network modelling in a naturally fractured carbonate reservoir in the Jingbei oilfield, China. Energies 10 (2), 183.

Favier, E., Lazarus, V., Leblond, J. B., 2006. Coplanar propagation paths of 3D cracks in infinite bodies loaded in shear. International Journal of Solids and Structures 43 (7-8), 2091–2109.

Fereshtenejad, S., Afshari, M. K., Bafghi, A. Y., Laderian, A., Safaei, H., Song, J. J., 2016. A discrete fracture network model for geometrical modeling of cylindrically folded rock layers. Engineering Geology 215, 81–90.

Fischer, K. A., Wriggers, P., 2005. Frictionless 2D contact formulations for finite deformations based on the mortar method. Computational Mechanics 36 (3), 226–244.

Follin, S., Hartley, L., Rhén, I., Jackson, P., Joyce, S., Roberts, D., Swift, B., 2014. A methodology to constrain the parameters of a hydrogeological discrete fracture network model for sparsely fractured crystalline rock, exemplified by data from the proposed high-level nuclear waste repository site at Forsmark, Sweden. Hydrogeology Journal 22, 313–331.

Fox, A., Pointe, P. L., Isaksson, H., Ab, G., Hermanson, J., Öhman, J., 2007. Site descriptive modelling, Forsmark stage 2.2. Tech. rep., Swedish Nuclear Fuel and Waste Management Company (SKB).

Francfort, G., Marigo, J.-J., 1998. Revisiting brittle fracture as an energy minimization problem. Journal of the Mechanics and Physics of Solids 46 (8), 1319–1342.

Fu, P., Johnson, S. M., Carrigan, C. R., 2013. An explicitly coupled hydro-geomechanical model for simulating hydraulic fracturing in arbitrary discrete fracture networks. International Journal for Numerical and Analytical Methods in Geomechanics 37 (14), 2278–2300.

Gao, H., Rice, J. R., 1989. A First-Order Perturbation Analysis of Crack Trapping by Arrays of Obstacles. Journal of Applied Mechanics 56 (4), 828.

Garipov, T. T., Karimi-Fard, M., Tchelepi, H. A., 2016. Discrete fracture model for coupled flow and geomechanics. Computational Geosciences 20 (1), 149–160.

Gawthorpe, R. L., Leeder, M. R., 2000. Tectono-sedimentary evolution of active extensional basins. Basin Research 12 (3-4), 195–218.

Germanovich, L. N., Salganik, R. L., Dyskin, A. V., Lee, K. K., 1994. Mechanisms of brittle fracture of rock with pre-existing cracks in compression. Pure and Applied Geophysics PAGEOPH 143 (1-3), 117–149.

Gertsch, L. S., 1995. Three-dimensional fracture network models from laboratory-scale rock samples. International Journal of Rock Mechanics and Mining Sciences and 32 (1), 85–91.

Ghahfarokhi, P. K., 2017. The structured gridding implications for upscaling model discrete fracture networks (DFN) using corrected Oda's method. Journal of Petroleum Science and Engineering 153, 70–80.

Ghosh, N., Hatui, K., Chattopadhyay, A., 2019. Propagation and coalescence of en-echelon cracks under a far-field tensile stress regime: an experimental study. Journal of Earth System Science 128 (23).

Gillespie, P. A., Howard, C. B., Walsh, J. J., Watterson, J., 1993. Measurement and characterisation of spatial distributions of fractures. Tectonophysics 226 (1-4), 113–141.

Goetze, C., 1971. High temperature rheology of westerly granite. Journal of Geophysical Research 76 (5), 1223–1230.

Gonzalez-Garcia, R., Huseby, O., Thovert, J.-F., Ledésert, B., Adler, P. M., 2000. Three-dimensional characterization of a fractured granite and transport properties. Journal of Geophysical Research: Solid Earth 105 (B9), 21387–21401.

Grechka, V., Kachanov, M., 2006. Effective elasticity of fractured rocks: A snapshot of the work in progress. Geophysics 71 (6), W45–W58.

Green, R. G., Greenfield, T., White, R. S., 2015. Triggered earthquakes suppressed by an evolving stress shadow from a propagating dyke. Nature Geoscience 8 (8), 629–632.

Griffith, A. A., 1921. The phenomena of rupture and flow in solids. Philosophical transactions of the royal society of london. Series A, containing papers of a mathematical or physical character, 163–198.

Gross, D., 1982. Stress intensity factors of systems of cracks. Ingenieur-Archiv. 51, 301–310.

Gupta, P., Duarte, C. A., 2014. Simulation of non-planar three-dimensional hydraulic fracture propagation. International Journal for Numerical and Analytical Methods in Geomechanics 38, 1397–1430.

Gupta, P., Duarte, C. A., Dhankhar, A., 2017. Accuracy and robustness of stress intensity factor extraction methods for the generalized/eXtended Finite Element Method. Engineering Fracture Mechanics 179, 120–153.

Gwo, J. P., Jardine, P. M., Wilson, G. V., Yeh, G. T., 1995. A multiple-pore-region concept to modeling mass-transfer in subsurface media. Journal of Hydrology 164 (1-4), 217–237.

Hadjab-Souag, H., Thimus, J.-F., Chabaat, M., 2007. Detecting the fracture process zone in concrete using scanning electron microscopy and numerical modelling using the nonlocal isotropic damage model. Canadian Journal of Civil Engineering 34 (4), 496–504.

Hambley, D., 2013. Technical basis for extending storage of the uk's advanced gas-cooled reactor fuel. International Nuclear Fuel Cycle Conference, GLOBAL 2013: Nuclear Energy at a Crossroads 2.

Hardebol, N. J., Maier, C., Nick, H., Geiger, S., Bertotti, G., Boro, H., 2015. Multiscale fracture network characterization and impact on flow: A case study on the Latemar carbonate platform. Journal of Geophysical Research B: Solid Earth 120 (12), 8197–8222.

He, L. H., Li, Z. R., 2006. Impact of surface stress on stress concentration. International Journal of Solids and Structures 43 (20), 6208–6219.

Henao, D., Mora-Corral, C., Xu, X., 2016. A numerical study of void coalescence and fracture in nonlinear elasticity. Computer Methods in Applied Mechanics and Engineering 303, 163–184.

Hernández, J., Huespe, A., Caicedo, M., Oliver, J., Roubin, E., 2015. Continuum approach to computational multiscale modeling of propagating fracture. Computer Methods in Applied Mechanics and Engineering 294, 384–427.

Hewitt, G. F., Collier, J. G., 2000. Introduction to nuclear power. London: Taylor and Francis.

Hoek, E., Bieniawski, Z. T., 1984. Brittle fracture propagation in rock under compression. International Journal of Fracture 26 (4), 276–294.

Hoek, E., Martin, C. D., 2014. Fracture initiation and propagation in intact rock - a review. Journal of Rock Mechanics and Geotechnical Engineering 6 (4), 287–300.

Holt, M., 2015. Civilian Nuclear Waste Disposal. Congressional Research Service.

Hyman, J. D., Karra, S., Carey, J. W., Gable, C. W., Viswanathan, H., Rougier, E., Lei, Z., 2018. Discontinuities in effective permeability due to fracture percolation. Mechanics of Materials 119, 25–33.

Imber, J., Tuckwell, G., Childs, C., Walsh, J., Manzocchi, T., Heath, A., Bonson, C., Strand, J., 2004. Three-dimensional distinct element modelling of relay growth and breaching along normal faults. Journal of Structural Geology 26 (10), 1897 – 1911.

Inglis, C. E., 1913. Stresses in a plate due to the presence of cracks and sharp corners. Transcripts of the Institution of Naval Architects, 219–242.

Inglis, G. H., Littlechild, J. E., Stewart, R., 1982. Fabrication of uranium oxide fuel pellets using the IDR powder process. Vol. 12. International Atomic Energy Agency, Vienna (Austria), pp. 553–564.

Ingraffea, A. R., Manu, C., 1957. Stress-intensity factor computation in three dimensions with quarter-point elements. International Journal for Numerical Methods in Engineering 15 (10), 1427–1445.

Irwin, G., 1956a. Onset of fast crack propagation in high strength steel and aluminum alloys. In: Sagamore Research Conference Proceedings. Vol. 2. pp. 289–305.

Irwin, G. R., 1956b. Analysis of stresses and strains near the end of a crack traversing a plate. Journal of Applied Mechanics 24 (79), 361–364.

Irwin, G. R., 1961. Plastic zone near a crack and fracture roughness. In: Proceedings of the 7th Sagamore Ordnance Materials Research Conference on Mechanical and Metallurgical Behavior of Sheet Materials. pp. 63–78.

Jackson, C. A., Rotevatn, A., 2013. 3D seismic analysis of the structure and evolution of a salt-influenced normal fault zone: A test of competing fault growth models. Journal of Structural Geology 54, 215–234.

Jaeger, J. C., Cook, N. G., Zimmerman, R., 2009. Fundamentals of rock mechanics. John Wiley & Sons.

Ji, S.-H., Koh, Y.-K., 2016. Appropriate domain size for groundwater flow modeling with a discrete fracture network model. Groundwater, 1–12.

Jing, L., Hudson, J. A., 2002. Numerical methods in rock mechanics. International Journal of Rock Mechanics and Mining Sciences 39 (4), 409–427.

Jing, L., Min, K. B., Baghbanan, A., Zhao, Z., 2013. Understanding coupled stress, flow and transport processes in fractured rocks. Geosystem Engineering 16 (1), 2–25.

Josnin, J.-Y., Jourde, H., Fénart, P., Bidaux, P., 2002. A three-dimensional model to simulate joint networks in layered rocks. Canadian Journal of Earth Sciences 39 (10), 1443–1455.

Jourde, H., Fenart, P., Vinches, M., Pistre, S., Vayssade, B., 2007. Relationship between the geometrical and structural properties of layered fractured rocks and their effective permeability tensor: a simulation study. Journal of Hydrology 337 (1-2), 117–132.

Kachanov, M., 1987. Elastic solids with many cracks: a simple method of analysis. International Journal of Solids and Structures 23 (1), 23–43.

Kachanov, M., 1993. Elastic solids with many cracks and related problems. Advances in Applied Mechanics 30, 259–445.

Kachanov, M., Laures, J. P., 1989. Three-dimensional problems of strongly interacting arbitrarily located penny-shaped cracks. International Journal of Fracture 41 (4), 289–313.

Kamaya, M., 2008a. Growth evaluation of multiple interacting surface cracks: Part I: Experiments and simulation of coalesced crack. Engineering Fracture Mechanics 75 (6), 1336–1349.

Kamaya, M., 2008b. Growth evaluation of multiple interacting surface cracks. Part II: Growth evaluation of parallel cracks. Engineering Fracture Mechanics 75 (6), 1350–1366.

Karamnejad, A., Sluys, L. J., 2014. A dispersive multi-scale crack model for quasi-brittle heterogeneous materials under impact loading. Computer Methods in Applied Mechanics and Engineering 278, 423–444.

Karampinos, E., Hadjigeorgiou, J., Hazzard, J., Turcotte, P., 2015. Discrete element modelling of the buckling phenomenon in deep hard rock mines. International Journal of Rock Mechanics and Mining Sciences 80, 346–356.

Karimi-Fard, M., Durlofsky, L., Aziz, K., 2004. An efficient discrete fracture model applicable for general purpose reservoir simulators. SPE Journal, SPE-88812-PA 9 (02), 227 – 236.

Karimi-Fard, M., Firoozabadi, A., 2003. Numerical Simulation of Water Injection in Fractured Media Using the Discrete-Fracture Model and the Galerkin Method. SPE Reservoir Evaluation & Engineering 6 (2), 117–126.

Kassir, M. K., Sih, G. C., 1975. Mechanics of Fracture 2, Three-Dimensional Crack Problems. Noordhoff International Publishing, Leyden.

Kazemi, H., Merrill, L., Porterfield, K., Zeman, P., 1976. Numerical simulation of water-oil flow in naturally fractured reservoirs. Society of Petroleum Engineers Journal 16 (06), 317–326.

Keilegavlen, E., Fumagalli, A., Berge, R., Stefansson, I., Berre, I., 2017. PorePy: an open-source simulation tool for flow and transport in deformable fractured rocks. arXiv 1712.00460.

Kemeny, J. M., 1991. A model for non-linear rock deformation under compression due to sub-critical crack growth. International Journal of Rock Mechanics and Mining Sciences 28 (6), 459–467.

Khoei, A. R., Eghbalian, M., Moslemi, H., Azadi, H., 2013. Crack growth modeling via 3D automatic adaptive mesh refinement based on modified-SPR technique. Applied Mathematical Modelling 37 (1-2), 357–383.

Kholi, R., Stahl, D., Pasupathi, V., Johnson, A., Gilbert, E., 1985. The behaviour of breached boiling water reactor fuel rods on long term exposure to air and argon at 598K. Nuclear Technology 86, 186–197.

Kim, J.-G., Deo, M. D., 2000. Finite element, discrete-fracture model for multiphase flow in porous media. AICHE Journal 46 (6), 1120–1130.

King, P. R., 1989. The use of renormalization for calculating effective permeability. Transport in Porous Media 4 (1), 37–58.

Kirkpatrick, S., 1973. Percolation and Conduction. Reviews of Modern Physics 45 (4), 574–588.

Ko, T. Y., Kemeny, J., 2013. Determination of the subcritical crack growth parameters in rocks using the constant stress-rate test. International Journal of Rock Mechanics and Mining Sciences 59, 166–178.

Kolditz, O., 1995. Modelling flow and heat transfer in fractured rocks: conceptual model of a 3-D deterministic fracture network. Geothermics 24 (3), 451–470.

Koudina, N., Gonzalez Garcia, R., Thovert, J.-F., Adler, P., 1998. Permeability of three-dimensional fracture networks. Physical Review E 57 (4), 4466–4479.

Krech, W. W., Henderson, F. A., Hjelmstad, K. E., 1974. A standard rock suite for rapid excavation research. Tech. rep., U.S. Bureau of Mines.

Kumar, D., Ghassemi, A., 2016. A three-dimensional analysis of simultaneous and sequential fracturing of horizontal wells. Journal of Petroleum Science and Engineering 146, 1006–1025.

Lam, K., Phua, S., 1991. Multiple crack interaction and its effect on stress intensity factor. Engineering Fracture Mechanics 40 (3), 585–592.

Lamarche, J., Chabani, A., Gauthier, B. D., 2017. Dimensional threshold for fracture linkage and hooking. Journal of Structural Geology 108, 171–179.

Lang, P. S., 2016. Multi-scale modelling of thermo-hydro-mechanical-chemical processes in fractured rocks. Ph.D. thesis, Imperial College London.

Lang, P. S., Paluszny, A., Nejati, M., Zimmerman, R. W., 2018. Relationship between the orientation of maximum permeability and intermediate principal stress in fractured rocks. Water Resources Research 54, 8734–8755.

Lang, P. S., Paluszny, A., Zimmerman, R. W., 2014. Permeability tensor of three-dimensional fractured porous rock and a comparison to trace map predictions. Journal of Geophysical Research: Solid Earth 119, 6288–6307.

Lang, P. S., Paluszny, A., Zimmerman, R. W., 2015. Hydraulic sealing due to pressure solution contact zone growth in siliciclastic rock fractures. Journal of Geophysical Research: Solid Earth 120 (6), 4080–4101.

Laures, J.-P., Kachanov, M., 1991. Three-dimensional interactions of a crack front with arrays of penny-shaped microcracks. International Journal of Fracture 48 (4), 255–279.

Lawn, B. R., 1993. Fracture of Brittle Solids. Cambridge University Press.

Lazarus, V., 2003. Brittle fracture and fatigue propagation paths of 3D plane cracks under uniform remote tensile loading. International Journal of Fracture 122 (1-2), 23–46.

Lazarus, V., 2011. Perturbation approaches of a planar crack in linear elastic fracture mechanics: a review. Journal of the Mechanics and Physics of Solids 59 (2), 121–144.

Leblond, J. B., Karma, A., Lazarus, V., 2011. Theoretical analysis of crack front instability in mode I+III. Journal of the Mechanics and Physics of Solids 59 (9), 1872–1887.

Leblond, J. B., Lazarus, V., Karma, A., 2015. Multiscale cohesive zone model for propagation of segmented crack fronts in mode I+III fracture. International Journal of Fracture 191 (1-2), 167–189.

Lecampion, B., Bunger, A., Zhang, X., 2018. Numerical methods for hydraulic fracture propagation: a review of recent trends. Journal of Natural Gas Science and Engineering 49, 66–83.

Leckenby, R. J., Sanderson, D. J., Lonergan, L., 2005. Estimating flow heterogeneity in natural fracture systems. Journal of Volcanology and Geothermal Research 148 (1-2), 116–129.

Ledésert, B., Dubois, J., Velde, B., Meunier, A., Genter, A., Badri, A., 1993. Geometrical and fractal analysis of a three-dimensional hydrothermal vein network in a fractured granite. Journal of Volcanology and Geothermal Research 56 (3), 267–280.

Lee, H. P., Olson, J. E., 2017. The effect of remote and internal crack stresses on mixed-mode brittle fracture propagation of open cracks under compressive loading. International Journal of Fracture 207 (2), 229–242.

Lee, S., Wheeler, M. F., Wick, T., Srinivasan, S., 2016. Initialization of phase-field fracture propagation in porous media using probability maps of fracture networks. Mechanics Research Communications 80, 16–23.

Lee, S. H., Lee, K.-K., Yeo, I. W., 2014. Assessment of the validity of Stokes and Reynolds equations for fluid flow through a rough-walled fracture with flow imaging. Geophysical Research Letters (41), 4578–4585.

Legrand, L., Lazarus, V., 2015. Front shape and loading evolution during cracks coalescence using an incremental perturbation method. Engineering Fracture Mechanics 133, 40–51.

Lei, Q., Latham, J. P., Tsang, C. F., 2017a. The use of discrete fracture networks for modelling coupled geomechanical and hydrological behaviour of fractured rocks. Computers and Geotechnics 85, 151–176.

Lei, Q., Latham, J.-P., Xiang, J., Lang, P., Tsang, C.-F., 2014a. Effects of geomechanical changes on the validity of a discrete fracture network representation of a realistic two-dimensional fractured rock. International Journal of Rock Mechanics and Mining Sciences 70, 507–523.

Lei, Q., Latham, J.-p., Xiang, J., Tsang, C.-f., Lang, P., Guo, L., 2014b. Effects of geomechanical changes on the validity of a discrete fracture network representation of a realistic two-dimensional fractured rock. International Journal of Rock Mechanics and Mining Sciences 70, 507–523.

Lei, Q., Wang, X., Xiang, J., Latham, J.-P., 2017b. Polyaxial stress-dependent permeability of a three-dimensional fractured rock layer. Hydrogeology Journal, 2251–2262.

Leung, C. T., 2012. Modelling the flow and transport properties of two-dimensional fracture networks, including the effect of stress. Ph.D. thesis, Imperial College London.

Leung, C. T.-o., Zimmerman, R. W., 2012. Estimating the hydraulic conductivity of two-dimensional fracture networks using network geometric properties. Transport in Porous Media 93 (3), 777–797.

Li, L., Lee, S. H., 2008. Efficient field-scale simulation of black oil in a naturally fractured reservoir through discrete fracture networks and homogenized media. SPE Reservoir Evaluation & Engineering 11 (04), 750–758.

Lisjak, A., Grasselli, G., 2014. A review of discrete modeling techniques for fracturing processes in discontinuous rock masses. Journal of Rock Mechanics and Geotechnical Engineering 6 (4), 301–314.

Lisjak, A., Mahabadi, O. K., He, L., Tatone, B. S., Kaifosh, P., Haque, S. A., Grasselli, G., 2018. Acceleration of a 2D/3D finite-discrete element code for geomechanical simulations using General Purpose GPU computing. Computers and Geotechnics 100, 84–96.

Lisjak, A., Tatone, B. S., Mahabadi, O. K., Grasselli, G., Marschall, P., Lanyon, G. W., de la Vaissière, R., Shao, H., Leung, H., Nussbaum, C., 2016. Hybrid finite-discrete element simulation of the EDZ formation and mechanical sealing process around a microtunnel in Opalinus Clay. Rock Mechanics and Rock Engineering 49 (5), 1849–1873.

Liu, F., Borja, R. I., 2008. A contact algorithm for frictional crack propagation with the extended finite element method. International Journal for Numerical Methods in Engineering 76 (10), 1489–1512.

Liu, W., Cui, J., Xin, J., 2018. A block-centered finite difference method for an unsteady asymptotic coupled model in fractured media aquifer system. Journal of Computational and Applied Mathematics 337 (11401289), 319–340.

Liu, Y. J., Li, Y. X., 2014. Revisit of the equivalence of the displacement discontinuity method and boundary element method for solving crack problems. Engineering Analysis with Boundary Elements 47 (1), 64–67.

Long, J. C., Billaux, D. M., 1987. From field data to fracture network modeling: An example incorporating spatial structure. Water Resources Research 23 (7), 1201–1216.

Long, J. C. S., Gilmour, P., Witherspoon, P. A., 1985. A model for steady fluid flow in random three dimensional networks of disc shaped fractures. Water Resources Research 21 (8), 1105–1115.

Long, J. C. S., Remer, J. S., Wilson, C. R., Witherspoon, P. A., 1982. Porous media equivalents for networks of discontinuous fractures. Water Resources Research 18 (3), 645.

Long, J. C. S., Witherspoon, P. A., 1985. The relationship of the degree of interconnection to permeability in fracture networks. Journal of Geophysical Research 90 (B4), 3087.

Maillot, J., Davy, P., Le Goc, R., Darcel, C., de Dreuzy, J., 2016a. Connectivity, permeability, and channeling in randomly distributed and kinematically defined discrete fracture network models. Water Resources Research 52 (11), 8526–8545.

Maillot, J., Davy, P., Le Goc, R., Darcel, C., de Dreuzy, J., 2016b. Connectivity, permeability, and channeling in randomly distributed and kinematically defined discrete fracture network models. Water Resources Research 52 (11), 8526–8545.

March, R., Doster, F., Geiger, S., 2018. Assessment of CO2 storage potential in naturally fractured reservoirs With dual-porosity models. Water Resources Research 54 (3), 1650–1668.

Marschall, P., Giger, S., De La Vassière, R., Shao, H., Leung, H., Nussbaum, C., Trick, T., Lanyon, B., Senger, R., Lisjak, A., Alcolea, A., 2017. Hydro-mechanical evolution of the EDZ as transport path for radionuclides and gas: insights from the Mont Terri rock laboratory (Switzerland). Swiss Journal of Geosciences 110 (1), 173–194.

Martin, C. D., Chandler, N. A., 1994. The progressive fracture of Lac du Bonnet granite. International Journal of Rock Mechanics and Mining Sciences and 31 (6), 643–659.

Marwick, A. D., 1978. Segregation in irradiated alloys: The inverse Kirkendall effect and the effect of constitution on void swelling. Journal of Physics F: Metal Physics (8), 1847.

Mas Ivars, D., Pierce, M. E., Darcel, C., Reyes-Montes, J., Potyondy, D. O., Paul Young, R., Cundall, P. A., 2011. The synthetic rock mass approach for jointed rock mass modelling. International Journal of Rock Mechanics and Mining Sciences 48 (2), 219–244.

Masihi, M., Gago, P. A., King, P. R., 2016. Estimation of the effective permeability of heterogeneous porous media by using percolation concepts. Transport in Porous Media 114 (1), 169–199.

Masihi, M., King, P. R., 2007. A correlated fracture network: Modeling and percolation properties. Water Resources Research 43 (7), 1–9.

Matthai, S. K., Geiger, S., Roberts, S. G., Paluszny, A., Belayneh, M., Burri, A., Mezentsev, A., Lu, H., Coumou, D., Driesner, T., Heinrich, C. A., 2007. Numerical simulation of multi-phase fluid flow in structurally complex reservoirs. Geological Society, London, Special Publications 292, 405–429.

McClure, M. W., Babazadeh, M., Shiozawa, S., Huang, J., 2016. Fully coupled hydromechanical simulation of hydraulic fracturing in 3D discrete-fracture networks. SPE Journal 21 (04), 1302–1320.

McGill, G. E., Schultz, R. A., Moore, J. M., 2000. Fault growth by segment linkage: an explanation for scatter in maximum displacement and trace length data from the Canyonlands grabens of SE Utah: Discussion. Journal of Structural Geology 22 (1), 135–140.

McKenzie, D., Jackson, J., Priestley, K., 2005. Thermal structure of oceanic and continental lithosphere. Earth and Planetary Science Letters 233 (3-4), 337–349.

Mediavilla, J., Peerlings, R. H., Geers, M. G., 2006. A robust and consistent remeshing-transfer operator for ductile fracture simulations. Computers and Structures 84 (8-9), 604–623.

Mella, R., Wenman, M. R., 2013. Axisymmetric whole pin life modelling of advanced gas-cooled reactor nuclear fuel. Journal of Nuclear Materials 437 (1-3), 154–165.

Mella, R., Wenman, M. R., 2015. Modelling explicit fracture of nuclear fuel pellets using peridynamics. Journal of Nuclear Materials 467, 58–67.

Meng, C., Maerten, F., Pollard, D. D., 2013. Modeling mixed-mode fracture propagation in isotropic elastic three dimensional solid. International Journal of Fracture 179 (1-2), 45–57.

Min, K.-B., Rutqvist, J., Tsang, C. F., Jing, L., 2004. Stress-dependent permeability of fractured rock masses: A numerical study. International Journal of Rock Mechanics and Mining Sciences 41 (7), 1191–1210.

Moreno, L., Tsang, C.-F., 1991. Multiple-Peak Response to Tracer Injection Tests in Single Fractures: A Numerical Study. Water Resources Research 27 (8), 2143–2150.

Morgan, S., Gate, A., Thompson, J., Barker, M., 2012. Understanding advanced gas-cooled reactor (CAGR) fuel using metallography. Top Fuel.

Morgan, S., Hambley, D., Foster, R., Rutherford, N., Barker, M., Woodman, F., Kyffin, J., Hillier, A., Townson, A., 2015. Post irradiation examination of UK advanced gas-cooled reactor fuel cladding (post reactor and post-storage). Hot Lab Annual Meeting, Manchester, UK.

Mourzenko, V. V., Thovert, J. F., Adler, P. M., 2011. Permeability of isotropic and anisotropic fracture networks, from the percolation threshold to very large densities. Physical Review E - Statistical, Nonlinear, and Soft Matter Physics 84 (3), 1–20.

Moussa, W. A., 2002. Investigating the interaction behavior between two arbitrarily oriented surface cracks using multilevel substructuring. Journal of Pressure Vessel Technology 124 (4), 440.

Munier, R., 2004. Statistical analysis of fracture data, adapted for modelling discrete fracture networks (version 2). Tech. Rep. R-04-66, Swedish Nuclear Fuel and Waste Management Company (SKB).

Nahta, R., Moran, B., 1993. Domain integrals for axisymmetric interface crack problems. International Journal of Solids and Structures 30 (15), 2027–2040.

Nakamura, T., Parks, D., 1988. Three-dimensional stress field near the crack front of a thin elastic plate. ASME, Transactions, Journal of Applied Mechanics 55, 805–813.

Nara, Y., Kaneko, K., 2006. Sub-critical crack growth in anisotropic rock. International Journal of Rock Mechanics and Mining Sciences 43 (3), 437–453.

Narsilio, G. A., Buzzi, O., Fityus, S., Yun, T. S., Smith, D. W., 2009. Upscaling of Navier-Stokes equations in porous media: Theoretical, numerical and experimental approach. Computers and Geotechnics 36 (7), 1200–1206.

Nasseri, M. H. B., Mohanty, B., Young, R. P., 2006. Fracture toughness measurements and acoustic emission activity in brittle rocks. Pure and Applied Geophysics 163 (5-6), 917–945.

Nejati, M., 2015. Finite element modelling of frictional contact and stress intensity factors in three-dimensional fractured media using unstructured tetrahedral meshes. Ph.D. thesis, Imperial College, London.

Nejati, M., Paluszny, A., Zimmerman, R. W., 2015a. A disk-shaped domain integral method for the computation of stress intensity factors using tetrahedral meshes. International Journal of Solids and Structures 69-70, 230–251.

Nejati, M., Paluszny, A., Zimmerman, R. W., 2015b. On the use of quarter-point tetrahedral finite elements in linear elastic fracture mechanics. Engineering Fracture Mechanics 144, 194–221.

Nejati, M., Paluszny, A., Zimmerman, R. W., 2016. A finite element framework for modeling internal frictional contact in three-dimensional fractured media using unstructured tetrahedral meshes. Computer Methods in Applied Mechanics and Engineering 306, 123–150.

Nelson, R., 2001. Geologic analysis of naturally fractured reservoirs. Gulf Professional Publishing.

Nemat-Nasser, S., Horii, H., 1982. Compression-induced nonplanar crack extension with application to splitting, exfoliation, and rockburst. Journal of Geophysical Research 87 (B8), 6805.

Neuman, S. P., 2005. Trends, prospects and challenges in quantifying flow and transport through fractured rocks. Hydrogeology Journal 13 (1), 124–147.

Nikishkov, G. P., Atluri, S. N., 1987. Calculation of fracture mechanics parameters for an arbitrary three-dimensional crack, by the "equivalent domain integral" method. International Journal for Numerical Methods in Engineering 24 (9), 1801–1821.

Ning, P., Feng, Z. Q., Quintero, J. A. R., Zhou, Y. J., Peng, L., 2018. Uzawa algorithm to solve elastic and elastic–plastic fretting wear problems within the bipotential framework. Computational Mechanics 62, 1327–1341.

Oda, M., 1985. Permeability tensor for discontinuous rock masses. Géotechnique 35 (4), 483–495.

O'Hara, P., Duarte, C. A., Eason, T., 2016. A two-scale generalized finite element method for interaction and coalescence of multiple crack surfaces. Engineering Fracture Mechanics 163, 274–302.

Oliver, J., Roubin, E., Caicedo, M., Huespe, A., Hernández, J., 2016. Reduced order modeling strategies for computational multiscale fracture. Computer Methods in Applied Mechanics and Engineering 313, 560–595.

Olson, J. E., 1993. Joint pattern development: effects of subcritical crack growth and mechanical crack interaction. Journal of Geophysical Research 98 (B7), 12251.

Olson, J. E., 2003. Sublinear scaling of fracture aperture versus length: An exception or the rule? Journal of Geophysical Research 108 (B9), 2413.

Olson, J. E., 2004. Predicting fracture swarms—the influence of subcritical crack growth and the crack-tip process zone on joint spacing in rock. Geological Society, London, Special Publications 231 (1), 73–88.

Olson, J. E., Pollard, D. D., 1991. The initiation and growth of en echelon veins. Journal of Structural Geology 13 (5), 595–608.

Otsu, N., 1979. A Threshold Selection Method from Gray-Level Histograms. IEEE Transactions on Systems, Man, and Cybernetics 9 (1), 62–66.

Paluszny, A., Matthäi, S. K., 2009. Numerical modeling of discrete multi-crack growth applied to pattern formation in geological brittle media. International Journal of Solids and Structures 46 (18), 3383–3397.

Paluszny, A., Matthäi, S. K., 2010. Impact of fracture development on the effective permeability of porous rocks as determined by 2-D discrete fracture growth modeling. Journal of Geophysical Research 115 (B2), 1–18.

Paluszny, A., Matthäi, S. K., Hohmeyer, M., 2007. Hybrid finite element-finite volume discretization of complex geologic structures and a new simulation workflow demonstrated on fractured rocks. Geofluids 7 (2), 186–208.

Paluszny, A., Tang, X., Zimmerman, R., 2013. Fracture and impulse based finite-discrete element modeling of fragmentation. Computational Mechanics 52 (5), 1071–1084.

Paluszny, A., Zimmerman, R. W., 2011. Numerical simulation of multiple 3D fracture propagation using arbitrary meshes. Computer Methods in Applied Mechanics and Engineering 200 (9), 953–966.

Paluszny, A., Zimmerman, R. W., 2013. Numerical fracture growth modeling using smooth surface geometric deformation. Engineering Fracture Mechanics 108, 19–36.

Pan, J. B., Lee, C. C., Lee, C. H., Yeh, H. F., Lin, H. I., 2010. Application of fracture network model with crack permeability tensor on flow and transport in fractured rock. Engineering Geology 116 (1-2), 166–177.

Paris, P. C., Erdogan, F., 1963. A critical analysis of crack propagation laws. Journal of Basic Engineering 85 (4), 528.

Paris, P. C., Gomez, M., Anderson, W. E., 1961. A rational analytic theory of fatigue. The Trend in Engineering (13), 9–14.

Pengcheng, F., Scott, M. J., Randolph, R. S., Charles, R. C., 2012. Generalized displacement correlation method for estimating stress intensity factors. Engineering Fracture Mechanics 88, 90 – 107.

Philip, Z. G., Jennings, J. W., Olson, J. E., Laubach, S. E., Holder, J., et al., 2005. Modeling coupled fracture-matrix fluid flow in geomechanically simulated fracture networks. In: SPE Annual Technical Conference and Exhibition. Vol. 8. Society of Petroleum Engineers, pp. 300–309.

Pollard, D. D., Holzhausen, G., 1979. On the mechanical interaction between a fluid-filled fracture and the earth's surface. Tectonophysics 53 (1-2), 27–57.

Pollard, D. D., Segall, P., Delaney, P. T., 1982. Formation and interpretation of dilatant echelon cracks. Geological Society of America Bulletin 93 (12), 1291–1303.

Pook, L. P., Berto, F., Campagnolo, A., Lazzarin, P., 2014. Coupled fracture mode of a cracked disc under anti-plane loading. Engineering Fracture Mechanics 128, 22–36.

Posiva Oy, 2018. General time schedule for final disposal.
URL www.posiva.fi/en/final_disposal/general_time_schedule_for_final_disposal

Prévost, J. H., Sukumar, N., 2016. Faults simulations for three-dimensional reservoir-geomechanical models with the extended finite element method. Journal of the Mechanics and Physics of Solids 86, 1–18.

Price, N., Cosgrove, J., 1990. Analysis of geological structures. Cambridge University Press.

Procter, A., Sanderson, D. J., 2018. Spatial and layer-controlled variability in fracture networks. Journal of Structural Geology 108, 52–65.

Pugno, N., Ciavarella, M., Cornetti, P., Carpinteri, a., 2006. A generalized Paris' law for fatigue crack growth. Journal of the Mechanics and Physics of Solids 54 (7), 1333–1349.

Puso, M. A., Laursen, T. A., 2004. A mortar segment-to-segment contact method for large deformation solid mechanics. Computer Methods in Applied Mechanics and Engineering 193 (6-8), 601–629.

Rabczuk, T., 2013. Computational methods for fracture in brittle and quasi-brittle solids: State-of-the-art review and future perspectives. International Scholarly Research Notices: Applied Mathematics 2013 (849231), 1–38.

Radioactive Waste Management, 2015. National geological screening guidance - providing information on geology. Tech. rep., Nuclear Decomissioning Authority.

Radioactive Waste Management, 2016a. Geological disposal: Geosphere status report. Tech. Rep. DSSC/453/01, Radioactive Waste Management.

Radioactive Waste Management, 2016b. Radioactive Wastes in the UK: A Summary of the 2016 Inventory. Tech. rep., Nuclear Decomissioning Authority.

Ren, F., Ma, G., Fan, L., Wang, Y., Zhu, H., 2017. Equivalent discrete fracture networks for modelling fluid flow in highly fractured rock mass. Engineering Geology 229, 21–30.

Ren, G., Jiang, J., Younis, R. M., 2016. A fully coupled XFEM-EDFM model for multiphase flow and geomechanics in fractured tight gas reservoirs. Procedia Computer Science 80, 1404–1415.

Renard, P., de Marsily, G., 1997. Calculating equivalent permeability: a review. Advances in Water Resources 20 (5-6), 253–278.

Renshaw, C. E., Park, J. C., 1997. Effect of mechanical interactions on the scaling of fracture length and aperture 386, 482–484.

Renshaw, C. E., Pollard, D. D., 1994. Numerical simulation of fracture set formation: a fracture mechanics model consistent with experimental observations. Journal of Geophysical Research 99 (B5), 9359–9372.

Renshaw, C. E., Pollard, D. D., 1995. An experimentally verified criterion for propagation across unbounded frictional interfaces in brittle, linear elastic materials. International Journal of Rock Mechanics and Mining Sciences and 32 (3), 237–249.

Riahi, A., Hammah, E. R., Curran, J. H., 2010. Limits of applicability of the finite element explicit joint model in the analysis of jointed rock problems. In: 44th US Rock Mechanics Symposium - 5th US/Canada Rock Mechanics Symposium. American Rock Mechanics Association.

Rice, J. R., 1968. A path independent integral and the approximate analysis of strain concentration by notches and cracks. Journal of Applied Mechanics 35, 379–386.

Rice, J. R., 1985. First-order variation in elastic fields due to variation in location of a planar crack front. Journal of Applied Mechanics 52 (3), 571.

Rice, J. R., Ben-Zion, Y., Klm, K. S., 1994. Three-dimensional perturbation solution for a dynamic planar crack moving unsteadily in a model elastic solid. Journal of the Mechanics and Physics of Solids 42 (5), 813–843.

Richard, H. A., Eberlein, A.and Schirmeisen, N.-H., 2013. Experiments on cracks under spatial loading. In: 13th International Conference on Fracture. pp. 1–10.

Richard, H. A., Fulland, M., Sander, M., 2004. Theoretical crack path prediction. Fatigue and Fracture of Engineering Materials and Structures 28, 3–12.

Richard, H. A., Schramm, B., Schirmeisen, N. H., 2014. Cracks on mixed mode loading - theories, experiments, simulations. International Journal of Fatigue 62, 93–103.

Rives, T., Razack, M., Petit, J.-P., Rawnsley, K., 1992. Joint spacing: analogue and numerical simulations. Journal of Structural Geology 14 (8-9), 925–937.

Robinson, P. C., 1983. Connectivity of fracture systems - a percolation theory approach. Journal of Physics A: Mathematical and General 16 (3), 605–614.

Robinson, P. C., 1984. Numerical calculations of critical densities for lines and planes. Journal of Physics A: Mathematical and General 17 (14), 2823–2830.

Roering, J. J., Cooke, M. L., Pollard, D. D., 1997. Why blind thrust faults do not propagate to the Earth's surface: Numerical modeling of coseismic deformation associated with thrust-related anticlines. Journal of Geophysical Research: Solid Earth 102 (B6), 11901–11912.

Rondinella, V. V., Papaioannou, D., Nasyrow, R., Goll, W., Rhem, M., 2015. Measurement of gas permeability along the axis of a spent fuel rod. Top Fuel.

Roque, V., Cros, B., Baron, D., Dehaudt, P., 2000. Effects of the porosity in uranium dioxide on microacoustic and elastic properties. Journal of Nuclear Materials 277 (2-3), 211–216.

Rutqvist, J., Figueiredo, B., Hu, M., Tsang, C. F., 2017. Continuum modeling of hydraulic fracturing in complex rock masses. In: Hydraulic fracture modeling. Elsevier.

Rutqvist, J., Stephansson, O., 2003. The role of hydromechanical coupling in fractured rock engineering. Hydrogeology Journal 11 (1), 7–40.

Sævik, P. N., Berre, I., Jakobsen, M., Lien, M., 2013. A 3D computational study of effective medium methods applied to fractured media. Transport in Porous Media 100 (1), 115–142.

Saevik, P. N., Jakobsen, M., Lien, M., Berre, I., 2014. Anisotropic effective conductivity in fractured rocks by explicit effective medium methods. Geophysical Prospecting 62 (6), 1297–1314.

Saksala, T., Brancherie, D., Harari, I., Ibrahimbegovic, A., 2015. Combined continuum damage-embedded discontinuity model for explicit dynamic fracture analyses of quasi-brittle materials. International Journal for Numerical Methods In Engineering 101, 230–250.

Salimzadeh, S., Paluszny, A., Zimmerman, R. W., 2017a. Three-dimensional poroelastic effects during hydraulic fracturing in permeable rocks. International Journal of Solids and Structures 108, 153–163.

Salimzadeh, S., Paluszny, A., Zimmerman, R. W., 2018. Effect of cold CO2 injection on fracture apertures and growth. International Journal of Greenhouse Gas Control 74, 130–141.

Salimzadeh, S., Usui, T., Paluszny, A., Zimmerman, R. W., 2017b. Finite element simulations of interactions between multiple hydraulic fractures in a poroelastic rock. International Journal of Rock Mechanics and Mining Sciences 99, 9–20.

Sanderson, D. J., Nixon, C. W., 2015. The use of topology in fracture network characterization. Journal of Structural Geology 72, 55–66.

Schlumberger Geoquest, 2009. ECLIPSE reservoir simulator.

Schultz, R. A., 2000. Fault-population statistics at the Valles Marineris Extensional Province, Mars: Implications for segment linkage, crustal strains, and its geodynamical development. Tectonophysics 316 (1-2), 169–193.

Segall, P., 1984. Formation and growth of extensional fracture sets. Geological Society of America Bulletin 95 (4), 454–462.

Shakiba, M., Cavalcante Filho, J. S. d. A., Sepehrnoori, K., 2018. Using Embedded Discrete Fracture Model (EDFM) in numerical simulation of complex hydraulic fracture networks calibrated by microseismic monitoring data. Journal of Natural Gas Science and Engineering 55, 495–507.

Sheibani, F., 2013. Solving three dimensional problems in natural and hydraulic fracture development: Insight from displacement discontinuity modeling. Ph.D. thesis, University of Texas at Austin.

Shokri, A. R., Babadagli, T., Jafari, A., 2016. A critical analysis of the relationship between statistical- and fractal-fracture-network characteristics and effective fracture-network permeability. SPE Reservoir Evaluation & Engineering (19), 494–510.

Šimůnek, J., Jarvis, N. J., van Genuchten, M., Gärdenäs, A., 2003. Review and comparison of models for describing non-equilibrium and preferential flow and transport in the vadose zone. Journal of Hydrology 272 (1-4), 14–35.

Simo, J. C., Laursen, T. A., 1992. An augmented Lagrangian treatment of contact problems involving friction. Computers and Structures 42 (1), 97–116.

SKB, 2018. Spent fuel repository factsheet. Tech. rep., Swedish Nuclear Fuel and Waste Management Company (SKB).

Snow, D. T., 1969. Anisotropic permeability of fractured media. Water Resources Research 5 (6), 1273–1289.

Stefansson, I., Berre, I., Keilegavlen, E., 2017. Hybrid-dimensional finite volume discretizations for fractured porous media Di.

Stonesifer, R., Brust, F., Leis, B., 1993. Mixed-mode stress intensity factors for interacting semi-elliptical surface cracks in a plate. Engineering Fracture Mechanics 45 (3), 357–380.

Stüben, K., Ruge, J. W., Clees, T., Gries, S., 2017. Algebraic multigrid: From academia to industry. Springer.

Sukumar, N., Chopp, D., Moran, B., 2003. Extended finite element method and fast marching method for three-dimensional fatigue crack propagation. Engineering Fracture Mechanics 70 (1), 29–48.

Tang, H., Winterfeld, P. H., Wu, Y. S., qin Huang, Z., Di, Y., Pan, Z., Zhang, J., 2016. Integrated simulation of multi-stage hydraulic fracturing in unconventional reservoirs. Journal of Natural Gas Science and Engineering 36, 875–892.

Tanné, E., Li, T., Bourdin, B., Marigo, J. J., Maurini, C., 2018. Crack nucleation in variational phase-field models of brittle fracture. Journal of the Mechanics and Physics of Solids 110, 80–99.

Tatone, B. S. A., Grasselli, G., 2014. Characterization of the effect of normal load on the discontinuity morphology in direct shear specimens using X-ray micro-CT. Acta Geotechnica 10 (1), 31–54.

Tesauro, M., Audet, P., Kaban, M. K., Brgmann, R., Cloetingh, S., 2012. The effective elastic thickness of the continental lithosphere: Comparison between rheological and inverse approaches. Geochemistry, Geophysics, Geosystems 13 (9), 1–18.

Thomas, A. L., Pollard, D. D., 1993. The geometry of echelon fractures in rock: implications from laboratory and numerical experiments 15 (3-5), 323–334.

Thomas, R. N., Paluszny, A., Hambley, D., Hawthorne, F. M., Zimmerman, R. W., 2018a. Permeability of observed three dimensional fracture networks in spent fuel pins. Journal of Nuclear Materials.

Thomas, R. N., Paluszny, A., Zimmerman, R. W., 2017a. Fracture interaction data supporting Thomas et al. 2017, 'Quantification of fracture interaction using stress intensity factor variation maps'.

Thomas, R. N., Paluszny, A., Zimmerman, R. W., 2017b. Quantification of fracture interaction using stress intensity factor variation maps. Journal of Geophysical Research: Solid Earth 122 (10), 7698–7717.

Thomas, R. N., Paluszny, A., Zimmerman, R. W., 2018b. Effect of fracture growth velocity exponent on fluid flow through geomechanically-grown 3D fracture networks. In: 2nd International Discrete Fracture Network Engineering Conference. American Rock Mechanics Association.

Thovert, J.-F., Mourzenko, V. V., Adler, P. M., 2017. Percolation in three-dimensional fracture networks for arbitrary size and shape distributions. Physical Review E 95 (4), 042112.

Trollé, B., Gravouil, A., Baietto, M. C., Nguyen-Tajan, T. M. L., 2012. Optimization of a stabilized X-FEM formulation for frictional cracks. Finite Elements in Analysis and Design 59, 18–27.

Tsang, C.-f., Neretnieks, I., 1998. Flow channeling in heterogeneous fractured rocks. Reviews of Geophysics 36 (2), 275–298.

Tsang, C.-F., Neretnieks, I., Tsang, Y., 2015. Hydrologic issues associated with nuclear waste repositories. Water Resources Research 51 (9), 6923–6972.

Tuckwell, G. W., Lonergan, L., Jolly, R. J. H., 2003. The control of stress history and flaw distribution on the evolution of polygonal fracture networks. Journal of Structural Geology 25 (8), 1241–1250.

Ucar, E., Keilegavlen, E., Berre, I., Nordbotten, J. M., 2018. A finite-volume discretization for deformation of fractured media. Computational Geosciences 22, 993–1007.

UK Government, 2018. Implementing geological disposal: a framework for the long-term management of higher activity radioactive waste. Department for Business, Energy & Industrial Strategy.

USDOE Blue Ribbon Committee, 2012. Report to the Secretary of Energy.

Vasoya, M., Unni, A. B., Leblond, J. B., Lazarus, V., Ponson, L., 2016. Finite size and geometrical non-linear effects during crack pinning by heterogeneities: an analytical and experimental study. Journal of the Mechanics and Physics of Solids 89, 211–230.

Vieira, A. P., Andrade, J. S., Herrmann, H. J., 2008. Subcritical crack growth: the microscopic origin of Paris' law. Physical Review Letters 100 (19), 8–11.

Vu, M. N., Pouya, A., Seyedi, D. M., 2018. Effective permeability of three-dimensional porous media containing anisotropic distributions of oriented elliptical disc-shaped fractures with uniform aperture. Advances in Water Resources 118, 1–11.

Walsh, J. B., Brace, W. F., 1964. A fracture criterion for brittle anisotropic rock. Journal of Geophysical Research 69 (16), 3449–3456.

Warren, J. E., Root, P. J., 1963. The behavior of naturally fractured reservoirs. Society of Petroleum Engineers Journal 3 (03), 245–255.

Wei, M. D., Dai, F., Xu, N. W., Zhao, T., Xia, K. W., 2016. Experimental and numerical study on the fracture process zone and fracture toughness determination for ISRM-suggested semi-circular bend rock specimen. Engineering Fracture Mechanics 154, 43–56.

Wettstein, S. J., Wittel, F. K., Arajo, N. a. M., Lanyon, B., Herrmann, H. J., 2012. From invasion percolation to flow in rock fracture networks. Physica A: Statistical Mechanics and its Applications 391 (1-2), 264–277.

Wiesner, C., Maddox, S., Xu, W., Webster, G., Burdekin, F., Andrews, R., Harrison, J., 2000. Engineering critical analyses to BS7910 - the UK guide on methods for assessing the acceptability of flaws in metallic structures. International Journal of Pressure Vessels and Piping 77 (14), 883–893.

Williams, M. L., 1957. On the stress distribution at the base of a stationary crack. Journal of Applied Mechanics 24 (1), 109–114.

Witherspoon, P., Bodvarsson, G. S., 2006. Geological challenges in radioactive waste isolation, fourth worldwide review. LBNL-59808.

Witherspoon, P. A., Wang, J. S. Y., Iwai, K., Gale, J. E., 1980. Validity of cubic law for fluid flow in a deformable rock fracture. Water Resources Research 16 (6), 1016–1024.

Wong, R. H. C., Tang, C. A., Chau, K. T., Lin, P., 2002. Splitting failure in brittle rocks containing pre-existing flaws under uniaxial compression. Engineering Fracture Mechanics 69 (17), 1853–1871.

Wriggers, P., Zavarise, G., 1993. Application of augmented lagrangian techniques for non-linear constitutive laws in contact interfaces. Communications in Numerical Methods in Engineering 9 (10), 815–824.

Yan, B., Wang, Y., Killough, J. E., 2016. Beyond dual-porosity modeling for the simulation of complex flow mechanisms in shale reservoirs. Computational Geosciences 20 (1), 69–91.

Yan, C., Zheng, H., 2017. FDEM-flow3D: A 3D hydro-mechanical coupled model considering the pore seepage of rock matrix for simulating three-dimensional hydraulic fracturing. Computers and Geotechnics 81, 212–228.

Yan, X., 2010. A boundary element analysis for stress intensity factors of multiple circular arc cracks in a plane elasticity plate. Applied Mathematical Modelling 34 (10), 2722–2737.

Yang, S., Cao, M., Ren, X., Ma, G., Zhang, J., Wang, H., 2018. 3D crack propagation by the numerical manifold method. Computers and Structures 194, 116–129.

Yu, H., Wu, L., Guo, L., Du, S., He, Q., 2009. Investigation of mixed-mode stress intensity factors for nonhomogeneous materials using an interaction integral method. International Journal of Solids and Structures 46 (20), 3710–3724.

Zachariasen, J., Sieh, K., 1995. The transfer of slip between two en echelon strike-slip faults: A case study from the 1992 Landers earthquake, southern California. Journal of Geophysical Research 100 (B8), 15281.

Zhan, S., Wang, T., 2006. Interactions of penny-shaped cracks in three-dimensional solids. Acta Mechanica Sinica/Lixue Xuebao 22 (4), 341–353.

Zhang, N., Yao, J., Xue, S., Huang, Z., 2016. Multiscale mixed finite element, discrete fracture–vug model for fluid flow in fractured vuggy porous media. International Journal of Heat and Mass Transfer 96, 396–405.

Zhou, R., Song, Z., Lu, Y., 2017. 3D mesoscale finite element modelling of concrete. Computers and Structures 192, 96–113.

Zimmerman, R. W., 2018. Fluid Flow in Porous Media. The Imperial College Lectures in Petroleum Engineering. World Scientific Publishing Company.

Zimmerman, R. W., Bodvarsson, G. S., 1996. Hydraulic conductivity of rock fractures. Transport in Porous Media 23 (1), 1–30.

Zimmerman, R. W., Gang Chen, Hadgu, T., Bodvarsson, G. S., 1993. A numerical dual-porosity model with semianalytical treatment of fracture/matrix flow. Water Resources Research 29 (7), 2127–2137.

Zimmerman, R. W., Paluszny, A., 2012. Some new developments in modelling the failure, fracture and fragmentation of rocks. 7th Asian Rock Mechanics Symposium, 3–18.

Zou, L., Jing, L., Cvetkovic, V., 2017. Shear-enhanced nonlinear flow in rough-walled rock fractures. International Journal of Rock Mechanics and Mining Sciences 97, 33–45.